Dissertation

submitted to the

Combined Faculty of Mathematics, Engineering and Natural Sciences

of Heidelberg University, Germany

for the degree of

Doctor of Natural Sciences

Put forward by

Elvira Beisel, M. Sc.

born in Speyer

Oral examination: 17.10.2024

Radiocarbon in Cold-Water Corals of the Eastern Atlantic Thermocline Over the Last 38,000 Years

Referees:

Prof. Dr. Norbert Frank

Prof. Dr. Werner Aeschbach

Abstract

The ocean is an important CO_2 reservoir that significantly shaped the climate over glacial-interglacial time scales. Radiocarbon (^{14}C) ventilation ages are a powerful tool to investigate the ocean circulation and carbon cycle. In this thesis, absolutely dated cold-water corals from the Eastern Atlantic thermocline were analyzed using ^{14}C dating to assess ^{14}C ventilation ages through time. An examination of quality control parameters at the Heidelberg ^{14}C Laboratory confirmed optimal conditions for accurate ^{14}C measurements. Prior to the establishment of modern circulation, the thermoclines of the North and South Atlantic acted as separate carbon reservoirs. During the last glacial, cold-water corals from the South Atlantic indicated storage of respired carbon, which likely contributed to the deglacial atmospheric CO_2 release. In contrast, North Atlantic cold-water corals documented a well-equilibrated thermocline. Subsequently, the phenomenon of "^{14}C ventilation anomalies" was investigated, which do not fit into the prevailing framework of ocean ventilation through time. The underlying causes were discussed. Furthermore, additional criteria for data filtering have been developed. Finally, rapid changes in the marine ^{14}C content and a relation to abrupt ^{14}C production rate changes, an underestimated atmospheric calibration curve, as well as with climatic fluctuations were discussed.

Zusammenfassung

Der Ozean ist ein bedeutsamer CO_2-Speicher, welcher das Klima über glaziale und interglaziale Zeitskalen hinweg maßgeblich beeinflusst hat. Radiokohlenstoff (^{14}C) Ventilationsalter eignen sich hervorragend zur Untersuchung der Ozeanventilation und des Kohlenstoffkreislaufs. In dieser Arbeit wurden absolut datierte Kaltwasserkorallen aus der Thermokline des Ostatlantiks mittels ^{14}C-Datierung analysiert um ^{14}C Ventilationsalter zu bestimmen. Eine Untersuchung der Qualitätskontrollparameter im Heidelberger ^{14}C-Labor bestätigte optimale Bedingungen für exakte ^{14}C-Messungen. Vor der Etablierung der modernen Zirkulation agierten die Thermokline des Nord- und Südatlantiks als getrennte Kohlenstoffreservoire. Während des letzten Glazials weisen südatlantische Kaltwasserkorallen auf die Speicherung von altem Kohlenstoff hin, der wahrscheinlich zur deglazialen Freisetzung von atmosphärischem CO_2 beigetragen hat. Im Gegensatz dazu dokumentierten nordatlantische Kaltwasserkorallen eine gut ventilierte Thermokline. Anschließend wurde das Phänomen von "Ventilationsanomalien" untersucht. Die zugrunde liegenden Ursachen wurden erörtert. Außerdem wurden zusätzliche Kriterien für die Datenfilterung entwickelt. Abschließend wurde ein Zusammenhang zwischen rapiden Veränderungen des marinen ^{14}C-Gehalts, ^{14}C-Produktionsratenänderungen, einer unterschätzten atmosphärischen Kalibrierungskurve, sowie rapiden Klimaänderungen diskutiert.

Contents

1. Motivation

The ocean, in constant exchange with the atmosphere, plays an essential role in glacial-interglacial atmospheric CO_2 changes. A thorough comprehension of the oceans' ability to store, accumulate, and disperse carbon over prolonged periods of time is essential for closing the carbon budget and for the understanding of the associated climate change. Paleoceanography seeks to gain insights into the ocean's past. Here, knowledge can be validated through observations and model results. It is hypothesized that dramatic changes in atmospheric CO_2 during the deglaciation are attributable to the outgassing of respired carbon that had been confined to the deep ocean during the last glacial (e.g. Adkins, 2013; Chen et al., 2015; Li et al., 2020; Marcott et al., 2014; Skinner et al., 2017, 2021, 2023).

Radiocarbon (^{14}C) usually serves as a radiometric dating tool. However, if the absolute age of a marine sample is known, a powerful tool to investigate the past ocean circulation and carbon cycle can be employed: ^{14}C ventilation ages. An understanding of ^{14}C ventilation ages over time is essential for accurate dating of marine samples and crucial to sharpen our understanding of the carbon cycle. An increasing number of ^{14}C records have contributed to our evolving understanding of past ocean circulation and ventilation, as well as the its role throughout climate change (e.g. compilations by Rafter et al. (2022); Skinner et al. (2017); Skinner and Bard (2022); Skinner et al. (2023); Zhao et al. (2018)). However, regional scatter and temporal restraint observed in the compiled data make interpretation challenging, underscoring the need for further research and a more comprehensive understanding of the carbon cycle and ocean ventilation processes (Rafter et al., 2022; Skinner et al., 2019; Skinner and Bard, 2022; Skinner et al., 2023). Especially the thermocline ($\sim$200-1000m), acting between well-equilibrated surface waters and deeper, less-equilibrated waters, revealed dynamic behavior through time and space (e.g. Burke and Robinson, 2012; Chen et al., 2015, 2020; Frank et al., 2004; Hines et al., 2015; Li et al., 2020; Mangini et al., 2010; Robinson et al., 2005; Schröder-Ritzrau et al., 2003).

To that end, this thesis further examines ^{14}C ventilation age variability in the Atlantic thermocline. As a paleocanographic archive, cold-water corals are utilized. They can be absolutely dated using the $^{230}Th/U$ method. As they grow, they record the

^{14}C content of the surrounding seawater and thus enable the reconstruction of ^{14}C ventilation ages, otherwise known as reservoir ages (e.g. Adkins, 1998; Adkins et al., 1998, 2002; Frank et al., 2004; Mangini et al., 1998).

Each chapter begins with an introduction to the respective question addressed. The fundamental concepts are introduced in Chapter 2, while the methodologies employed are outlined in Chapter 3.

In order to evaluate the quality of the ^{14}C measurements, Chapter 4 conducts a detailed examination of the ^{14}C data from the Heidelberg ^{14}C laboratory, assessing quality parameters.

Chapter 5 deals with the question of how ^{14}C ventilation ages of the eastern Atlantic thermocline have evolved over the last 32,000 years. The results are compared with modeling results provided by Dr. Martin Butzin, and ^{14}C ventilation age variability is interpreted. This chapter has been published in the journal *Paleoceanography and Paleoclimatology* (Beisel et al., 2023).

However, the generation of new ^{14}C ventilation ages still poses challenges in some regions. "^{14}C ventilation anomalies" have been observed on numerous occasions, i.e. ventilation ages that do not fit into the prevailing framework of ocean ventilation through time or appear to be above the atmospheric reference. Moreover, subsequent studies have been unable to corroborate or reject these observations. While this phenomenon has already been discussed and explanations have been attempted for the archive foraminifera (Skinner and Bard (2022) and references therein), the topic has received less attention for $^{230}Th/U$-dated cold-water corals. Chapter 6 examines the question of what causes these anomalies in cold-water corals and refines data selection criteria to remove affected samples.

Chapter 7 addresses a time range that has been sparsely investigated with respect to ^{14}C ventilation ages: 38,000 - 30,000 years ago. Within the last glacial, this period is characterized by several abrupt, short-term warming events (e.g. EPICA, 2006; Li and Born, 2019; Menviel et al., 2020; Rahmstorf, 2002). Moreover, several rapid changes in the ^{14}C production rate are postulated (e.g. Korte et al., 2019; Laj et al., 2014). This chapter examines the implications for the ^{14}C ventilation ages of the upper Eastern Atlantic thermocline and explores the question of when the shoaling of the thermocline and increased carbon storage was initiated.

Finally, in Chapter 8, this thesis' conclusions are summarized, along with suggestions for future research.

2. Fundamentals

2.1. Ocean Circulation

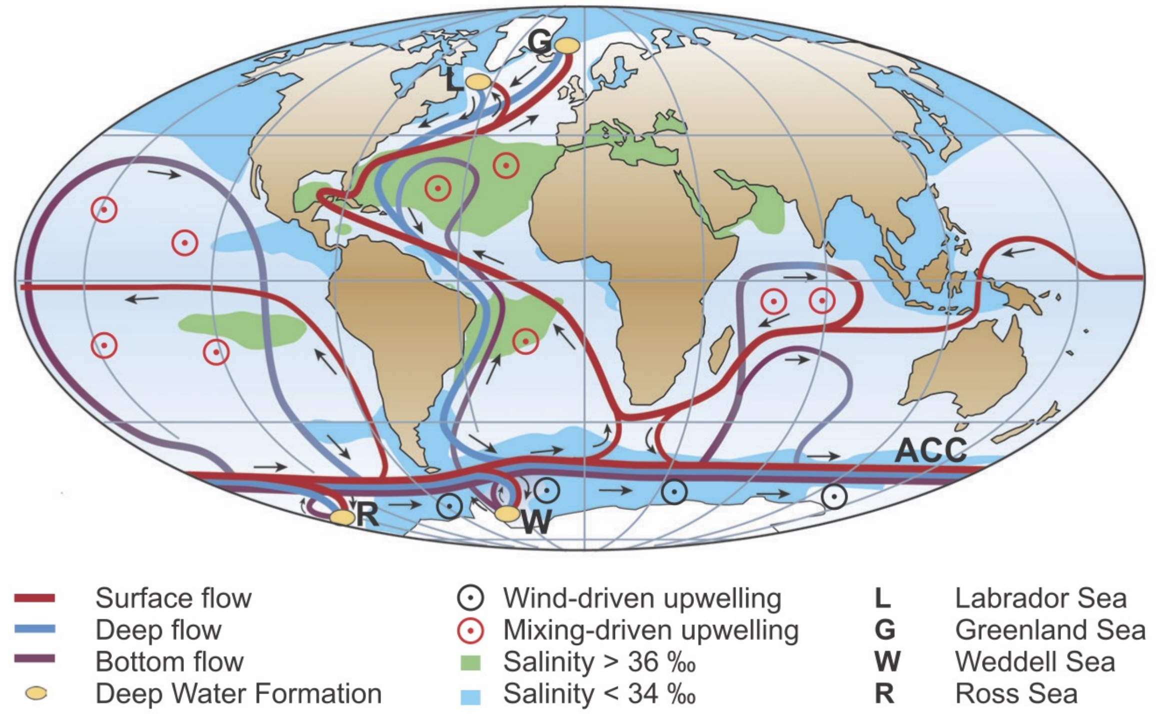

Figure 2.1.: Simplified thermohaline circulation. Figure taken from Kuhlbrodt et al. (2007), after Rahmstorf (2002).

The ocean covers about 71 % of the Earth's surface and has an average depth of 3.8 km. Key features are its large heat storage capacity and its ability to store and transport dissolved elements and gases. In constant exchange with the atmosphere, the ocean plays an important role in modulating the Earth's climate (Broecker, 1991). With a global mixing time for the ocean interior of approximately 1000a, the ocean acts rather slowly compared to the atmosphere. Movement, i.e. circulation patterns, can be traced through water masses. Water masses are defined by their formation history and properties such as salinity, (potential) temperature, and (potential) density (Liu and Tanhua, 2021). In addition, oxygen, silicate, phosphate, and nitrate content can be included in the characterization of water masses (Liu and Tanhua, 2021).

The Meridional Overturning Circulation (MOC) is a combination of wind-driven transfer of momentum in the upper layer (∼100m) and the Thermohaline Circulation (THC). The THC is driven by heat and freshwater fluxes, which affect the density distribution and hence the pressure gradients in polar regions (Rahmstorf, 2006). Both are intertwined, and changes in one cause changes in the other. There are four major deep water formation areas where high latitude cooling combined with less stratified water masses allows cold and dense water to sink: Greenland-Norwegian Sea and Labrador Sea, resulting in the formation of North Atlantic Deep Water (NADW), and the Weddell Sea and Ross Sea, resulting in the formation of Antarctic Bottom Water (AABW) (Rahmstorf, 2006; Kuhlbrodt et al., 2007)(figure 2.1). At present, the balance between advection of cold water from the pole and diffusion of heat by turbulent mixing leads to a steady and slow overturning circulation (Rahmstorf, 2006; Talley, 2013).

Climate change alters the main driving forces of ocean circulation, therefore ocean circulation is thought to have significantly changed during glacial and interglacial periods. The following chapter provides an overview of climatic changes over the last 40 ka.

2.2. Climatic Changes Over the Last 40,000 years

By using the radiocarbon method (chapter 2.5), the focus of this work is limited to the last 40,000 years. This period includes part of the last glacial, the Last Glacial Maximum (LGM) and the subsequent deglaciation, as well as several abrupt climate changes (figure 2.2).

Dansgaard/Oeschger (D/O) events refer to rapid temperature changes in the Northern Hemisphere (e.g. Dansgaard et al., 1982, 1993; Pedro et al., 2022; Rasmussen et al., 2014). The climate system fluctuates between stadial (cold) and interstadial (warm) conditions of varying duration. Over the past 40,000 years, eight D/O events have been documented (figure 2.2). These D/O events are characterized by a rapid, average warming of 8.5°C (D/O 2) to 15.5°C (D/O 7) (with a ±3°C (2σ) uncertainty range) over several decades at the North Greenland Ice Core Project (NGRIP) site (Kindler et al., 2014). Unforced or "spontaneous" oscillations of the atmosphere-ice-ocean system, disturbances such as meltwater and ice sheet expansion, and instability are discussed as potential causes (e.g. Li and Born, 2019; Malmierca-Vallet et al., 2023; Menviel et al., 2020). These events were accompanied by changes in climate and the carbon cycle, and potentially the strength of the Atlantic Meridional Overturning Circulation (AMOC) (Menviel et al., 2020). The Southern Hemisphere exhibited a

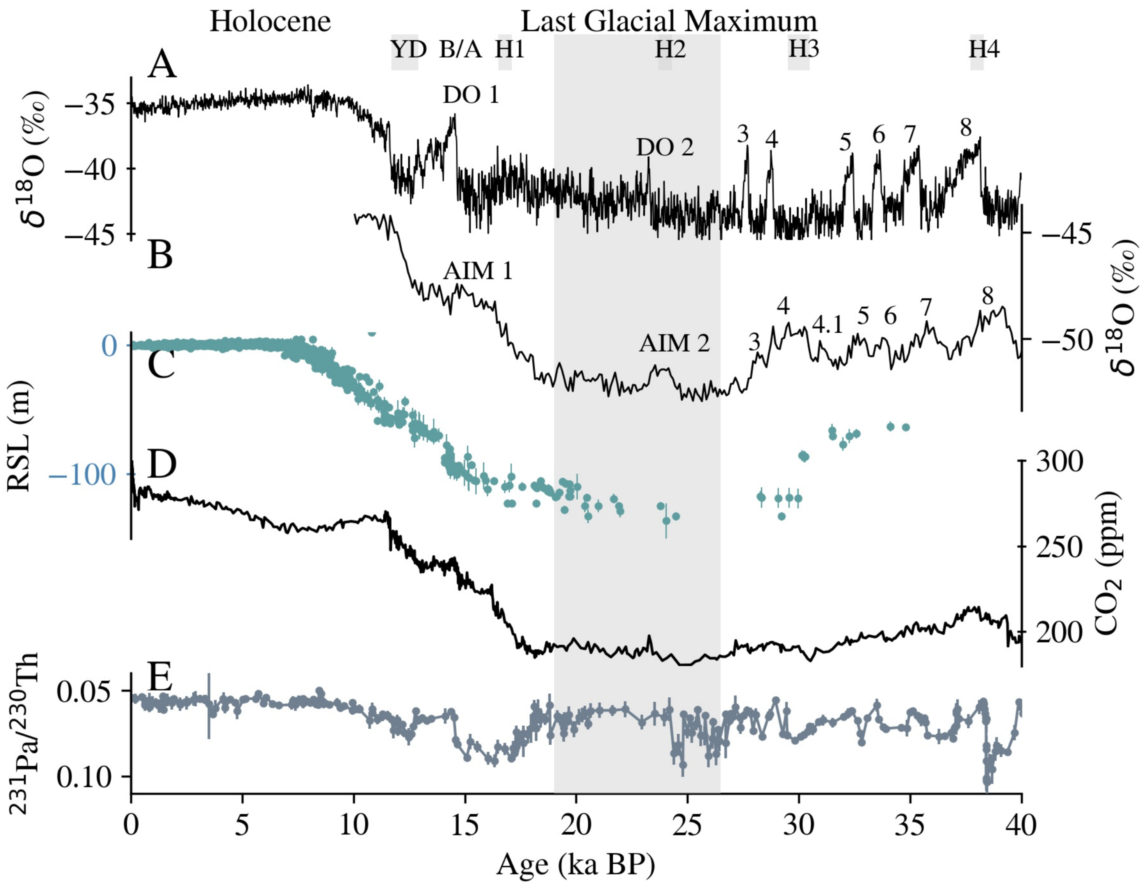

Figure 2.2.: Climate change over the last 40.000 years in various climate records from ice cores to marine sediments. Gray shading indicates climatic events. Age is given relation to the year 1950 (*BP*, before present). (A) δ^{18}O isotope record obtained from an ice core from the NGRIP site in Greenland (Bazin et al., 2013). Lower values indicate cold (glacial) periods, higher values warmer (interglacial) periods. (B) δ^{18}O isotope record obtained from an ice core from the EDML site in Antarctica (EPICA, 2006). (C) Reconstruction of changes in relative sea level (RSL) over time based on tropical coral data (Lambeck et al., 2014). (D) Compiled atmospheric CO_2 concentration reconstructed from ice cores in Antarctica (Bereiter et al., 2015). (E) ^{231}Pa/^{230}Th record from the Atlantic, as a reconstruction of the strength of the Atlantic Meridional Overturning Circulation (AMOC) (Böhm et al., 2015; Henry et al., 2016; Lippold et al., 2019; McManus et al., 2004). Higher values indicate a weaker AMOC, while lower values indicate a stronger AMOC.

contrasting pattern to that observed in the Northern Hemisphere, a phenomenon known as "seesaw behavior", and characterized by **Antarctic Isotope Maxima** (AIM) (Anderson et al., 2021; Buizert and Schmittner, 2015; EPICA, 2006; Rahmstorf, 2002; Zheng et al., 2021). AIM are characterized by a 1-3°C warming in the Southern Hemisphere that occured well before the onset of a D/O event (EPICA, 2006). A connection through the MOC is assumed, since the amplitude of AIM events depends linearly on the duration of D/O events (EPICA, 2006).

Heinrich events are rapid changes caused by the massive discharge of icebergs from the Laurentide Ice Sheet that lasted 500 ± 250 years (Hemming, 2004). They have been detected by ice-rafted debris, including drop stones, in sediment cores (e.g. Barker et al., 2015; Heinrich, 1988). The lowering of the surface density in the polar North Atlantic provides a positive feedback to the so-called Heinrich stadials, longer cold periods (e.g. Barker et al., 2015). They are associated with a weak or even shutdown Atlantic Meridional Overturning Circulation (AMOC) (e.g. Böhm et al., 2015; Hemming, 2004; Henry et al., 2016; Menviel et al., 2020).

The **Last Glacial Maximum** (LGM) is the period of maximum extent of the ice sheets, which they reached between 33-26.5 ka and lasted until 20-19 ka (e.g. Clark et al., 2009; Yokoyama et al., 2000). It was accompanied by a lower sea level, approximately 140 meters lower than today (figure 2.2c, Lambeck et al. (2014)). Moreover, it is assumed that the reduced heat transport and increased salt concentration led to a haline deep circulation (Adkins, 2013), rather than a *thermo*haline circulation as today (chapter 2.1). Furthermore, it is assumed that the glacial ocean was more stratified and stored more CO_2, reflected in a lower atmospheric CO_2 concentration of ∼180ppm (e.g. Adkins, 2013; Bereiter et al., 2015; Lund et al., 2011; Skinner et al., 2010) (chapter 2.5.3).

The LGM was succeeded by the **deglaciation**, also known as **Termination 1** (e.g. Clark et al., 2012; Waelbroeck et al., 2001), with global sea level rise through melting of ice sheets (figure 2.2c, Lambeck et al. (2014)) and increasing atmospheric CO_2 (figure 2.2d, Bereiter et al. (2015); Marcott et al. (2014)). This was followed by a brief and abrupt warm period between 14.7-12.9 ka in the Northern Hemisphere, known as the **Bølling-Allerød** interstadial, which can be used as a synonym for D/O 1 (e.g. Naughton et al., 2023; Rasmussen et al., 2014). Its Southern Hemisphere counterpart, the **Antarctic Cold Reversal**, is a millennial-scale cooling event that occurred between 14.7-13 ka (e.g. Blunier et al., 1997; Pedro et al., 2016). It preceeded an abrupt cooling to near-glacial conditions in the Northern Hemisphere, the **Younger Dryas**, which occurred between 12.9-11.6 ka (Broecker et al., 2010; Dansgaard et al., 1989). Following the Younger Dryas, the **Holocene**, the current warm period, began

(Walker et al., 2009).

A variety of archives, including ice cores and stalagmites for the reconstruction of atmospheric changes, as well as sediments and the remains of organisms such as foraminifera and corals for the reconstruction of oceanic changes, can be utilized to obtain information about past climate conditions and their effects. The following section provides information about cold-water corals as a climate archive. Their wide temporal and spatial distribution and their ability to record water mass properties make them a valuable paleoclimatic archive.

2.3. Cold-Water Corals

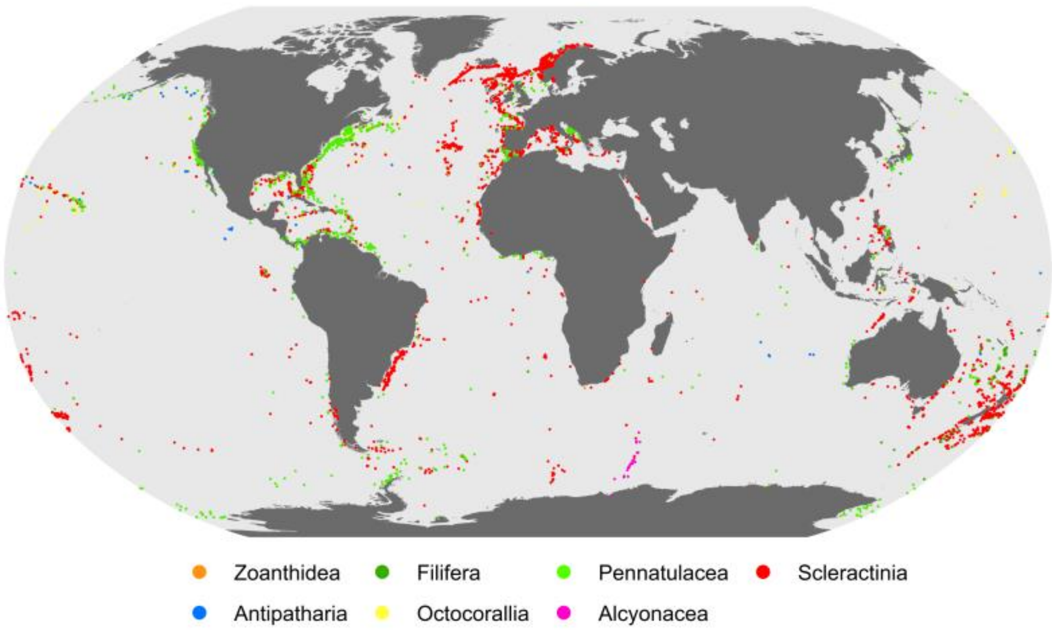

Figure 2.3.: Global distribution of CWCs, with subdivision into different subclasses. This study used mainly Scleractinia CWCs. The distribution may be biased as most of the CWC studies were conducted in the North Atlantic. Figure taken from Freiwald et al. (2017).

In contrast to the well-known tropical corals, cold-water corals (CWC), also known as deep-sea corals, live at greater depths and in much colder conditions, as the name suggests. Depending on the species, they occur solitary or in reefs throughout the entire ocean (figure 2.3) (Balogh et al., 2023; Cordes et al., 2023; Freiwald et al., 2017) and at depths from 50 m to 1000 m or below 4000 m depending on the region (e.g. Cairns, 2007; Freiwald et al., 2017; Roberts et al., 2006; Roberts, 2009). This thesis utilizes Scleractinia corals with aragonite skeletons (ret dots in figure 2.3), mainly *Desmophyllum pertusum* (formerly known as *Lophelia pertusa*, Addamo et al. (2016)) and *Madrepora oculata*.

The relevant habitat conditions vary depending on the species. Generally, CWCs require a hard substrate on which the larvae can settle, sufficient temperature (between 4-12°C) and salinity (31.7-38.8 psu) (Büscher et al., 2022; Cairns, 2007; Davies et al., 2008; Roberts et al., 2006). Moreover, they depend on the oxygen content, the aragonite saturation state, sufficient nutrients and strong currents (e.g. Büscher et al., 2022; Cairns, 2007; Davies et al., 2008; Freiwald et al., 2004; Roberts et al., 2006; Wienberg and Titschack, 2016). Strong currents are particularly important here. They not only provide a constant supply of nutrients, which can be in the form of zooplankton, algae, bacteria, etc. (Mueller et al., 2014), but also ensure that the corals are not buried in the surrounding sediment. The preferred environmental conditions depend on the species. In general, CWCs can tolerate a wider range of environmental factors, such as temperatures as low as -1.8°C or hypoxic waters (e.g. Buhl-Mortensen et al., 2024; Davies et al., 2008; Dullo et al., 2008; Gori et al., 2023; Hanz et al., 2019; Hebbeln et al., 2020; Moctar et al., 2024; Naumann et al., 2014).

Under optimal conditions, CWCs can form gigantic reefs and mounds, complex three-dimensional structures on the seafloor, up to several hundred meters in height and several kilometers in diameter (e.g. Freiwald et al., 2004; Roberts et al., 2006; Wienberg and Titschack, 2016). Coral mounds are formed by a balance between sedimentation and coral growth (figure 2.4) (e.g. Dorschel et al., 2005; Roberts et al., 2006; Wienberg and Titschack, 2016). First, the coral larvae settle on hard substrate (figure 2.4a,b). If the environmental conditions are suitable, mound development begins (figure 2.4c), in which the sediment stabilizes the coral remnants and the new coral generation grows on top (Dorschel et al., 2005; Roberts et al., 2006; Titschack et al., 2015; Wienberg and Titschack, 2016). If the habitat conditions are suitable over several centuries to millennia, gigantic structures can form that are finally archived in the sediment (figure 2.4d). However, their local development over time is often discontinuous, and there can be several thousand years between growth phases, which limits the generation of continuous CWC time series (figure 2.4e, e.g. Dorschel et al., 2005; Eisele et al., 2011; de Carvalho Ferreira et al., 2022; Frank et al., 2009, 2011a; Raddatz et al., 2016, 2020; Roberts et al., 2006; Wienberg et al., 2010, 2018, 2022; Wienberg and Titschack, 2016). Nonetheless, buried in the sediment, corals can be several thousand to several million years old - a very important climate archive (e.g. Frank et al., 2011a; Freiwald et al., 2004; Kano et al., 2007; Robinson et al., 2007; Thierens et al., 2013).

Average growth rates of CWCs such as *D. pertusum* and *M. oculata* are between 4-25 mm/year, depending on environmental factors (e.g. Büscher et al., 2019, 2022; Freiwald et al., 2004; Sabatier et al., 2012). During formation of their $CaCO_3$ skeleton, they obtain carbon exclusively from the dissolved inorganic carbon (DIC) in the seawater in which they grow (Griffin and Druffel, 1989). Hence, in addition to ^{12}C,

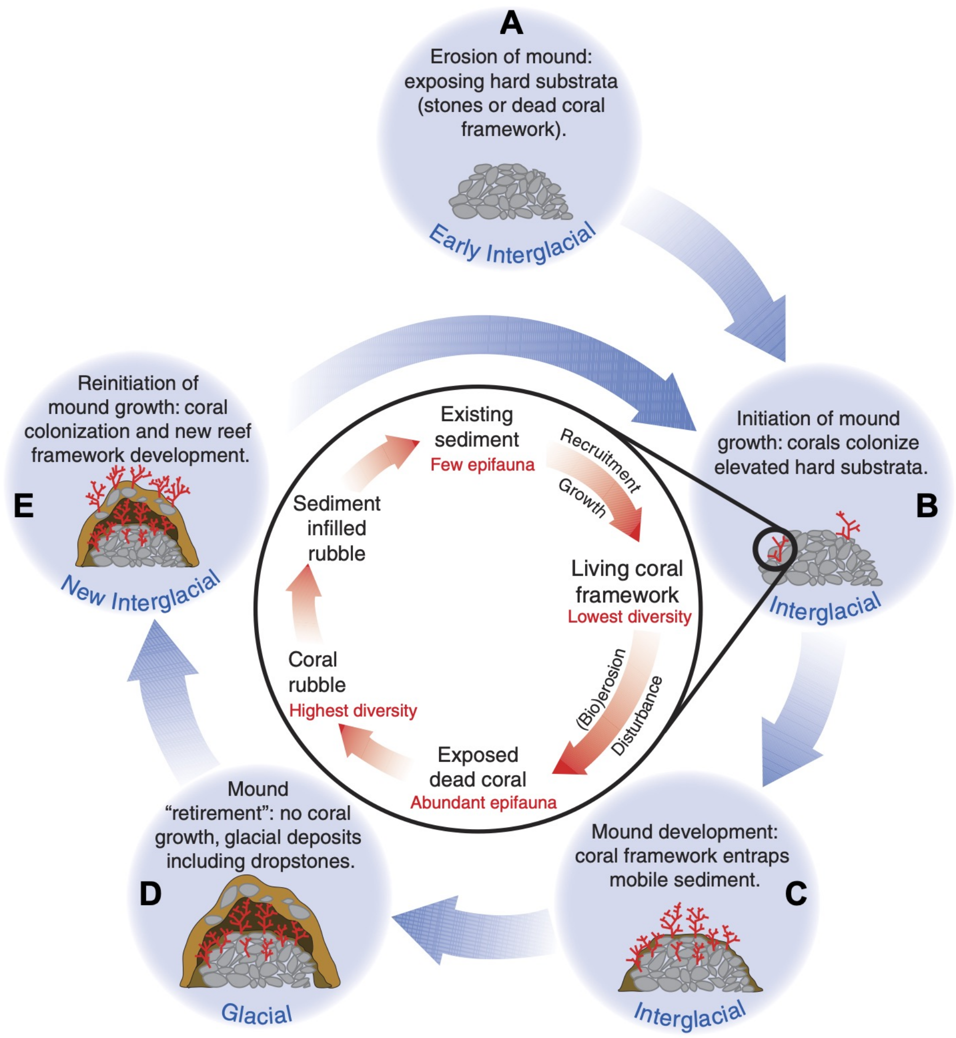

Figure 2.4.: Illustration of CWC mound formation. Mound formation can be linked to glacial and interglacial cycles, as these change the environmental conditions. Figure taken from Roberts et al. (2006), modified.

the carbon isotopes ^{13}C and ^{14}C (chapter 2.5) are incorporated into the skeleton. While ^{13}C varies within CWCs up to 12 ‰ (e.g. Adkins et al., 2003; Blamart et al., 2005; Robinson et al., 2014; Rollion-Bard et al., 2003; Smith et al., 2000), studies have confirmed that ^{14}C measurements in CWC reflect the ^{14}C content of the surrounding seawater (Adkins, 1998; Adkins et al., 2002; Frank et al., 2004). Moreover, corals incorporate trace elements from the surrounding seawater throughout their lifetime, which makes them a valuable archive of past ocean conditions (e.g. Robinson et al., 2014). Trace elements such as uranium can replace calcium in the $CaCO_3$ lattice, providing a radiometric clock (Frank and Hemsing (2021), chapter 2.4), whereas the Li/Mg ratio is controlled by temperature (e.g. Case et al., 2010; Cuny-Guirriec et al., 2019; Montagna et al., 2014; Raddatz et al., 2013; Stewart et al., 2023). In addition, their large carbonate skeletons offer a crucial advantage over other marine organisms such as foraminifera: there is usually enough material to perform several isotopic measurements on a single piece. This direct record of ambient seawater conditions in combination with absolute dating methods makes CWC a very valuable paleoclimate archive that has already been used in numerous studies (e.g. Beisel et al., 2023; Chen et al., 2015, 2016, 2020; Colin et al., 2010, 2019; Frank et al., 2004, 2011a; Hines et al., 2015, 2019; Li et al., 2020, 2023; Raddatz et al., 2023; Robinson et al., 2005; Schröder-Ritzrau et al., 2003, 2005; Wienberg et al., 2022).

2.4. Principles of ^{230}Th/U dating

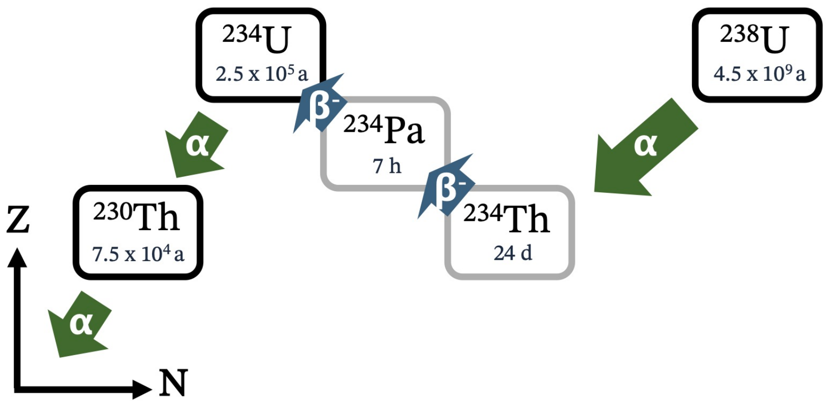

Figure 2.5.: Part of the ^{238}U decay chain. The half-lives are listed under the respective isotope.

The ^{230}Th/U dating method is used here as an absolute age dating method for CWCs (chapter 2.3), as they incorporate uranium into their $CaCO_3$ skeleton (chapter 2.3, e.g., Cheng et al., 2000; Frank et al., 2004; Smith et al., 1997; Schröder-Ritzrau et al., 2003). The method is based on the decay series of the isotope ^{238}U, and it can provide absolute ages up to 600-800 ka (Cheng et al., 2013). After a half-life of $t_{1/2} = 4.5 \cdot 10^9$ a, ^{238}U decays first to ^{234}Th and then to ^{234}Pa (figure 2.5). Nevertheless, these two decay products can be neglected, as they only have very short half-lifes (figure 2.5). Subsequently, ^{234}Pa decays to ^{234}U with a half-life of $2.5 \cdot 10^5$ a, which in turn decays into ^{230}Th with a half-life of $7.5 \cdot 10^4$ a. The age calculation utilizes the ratios (^{230}Th/^{238}U) and (^{234}U/^{238}U):

$$\left(\frac{^{234}\mathrm{U}}{^{238}\mathrm{U}}\right)(t) = (\left(\frac{^{234}\mathrm{U}}{^{238}\mathrm{U}}\right)_{\mathrm{initial}} - 1) \cdot e^{-\lambda_{234} t} + 1 \tag{2.1}$$

$$\left(\frac{^{230}\mathrm{Th}}{^{238}\mathrm{U}}\right)(t) = \left(1 - e^{-\lambda_{230}t}\right) + \left(\left(\frac{^{234}\mathrm{U}}{^{238}\mathrm{U}}\right) - 1\right)\frac{\lambda_{230}}{\lambda_{230} - \lambda_{234}}\left(1 - e^{-(\lambda_{230}-\lambda_{234})t}\right) \quad (2.2)$$

with

$$\delta^{234}U = (\left(\frac{^{234}\mathrm{U}}{^{238}\mathrm{U}}\right)_{\mathrm{meas}} - 1) \cdot 1000\,(‰). \quad (2.3)$$

For a comprehensive derivation, please refer to the work of Ivanovich and Harmon (1982). λ denotes the decay constants and t the age of the sample to be calculated. The equations must be solved numerically using a Monte Carlo simulation.

Weathering of the continental crust causes ^{238}U to enter the seawater, where it can be regarded as homogeneously distributed with a residence time of ~400 ka (Chen et al., 2021b; Ivanovich and Harmon, 1982). The concentration is approximately 3.3 µg/l (Frank and Hemsing, 2021). The ^{230}Th/U dating method utilizes the secular disequilibrium between ^{238}U and ^{230}Th. While uranium is water-soluble and remains in the water for a very long time, thorium is very particle-reactive with a residence time of 40 a and has only a low solubility (Ivanovich and Harmon, 1982).

In order to successfully carry out ^{230}Th/U dating, two essential requirements must be met. First, it is necessary to ensure that the closed system condition is fulfilled. This implies that no alteration in the initial uranium content must have occurred. In practice, this criterion is verified by employing the δ^{234}U ratio (equation 2.3). Today, the $\delta^{234}\mathrm{U}_i$ ratio of seawater is 146.8 ‰± 0.1 ‰ (Andersen et al., 2010). Kipp et al. (2022) recently revised the $\delta^{234}\mathrm{U}_{sw}$ to 145.55 ‰ ± 0.28 ‰. This thesis refers to the value published by Andersen et al. (2010), to be consistent with the normalization approach of the IUP laboratory. More details are available in chapter 3.4. It is assumed that the $\delta^{234}\mathrm{U}_i$ ratio of the ocean has fluctuated over time (e.g. Chutcharavan et al., 2018; Esat and Yokoyama, 2006; Li et al., 2023; Reimer et al., 2009). For example, during the LGM (chapter 2.2), it is assumed that $\delta^{234}\mathrm{U}_i$ was approximately -5 ‰ ± -2 ‰ lower than today, resulting in a glacial threshold of 141.7±7.8 ‰ (Chutcharavan et al., 2018; Reimer et al., 2009). Hence, most studies apply a range of ±7-15 ‰ around the modern δ^{234}U value to ensure closed system behavior (e.g. Chen et al., 2015; de Carvalho Ferreira et al., 2022; Hines et al., 2019; Raddatz et al., 2023).

The second requirement assumes that no ^{230}Th was originally present in the coral. To fulfill this condition, a rigorous cleaning procedure is employed to remove non-carbonate thorium, and a ^{230}Th-correction is applied, to correct for residual thorium.

For this purpose, the ^{232}Th isotope is used, which is the most common isotope of thorium and not part of the ^{238}U decay series. It can be assumed to be quasi-stable with a half-life of $1.4 \cdot 10^{10}$ a. To date, no fractionation effects have been identified. Depending on the location and depth in the ocean, a ratio of ^{230}Th to ^{232}Th for sewater is assumed, which is used to correct the isotope values. In the case of the CWC utilized in this thesis, a ratio of 8 ± 4 is applied (e.g. Frank et al., 2009; Schröder-Ritzrau et al., 2003; Wefing et al., 2017). Consequently, the greater the concentration of ^{232}Th in the coral, the greater the age uncertainty due to the propagation of errors of the correction model. Therefore, it is essential to utilize ^{230}Th/U ages with as low as possible ^{232}Th concentrations (below 2-3 ng/g).

2.5. Radiocarbon Dating

The radiocarbon method is used to date carbon bearing materials. Besides, radiocarbon serves as a tracer for the carbon cycle (e.g. Skinner and Bard, 2022). First evidence of radiocarbon emerged in 1934 (Kurie, 1934). However, the discovery is generally attributed to Willard F. Libby (Libby, 1946; Libby et al., 1949), who received the Nobel Prize for the discovery in 1960. The cosmogenic isotope ^{14}C is produced in the upper layers of the atmosphere, in the transition region between the stratosphere and troposphere. When cosmic radiation hits the atmosphere, thermal neutrons are released by spallation. These react with the nitrogen in the atmosphere, forming, among other nuclei, ^{14}C:

$$^{14}_{7}\mathrm{N} + ^{1}_{0}\mathrm{n} \rightarrow ^{14}_{6}\mathrm{C} + ^{1}_{1}\mathrm{p} \tag{2.4}$$

Consequently, there is a continuous yet fluctuating production of ^{14}C, which is contingent upon cosmic radiation and the strength of Earth´s geomagnetic shielding. ^{14}C occurs in very low concentrations in the atmosphere, making up about 1.2×10^{-10}% of total carbon. It is highly reactive and oxidizes rapidly to ^{14}CO and finally to $^{14}CO_2$, which is integrated into the carbon cycle. With a half-life of about 5700 ±30 years, it decays to nitrogen by beta decay:

$$^{14}_{6}\mathrm{C} \rightarrow ^{14}_{7}\mathrm{N} + e^{-} + \bar{\nu} \tag{2.5}$$

Originally the half-life of radiocarbon was estimated to 5568 ± 30 years (Libby and Johnson, 1955), later it was corrected to 5730 ± 40 years by Godwin in 1962 (Godwin, 1962). Today, the generally accepted half-life is 5700 ± 30 years, although it could be lower (Roberts and Southon, 2007). In 1962, however, it was decided to continue using the Libby half-life to ensure comparability of new results with older samples (Godwin, 1962). The resulting radiocarbon age is therefore referred to as the *conventional radiocarbon age*.

Living organisms, such as CWCs (chapter 2.3) incorporate carbon and hence ^{14}C during their lifetime. After their death, no further exchange takes place, and the decay law can be used to determine their age:

$$\left(\frac{^{14}\mathrm{C}}{^{12}\mathrm{C}}\right)_t = \left(\frac{^{14}\mathrm{C}}{^{12}\mathrm{C}}\right)_{t=0} \cdot \exp(-\lambda_L t) \tag{2.6}$$

The decay constant is determined with: $\lambda_L = \frac{1}{8033}$. The resulting uncalibrated radiocarbon age can be converted to a calendar age using a calibration curve (chapter 2.5.1).

In addition to the radiocarbon age, the radiocarbon activity a^{14}C in *percent modern carbon* (pmC) (Stenström et al., 2011) is commonly reported:

$$a^{14}\mathrm{C} = \exp(-\lambda_L t) \cdot 100\ [\%] \tag{2.7}$$

Furthermore, the radiocarbon community has agreed upon several guidelines for the reporting of radiocarbon ages. ^{14}C ages are reported relative to the year 1950 (indicated by BP, *before present*), to ensure comparability between laboratories. Moreover, fractionation occurs within the carbon cycle, which must be considered when measuring ^{14}C. Fractionation refers to shifts in the abundance of isotopes that are caused by physical or chemical processes, such as phase transitions or chemical reactions. The ^{13}C standard *Vienna Pee Dee Belemnite* (VPDB), which is derived from a marine fossil, is used in this context (Friedman et al., 1982):

$$\delta^{13}\mathrm{C} = \left(\frac{\left(\frac{^{13}\mathrm{C}}{^{12}\mathrm{C}}\right)_{sample}}{\left(\frac{^{13}\mathrm{C}}{^{12}\mathrm{C}}\right)_{VPDB}} - 1 \right) \cdot 1000\ [‰] \tag{2.8}$$

Subsequently, all ^{14}C results are normalized to $\delta^{13}\mathrm{C} = -25$ ‰, under the assumption that the ^{14}C fractionation is provided approximately by the squared value of the ^{13}C fractionation factor (Stuiver and Robinson, 1974).

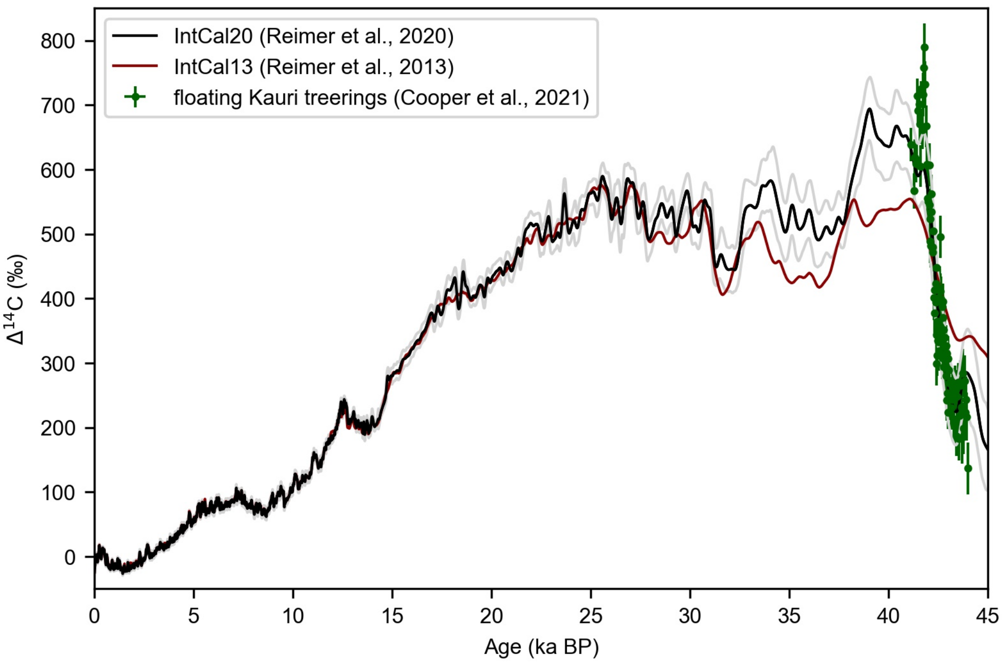

Figure 2.6.: Current atmospheric radiocarbon calibration curve IntCal20 (Reimer et al., 2020) with 2σ errors (thin gray lines) compared to the previous version IntCal13 (Reimer et al., 2013). New floating tree-ring data prior to 40 ka show a higher $\Delta^{14}C$ increase than previously assumed (Cooper et al., 2021).

2.5.1. Radiocarbon Calibration Curves

Due to fluctuations in the production rate of ^{14}C and the carbon cycle, a calibration curve is necessary for the conversion of ^{14}C ages to calendar ages (Stuiver and Suess, 1966). Since the Southern Hemisphere differs from the Northern Hemisphere by an average offset of 36 ± 27 ^{14}C years (Hogg et al., 2020), there are currently two atmospheric calibration curves: **IntCal20** (Reimer et al. (2020), figure 2.6) for the Northern Hemisphere and **SHCal20** for the Southern Hemisphere (Hogg et al., 2020).

These calibration curves represent an estimate of atmospheric radiocarbon activity based on data from various archives, combined with a Bayesian spline approach, and get updated every few years (Reimer et al., 2020; Hogg et al., 2020). Up to 13.900 cal BP, IntCal20 is based on tree rings alone, prior to that, it is based on "statistically integrated evidence from floating tree-ring chronologies, lacustrine and marine sediments, speleothems, and corals" (Reimer et al., 2020). The calibration curve for the Southern Hemisphere, SHCal20, is largely based on IntCal20 (Hogg et al., 2020). Furthermore it utilizes a statistical model of the N-S atmospheric radiocarbon offset, as there are not yet enough direct Southern Hemisphere radiocarbon observations (Hogg et al., 2020).

It is important to note that this is only an estimate of the atmospheric ^{14}C value (e.g.

Muscheler et al., 2020). This is particularly evident during the last ice age, when IntCal20 was based on only a few data sets (Muscheler et al., 2020; Reimer et al., 2020). For example, a new Kauri tree-ring dataset from New Zealand shows a 200 ‰ higher increase in $\Delta^{14}C$ during the Laschamp event (Cooper et al. (2021), figure 2.6), a geomagnetic excursion that dramatically increased the production rate of ^{14}C (e.g. Channell et al., 2020; Laj et al., 2014; Singer, 2014). Therefore, especially for data older than 30 ka, the uncertainty of the atmospheric $\Delta^{14}C$ must be taken into account.

The integration of ocean data is not straightforward, because in addition to the time scales required for the incorporation of ^{14}C from the atmosphere into the ocean, the local reservoir effect (chapter 2.5.2) requires consideration. The local reservoir effect is often not readily known, so marine data from benthic foraminifera or CWCs cannot be included in the calibration curve without further information. Tropical corals that grew near the sea surface were only considered < 25ka BP in IntCal20 to exclude potentially diagenetically altered ages due to sea level rise (Reimer et al., 2020).

To calibrate marine ^{14}C ages, there is a calibration curve for the sea surface, the Marine20 (Heaton et al., 2020). Similarly to SHCal20, Marine20 was created using IntCal20, along with an ocean/atmosphere/biosphere box model of the global carbon cycle and reconstructed CO_2 changes from ice core data (Heaton et al., 2020). It provides the *non-polar global average* and can be used as a basis for regional oceanic variations (Heaton et al., 2020), assuming that the carbon cycle and ocean circulation have remained constant and that the radiocarbon activity in the ocean depends only on the atmosphere (e.g. Stuiver et al., 1986; Skinner and Bard, 2022). Accordingly, a constant reservoir effect over time is assumed for the marine calibration (Heaton et al., 2020). Of course, these conditions are not necessarily fulfilled. In particular, caution is needed during periods of strong climatic change, which may induce variance in the local reservoir effect (see chapter 2.5.3). Therefore, it is useful to establish regional marine radiocarbon calibration curves in the future (Skinner et al., 2019).

2.5.2. Radiocarbon in the Ocean

Through gas exchange between the atmosphere and the ocean, CO_2 and, consequently, $^{14}CO_2$ enters the ocean. CO_2 reacts with seawater to ${CO_3}^{2-}$, ${HCO_3}^{-}$, and H_2CO_3, which is commonly referred to as *dissolved inorganic carbon* (DIC). It is distributed in the ocean through advection and diffusion. The concentration of ^{14}C in the ocean is lower than in the atmosphere (chapter 2.5.1), which can be attributed to the rate of gas exchange between the atmosphere and the ocean, as well as the constant mixing with deeper water that is depleted in ^{14}C. This phenomenon is referred to as **reservoir effect**. ^{14}C signals from the atmosphere appear therefore smoothed and

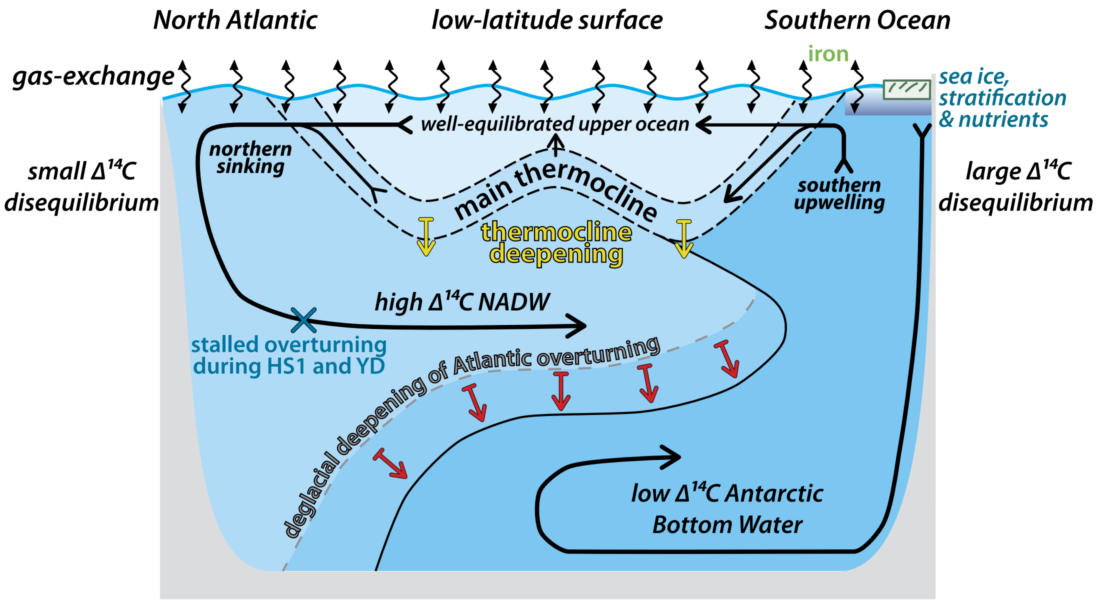

Figure 2.7.: Schematic representation of ocean circulation and Δ^{14}C distribution, figure taken from Hain et al. (2014).

phase-shifted in the ocean (Heaton et al. (2023) and references therein). To specify the radiocarbon content, usually, the deviation from the present-day ratio, Δ^{14}C, is given by the following formula (Adkins and Boyle, 1997; Stuiver and Polach, 1977):

$$\Delta^{14}\mathrm{C} = \left(\frac{\exp(-^{14}\mathrm{C}_{age}/8033)}{\exp(-\mathrm{cal}_{age}/8267)} - 1 \right) \cdot 1000‰ \tag{2.9}$$

With cal_{age} as the absolute age of the marine sample. For example, in the Atlantic, the NADW is associated with a high Δ^{14}C value, while the AABW is associated with a low Δ^{14}C value due to limited gas exchange via sea ice and increased stratification (chapter 2.1, figure 2.7).

To describe the difference between the ocean and the atmosphere directly, $\Delta\Delta^{14}$C can be calculated:

$$\Delta\Delta^{14}\mathrm{C} = \Delta^{14}\mathrm{C}_{ocean} - \Delta^{14}\mathrm{C}_{atmosphere} \tag{2.10}$$

However, $\Delta\Delta^{14}$C is dependent on the absolute value of $\Delta^{14}\mathrm{C}_{atmosphere}$ (IntCal, chapter 2.5.1), which is subject to temporal fluctuations. Therefore, $\Delta\Delta^{14}$C may fluctuate without a corresponding change in the relative isotopic enrichment between the two reservoirs (e.g. Hines et al., 2015; Skinner and Bard, 2022). Consequently, the preferred approach is to utilise *measures of isotopic imbalance* between two different carbon reservoirs (e.g. Cook and Keigwin, 2015; Skinner and Bard, 2022; Skinner et al., 2023; Soulet et al., 2016), such as the **Benthic-Atmosphere ($\mathbf{B}_{atm}$)** age:

$$B_{atm}\ age = {}^{14}\mathrm{C}_{age} - {}^{14}\mathrm{C}_{age,atmosphere} \tag{2.11}$$

Whereas ${}^{14}\mathrm{C}_{age}$ denotes the ^{14}C age of the specimen in the ocean, such as CWCs or benthic foraminifera. In paleoceanography, B_{atm} ages are often referred to as **reservoir ages** or **radiocarbon ventilation ages**. However, it should be noted that B_{atm} ages do *not refer to actual ages or transit times* (Marchal and Zhao, 2021). B_{atm} ages are always a degree of isotopic disequilibrium between the ocean and the atmosphere (Skinner and Bard, 2022; Skinner et al., 2023), while the term **ventilation** strictly refers to "the collective effect of the physical and chemical processes that convey atmospheric properties into the ocean interior" (definition after Skinner and Bard (2022)).

As the ^{14}C concentration in the ocean is influenced by a multitude of variables, B_{atm} ages always reflect a combination of these processes. These include the ^{14}C content of the atmosphere (and thus indirectly changes in the production rate or carbon cycle), gas exchange between the ocean and the atmosphere, and the transport and mixing times in the ocean itself (Skinner and Bard, 2022). Today, typical reservoir ages range from a few decades to centuries for the surface layers to between 1500 and 2500 years for the deep waters of the Pacific Ocean (e.g. Rafter et al., 2022).

2.5.3. Radiocarbon in the Ocean Through Time

Over time, the ^{14}C content of the ocean has changed due to processes such as reduced air-sea gas exchange and changes in circulation patterns (figure 2.8) (e.g. Adkins, 2013; Rafter et al., 2022; Skinner et al., 2010, 2023; Skinner and Bard, 2022). In order to gain a precise understanding of these processes, marine reservoir ages for specific time periods and locations are investigated through modelling and detailed paleoceanographic studies (e.g. Beisel et al., 2023; Burke et al., 2015; Burke and Robinson, 2012; Butzin et al., 2017; Chen et al., 2015; Frank et al., 2004; Hines et al., 2015, 2019; Köhler et al., 2024; Raddatz et al., 2023; Robinson et al., 2005; Schröder-Ritzrau et al., 2003, 2005; Skinner et al., 2010, 2014, 2019, 2021). Over the years, more and more ^{14}C compilation papers have been published, investigating the development of radiocarbon ventilation over time (Rafter et al., 2022; Skinner et al., 2017, 2023; Skinner and Bard, 2022; Zhao et al., 2018).

In general, the ocean was more radiocarbon depleted during the last glacial period than during the Holocene (e.g. Rafter et al., 2022; Skinner et al., 2023; Skinner and Bard, 2022, figure 2.8), with a mean ocean B_{atm} age offset of about 2123 ± 32 a during the LGM, compared to 1335 ± 22 a during the Holocene (Skinner et al. (2023), time-slice global average values based on interpolations). However, it is difficult to distinguish to what extent the ocean circulated more slowly during the LGM, or whether it was simply more isolated from the atmosphere (Skinner and Bard, 2022). In general, the upper ocean is thought to have been more influenced by the efficiency of gas exchange at high latitudes, while the deep ocean was more influenced by transport processes (Skinner et al., 2023). However, these compilations sometimes contain large ^{14}C variations that can be challenging to interpret (Rafter et al., 2022; Skinner et al., 2017, 2023; Skinner and Bard, 2022; Zhao et al., 2018).

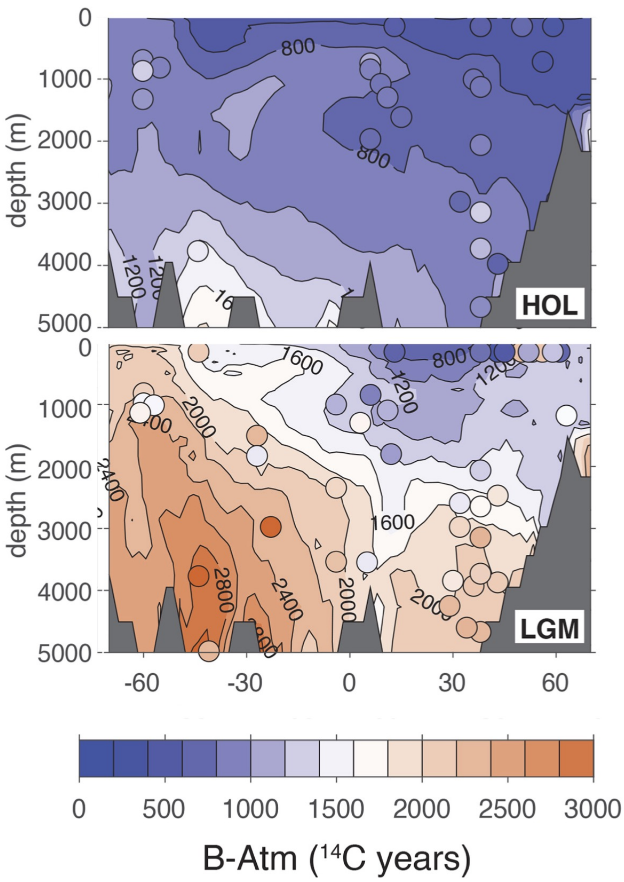

Figure 2.8.: Radiocarbon in the Atlantic over time. Skinner et al. (2023) determined the zonally averaged interpolated B_{atm} age offsets for the Holocene (upper panel, defined as <6 ka BP) and the LGM (lower panel, defined as 19-21.8 ka BP). The circles indicate the input data. Figure taken from Skinner et al. (2023), modified.

In search of the reasons for this large scatter of reconstructed ^{14}C values through time, the archives used can be examined more closely. Most of these ^{14}C studies have been performed on archives such as CWC (chapter 2.3) or foraminifera. Foraminifera are small single-celled organisms, either planktonic (living near the ocean surface) or benthic. Both archives have different advantages and disadvantages. While CWCs allow multiple isotope measurements on the same sample due to their sheer size (chapter 2.3, 2.4), this is not the case for the small foraminifera. To obtain a sufficient amount for ^{14}C measurements, several individuals must be collected from a sediment section. Therefore, the method is susceptible to factors such as bioturbation and low sedimentation rates (Skinner and Bard, 2022, and references therein). In addition, the chronology depends on the age model of the sediment core from which the foraminifera were recovered. When possible, researchers prefer ^{14}C-independent age models to determine the absolute age of foraminifera, such as the δ^{18}O method. In these cases, the δ^{18}O record of the foraminifera in the sediment can be stratigraphically linked to independently dated ice cores (e.g. Skinner et al., 2010, 2014). However, this is not possible for low-latitute cores, because the signals from these are generally attenuated and synchrony with high-latitude climate changes may be questionable (e.g. Freeman et al 2016). Therefore, some studies use ^{14}C ages of planktonic foraminifera to construct the age models of the sediment cores, under the assumption of a constant surface reservoir age and the usage of calibration curves (chapter 2.5.1) (e.g. Cléroux et al., 2011; Freeman et al., 2015; Ronge et al., 2020). These surface reservoir ages are only estimated and often assumed to be constant over time, although they vary and may have been in significant disequilibrium with the atmosphere (e.g. Lindsay et al., 2015). Furthermore, ^{14}C ages of different foraminifera species may be biased, even at high accumulation rates of the sediment (Ausín et al., 2019; Ezat et al., 2017; Magana et al., 2010). Therefore, care must be taken when comparing ^{14}C records from different archives, and individual uncertainties must be taken into account.

3. Methods

3.1. Sample Collection and Preparation: Cold-Water Corals

Corals utilized in this thesis have been collected from the seafloor using various methods. Most have been recovered using a gravity corer (GC). In this case, a metal tube with a plastic liner is pressed into the sediment by weight, allowing several meters of sediment to be recovered (e.g. Hebbeln et al., 2017). The extracted sediment cores are frozen and cut in half. One half is stored in an archive and the other half used for sampling. I sampled eight sediment cores, six of them yielded cold-water corals younger than 40,000 years. An example of such a sediment core is shown in figure 3.1. Coral fragments are clearly visible as bright patches in the surrounding sediment.

Another method is to collect corals directly from the seafloor. For this purpose, either a remotely operated vehicle (ROV), for example of the type SQUID (MARUM), or a Van-Veen-type grab sampler (GS) is used (e.g. Frank et al., 2023; Hebbeln et al., 2017; Westphal et al., 2014). Additionally, a Giant Box Corer was used to collect undisturbed surface sediments along with coral fragments (e.g. Frank et al., 2023; Hebbeln et al., 2017).

The recovered coral pieces require mechanical cleaning to exclude diagenesis and contamination with organic material and non-coral carbonate. First, the corals are thoroughly cleaned with water to remove sediment residues. This is done first mechanically with a brush and then in an ultrasonic bath. A visual inspection will first note the preservation state of the coral material, focusing on heavily contaminated sections of the skeleton that could contain reprecipitation of $CaCO_3$. This includes coatings, bioerosion, and non-coral carbonate such as calcified tubes of Eunice spp., serpulids, etc., as well as other forms of organisms such as sponges and bryozoans. To exclude distortion of the actual isotopic signal, the large, calcified Eunice-tubes should be generously avoided. Smaller impurities and coatings (e.g. organic carbon-rich crusts (Cheng et al., 2000)) are removed mechanically with a Dremel tool. For this purpose, several micrometers to even millimeters of the surface are grinded off, depending on

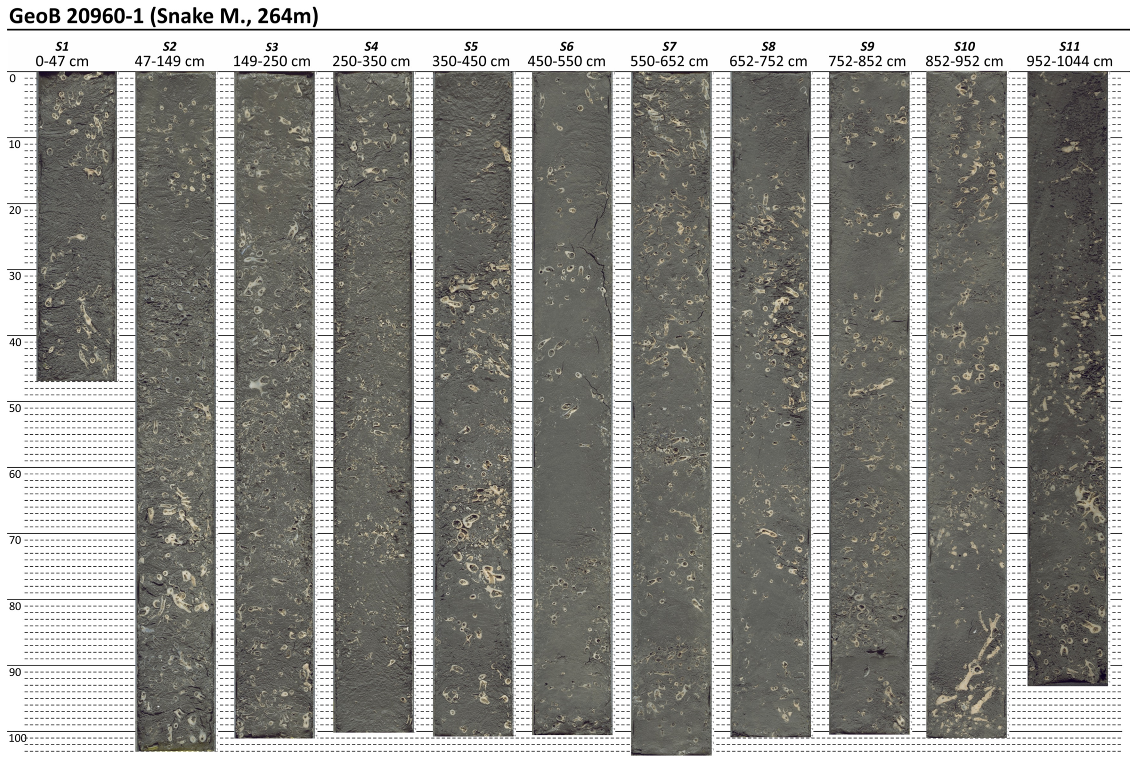

Figure 3.1.: Cut sediment core of GeoB 20960-1 from the Angola margin (Hebbeln et al., 2017), with embedded coral fragments clearly visible. Core image courtesy of C. Wienberg; sediment core has been provided by the GeoB Core Repository at the MARUM, Center for Marine Environmental Sciences, University of Bremen, Germany.

the state of preservation of the coral. Afterwards, a fragment of the coral branch, the corallite, is cut in half to continue the cleaning inside and to remove all septa. This is followed by a visual inspection under a binocular microscope to ensure that any secondary organic or other non-carbonate coating and signs of bioerosion (e.g., borings of sponges) have been removed.

In order to ensure the accuracy of ^{14}C ventilation age reconstructions, it is imperative that the same piece of coral is utilized for both ^{230}Th/U and ^{14}C dating. While the age of a *D. pertusum* or *M. oculata* coral polyp is typically on the order of several years (chapter 2.3), coalescence with older coral material during the growth of the coral branch can result in significant age discrepancies between corallites. This thesis presents only ^{14}C ventilation ages obtained from paired ^{230}Th/U and ^{14}C dating on the same polyp of a coral.

3.2. ^{230}Th/U Dating

The ^{230}Th/U-method is used to accurately determine the absolute age of corals (chapter 2.4). After the mechanical preparation (chapter 3.1), a chemical purification of uranium and thorium from the $CaCO_3$ matrix follows before the measurement on the Multi-Collector Inductively Coupled Plasma Mass Spectrometer (MC-ICP-MS) can take place.

3.2.1. Extraction of Uranium and Thorium

The chemical extraction of uranium and thorium followed the method of Frank et al. (2004) and Wefing et al. (2017). Sample pieces between 40 mg and 80 mg are first leached briefly with 3M HNO_3 for about 15-20 seconds and then dried at 60°C overnight. Following, the samples are weighted again to check how much material has been leached. The sample is then dissolved with 7M HNO_3 , again overnight. Next, 0.1 ml of TriSpike is added to the solution. Before and after this step, the sample is weighted again to check the exact amount of TriSpike added. This step is very important, since the TriSpike contains known concentrations of the artificial isotopes ^{229}Th, ^{233}U, and ^{236}U. This information is later used to determine the concentration of natural isotopes from the sample. The resulting solution is evaporated overnight at 60°C. Then 0.5 ml of 7M HNO_3 is added to the beaker and again left overnight to dissolve completely. This is followed by the first column for the removal of the calcium matrix and the extraction of thorium and uranium (wet column chromatography). For this, the columns are filled with 500 μl UTEVA ion exchange resin. They are rinsed with MilliQ water and charged with 7N HNO_3. Afterwards, the sample is added drop-wise. Next, 3 x 0.5 ml of 7M HNO_3 are added. Now the sample beaker is placed under the column. This is followed by 3 x 0.5 ml 3M HCl and 3 x 0.5 ml 1M HCl, to collect thorium and uranium. After a final rinse with MilliQ water, the beaker is removed and dried overnight at 60°C. The columns are filled with MilliQ water and sealed until the second column. The second column proceeds similarly to the first. First, the MilliQ water is drained, then the column is filled with 0.75 ml 7M HNO_3, which was previously added to the sample beaker. Then the sample beaker is placed underneath again, followed by 3 x 0.5 ml 3M HCl and 3 x 0.5 ml 1M HCl. Finally, 3 x 0.5 ml 1M HF follows. Lastly, the sample is evaporated again overnight at 60°C. The columns are neutralized with $CaCl_2$. The next day, 1.5 ml of a solution consisting of 1 % HNO_3 + 0.05 % HF is added to the beaker and is allowed to dissolve the remaining sample for at least 3 hours. Then the sample is centrifuged and filled into tubes for the measurement on the mass spectrometer.

3.2.2. Isotope Analysis of Uranium and Thorium

The model “Thermo Fisher Scientific Neptune Plus”, a multiple collector inductively coupled plasma mass spectrometer (MC-ICP-MS) is used at the Institute of Environmental Physics (IUP), Heidelberg University, Germany, to measure high precision isotopic abundances of ^{229}Th, ^{230}Th, ^{232}Th, ^{233}U, ^{234}U, ^{235}U, and ^{238}U. Precision in the epsilon (10^{-4}) to permil range can be achieved (Kerber et al., 2023). Details on the mass spectrometry setup, data treatment, calculation, measurement protocols, and uncertainties have been published in detail in Kerber et al. (2023) and Kerber (2023). Age calculations were performed using the half-lives of Cheng et al. (2013). ^{230}Th/U ages are given in ka BP with 2σ uncertainties.

3.3. ^{14}C Dating

For ^{14}C dating, a subsample of 15 – 20 mg of the mechanically cleaned coral material is collected and leached in 4 % HCl for at least 30 seconds, to remove absorbed modern CO_2 (Adkins et al., 2002). The sample is subsequently dried at 60°C for 1.5 hours, the goal weight after leaching is 8 – 12 mg. Afterwards, extraction and graphitization can take place, to prepare the sample for AMS measurement.

3.3.1. Extraction

The extraction line (figure 3.2) has been introduced and described by Therre et al. (2021) and is based on the design of the semi-automated extraction line described by Tisnérat-Laborde et al. (2001). Before the extraction procedure can start, the setup is evacuated for at least three hours to obtain pressure levels below 10^{-5} mbar. It has proven useful to prepare the setup the day before extraction and evacuate it overnight, allowing pressure levels up to 10^{-6} mbar to be achieved. The pressure levels are constantly monitored, to ensure that there is no contamination with ambient air.

Custom-made glass vials are used for the samples (figure 3.2b). One side contains the sample, and the other side is filled with 0.5 ml of 10 % hydrochloric acid, which acts as a hydrolyzing agent (Therre et al., 2021). The vials prepared in this way are successively connected to the extraction line and evacuated to a pressure below 10^{-4} mbar. To exclude contamination with ambient air, the isolation of the system is checked after connecting the sample vials. If this check was successful, the reaction is started by turning the glass vials, allowing the acid to flow to the sample (Therre et al., 2021). The following reaction takes place:

$$CaCO_3 + 2\,HCl \longrightarrow CO_2 + H_2O + CaCl_2$$

The resulting gas mixture, consisting of CO_2 and H_2O vapor, is passed over a freezing trap, which uses a dry ice and acetone mixture to remove the resulting water vapor at about -78°C (Therre et al., 2021). Subsequently, the remaining CO_2 is directed into the calibration volume using liquid nitrogen. Measuring the pressure under lab conditions in the calibration volume allows determining the efficiency of the reaction. It also provides an additional control for any contamination with ambient air. Finally, the CO_2 is directed into a gas container using liquid nitrogen again. Between each run, the extraction line is evacuated for approximately 5 – 10 minutes to prevent memory effects (Therre et al., 2021). During a cycle, pressure levels between each step are monitored and documented to quickly identify any discrepancies.

Figure 3.2.: CO_2 extraction setup in the Heidelberg Radiocarbon Lab. Figure taken from Therre et al. (2021).

3.3.2. Graphitization

The graphitization setup was built by Unkel (2006), and further details are available in Unkel (2006) and Therre et al. (2021). Before starting the graphitization, 3 – 4 mg of iron powder, which serves as a catalyst for the Bosch reaction, is filled into the reactor tubes. After a leakage check, the catalyst is chemically purified by oxidization with ambient air and subsequent two-fold reduction with hydrogen gas at 400°C (Therre et al., 2021). The system is subsequently evacuated to a pressure of 10^{-4} mbar.

The glass containers with the extracted CO_2 are connected to the graphitization setup. The CO_2 is loaded into the reaction containers using liquid nitrogen. The reduction to graphite requires hydrogen gas, which is also loaded into the containers. The reactors are then heated to 575°C. Now, the Bosch reaction can take place:

$$CO_2 + 2\,H_2 \longrightarrow C + 2\,H_2O.$$

It takes approximately 3 - 4 hours, depending on the amount of sample. Constant pressure levels mark the completion of the reaction. Afterwards, the iron-graphite mixture is stored in glass tubes until the targets for the measurement on the AMS can be prepared.

3.3.3. AMS Measurement

The ^{14}C measurements were performed on accelerator mass spectrometers of type "Mini-Carbon-Dating-System" (MICADAS, Synal et al. (2007)) at the Curt-Engelhorn-Center Archaeometry (CEZA) in Mannheim, Germany (Kromer et al., 2013; Synal et al., 2007). The graphitized iron-graphite is pressed into aluminum targets using a pneumatic press. One set of measurements consists of 39 samples, including 5 blanks, 5 oxalic-acid II standards, 2 - 3 IAEA-C2 standards and 26 - 27 samples, measured using a bracketing pattern. Standards are interspersed between samples in regular intervals to accurately track the sensitivity and background of the AMS system throughout the measurement procedure. The conventional ^{14}C-ages are normalized to $\delta^{13}C = -25‰$ (chapter 2.5). The analytical precision is calculated using the error propagation of the uncertainties of standards and blanks. An additional error of 0.1 % is added onto the $^{14}C/^{12}C$ ratio to account for uncertainties that are not covered by pure counting statistics and uncertainty of the measured standards at that time. ^{14}C ages are reported as uncalibrated ^{14}C ages in ka BP with 1σ error.

Detailed information about the uncertainty ellipses using a Monte-Carlo approach can be found in Ruckelshausen (2013). Data evaluation and visualization is based on the python script of Freya Hemsing (Hemsing, 2017).

3.4. Selection Criteria

Throughout the course of this thesis, the data selection criteria were modified and refined. The following sections provide a detailed explanation of these, along with modifications and further development of the criteria.

3.4.1. Initial Selection Criteria

The following description of the initial selection criteria is taken from my first publication (Beisel et al., 2023) and has been slightly modified.

At first, the initial δ^{234}U value and ^{232}Th contamination were used to evaluate the quality of the ^{230}Th/U ages. The ^{232}Th concentration is directly related to deposition of thorium from seawater or non-carbonate material and induces an increase in ^{230}Th, that is, age correction and increasing uncertainty when propagating correction errors. Here, solely corals with a ^{232}Th content below 3.6 ng/g were selected. To test the U series closed system presumption, it is assumed that all corals must have an initial ^{234}U/^{238}U ratio ($\delta^{234}U_{initial}$) of $\pm$ 7 ‰ of the modern ocean $\delta^{234}U_{sw}$ (146.8 ‰) (Andersen et al., 2010; Reimer et al., 2009). The selected range of $\delta^{234}U_{sw}$ variability of $\pm$ 7 ‰ includes the known glacial reduction in seawater δ^{234}U by some -5 ‰ $\pm$ 2 ‰ (Chutcharavan et al., 2018). Due to differences in the use of isotope standards, seawater values can differ by about $\sim$ 1.2 ‰ between laboratories and publications. Kipp et al. (2022) recently reassessed $\delta^{234}U_{sw}$ to 145.55 ‰ $\pm$ 0.28 ‰ using a normalization of the data to the CRM 112A certified value, whereas the ^{230}Th/U lab at the IUP measures a value of CRM 112A (also known as SRM 960) which is 1.2 ‰ higher. Here, the seawater value of 146.8 ‰ (Andersen et al., 2010) is used to be self-consistent with the normalization approach to the HU1 standard, which is presumed to be in secular equilibrium (Wefing et al., 2017). Such difference in normalization does not impact the absolute ages as those are always normalized to a presumed secular equilibrium value using the half-lives of Cheng et al. (2013).

3.4.2. Refined Selection Criteria

To ensure the reliability of the results, data selection criteria were refined throughout this thesis (chapter 6). The application of these revised criteria has no notable effect on the data set presented in chapter 5 (Beisel et al., 2023) (see statement in chapter 5.2.2), which reflects the high quality of the data. However, recent developments (chapter 6) underline the need to refine selection criteria for CWCs in general.

The updated ^{232}Th threshold is now 2 ng/g, to reduce age uncertainty even further. Unchanged is the $\delta^{234}U_i$ value of about $\pm$7 ‰ of the modern ocean value ($\delta^{234}U_i$ =146.8 ‰, Andersen et al. (2010)). However, the update includes a glacial threshold value of 141.7 $\pm$ 7.8 ‰ (Reimer et al., 2009), which is consistent with the glacial reduction of about -5 ‰ $\pm$ 2 ‰ (Chutcharavan et al., 2018). This incorporates the observed trend towards lower $\delta^{234}U_i$ values during the last glacial more clearly (e.g. Chen et al., 2016; Chutcharavan et al., 2018).

If corals were obtained from sediment cores, the criterion of consistent chronology (chapter 6) should be applied. Age-depth inversions in the ^{230}Th/U age-depth profile should be discarded, as the majority can be attributed to coral alterations (chapter 6). In contrast, if they occur simultaneously with ^{14}C age-depth inversions, the observed changes may be due to reef formation/external influences.

The regional consistency of ^{14}C ventilation ages was first demonstrated by Skinner et al. (2019). This criterion not only enables the development of regional marine radiocarbon calibration curves (Skinner et al., 2019), but can also be employed to ensure the reliability of ^{14}C ventilation ages. Considering spatial proximity and flow patterns, one should be able to verify a true ^{14}C ventilation age signal through multiple measurements.

4. Status Report of the Heidelberg Radiocarbon Laboratory: Precision and Application in Cold-Water Corals

4.1. Introduction

The Heidelberg Radiocarbon Laboratory at the Institute of Environmental Physics (Heidelberg, Germany) has been investigating various carbonate climate archives for many years with a main focus on stalagmites (Therre, 2020; Therre et al., 2020; Voarintsoa and Therre, 2022) and cold-water corals (CWCs) (Beisel et al., 2023; Hemsing, 2017; Raddatz et al., 2023). By combining radiocarbon (^{14}C) measurements with absolute age determinations, such as the $^{230}Th/U$ method (Kerber et al., 2023), complex reconstructions of the temporal evolution of reservoir ages can be derived (Beisel et al., 2023; Raddatz et al., 2023; Therre et al., 2020). In 2018, a new extraction line based on a semi-automated system presented in Tisnérat-Laborde et al. (2001) was installed at the Heidelberg Radiocarbon Laboratory. A first characterization and quality assessment has been introduced by Therre et al. (2021). Here, the current status is presented, and current quality control parameters, such as blanks, standards and, for the first time, duplicates are discussed.

4.2. Methods

The method to prepare samples consisting of calcium carbonate ($CaCO_3$) for accelerator mass spectrometer (AMS) ^{14}C measurements is described in chapter 3.3. Depending on the material, various preparation steps must be carried out before CO_2 extraction can take place. The following outlines the preparation for blanks and ^{14}C standards.

Blanks

Carbonates such as marble (in-house secondary standard and the IAEA C1 standard (Rozanski et al., 1992)) are used as blank material for background determination. They are treated like the remaining samples to provide a realistic estimate of the background signal. Additionally, they are used for further identification of contamination during sample processing.

Standards

The IAEA-C2 standard, a fresh water travertine deposit (Rozanski et al., 1992), is measured regularly to ensure the accuracy and judge the level of reproducibility of the measurements. This standard comes as a powder, therefore leaching prior to extraction is not possible. Approximately 8 - 12 mg of the material is weighted directly before extraction. An antistatic device is used to ensure that all material in the sample vial reacts and is used for CO_2 extraction.

In addition, the Oxalic Acid II standard (NIST, 1983; Stuiver, 1983) is used to calibrate the AMS measurements. This standard is available in gas form, hence only graphitization is carried out here.

4.3. Results and Discussion

4.3.1. Blanks

Blank results are essential to determine the background signal and to detect and exclude any memory effects and contamination that might occur during sample processing, graphitization, or measurement. Overall, 155 blanks have been measured since commissioning of the new extraction setup in 2018, extending the results presented in Therre et al. (2021) (n=67), of which, 17 (11 %) were rejected due to assumed contamination (figure 4.1). Reasons for possible contamination include insufficient leaching time and leakage in the setup (verifiable by monitoring pressures during a run). In addition, contamination could occur during processing (no organic material should come in contact with the sample). The storage time, the time between graphitization and measurement when graphite is exposed to air, on the other hand, should only have a minor effect on the blanks. In other laboratories, the influence of storage time of the iron-graphite sample is considered to be small (Dumoulin et al., 2017) or not relevant (Steinhof et al., 2017). Here, there is no correlation between the storage time and the absolute blank value. Therre et al. (2021) reported an long-term blank of 0.205 ± 0.065 pmC, with a median of 0.207 pmC. The updated value for

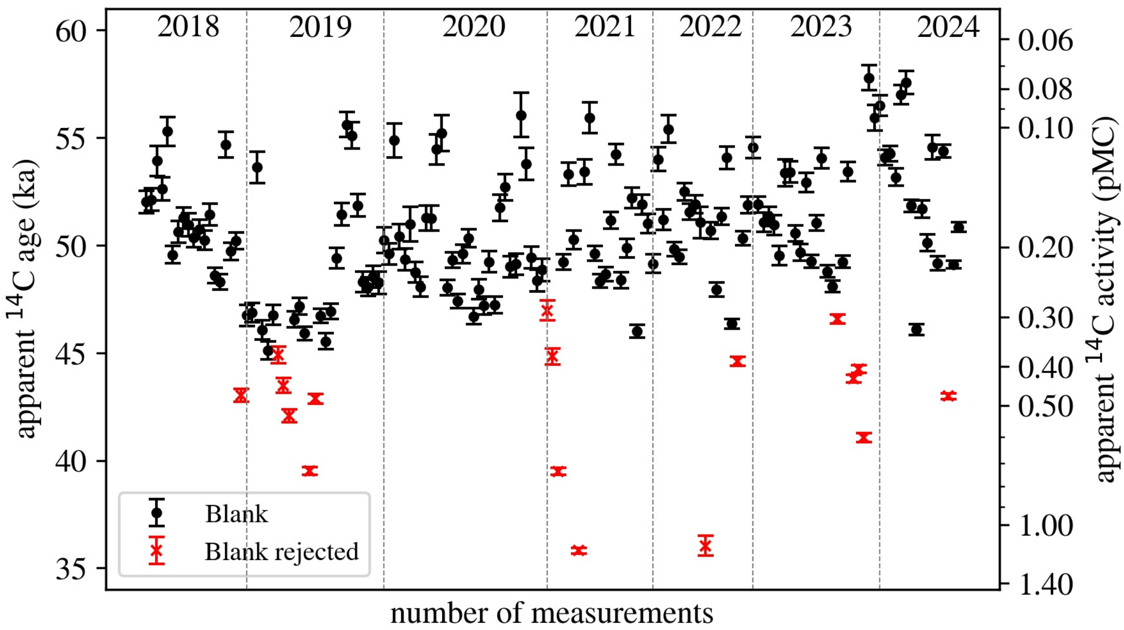

Figure 4.1.: Blank results (n=155; this study (n=88) and Therre et al. (2021) (n=67)) since commissioning of the new extraction setup in the year 2018. Rejected blanks due to contamination (n=17) have been marked in red.

the long-term blank is 0.190 ± 0.064 pMC (50.794 ± 2.813 ka), with a median of 0.184 pMC (50.594 ka).

4.3.2. Reproducibility: IAEA-C2 Standard

IAEA-C2 standards are measured regularly to check the accuracy and reproducibility of the measurements. Since commissioning of the new extraction setup, a total of 83 IAEA-C2 standards have been measured (figure 4.2), of which 8 (∼9 %) were rejected due to contamination with ^{14}C depleted CO_2. Therre et al. (2021) reported a mean value of 41.08 ± 0.24 pmC and a median of 41.12 pmC. The updated mean value is 41.15 ± 0.16 pMC (7.132 ± 0.031 ka), while the median is 41.16 pMC (7.130 ka). They agree to the reference value of 41.14 ± 0.03 pMC (Rozanski et al., 1992).

4.3.3. Cold-Water Coral Duplicates

In addition to the regular measurements of the IAEA-C2 standard, duplicate measurements of CWCs are regularly performed to ensure reproducibility (figure 4.3, table C.2). In total, 33 CWCs with ages between 9.5 and 43 ka BP (uncalibrated ^{14}C age) were measured twice, of which 13 measurements have already been published in Beisel et al. (2023) and one in Raddatz et al. (2023). All measurements agree within 2σ and 85 % of the measurements even in the 1σ range (figure 4.3). This shows

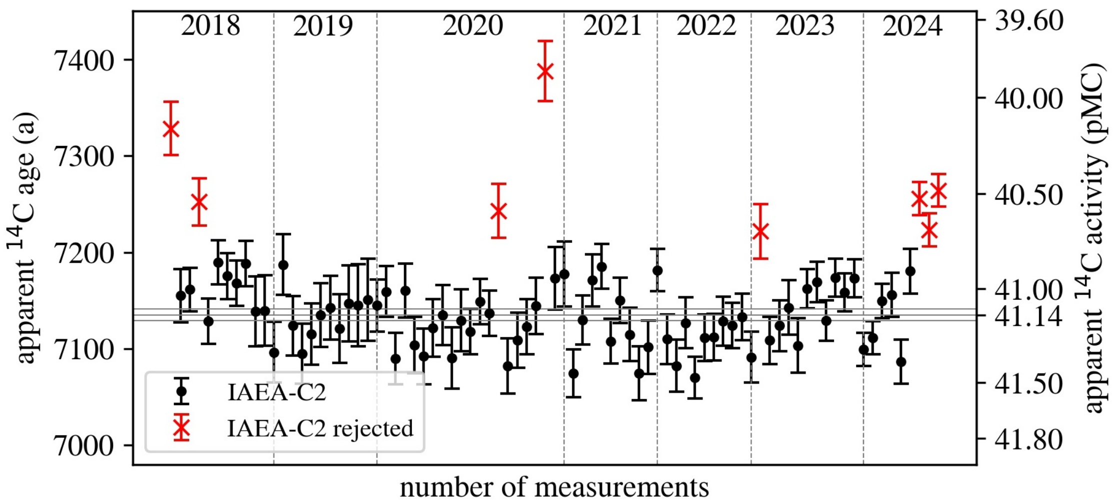

Figure 4.2.: IAEA-C2 results (n=83; this study (n=45) and Therre et al. (2021) (n=38)) since commissioning of the new extraction setup in the year 2018. The individual values are shown with 1σ uncertainty. The horizontal grey lines show the literature value of 41.14 ± 0.03 pMC (Rozanski et al., 1992), including 1σ uncertainty. Eight data points marked in red were rejected due to contamination. The last three data points were measured in one magazine and discarded due to contamination. The reproducibility was checked by duplicate CWC measurements in the magazine, in which the preparations were carried out without any noticeable incidents (n=3).

that the uncertainties of the ^{14}C ages reported by the AMS laboratory are slightly overestimated.

4.4. Conclusion

In this study, I provided an updated overview of the performance of the radiocarbon laboratory at the Heidelberg Institute of Environmental Physics and the AMS facility of the Curt-Engelhorn-Center Archaeometry. The laboratory maintains a long-term blank value of 0.190 ± 0.064 pMC (n=138) and is able to reproduce the international IAEA-C2 standard (41.15 ± 0.16 pMC, n=75) and internal CWC duplicates (n=33) excellently. This testifies to the consistently high quality of ^{14}C dating to date, which is ensured by ongoing quality controls.

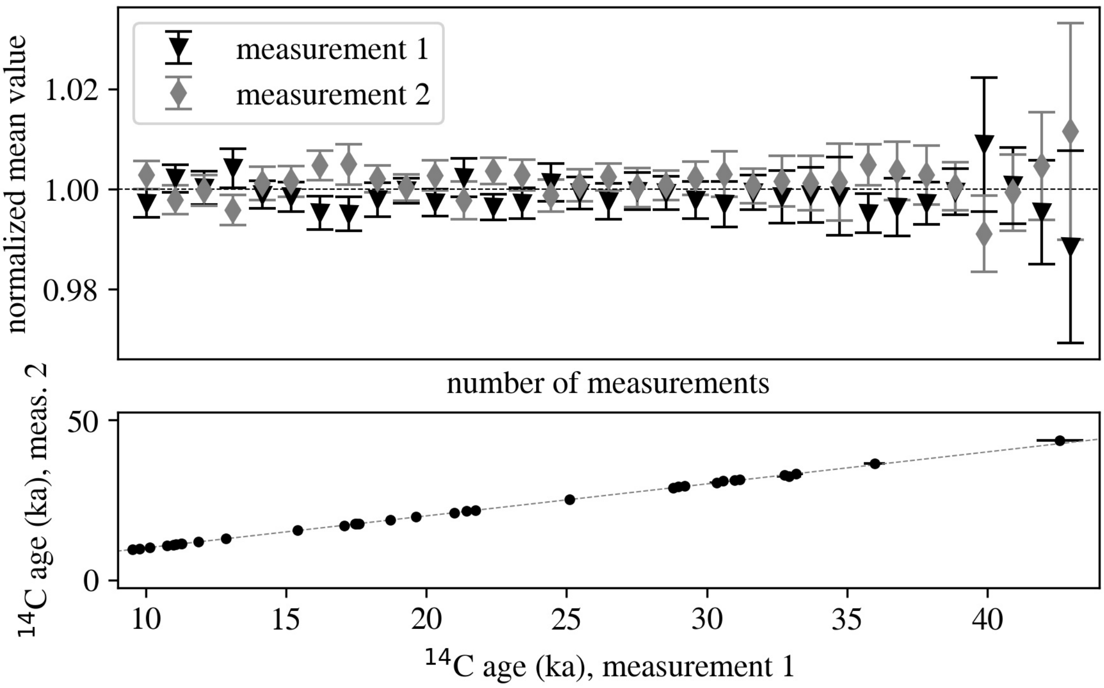

Figure 4.3.: Duplicate ^{14}C measurements (n=33; this study (n=19), Beisel et al. (2023) (n=13), and Raddatz et al. (2023) (n=1)). The top panel shows the two measurements plotted against their respective normalized mean values with 1σ uncertainties. Older samples (>32 ka) show a larger apparent difference due to large measurement uncertainty. However, there are no significant offsets. The lower panel shows the same duplicates, this time plotted against the uncalibrated ^{14}C age to illustrate the age range.

5. Climate Induced Thermocline Aging and Ventilation in the Eastern Atlantic Over the Last 32,000 Years

The content of the following chapter was published July 2023 in the journal *Paleoceanography and Paleoclimatology* ((Beisel et al., 2023), `https://doi.org/10.1029/2023PA004662`) and has been slightly modified.

Precise ^{230}Th/U and ^{14}C data allow for the investigation of thermocline radiocarbon ventilation ages through time. This work benefited from ^{230}Th/U data from the large collection of the Institute of Environmental Physics, Heidelberg, some of which have already been published in other publications (Fentimen et al., 2020, 2023; Krengel, 2020; Lausecker, 2021; Wefing et al., 2017; Wienberg et al., 2018, 2022). Initial ^{14}C data and a qualitative evaluation were part of a master thesis (Beisel, 2021) and two bachelor theses (Roesch (2017) and Beisel (2017)). As a part of this PhD project, the evaluation was further developed, substantiated and put into context of current paleoceanographic research. The original discussion has been greatly expanded. Moreover, further ^{230}Th/U and ^{14}C data were generated during this PhD project, and a collaboration with Dr. Martin Butzin enabled the inclusion and discussion of results from the Large Scale Geostrophic Ocean General Circulation Model.

Quality Control, data evaluation, and visualization was done by myself. I conceptualized the ideas, interpreted the data, and wrote the manuscript with contributions from all co-authors. Co-authors are Prof. Dr. Norbert Frank, Prof. Dr. Laura Robinson, Dr. Marleen Lausecker, Dr. Ronny Friedrich, Dr. Steffen Therre, Dr. Andrea Schröder-Ritzrau and Dr. Martin Butzin. The coral samples have been provided by an IUP collection and by the GeoB Core Repository at the MARUM – Center for Marine Environmental Sciences, University of Bremen, Germany. I sampled one sediment core at MARUM myself, cleaned the corals and prepared the samples for the ^{230}Th/U and ^{14}C measurement with help from student assistants. Dr.

Ronny Friedrich conducted the AMS measurements at the Curt-Engelhorn-Center Archaeometry (CEZA) in Mannheim. Prof. Dr. Norbert Frank supervised the project and provided the ^{230}Th/U results. Dr. Martin Butzin provided the results of the Large Scale Geostrophic Ocean General Circulation Model. Dr. Sophia Hines and two anonymous reviewers provided further comments in the review process. The associated data are deposited in PANGAEA ((`https://doi.org/10.1594/PANGAEA.959508`). Supplementary figures are provided in the Appendix B.1.

5.1. Introduction

The Atlantic overturning circulation plays a crucial role in the transfer and storage of carbon across latitudes and thus determines the ventilation state. The term "ventilation" refers to "the collective effect of the physical and chemical processes that convey atmospheric properties into the ocean interior" (definition after Skinner and Bard, 2022). During the climate transition from the Last Glacial Maximum (LGM) to its modern strong circulation state, the overturning depth and its volume flux likely increased when compared to the glacial, probably shoaled circulation (e.g. Adkins, 2013; Bradtmiller et al., 2014). In addition, some studies suggest mainly two circulation cells, with presumably low mixing in between (Adkins, 2013; Lund et al., 2011). The Atlantic is a vital carbon reservoir, in which small changes in ocean-atmosphere exchange and wind forcing impact the atmospheric partial pressure of CO_2 (pCO_2, Barnola et al., 1987; Petit et al., 1999; Sigman and Boyle, 2000). The thermocline responds to atmospheric forcing via wind driven eddy flow and provides a way to store water properties such as dissolved carbon over decades to centuries (Lozier, 1997). Consequently, the Atlantic thermocline is a fast-acting part of the global marine carbon reservoir, barely studied for its ventilation history. A detailed reconstruction of ^{14}C ventilation ages is essential to fully reconstruct the spatiotemporal variability of Atlantic interior ventilation. Cold-water corals (CWCs) provide the means to establish high-resolution and high-precision records of the thermocline ventilation of the past. Their aragonite skeleton traps trace elements of surrounding water as they grow, allowing ^{230}Th/U dating (Smith et al., 1997) for absolute age determination. This provides absolute time scales allowing to resolve past seawater dissolved inorganic carbon ^{14}C levels through combined ^{230}Th/U and ^{14}C dating (Adkins et al., 1998; Frank et al., 2004; Mangini et al., 1998). The resulting age difference between the ocean and the contemporaneous atmosphere, that is, the Benthic-Atmosphere (B_{atm}) ages (Skinner and Bard, 2022), are valuable indicators of the Atlantic interior water mass advection pathways, and thus provide the key to reconstruct the prevailing circulation.

While several studies suggest two distinct meridional overturning circulation cells in the Atlantic during the LGM (Adkins, 2013; Lund et al., 2011), the growing number of radiocarbon studies provides constrains on the ventilation state and thus vertical extension of these cells. First evidence of past mid-depth circulation changes and water mass aging in the Atlantic Ocean were collected using intermediate to deep dwelling CWCs and foraminifera (e.g. Chen et al., 2015; Eltgroth et al., 2006; Frank et al., 2004; Freeman et al., 2016; Keigwin and Schlegel, 2002; Mangini et al., 2010; Robinson et al., 2005; Schröder-Ritzrau et al., 2003; Skinner et al., 2014, 2021). Numerous radiocarbon records across the deep and South Atlantic showed significant aging, with a highest reservoir age increase in the mid-depth ocean of up to ∼2,500 years (Rafter et al., 2022; Skinner and Bard, 2022). Two different reasons, or a combination of both, may account for the interior water mass aging: (a) a reduced interior circulation, hence longer turn-over times for water, or (b) a reduction in air-sea gas exchange in deep-water formation regions at high-latitudes (Schmittner, 2003; Skinner and Bard, 2022). Both processes are well attested, with the global sea ice cover expanding during the last glacial (WAIS, 2015) and periods of reduced Atlantic Meridional Overturning Circulation (AMOC), as attested in numerous studies (Böhm et al., 2015). Furthermore, a variety of studies suggests a shallow, well-ventilated water mass with fast overturning in the North Atlantic during the LGM (e.g. Böhm et al., 2015; Chen et al., 2015; Cléroux et al., 2011; Freeman et al., 2016; Lippold et al., 2012; Skinner et al., 2017; Slowey and Curry, 1992). However, previous radiocarbon reconstructions above 1,000 m depth in the North Atlantic are derived mostly from foraminifera and show large scatter, ranging from very well-ventilated waters to strongly depleted waters with B_{atm} ages of up to 2,000 years (compilation by Skinner and Bard, 2022). As stated by Skinner and Bard (2022), one outstanding challenge for the interpretation of radiocarbon as ventilation age tracer is to narrow down the observed scatter in marine radiocarbon reservoir age estimates.

^{230}Th/U dated CWCs overcome some of the impediments associated with the use of foraminifera (Skinner and Bard, 2022), and provide ventilation ages with higher precision regarding the absolute age determination and reservoir age uncertainty. Here, this part of the Atlantic thermocline ocean is investigated using framework forming CWCs to retrieve the evolution of the east Atlantic north-south ventilation difference since the last glacial. In addition, the regional consistency of available ventilation age observations from deep dwelling corals is tested, which permit to infer a strong Southern Hemisphere connectivity of aged water masses and its upper age limit relevant for calibration purposes. Four new Δ^{14}C datasets obtained on a total of 122 CWCs are presented, which dwelled between 259 and 970 m depth at hydrographically important locations in the central and east Atlantic Ocean (Azores Front Corals

(AFC), Mauritania, and Angola) as well as in the Alboran Sea (figure 5.1). The observations are compared to ^{14}C simulation results and show good agreement for most of the Atlantic, whereas differences between model results and observations appear most significant for the North Atlantic north of the Azores Front (AF) and Mauritania during the last glacial.

5.2. Materials and Methods

5.2.1. Sites and Hydrography

Corals from 33 individual sites representing four distinct regions were selected for this study: (a) Alboran Sea, at the entrance/exit of the Mediterranean Sea, (b) Azores and Great Meteor Seamount, summarized under the term "AFC" and positioned near todays meandering AF, (c) offshore Mauritania in the subtropical North Atlantic, and (d) offshore Angola in the subtropical South Atlantic (figure 5.1). Corals were recovered using a variety of equipment, including remotely operated vehicles, gravity corers and grab samplers. Predominantly framework forming species such as *Desmophyllum pertusum* (formerly known as *Lophelia pertusa*) and *Madrepora oculata* were selected, with a few solitary species such as *Desmophyllum dianthus*. Corals were well preserved, with occasional minor traces of bioerosion and coating, that were removed through mechanical cleaning. The selected sites reflect a slightly uneven depth distribution with a median depth of 600 ± 250m. Alboran Sea, Mauretania, and Angola represent depth intervals of 300–500 m, whereas the various sites near the Azores and Great Meteor Seamount reflect deeper habitats at 600–970 m. However, the sites are strongly connected via the thermocline water circulation (see below).

To determine the radiocarbon contribution of Mediterranean Outflow Water (MOW), corals from the Alboran Sea (35°N, 2°W) are included. The Alboran Sea is directly connected to the North Atlantic Ocean via the inflow of Atlantic surface water due to the west-east sea surface height gradient from excess evaporation. Deep convection in the Mediterranean balances the flow with an outflow of warm and salty MOW into the North Atlantic. Given the short overturning time, these waters are today well-ventilated compared to the surrounding Atlantic waters. At 330 m depth within the Alboran Sea, $\Delta^{14}C$ reaches values of +50 ‰ today, which reflects the rapid overturning and thus bomb radiocarbon propagation from the Atlantic surface to the MOW. The selected corals were recovered at a depth of $\sim 330 \pm 6$ m from coral bearing gravity cores taken on the top of the Brittlestar coral mounds (Fentimen et al., 2020; Hebbeln et al., 2015; Krengel, 2020; Van Rooij et al., 2013), nowadays under persisted influence of MOW.

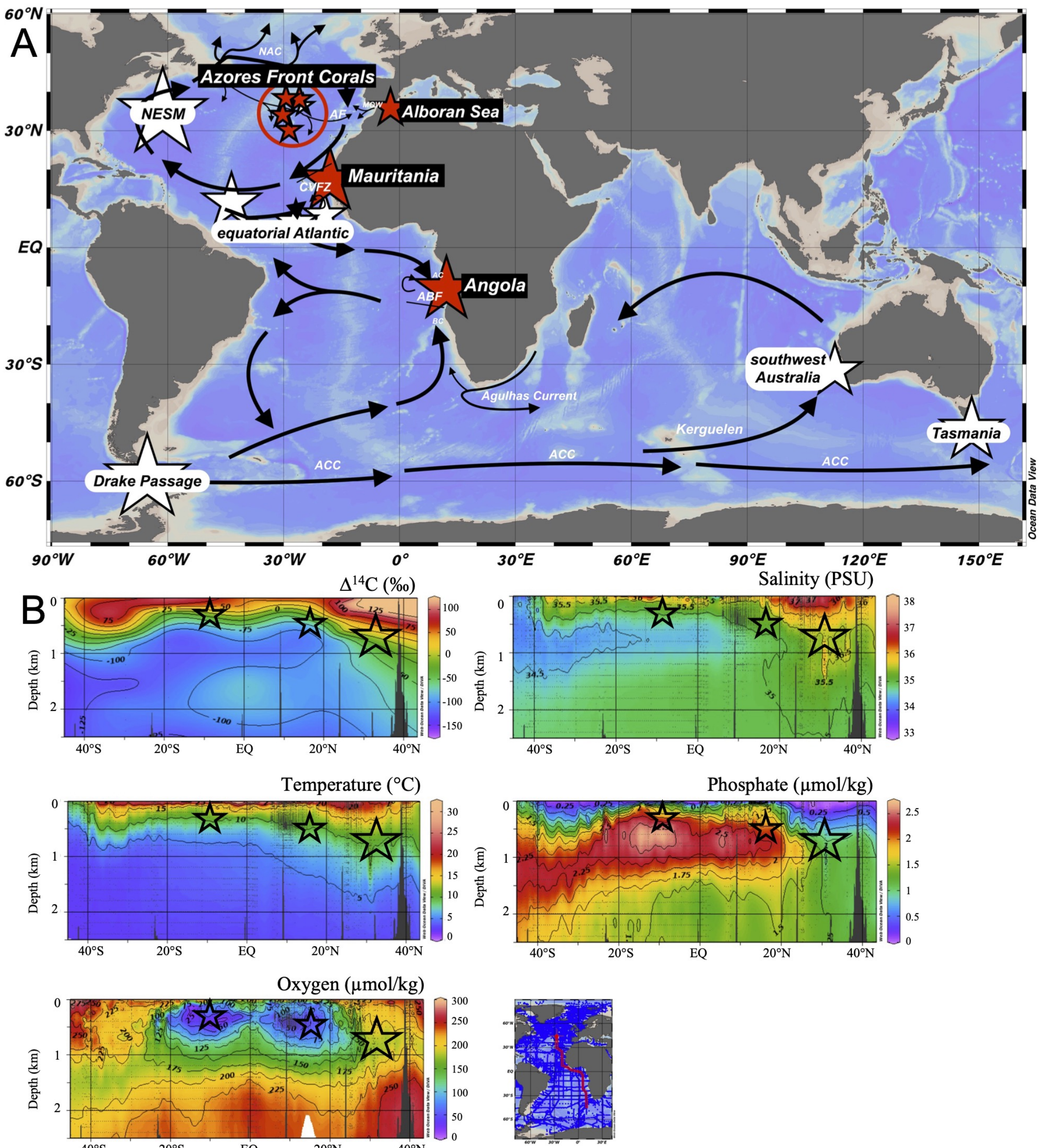

Figure 5.1.: (a) Map of investigated sites, including major surface currents and fronts, as well as locations of previously published radiocarbon results using cold-water corals (CWC). Four new datasets are presented here (red stars): Alboran Sea (∼330 m), Azores Front Corals (AFC; Azores and Great Meteor Seamount region; 560–970 m), Mauritania (492–580 m) and Angola (259–457 m). Alboran Sea CWCs reveal the influence of Mediterranean Outflow Water in the Atlantic, where it nowadays influences AFC near the present-day AF. The CWCs off Mauritania are located near the Cap Verde Frontal Zone, while those off Angola are situated near the Angola-Benguela-Front. The Benguela Current carries water from the Antarctic Circumpolar Current and Agulhas Current, while the Angola Current flows southward. The observations are compared to previously published CWC results (white stars) from the New England Seamount (Adkins et al., 1998; Eltgroth et al., 2006; Hines et al., 2019; Robinson et al., 2005; Thiagarajan et al., 2014), equatorial Atlantic (Chen et al., 2015, 2020), Drake Passage (Burke and Robinson, 2012; Chen et al., 2015; Li et al., 2020), southwest Australia (Trotter et al., 2022) and Tasmania (Hines et al., 2015). (b) Hydrography around sample locations. Black stars mark sampled areas. Figure created using Ocean Data View (Schlitzer, 2023).

Further corals were selected from the Azores and Great Meteor Seamount region (29°N–38°N, 25°W–29°W, figure 5.1a). They were recovered near the present-day AF by using a remotely operated vehicle (SQUID-MARUM) and a grab sampler. In this region, CWCs reflect singular occurrences instead of coral mounds (Frank et al., 2023). Today, the corals sites are mainly under the influence of Eastern North Atlantic water with a residual component of MOW (Frank et al., 2023; Palma et al., 2012). They are situated in a highly dynamic Atlantic frontal zone at the interface between subpolar and subtropical Atlantic waters, characterized by a strong latitudinal gradient of water mass properties. From south to north the nutrient concentration at upper thermocline depths decreases across the front by a factor of three, while oxygen increases by a factor of three (figure 5.1b). Temperature and salinity increase with depth within the frontal zone due to Ekman pumping and heat and salt contributions from MOW, while north of the AF salinity and temperature decrease again. The downward flux of heat and carbon within the frontal zone is well attested through the penetration depth of bomb radiocarbon, which reaches $\Delta^{14}C$ values of 0 ‰ in 800 m depth compared to −50 ‰ in pre-bomb times (figure 5.1b). Here, the corals from this dynamic region are summarized under the term "AFC."

The third site is situated off Mauritania (17°N–18°N, 16°W) (Westphal et al., 2014; Wienberg et al., 2018). The corals have been taken from five coral bearing gravity cores taken in one of the largest CWC provinces, known as the great wall of Mauritania (Wienberg et al., 2018). They periodically occur near the Cap Verde Frontal Zone (CVFZ), a region influenced by South Atlantic Central Water (SACW) with low oxygen concentrations and temperatures of 10–12°C (GLODAPv2.2022, Lauvset et al., 2021, figure 5.1b). Therefore, the regions off Mauritania are nowadays predominantly characterized by a pronounced oxygen minimum zone, due to the sluggish recirculation and significant organic matter remineralization. The observed modern $\Delta^{14}C$ shows identical patterns to the ones off Angola, that is, slow downward penetration of bomb radiocarbon (figure 5.1b).

Lastly, corals were studied from offshore Angola (9°S, 12°E), a major coral mound province (Hebbeln et al., 2017). CWCs were collected from three coral bearing sediment cores from two mounds, complemented by several coral fragments collected using a grab sampler and box corer. The sites are currently influenced by the southward flow of equatorial thermocline water through the Angola Current, and slow northeastward recirculation of subsurface waters from the Benguela Current. The pathways of advection strongly depend on the intensity of the Agulhas leakage at the southern tip of Africa (Veitch et al., 2010). The northward propagating SACW, and possibly Antarctic Intermediate Water (AAIW), are injected into the thermocline underneath the Angola Dome upwelling system (figure 5.1a). Water masses at the coral sites are today characterized by low oxygen contents of 25–50 μmol kg^{-1} and temperatures of 8–10°C, as well as high phosphate concentrations of >2.25 μmol kg^{-1} (GLODAPv2.2022, Lauvset et al. (2021); figure 5.1b). According to Δ^{14}C observations collected as additional information by GLODAPv2.2022, Δ^{14}C ranges from -75 ‰ to $+25$ ‰ between 600 and 250 m depth, indicating an increase of Δ^{14}C of $+100$ ‰ in the upper most thermocline since the late 60s, while lower thermocline waters remain without influence of bomb-radiocarbon.

5.2.2. Uranium Series Dating and Selection Criteria

Solely well preserved CWC samples were selected based on precisely measured ^{230}Th/U, with ages of up to 32 ka. Cleaning, preparation and measurement of the corals is described in detail in chapter 3.

The initial δ^{234}U value and ^{232}Th contamination were used to evaluate the quality of the ^{230}Th/U ages. Here, solely corals with a ^{232}Th content below 3.6 ng/g were selected. To test the U series closed system presumption, it is assumed that all corals must have an initial ^{234}U/^{238}U ratio ($\delta^{234}U_{initial}$) of ± 7 ‰ of the modern ocean $\delta^{234}U_{sw}$ (146.8 ‰) (Andersen et al., 2010; Reimer et al., 2009). The selected range of $\delta^{234}U_{sw}$ variability of ± 7 ‰ includes the known glacial reduction in seawater δ^{234}U by some -5 ‰ ± 2 ‰ (Chutcharavan et al., 2018). ^{230}Th/U ages are reported referenced to 1950 AD (years BP).

Note: In the course of this thesis, the selection criteria for ^{230}Th/U ages were refined. The revised selection criteria now include a threshold for ^{232}Th of 2 ng/g, instead of 3.6 ng/g, to further reduce age uncertainty. The application of the 2 ng/g threshold to the data utilized in this study would result in the elimination of only six out of 122 data points (5 %), with no impact on the conclusions. The latest developments (chapter 6) demonstrate the necessity of the criterion of chronological consistency, as well as regional consistency. The application of these criteria would not result in a notable impact on the data set published in Beisel et al. (2023). I have therefore decided to show the data set presented in Beisel et al. (2023) here without any changes.

5.2.3. Radiocarbon Dating

The method for preparing coral samples for radiocarbon measurements is described in detail in chapter 3.3.

For data presentation, Δ^{14}C, the known-age radiocarbon correction, is calculated: $\Delta^{14}C_{coral} = (Fm \cdot e^{(calendar\ age/8267)} \cdot 1,000$ (Stuiver and Polach, 1977). Since this value is best used in combination with the reconstructed ^{14}C content of the atmosphere, the offset $\Delta\Delta^{14}$C, as $\Delta^{14}C_{coral} - \Delta^{14}C_{atmosphere}$, is calculated, as well as the Benthic-Atmosphere (B_{atm}) age, as $^{14}C_{age,\ coral} - {}^{14}C_{age,\ atmosphere}$, to account for the varying atmospheric ^{14}C inventory (Chen et al., 2015). IntCal20 (Reimer et al., 2020) and SHCal20 (Hogg et al., 2020) were used as atmospheric references. All previously published ^{14}C data presented here were recalculated according to the updated atmospheric calibration curves.

Even after rigorous quality control, four of the 122 fossil corals had to be excluded from the results and discussion, because they showed Δ^{14}C values identical or above the IntCal20 reconstruction (seawater ^{14}C > atmospheric ^{14}C).

5.2.4. Modeling Radiocarbon

The observations are compared with the simulation results of three numerical simulations obtained from an enhanced version of the Large Scale Geostrophic Ocean General Circulation Model (LSG, Maier-Reimer et al. (1993), for the enhancements see Butzin et al. (2005), and further references therein). The model has a horizontal resolution of 3.5° and a vertical resolution of 22 unevenly spaced levels. Radiocarbon is simulated as Δ^{14}C following Toggweiler et al. (1989). The oceanic uptake of ^{14}C is calculated according to Sweeney et al. (2007), using atmospheric CO_2 values (Köhler et al., 2017) and concentrations of dissolved inorganic carbon in surface water simulated by Hesse et al. (2011). The LSG model is forced with monthly fields of recent and glacial wind stress, surface air temperature, and freshwater flux derived in previous climate simulations (Lohmann and Lorenz, 2000; Prange et al., 2004). To capture the range of past ocean-climate variability and its impact on marine ^{14}C records, three climate forcing scenarios are considered, which are discussed in detail by Butzin et al. (2005). In summary, one scenario (PD) employs present-day climate background conditions approximating the Holocene and interstadials. Another scenario (GS) aims at representing the LGM and features a shallower AMOC than scenario PD weakened by about 30 %. The third climate scenario (CS) mimics cold stadials with further AMOC weakening by about 60 % compared to PD. Scenarios PD and CS typically represent the lower and upper bounds of marine ^{14}C depletion with respect to the contemporaneous atmosphere ($\Delta\Delta^{14}$C). The simulations were run with transient values of atmospheric Δ^{14}C (Reimer et al., 2020) and evaluated at the model coordinates nearest to the CWC sites.

5.3. Results

5.3.1. ^{230}Th/U Dating

Overall, U concentrations are within the typical range of 2.5–5.5 μg/g. Median ^{232}Th concentrations are 0.5 ng/g due to the strict selection criteria, and median δ^{234}U values are 146.3 ‰, identical within uncertainty to the expected modern seawater value. Note that δ^{234}U clearly shows the known systematic deviation from constant δ^{234}U values during the last glacial for corals from Mauretania and Angola, while observations from the AFC and Alboran Sea reveal punctuated and even systematic higher values in agreement with the northern source of excess ^{234}U derived by Chen et al. (2016). In conclusion, it is assumed that all ^{230}Th/U ages are reliable and that the initial δ^{234}U isotopic composition reflects past seawater. The ages used for radiocarbon reconstruction range from 31.56 ka to 52 years. The distribution of ages is different for each site. For the Alboran Sea, coral ages are only available for the end of the deglaciation from 14.73 to 9.65 ka. For AFC, ages from 21.1 ka to 52 years are obtained, reflecting the LGM, termination 1, and the Holocene. At Mauritania, ages range from 25.5 to 12.5 ka, representing the LGM as well as the Bølling-Allerød (B/A) and Younger Dryas (YD). Most of the results were obtained from Angola, where corals provide ages from 31.6 ka to 41 years. Consequently, Angola provides observations from the last glacial and LGM to the present.

5.3.2. Radiocarbon Dating

In general, the Δ^{14}C values follow the atmospheric trend with Δ^{14}C values decreasing from 400 ‰ to -65 ‰ over the past 32 ka (figure 5.2a; IntCal20, Reimer et al. (2020)).

Alboran Sea corals confirm previous results (McCulloch et al. (2010); figure B.1), showing overall well-ventilated water with an average $\Delta\Delta^{14}$C value of -55 ‰ $\pm$ 34 ‰ and B$_{atm}$ age of 400 $\pm$ 230 years. Two values are strongly depleted with $\Delta\Delta^{14}$C of -140 ‰ and -130 ‰ corresponding to a doubling of B$_{atm}$ ages from 450 to 900 years at 12.4 $\pm$ 0.04 ka and at 13.6 $\pm$ 0.2 ka. The second depletion coincides with the YD cold reversal. A comparison with numerical simulations is not possible here, since the Alboran Sea is not represented in the LSG Ocean General Circulation model.

AFC reveal well-ventilated water with an average $\Delta\Delta^{14}$C of -66 ‰ $\pm$ 30 ‰ and B$_{atm}$ age of 450 $\pm$ 170 years since the LGM. The mean $\Delta\Delta^{14}$C value is thus $\sim$ 10 ‰ lower compared to the one of the Alboran Sea, but identical within uncertainty (figure 5.2b). Over the last 14 ka, the results agree within uncertainty with the upper bound of the numerical simulation, which corresponds to the lowest B$_{atm}$ ages (figure B.2. In contrast, for the LGM and beginning deglaciation, the numerical simulation yields

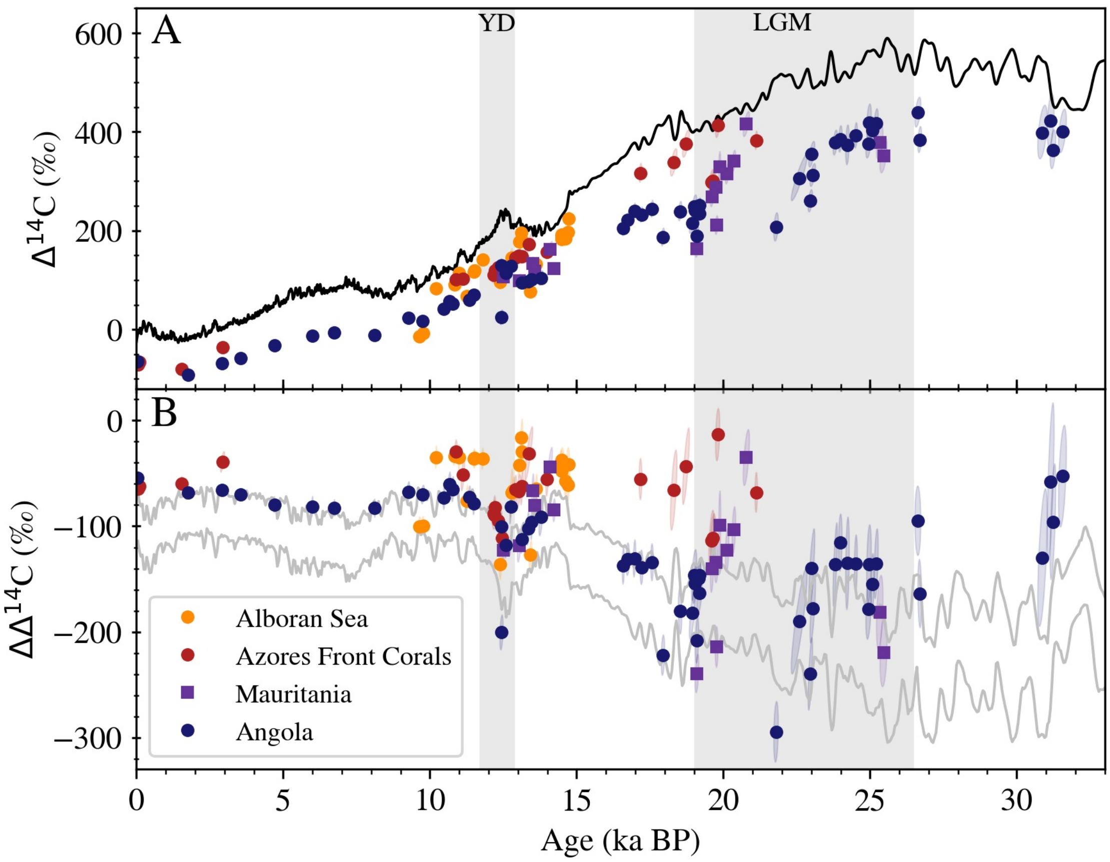

Figure 5.2.: Radiocarbon variability of the east Atlantic thermocline obtained from cold-water corals (CWC) in this study. (a) Δ^{14}C with IntCal20 as atmospheric reference (black line, Reimer et al. (2020)). (b) $\Delta\Delta^{14}$C evolution (Δ^{14}C offset between ocean and atmosphere), including upper and lower bounds of the LSG model simulation results off Angola (gray lines). Error ellipses represent the 2σ uncertainty. Angola basin CWC results are mostly at the upper bound of the simulation. The ^{14}C values of the Northern Hemisphere remain well-ventilated, in sharp contrast to the corresponding simulation results (figures B.2 and B.3). Differences between south and northeast Atlantic vanish with the onset of the Younger Dryas.

$\Delta\Delta^{14}$C of -120 ‰, while the observations are on average -70 ‰ (figure B.2. Only at 19.6 ka do model and observations agree, with two individual observations of -110 ‰, again corresponding to the upper bound of the model output. Prior to the YD, from 14 to 12.9 ka, the results reveal low B_{atm} ages of 220 – 460 years. During the YD, the observations confirm a 250 year long decrease in ventilation, followed by an increase in ventilation at 11.5 ka to modern values. The AFC results support previously documented synchronous B_{atm} age excursions reconstructed at significantly deeper depth west of the New England Seamounts (NESM) (Eltgroth et al., 2006; Robinson et al., 2005).

Between 25 and 12.5 ka, the corals off Mauritania show $\Delta\Delta^{14}$C values with a mean of -125 ‰ ± 60 ‰, corresponding to a mean B_{atm} age of 770 years. Therefore, the CWCs from Mauritania report water masses that are on average 320 years older than the more northerly sites. However, within the overall high variability of B_{atm} ages from 1,500 to 300 years, the ventilation is partially identical to the northern sites as well as the southern sites (see below). If compared to the LSG model, the observations at 14 to 12.5 ka and at 25.3 to 25.4 ka are in perfect agreement with the simulation, while the observed $\Delta\Delta^{14}C$ values around the LGM and the onset of deglaciation are initially higher by up to 70 ‰ (21 ka) and then lower by up to 50 ‰ (19 ka) (figure B.3.

The overall most important data set is generated for Angola. Here, well-ventilated waters were reconstructed around 31 ka and from 13.8 ka (figure 5.2 and figure B.4), with a mean $\Delta\Delta^{14}C$ of -80 ± 17 and B_{atm} age of 580 ± 120 years. In between, $\Delta\Delta^{14}C$ values and B_{atm} ages are highly variable, showing lowest values of -295 ‰ (1,700 years B_{atm} age) at 21.8 ka. In contrast to the results of the northern sites, the radiocarbon record from Angola is mainly at the upper bound of the LSG model results. Note that the model does not resolve the Angola gyre circulation and therefore cannot correctly simulate the associated upwelling in this region. Nonetheless, 92 % of the data are captured by the range of $\Delta\Delta^{14}C$ values simulated by the LSG model. Solely at 31 ka do the observations systematically exceed the model results (figure B.4). The record reveals several periods of centennial variations from 50 ‰ to 100 ‰ (250–500 years B_{atm} age), with only the last two within model uncertainty (19 and 23 ka). The LSG model simulates a gradual increase of ventilation between 18 and 14 ka, which is confirmed in terms of measured values. It is important to note that the B_{atm} ages prior to the simulated ventilation increase show high B_{atm} ages and large scatter with an average value of 1,060 ± 180 years between 19.2 and 17.9 ka, followed by a 980 year long period of moderately higher but extremely constant B_{atm} ages averaging 840 ± 30 years during the simulated increase between 17.5 and 16.6 ka. Between 16.6 and 13.8 ka, the water off Angola reduced the age by another 130 years to an average of 650 ± 25 years from 13.8 to 13.5 ka. This ventilation trend was interrupted during the Antarctic Cold Reversal (ACR) some 13.5 to 13.1 ka ago, when B_{atm} ages increased again by 100 ± 50 years, as simulated. Subsequently, a decrease in ventilation is recorded during the YD period until, finally the well-ventilated (quasi modern) state during the Holocene is reached.

The observed radiocarbon ages off Angola are broadly consistent with observations in the equatorial Atlantic at 750–1,492 m depth (Chen et al., 2015, 2020), southwest Australia at 675–1,788 m depth (Trotter et al., 2022), and south of Tasmania at 1,430–1,950 m depth (Hines et al., 2015) (figure 5.3c). These deeper and more distant sites show identical values within uncertainty or moderately higher B_{atm} ages. At 21.8 ka, the B_{atm} age at Angola increased to a similar high value as observed off southwest

Australia (figure 5.3c).

Lastly, a remark on the B/A and YD period of Northern Hemisphere warming some 14.9 ka and 12.5 ka ago. The northern and southern Atlantic records deviate by $\sim 250 \pm 50$ years (B_{atm} age, figure 5.4c). With the onset of the YD at 12.5 ka, the ^{14}C gradient between the North and South Atlantic ultimately vanished. The YD resolves a pronounced $\Delta^{14}C$ decline of ~ 80 ‰ within 1,000 years at all sites (figure 5.2b).

5.4. Discussion

The above presented results fill out an important data gap in the recent compilation by Skinner and Bard (2022). Corals from Angola and Mauritania enable to investigate the southern extent of the well-ventilated water, as well as the northern and vertical extent of aged, southern-sourced water. Thus, the focus is on the upper branch of the Atlantic circulation and its horizontal fronts. The physical nearness of the investigated corals to oceanic fronts makes them sensitive to water mass changes, particularly the intrusion of older, southern sourced or underlying water. AFC shed light on the important role of the AF in the North Atlantic. In general, low mixing is thought to have occurred between the two circulation cells during the LGM (Adkins, 2013; Lund et al., 2011), with a boundary at roughly 2,000–2,500 m depth (Rafter et al., 2022), thus well below the coral sites. The following discussion will focus on several key observations. First, the overall Atlantic thermocline ventilation since 32 ka is examined. Subsequently, the well-ventilated state in the North Atlantic during the LGM is investigated. Corals from Angola show striking similarities to previous radiocarbon records, hence the South Atlantic connectivity and its northern limit are explored. Finally, the first insights into thermocline ventilation during the B/A warm period, the ACR, and YD provided by these records are discussed in detail.

5.4.1. The Atlantic Thermocline Ventilation Since 32 ka

Here, the thermocline is defined as the interface between the well-mixed surface layer and the underlying colder water at intermediate depths between 200 and 1,000 m. Note that the physical thermocline, as the region of downward temperature drop, can extend to 2,000 m in the Atlantic. The upper part of the ocean at mid-depth discussed here is closely related to the dynamics in the surface ocean, as it is the host of strong eddy driven re-circulation gyres, mid-depth boundary currents and specific intermediate water masses (such as MOW and AAIW). Moreover, this depth interval is influenced by the presence of oceanic fronts, such as the AF, CVFZ, and the ABF, which locally cause horizontal water mass gradients and/or vertical exchanges.

Overall, this part of the ocean is today generally influenced by recent ^{14}C changes in the atmosphere, that is, bomb ^{14}C. Consequently,the apparent age of all these water masses must be less than 60 years (figure 5.1b). Assuming an average reservoir effect of 380 years (Heaton et al., 2020) of the modern Atlantic (neglecting regional variability), the radiocarbon age of these water masses would be expected in the order of 440 years. The reason for the good ventilation state of these water masses is their close connection to the surface via turbulent seasonal mixing, wind driven upwelling and downwelling, and shallow overturning of intermediate waters in subpolar and subtropical regions (Skinner and Bard, 2022).

In fact, all studied sites reveal similarly young B_{atm} ages since the YD and in various regions prior to it. In particular, AFC show persistently such well-ventilated waters, as reflected in the median B_{atm} age (450 ± 170 years), whereas further south such low B_{atm} ages occur only at 31 ka (Angola), 20 ka (Mauritania) and the B/A. Consequently, during most of the glacial period between 26.8 to 16.5 ka, the thermocline south of the modern AF aged 330–440 years, as indicated by the difference between the expected modern age (440 years) and the median observed age (770 and 880 years). In addition, the median B_{atm} age reveals a moderate north-south gradient of 110 years, while a similar ventilation age difference exists between AFC and Angola since the B/A. Therefore, the glacial intermediate depth age gradient per latitude was enhanced.

5.4.2. North Atlantic Ventilation During the Last Glacial Maximum

The ^{14}C reconstructions of the AFC are within the transition zone between subtropical and subpolar North Atlantic thermocline waters (located around the Azores and Great Meteor Seamount, 800–1,000 m depth). Within uncertainty, the AFC are in accordance with ventilation ages off Mauritania at ∼560–590 m depth, ranging from 80 to 680 years between 20 and 21 ka (figure 5.3c). The mean age of ∼500 years is close to the common pre-bomb surface reservoir age of 380 years, demonstrating the strong surface to thermocline ocean connectivity. Today, the presence of well-ventilated thermocline waters within this region is caused by the regional downwelling of carbon due to Ekman pumping, the injection of well-ventilated MOW and shallow convection in the Labrador Sea as part of the subpolar gyre. These processes permit a fast overturning of carbon as detected today in the decadal turnover of bomb-radiocarbon and other ventilation tracers (GLODAPv2.2) and must have operated at all times north of the AF to sustain the high degree of ventilation throughout the last glacial and even deglaciation. The strong resemblance of B_{atm} ages near the glacial AF and CFVZ (Mauritania) argues for basin scale recirculation of well-ventilated water north

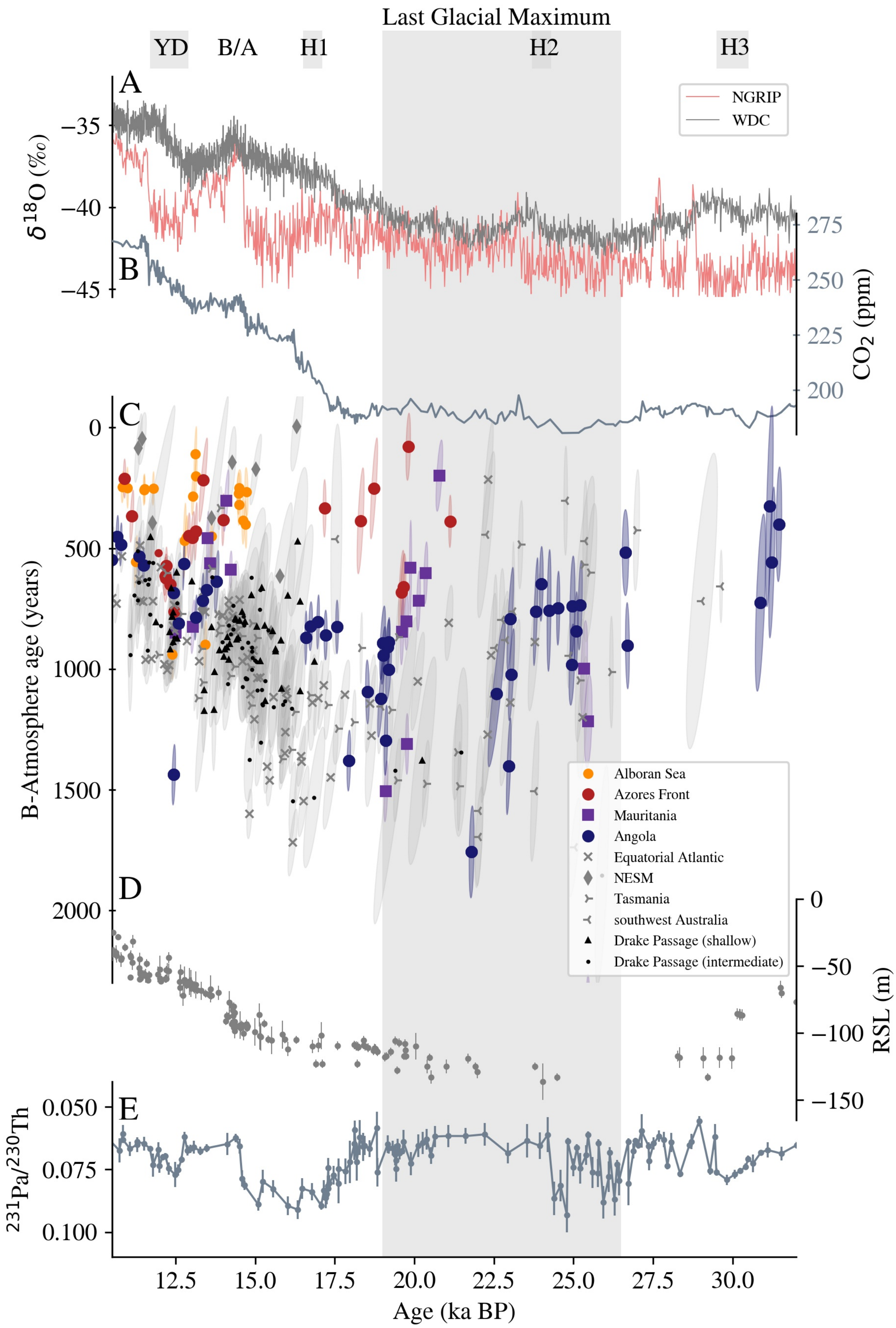
Last Glacial Maximum
YD
B/A
H1
H2
H3
A
B
C
D
E
NGRIP
WDC
δ18O (‰)
−35
−40
−45
275
250
225
200
CO2 (ppm)
0
500
1000
1500
2000
B-Atmosphere age (years)
Alboran Sea
Azores Front
Mauritania
Angola
Equatorial Atlantic
NESM
Tasmania
southwest Australia
Drake Passage (shallow)
Drake Passage (intermediate)
0
−50
−100
−150
RSL (m)
231Pa/230Th
0.050
0.075
0.100
12.5
15.0
17.5
20.0
22.5
25.0
27.5
30.0
Age (ka BP)

Figure 5.3.

Figure 5.3.: Radiocarbon age variability and climate change between 10 and 32 ka. (a) $\delta^{18}O$ records of NGRIP, Greenland (Bazin et al., 2013) and WDC, Antarctica (WAIS, 2015). (b) CO_2 compilation record (Bereiter et al., 2015). (c) B-Atmosphere age reconstructed from cold-water corals: Azores Front Corals, Mauritania, and Angola (this study), as well as equatorial Atlantic (Chen et al., 2015, 2020), New England Seamounts in 1,100–1,400 m depth (NESM; Eltgroth et al., 2006; Hines et al., 2019; Robinson et al., 2005; Thiagarajan et al., 2014), Tasmania (Hines et al., 2015), southwest Australia (Trotter et al., 2022) and Drake Passage (DP, Burke and Robinson, 2012; Chen et al., 2015; Li et al., 2020). Note: All B_{atm} ages have been recalculated using IntCal20 and SHCal20 (Hogg et al., 2020; Reimer et al., 2020). DP sections after (Li et al., 2020), depending on the location and depth of the corals. (d) Observed relative sea level (Lambeck et al., 2014). (e) $^{231}Pa/^{230}Th$ records of sediments from the Bermuda rise (Böhm et al., 2015; Henry et al., 2016; Lippold et al., 2019; McManus et al., 2004).

of the wind-driven front separating southern and northern sourced waters. In addition, this observation suggests a southward shift of the AF, to remove the difference in B_{atm} ages between south and north of the modern AF. The abundance of specific planktic foraminifers as an indicator for the presence of the AF during glacial times supports this view (Reißig et al., 2019; Schiebel et al., 2002).

Strikingly, Mauritania CWCs not only show similarities with AFC, but also punctually match the radiocarbon signal observed in corals further south at 19.7 and 19.1 ka (equatorial Atlantic and Angola, figure 5.3c). Previous studies suggested a southward displacement of the CVFZ during the LGM (Huang et al., 2012; Wienberg et al., 2018), which would lead to an influence of northern-sourced water near Mauritania, in contrast to the southern-sourced water bathing the corals today. This is consistent with the well-ventilated signal, with reconstructed B_{atm} ages $<$1,000 years, matching the AFC and the predicted pattern by Skinner and Bard (2022) (figure B.6). However, the episodic resemblance with southern coral B_{atm} ages ($>$1,000 years) argues for multiple shifts of the CVFZ, causing punctually drastic decreases in ventilation through the advance of older southern water. Between 19.7 and 19.1 ka (figure 5.2c), two Mauritanian corals show strong B_{atm} age increases, which are likely caused by latitudinal movements of the CVFZ, such that the subtropical and subpolar North Atlantic thermocline was located between well and poorly ventilated waters. In addition to the horizontal frontal movement, a severe contrast between the well-ventilated water of the northern thermocline and the strongly aged water below the thermocline results in a high sensitivity to vertical fluctuations. However, it is not yet possible to resolve the depth profile and thus cannot distinguish from the few age measurements, whether horizontal or vertical changes caused the two elevated reservoir ages.

5.4.3. The South Atlantic Connectivity and Its Northern Limit During the Last Glacial

While the South Atlantic upper thermocline ^{14}C record (Angola) shows well-ventilated thermocline waters during the Holocene, a different picture emerges during the LGM. Apparently, at 31 ka aged waters replaced the well-ventilated water off the coast of Angola. The clear aging of thermocline water and amplified glacial age depth gradients compared to today (Skinner and Bard, 2022) may reflect a combination of numerous processes, which, however, influence all southern oceans. Such processes are increasing sea ice cover in south polar regions inhibiting gas exchange and thus ventilation, and/or overall reduced ventilation of the deep oceans (AMOC weakening), and/or increased storage of respired CO_2 in the deepest layers and upward mixing into the thermocline ocean (Skinner and Bard, 2022). In the deep ocean, glacial haline stratification is thought to decrease vertical mixing across water masses as compared to the thermohaline stratification today, leading to more stratification (Adkins, 2013). Aged Glacial Pacific Deep Water can invade the deep South Atlantic through the Drake Passage (DP) (Howe et al., 2016; Williams et al., 2021; Yu et al., 2020). Simultaneously, a reduced Agulhas leakage occurs (Franzese et al., 2006), limiting the influence of the Indian Ocean on the southern Atlantic. During the LGM, an enhancement of the Antarctic Circumpolar Current (ACC) increased eastward transport mainly in the intermediate water layers through the DP (Clauzet et al., 2007). This strengthened the intermediate layer exchange between the Pacific and the South Atlantic, as well as with the Indian Ocean, and would thus cause similar ventilation conditions in far distant regions across the deep Southern Oceans. Additionally, the Tasman Sea could have played an important role in the interoceanic exchange of intermediate water masses (Struve et al., 2022). The combination of all these processes would lead to a strong Southern Ocean connectivity, but also far higher sensitivity to differently aged water masses.

CWCs located in the DP recorded radiocarbon depleted waters during the last glacial period (figure 5.3c and figure B.5) (Burke and Robinson, 2012; Chen et al., 2015; Li et al., 2020), and model results suggest a South Atlantic thermocline dominated by water originating from the DP (Paul and Schäfer-Neth, 2003), likely penetrating to at least 800 m depth at the equator (Clauzet et al., 2007). Indeed, B_{atm} ages off Angola at 259–457 m depth are observed, which are identical to previously recorded ages from the equatorial Atlantic at 795–845 m depth (Chen et al. (2015); figure 5.3c). Furthermore, B_{atm} ages at Angola are similar to those observed in far distant locations from the Southern Ocean, that is, Tasmania and southwest Australia. Given the prominent similarities between records from Angola, southwest Australia (Trotter et al., 2022) and Tasmania (Hines et al., 2015), as well as the equatorial Atlantic

(Chen et al., 2015) and parts of the DP (Burke and Robinson, 2012; Chen et al., 2015; Li et al., 2020), the new Δ^{14}C data from CWCs off Angola strengthens the evidence of intermediate water connectivity and ventilation of the thermocline across the South Atlantic up until the equatorial Atlantic and large parts of the Southern Ocean.

The shallow depth of the corals off Angola and its radiocarbon similarity with deeper and far distant sites implies an influence of interior advective patterns. Those connect in the mid-depth southern and equatorial Atlantic and fuel ^{14}C depleted waters below the wind driven surface ocean. As a consequence, aged water distributed by the ACC must be transported by currents over a wide depth range during the LGM. Remarkably, high temporal variability of the ^{14}C signal, expressed as abrupt shifts in B_{atm} age between 240 and 600 years magnitude, are recorded simultaneously by CWCs off Angola (259–457 m depth) and in the Southern Ocean (675–1,950 m depth) (Hines et al., 2015; Trotter et al., 2022) at 26.6, 25, 23, and 19 ka. These observations indicate short periods of injection of very old, likely deep water into the thermocline, causing a dynamic radiocarbon range within the mid-depth circulation patterns. This coherence of multiple independent time-series strengthens the hypothesis of advective connectivity (Skinner and Bard, 2022). The close connection of thermocline and surface ocean highlights the importance to consider ventilation age variability in marine radiocarbon age calibrations for the Southern Oceans.

During deglaciation, the southern connectivity, expressed in the similarity of the ^{14}C signals, seems to continue (figure 5.3c), until the Angola record shows moderately lower B_{atm} ages of $\sim$830 years at 17.6 ka compared to the equatorial Atlantic, Tasmania, and DP. Since advection from well-ventilated water from the north can be ruled out due to the lower ventilation signal near the equator, this sudden increase in ventilation off Angola must be related to downward mixing of carbon from the surface ocean. It coincides with AMOC weakening indicated by ^{231}Pa/^{230}Th (figure 5.3e), and it is simultaneous to a change in intermediate and circumpolar circulation regimes across the Indo-Australian Southern Ocean (Trotter et al., 2022). Moreover, atmospheric CO_2 concentrations increased by 20 ppm (figure 5.3b; Bereiter et al. (2015)). In addition, these changes coincide with an Antarctic Sea-Ice Retreat (WAIS, 2013), rising sea-level (Lambeck et al., 2014) (figure 5.3d), and Southern Hemisphere warming (e.g., WAIS (2015); figure 5.3a). Accordingly, at least since 17.6 ka, the upper southern Atlantic thermocline has been less influenced by old, deeper water masses from the south and has likely contributed to the increase in atmospheric CO_2 through the transfer of respired carbon. Overall, the Angola corals provide a strong connectivity to all other thermocline to mid-depth ocean sites studied so far, with Angola thermocline water ages constituting the "young" envelop of the strong age depth gradients. The observed variability reflects the expected larger depth gradients and dynamics during the last glacial.

5.4.4. The Bølling-Allerød, Antarctic Cold Reversal and Younger Dryas

With the start of the B/A warm period and the subsequent ACR, all thermocline water sites investigated here show strong ventilation (figure 5.4c), which reflects the increase in AMOC toward its modern state. In addition, CO_2 increased by 50 ppm, and most of the global warming and a significant sea-level rise were achieved (figure 5.3). Accordingly, old carbon previously stored in the Southern Hemisphere oceans at depths of 250–1,500 m was rejuvenated. The deglacial ventilation caused the high variability of the last glacial to vanish and lead to a decrease of average B_{atm} ages between 800 and 1,500 years to values <700 years, which were already similar to modern ages.

Previous studies showed evidence of a ventilation anomaly during the B/A and ACR (e.g. Barker et al., 2010; Chen et al., 2015; Li et al., 2020; Robinson et al., 2005; Skinner et al., 2021), characterized by well-ventilated deep and mid-depth water throughout the entire Atlantic, with a maximum B_{atm} ages of 1,000–1,500 years (Rafter et al., 2022). Note that the LGM represented a time with B_{atm} age of up to ∼2,500 years in the deep Atlantic (Rafter et al., 2022; Skinner and Bard, 2022). The B/A represents a warm period in the Northern Hemisphere, while the ACR describes a synchronous cooling of the Southern Hemisphere. During this time, both atmospheric CO_2 (Marcott et al., 2014) and $\Delta^{14}C_{atm}$ (Hogg et al., 2020; Reimer et al., 2020) remained constant, possibly marking the end of the massive outgassing of respired carbon from the deep ocean at 16.3 ka, which was proposed previously (Marcott et al., 2014). The new ^{14}C results provide further evidence of the complex ventilation history of the Atlantic, giving first insights into thermocline ventilation during the millennial climate variability of the B/A, ACR and the following Northern Hemisphere cold reversal of the YD period. An enhancement of ventilation during the B/A and ACR was previously suggested for the deep and lower intermediate North Atlantic (900–2,000 m depth) through the reconstruction of ^{14}C using foraminifera and CWCs (Skinner and Bard (2022), and references therein). The new findings are clearly in line with these earlier suggestions of enhanced Atlantic ventilation during the B/A and ACR, most likely caused by significant deepening of the AMOC (Barker et al., 2010). Between 14.5 and 11 ka, ventilation ages in the equatorial and South Atlantic thermoclines overall decreased from 1,000 to 450 years (figure 5.4c). However, the intensified ventilation paused at 13.8 ka, leading to a re-aging of thermocline water masses until the start of the YD.

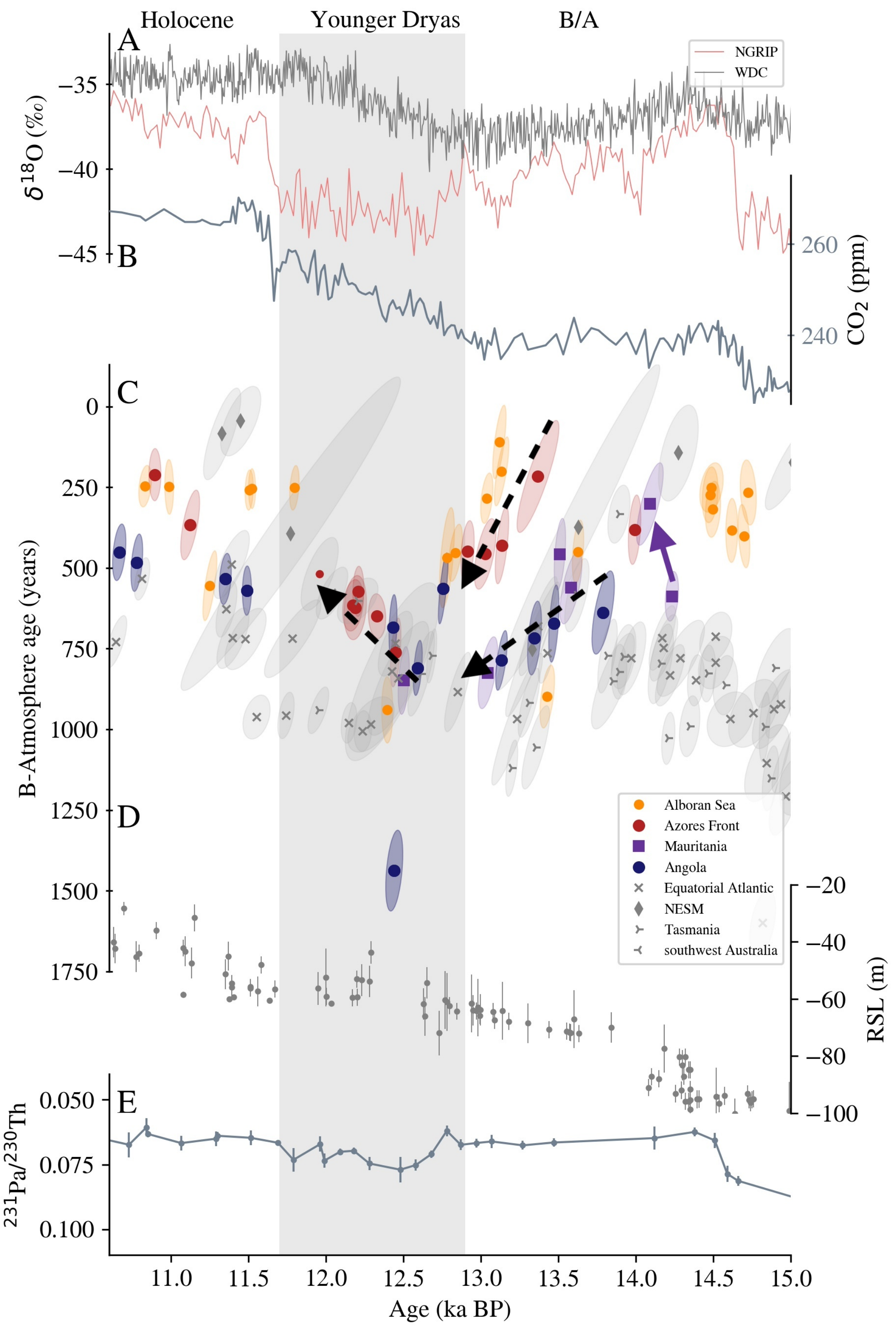

Holocene
Younger Dryas
B/A
A
B
C
D
E
NGRIP
WDC
δ^{18}O (‰)
−35
−40
−45
260
240
CO$_2$ (ppm)
B-Atmosphere age (years)
0
250
500
750
1000
1250
1500
1750
Alboran Sea
Azores Front
Mauritania
Angola
Equatorial Atlantic
NESM
Tasmania
southwest Australia
−20
−40
−60
−80
−100
RSL (m)
^{231}Pa/^{230}Th
0.050
0.075
0.100
11.0
11.5
12.0
12.5
13.0
13.5
14.0
14.5
15.0
Age (ka BP)

Figure 5.4.

Figure 5.4.: Radiocarbon age variability during the Termination, 15–11 ka. (a) $\delta^{18}O$ record of NGRIP, Greenland (Bazin et al., 2013) and WDC, Antarctica (WAIS, 2015). (b) CO_2 compilation record (Bereiter et al., 2015). (c) B-Atmosphere age reconstructed from cold-water corals from the Alboran Sea (this study), Azores Front (this study and Eltgroth et al. (2006)), Mauritania (this study), Angola (this study), New England Seamounts in 1,100–1,400 m depth (NESM; (Eltgroth et al., 2006; Hines et al., 2019; Robinson et al., 2005; Thiagarajan et al., 2014)) and equatorial Atlantic (Chen et al., 2015, 2020). Northern and southern thermocline water differ by $\sim 250 \pm 50$ years, they join with the onset of the Younger Dryas (YD). (d) Observed relative sea level, (Lambeck et al., 2014). (e) $^{231}Pa/^{230}Th$ records of sediments from the Bermuda rise (gray line, Böhm et al., 2015; Lippold et al., 2019; McManus et al., 2004). The gray bar indicates the duration of the YD.

In contrast to this southern behavior, ^{14}C records near the AF and within the Alboran Sea reveal an even more complex pattern within their overall well-ventilated state (B_{atm} ages between 220 and 450 years on average). Assuming a strong teleconnection between these locations via the spreading of MOW and Ekman pumping near the AF, a combined view of those two northern records is proposed. B_{atm} ages differed between waters north and south of the AF by $\sim 250 \pm 50$ years between 13.5 and 13 ka (figure 5.4c). The AF ventilation state decreased from 250 to 750 years between $\sim$13.4 and 12.5 ka, while South Atlantic records decreased from 500 to 850 years between $\sim$13.6 and 13 ka. An abrupt interruption of the general AF aging trend can be observed with sudden aging of Alboran Sea water at 13.6 ± 0.2 ka. This implies a northward shift of the AF, allowing aged water of southern origin to penetrate more efficiently into the thermocline of the North Atlantic and thus into the Mediterranean Sea. Since the position of the AF is presently north of the position expected for colder climates, periods of merged Southern Hemisphere and North Atlantic B_{atm} ages likely reflect enhanced northward salt exports required to trigger deep convection. This implies possibly multiple launches and failures of the AMOC, which are not yet visible in the sparse temporal resolution of $^{231}Pa/^{230}Th$ records (figure 5.4e).

Regarding CWCs from Mauritania, observed rapid radiocarbon fluctuations at the beginning of the B/A period must be related to the position of the CVFZ. Nowadays the sites are under the influence of southern sourced water. At 14.2 ka, Mauritania shows a poorly ventilated radiocarbon signal, which is assumed to reflect a southern source as well. In the following hundred years, the signal switches to better ventilation and thus most likely a northern source (14.1 ka), consistent with corals from the AF and NESM, and clearly distinct to the equatorial Atlantic (figure 5.4c). This observation confirms previous studies, describing a sudden southward displacement of the CVFZ during the B/A (Huang et al., 2012; Romero et al., 2008; Wienberg et al., 2018). This frontal displacement was, however, not permanent. It coincides with the Older Dryas, during which weakening of the AMOC was suggested (Stanford et al., 2006; Thornalley et al., 2011), which has been linked to changes in freshwater input and routing into the ocean (review by Carlson and Clark (2012) and references therein). Following the series of events, the Mauritania ventilation signal returned to the southern less ventilated signal, which prevails until present. This indicates an alternating water mass influence off Mauritania during the Northern Hemisphere warming and ice sheet decay, and thus multiple displacements of both the AF and CVFZ across the B/A and YD.

With the onset of the YD at 12.5 ka, the ^{14}C gradient between the North and South Atlantic finally vanished, and homogenous radiocarbon ages were established of the intermediate waters from the NESM in the west to the equatorial Atlantic (Chen et al., 2015, 2020; Eltgroth et al., 2006; Robinson et al., 2005) and the intermediate waters of the AF (this study and Eltgroth et al. (2006)), Mauritania, and partially Angola (this study). Previous observations have inferred decreased ventilation during the YD (e.g. Chen et al., 2015; Eltgroth et al., 2006; Robinson et al., 2005; Schröder-Ritzrau et al., 2003; Skinner and Shackleton, 2004; Skinner et al., 2014, 2021; Waelbroeck et al., 2001), consistent with a collapse of the AMOC and a reduction in North Atlantic Deep Water export, as seen in the $^{231}Pa/^{230}Th$ record (McManus et al. (2004); figure 5.4e). The new results advocate that the aging of the North Atlantic is significantly stronger and in situ compared to the southern Atlantic when excluding one exceptionally low ^{14}C value at 12.45 ka, recording a signal even older than CWCs from the DP (Burke and Robinson, 2012; Chen et al., 2015; Li et al., 2020, figure B.5). This one exceptional value off Angola is, however, consistent with ^{14}C dating on benthic foraminifera from the Brazil margin (Skinner et al. (2021), figure B.6). Thus, it remains unclear whether this value can be excluded or whether it indicates a sudden aging of the subtropical South Atlantic thermocline, which could also be caused by frontal movement. The combination of all available records suggests that deep convection was interrupted for 300–500 years between 12.8 and 12.4 ka (figure 5.4c). The full rejuvenation of the subtropical thermocline waters north and south of the equator was achieved during the YD but not only after the event.

Note that sea-level was still some 60 m below present (Lambeck et al. (2014); figure 5.4d). This implies that the size of the residual Northern Hemisphere ice sheets was still vast, when modern type ventilation patterns have been ultimately established.

5.5. Conclusion

A radiocarbon time series of the Atlantic thermocline ocean was presented here, which allows several important conclusions on the evolution of the Atlantic ventilation.

A consistent radiocarbon aging of thermocline waters occurred off Angola, at the equatorial Atlantic, and within the Southern Ocean, from which a strong teleconnection of Southern Hemisphere thermocline waters during the last glacial is interfered. Simultaneously recorded abrupt shifts of B_{atm} ages highlight the strong glacial dynamic range of mid-depth ventilation and could indicate short periods of injection of aged deep water likely from the Pacific Ocean. The synchronous pattern of the Southern Hemisphere thermocline waters reveals that Angola thermocline water ages represents the “young” envelop of the strong age depth gradients, which provides a possibility to use the Angola record as a best guess of a Southern Hemisphere surface water calibration curve. In addition, the LSG model agrees well with the observed radiocarbon trends.

During the LGM and deglaciation, the thermoclines of the Atlantic north and south of the AF acted separately. Radiocarbon reconstructions from North Atlantic thermocline dwelling corals show mostly well-ventilated water. The data further supports a southward shift of the AF and CVFZ as the most likely reason for the observed separation. Here, the LSG model mostly overestimates the role of southern sourced thermocline and intermediate waters in the regions of the AFC and Mauritania.

CWCs from Mauritania are sensitive to meridional water mass property change, due to their proximity to both the AF and CVFZ. Throughout the LGM, Mauritania is under the influence of ^{14}C rich water from northern sources contrasting the modern influence of southern sourced waters. The change to an Atlantic wide well-ventilated modern state of the thermocline waters and a more northern position of the AF and CVFZ occurred during the B/A period of initial Northern Hemisphere warming.

Lastly, further evidence of enhanced ocean ventilation during the B/A was found, with a clear meridional B_{atm} age difference of waters north and south of the AF of $\sim 250 \pm 50$ years. The data indicates a five century long in-situ aging of the Atlantic north of the AF followed by a resumption of ventilation in the middle of the YD at 12.5 ka to reach a modern subtropical Atlantic ventilation state by the end of the YD.

6. Radiocarbon to Trace U-Series Open System Behavior in Cold-Water Corals Through Reservoir Age Anomalies

6.1. Introduction

A topic of ongoing discussion among paleoceanographers is the occurrence of strong radiocarbon (^{14}C) depletions in the ocean, which indicate very old ^{14}C ventilation ages (e.g. Skinner and Bard, 2022). The data sets in question are primarily derived from foraminifera (e.g. Bryan et al., 2010; Lindsay et al., 2015; Marchitto et al., 2007; Rafter et al., 2019, 2018; Stott et al., 2009; Thornalley et al., 2011), only a few data sets were obtained from cold-water corals (CWC) (Mangini et al., 2010; Ruckelshausen, 2013). In general, they do not fit into the general framework of ocean circulation over time (Rafter et al., 2022; Skinner and Bard, 2022; Skinner et al., 2023; Zhao et al., 2018). The explanations proposed to account for these discrepancies range from a previously isolated (^{14}C depleted) water mass such as the Antarctic Intermediate Water (AAIW) (e.g. Bryan et al., 2010; Lindsay et al., 2015; Marchitto et al., 2007; Rafter et al., 2018), to local influences of geological, ^{14}C-depleted respired carbon (e.g. Adkins, 2013; Rafter et al., 2019; Ronge et al., 2016; Stott et al., 2019) or, in the case of foraminifera, inaccurate age models caused by undetected sedimentation hiatus and bioturbation (e.g. Ronge et al., 2019; Stott, 2023). Nevertheless, some of these theories have not yet been conclusively proven. Subsequent studies have found no evidence for such isolated, old water masses (e.g. Chen et al., 2020; Cléroux et al., 2011; De Pol-Holz et al., 2010; Freeman et al., 2015), or considered their existence unlikely over long periods of time (Hain et al., 2011). So far, Skinner and Bard (2022) have proposed that the most promising theory for foraminifera is a geological carbon source in the sedimentary environment. In contrast, there have been few attempts to explain the occurrences of unusual ^{14}C signatures in CWCs, hereafter referred to as "^{14}C ventilation anomalies". These include assumptions of an isolated, aging water mass over a long period of time (Ruckelshausen, 2013), a reduction in North Atlantic deep-water formation (Mangini et al., 2010), or a local (geologic) carbon influence like methane (Adkins, 2013; de Carvalho Ferreira, 2022). However, ^{13}C measurements have not confirmed such theories (Mangini et al., 2010; Ruckelshausen, 2013), and their large isotopic variability makes it difficult to decipher smaller amounts of methane (e.g. Blamart et al., 2005; Rollion-Bard et al., 2003; Smith et al., 2000).

In contrast to foraminifera, whose age is determined from an age model of the sediment core, a major advantage of CWCs is that they can be dated with high precision using the ^{230}Th/U disequilibrium method presuming an U-series closed system behavior (e.g. Frank and Hemsing, 2021). U-series open system behavior, a result of diagenesis, is minimized by strict sample and data selection criteria. These include the concentration of ^{238}U, the concentration of ^{232}Th, the initial activity ratio of ^{234}U/^{238}U (δ^{234}U$_i$), and the physical appearance of cold-water corals through the essentially mechanical cleaning process. These parameters are generally considered sufficient to identify U-series open system behavior as a deviation from the theoretical evolution of the isotope ratios according to the coupled decay law. Furthermore, multiple samples and isochron techniques can be employed to constrain ^{232}Th-based correction models (Lomitschka and Mangini, 1999; Schröder-Ritzrau et al., 2005).

Due to the reservoir effect, the ocean must have lower ^{14}C signatures compared to the atmosphere at almost any time. Accordingly, the current calibration curve for the atmosphere, IntCal20 (Reimer et al., 2020), provides a strong constraint on the minimum expected ^{14}C ventilation age. Nevertheless, ^{14}C ventilation ages above the atmosphere obtained from CWCs have been reported in several studies (Beisel et al., 2023; de Carvalho Ferreira, 2022; Hemsing, 2017; Hines et al., 2015, 2019; Mangini et al., 2010; Ruckelshausen, 2013). Depending on their magnitude, these observations are difficult to explain and are frequently excluded from scientific discussion (Beisel et al., 2023; Hemsing, 2017; Mangini et al., 2010; Ruckelshausen, 2013). Possible explanations include an underestimated atmospheric ^{14}C value (de Carvalho Ferreira, 2022; Hines et al., 2015), or diagenesis interfering with either one or both of the applied dating methods.

This chapter investigates the phenomenon of ^{14}C ventilation anomalies and values above the atmosphere in CWCs. ^{14}C compilation papers (Rafter et al., 2022; Skinner and Bard, 2022; Skinner et al., 2017, 2023; Zhao et al., 2018) provide constrains on the maximum expected ^{14}C ventilation age and allow the generation of coarse boundaries. Furthermore, ^{14}C ventilation ages can be tested against their regional consistency (Skinner et al., 2019). Deviations are most likely to indicate local influences or an influence of diagenesis. In this context, thresholds for ^{14}C ventilation anomalies will be defined. Existing CWC studies are reviewed and compiled with respect to ^{14}C ventilation anomalies and values above the atmosphere. This study is complemented by new CWC datasets from the Gulf of Cádiz and Mauritania. Coupled $^{230}Th/U$ and ^{14}C measurements, as well as ^{13}C measurements were performed. The $^{230}Th/U$ and ^{14}C depth profiles of coral-bearing sediment cores are compared and analyzed in relation to anomalous ^{14}C ventilation values. The results indicate that ^{14}C ventilation anomalies, as well as values above the atmosphere, are associated with age-depth inversions in the $^{230}Th/U$ chronology of certain sediment cores. Potential causes are discussed, and consequently additional quality control criteria are recommended for future studies. Supplementary figures are provided in the Appendix B.2

6.2. Materials and Methods

6.2.1. Sites and Hydrography

Gulf of Cádiz

The Gulf of Cádiz (GoC) is situated in the northeast Atlantic Ocean, southeast of the Iberian Margin and west of the Strait of Gibraltar (figure B.7, B.8). The GoC serves as a direct conduit between the Atlantic Ocean and the Mediterranean Sea. Its distinctive location is also reflected in its hydrography. The uppermost layers are influenced by the Surface Atlantic Water (SAW) and the Eastern North Atlantic Central Water (ENACW). Nevertheless, the ENACW can reach depths of 500 – 1,000 m (Liu and Tanhua, 2021). The intermediate layer is primarily influenced by a combination of AAIW and Mediterranean Outflow Water (MOW), or Mediterranean Water (MW) (Hebbeln et al., 2015). The extremely salty and warm MOW flows through the Strait of Gibraltar into the eastern Atlantic Ocean, where it entrains surrounding water (ENACW) and forms MW (Baringer and Price, 1997). Currently, the AAIW is probably the largest component in the southern GoC (Hebbeln et al., 2015). Below, the North Atlantic Deep Water (NADW) prevails.

Thousands of CWC mounds have developed between ∼500 to ∼1100 m water depth along the slopes of the GoC, within influence of MOW and AAIW (Foubert et al., 2008; Hebbeln et al., 2019; Mienis et al., 2012; Wienberg et al., 2010). However, living, framework forming CWC occurrences are scarce, and the majority of the observed deposits were comprised of dead coral rubble (Wienberg et al., 2009). Such CWC mounds can reach heights of several tens of meters (Wienberg et al., 2010). The site is geographically distinctive due to the convergence of the Eurasian and African tectonic plates, which has resulted in the formation of numerous mud volcanoes and diapiric ridges (e.g. Foubert et al., 2008; León et al., 2007) and contourite deposits (Hebbeln et al., 2016, 2019). Active fluid venting, as well as sulfate reduction, methane deposits, and punctuated even gas hydrates, have been reported in the GoC (Van Rooij et al., 2005). The sediment cores examined in this study were situated in close proximity to several mud volcanoes (figure B.8). The framework forming CWC species *Desmophyllum pertusum* and *Madrepora oculata* in the temperate Atlantic occurred predominantly during glacial times (Frank et al., 2011a; Wienberg et al., 2010).

This study examines six coral-bearing sediment cores from the GoC (figure B.8). Five cores were recovered from depths between 523 and 944 m using piston and gravity corers (MD08-3231, GeoB 12725-1, GeoB 12740-1, GeoB 18139-1) and one core was obtained using the sea-floor drill rig MeBo (MARUM) (GeoB 18141-1). Detailed descriptions of the cores can be found in the respective expeditions reports 64PE284, MSM36, MD169 and 64PE229 (Hebbeln et al., 2008, 2015; Mienis et al., 2004; Van Rooij et al., 2008). The core M2004-02 (523m depth) is situated close to MD08-3231 (550m depth), while GeoB 18139-1 (940m depth) and GeoB 18141-1 (944m depth) are located on the same mound (figure B.8). Further details regarding the exact locations can be found in the appendix (table C.1). Previously, core M2004-02 was investigated by (Wienberg et al., 2010). Two cores were (re-)analyzed using the ^{230}Th/U and ^{14}C methods as described by Beisel (2021); Hemsing (2017); Kerber et al. (2023): MD08-3231 and GeoB 18141-1.

Mauritania

Offshore Mauritania, one of the largest CWC mound provinces developed (Wienberg et al., 2018). Situated in the Northeastern Atlantic (figure B.7), the region is influenced by the Cap Verde Frontal Zone, which separates North Atlantic Central Water (NACW) from South Atlantic Central Water (SACW). Those surface and subsurface water masses span a depth range of 600 m. The intermediate water is influenced by AAIW, as in the GoC, and the deep water by NADW.

Coral mounds have evolved into sometimes enormous topographical features of the seabed, reaching heights of up to 60 m (Wienberg et al., 2018). The most common species is *Desmophyllum pertusum*, with occasional occurrences of *Madrepora oculata*. A compilation of ^{230}Th/U ages has revealed that framework forming CWCs were, as in the GoC, predominant during glacial times, with sporadic modern occurrences in nearby canyons (Wienberg et al., 2018). The region´s structure is complex, and the presence of gas hydrates, pockmarks and methane seepage has been documented (e.g. Antobreh and Krastel, 2007; Davies et al., 2023; Davies and Clarke, 2010; Davies et al., 2015; Sanz et al., 2017; Yang et al., 2013, 2021).

Five coral-bearing sediment cores were revisited at depths between 485-580 m (figure B.9). These include one sediment core from the Timris Mound Complex (GeoB 14884-1), one from the Tioulit Mound (GeoB 14890-2), one from the Banda Mound Complex (GeoB 14899-1) and two from the Tamxat Mound Complex (GeoB 14904-2, GeoB 14905-2). All were recovered with a gravity corer during the MSM16/3 research cruise (Westphal et al., 2014). Further ^{230}Th/U ages were presented in Schneider (2018), Stuhrmann (2023), Wienberg et al. (2018), and ^{230}Th/U and ^{14}C measurements by Beisel et al. (2023) (chapter 5), respectively.

6.2.2. Sample Preparation and Isotope Measurement

Sample preparation and isotope measurements followed the procedure outlined in chapter 3.

In certain, but not all instances, further ^{230}Th/U measurements were performed on an additional piece of the cleaned coral. Data from Hemsing (2017) and Schneider (2018) were subsequently corrected for the recently discovered U scatter ions termed "ghost signal" (Kerber et al., 2023). In order to be consistent within the data set, measurements from the GoC conducted with ICP-QMS were excluded, as internal precision was not comparable to MC-ICPMS analysis (Hemsing, 2017). ^{230}Th/U ages are reported referenced to 1950 AD (years BP).

To present the data, I calculated Δ^{14}C after equation 2.9, and the benthic-atmosphere (B$_{atm}$) age after equation 2.11. Figures show 2σ error ellipses, calculated according to the python script developed by Hemsing (2017). As atmospheric reference, the IntCal20 is used (Reimer et al., 2020) for the Northern Hemisphere and SHCal20 (Hogg et al., 2020) for the Southern Hemisphere. The uncalibrated ^{14}C ages are provided, referenced to years BP.

δ^{13}C measurements were performed as part of the bachelor thesis of Max Stellbrink (2023), using a ThermoFinnigan MAT253 gas source mass spectrometer equipped with a Thermo Fisher Scientific Kiel IV carbonate analyzer at the Institute of Geosciences, University of Heidelberg, Germany. For the δ^{13}C measurements, 40-70 μg of carbonate in powder form was scraped off the cleaned coral polyps using a micro drill (Stellbrink, 2023). The centers of calcification were avoided during the process (Stellbrink, 2023).

6.2.3. Definition of “^{14}C Ventilation Anomalies” and “Above the Atmosphere“

In this study, the term “^{14}C ventilation anomalies“ is used to summarize data that does not align with the prevailing framework of ocean ^{14}C ventilation over time (Rafter et al., 2022; Skinner and Bard, 2022; Skinner et al., 2023). As CWCs up to 1000 m depth are analyzed, these include ^{14}C ventilation ages (B_{atm} ages) of < 2000 a between 15-40 ka and < 1500 a between 0-15 ka. These limits were chosen with regard to the compilations of Rafter et al. (2022), Skinner and Bard (2022), Skinner et al. (2023), and Zhao et al. (2018). Data above the current calibration curve for the atmosphere, IntCal20 for the Northern Hemisphere (Reimer et al., 2020) or SHCal20 for the Southern Hemisphere (Hogg et al., 2020), are referred to as ”above the atmosphere”. Some of these data points have already been flagged in compilations (e.g. Mangini et al. (2010) in Skinner et al. (2023) with “time-series flag”). It should be noted that the aforementioned definition is contingent upon the current atmospheric calibration curve (for further details, please refer to section 6.4.1). Please note that this is a very generous definition and does not imply that data inside of these boundaries are necessarily reliable.

6.2.4. Data Compilation

This study presents both new CWC age data (GoC and Mauritania), as well as a summary of previously published CWC ages with ^{14}C ventilation anomalies and values above the current atmospheric calibration curve. These include the following sites: GoC (Beisel (2021), Hemsing (2017) and references therein, and this study), Tropic Seamount (de Carvalho Ferreira, 2022), Mauritania (Beisel (2021); Beisel et al. (2023), and this study), Brazil (Mangini et al., 2010; Ruckelshausen, 2009, 2013) and south of Tasmania (Hines et al., 2015). The compiled data were subject to the quality control (QC) in chapter 3.4.2. B_{atm} ages were recalculated using IntCal20 (Reimer et al. (2020), Northern Hemisphere) or SHCal20 (Hogg et al. (2020), Southern Hemisphere), as required. The compiled data set of anomalous values can be found in the appendix, table C.9.

6.3. Results

6.3.1. Gulf of Cádiz

In general, GoC corals exhibit ^{230}Th/U ages between 17 – 41 ka and uncalibrated ^{14}C ages between 15,5 - 41 ka, with only sporadic dating prior to that period (figure 6.1, 6.2,

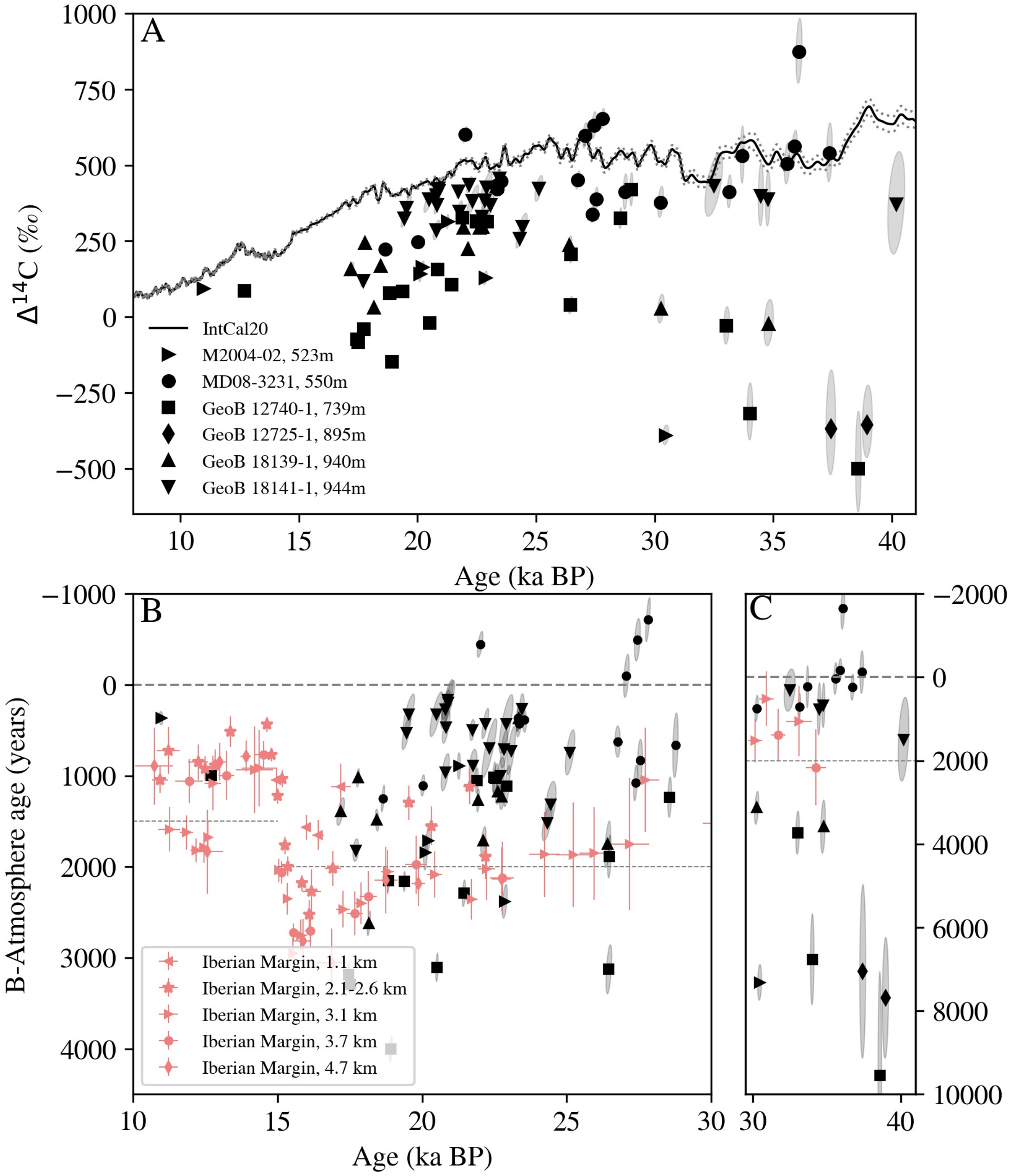

Figure 6.1.: Radiocarbon records obtained from cold-water corals in the Gulf of Cádiz from six different sediment cores (this study, Beisel (2021), Hemsing (2017) and references therein, Hemsing unpublished), after applying the quality control criteria in chapter 3.4.2. (A) Δ^{14}C record with IntCal20 (Reimer et al., 2020) as atmospheric reference. (B) Calculated B-Atmosphere (B_{atm}) age record, i.e. the difference in ^{14}C ages between coral and atmosphere, for the time span 10-30 ka and (C) 30-41 ka, together with the B_{atm} age record obtained from foraminifera (red) in 1.1-4.7 km depth in the nearby Iberian Margin (Skinner et al., 2021), 1σ error). Note the different y-axis scaling between B and C. Horizontal lines mark the threshold values for the defined ^{14}C ventilation anomalies (chapter 6.2.3).

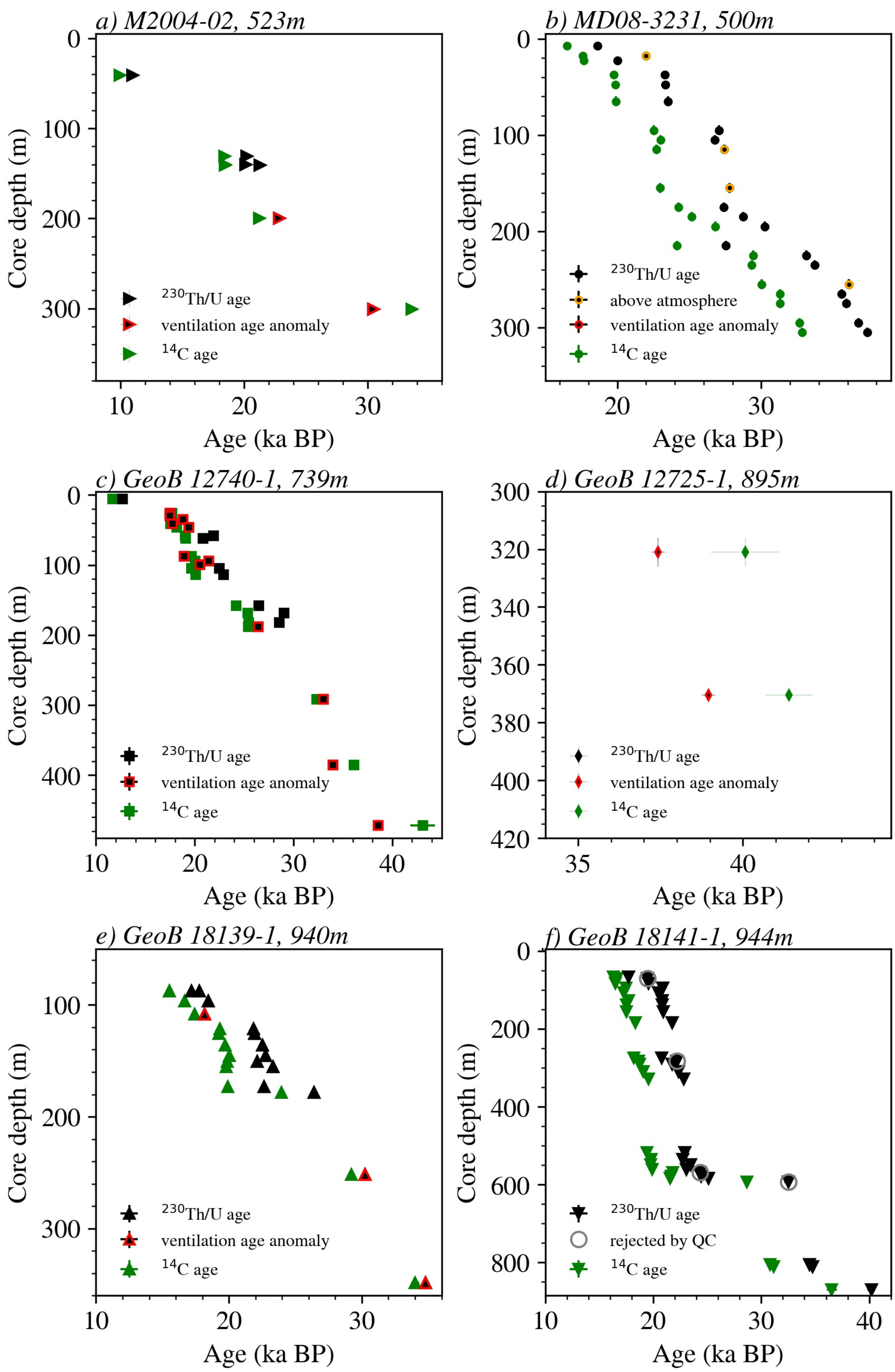

Figure 6.2.: Depth profiles of the six sediment cores investigated in the Gulf of Cádiz (this study, Beisel (2021), Hemsing (2017) and references therein, Hemsing unpublished). Coupled ^{230}Th/U ages (black) and uncalibrated ^{14}C ages (green) are shown. ^{230}Th/U ages that lead to ^{14}C ventilation anomalies, defined as ^{14}C ventilation ages above 2000 a (B_{atm} age) between 15-40 ka, are highlighted in red. ^{230}Th/U ages associated with ^{14}C ventilation ages above the atmospheric reference (IntCal20, Reimer et al. (2020)) are highlighted in orange. Gray circles indicate data that did not pass the quality control (chapter 3.4.2).

table C.3). The ^{238}U concentrations fall within the typical CWC range, between 2.3-5.3 µg/g. The mean ^{232}Th concentration is 0.8 ng/g, with a median value of 0.5 ng/g. $\delta^{234}U_i$ varies between 134-154 ‰, with lower values observed during the glacial. The calculated ^{14}C ventilation ages (B$_{atm}$ age) range between -3400 a and 9500 a (figure 6.1b, c). In summary, ^{14}C ventilation anomalies are observed in 24 % of the calculated data, while 4 % of the calculated data exhibit values above the atmosphere (figure 6.1, 6.2). Furthermore, additional performed ^{230}Th/U measurements on the coral skeletons examined revealed absolute age fluctuations of up to 1.5 ka within a single coral (figure B.17). All corals were recovered from sediment cores (chapter 6.2.1). Therefore, it is possible to analyze the respective depth profiles in addition to the age distribution and calculated ventilation ages (figure 6.2). Here, only the ^{230}Th/U and ^{14}C measurements performed on the same piece of coral are presented.

For core M2004-02, only six paired ^{230}Th/U and ^{14}C measurements are available between 11-30.5 ka (figure 6.2a). The ventilation ages are calculated between 380-7300 a. Only two of the B$_{atm}$ ages are greater than 2000 a (33 %): 22.9 ka and 30.5 ka. δ^{13}C measurements were carried out on these samples, yielding values of -0.5 ‰ and -4.5 ‰. In the depth profile, the depth between 140-141 cm is noteworthy: ^{14}C dating on two corals yielded an identical age of 18.5 ka, while the ^{230}Th/U ages exhibited a range between 20.2-21.3 ka.

The data set for MD08-3231 was previously investigated in Hemsing (2017) and references therein, Beisel (2021), and Hemsing unpublished (figure 6.2b). Combined ^{230}Th/U and ^{14}C measurements of sufficient quality are available for 20 corals. The ^{230}Th/U ages range between 18.6-37.4 ka, while ^{14}C ages range between 16.4-32.8 ka. Calculated B$_{atm}$ ages range between -1650 a and 1250 a. Four data points lie above the atmosphere (19 %, negative B$_{atm}$ ages). For these data points, the ^{230}Th/U age-depth profile shows several age-depth inversions, whereas the ^{14}C age-depth profile does show only one at 210 cm depth in core (figure 6.2b).

Core GeoB 12740-1 exhibits ^{230}Th/U ages between 12.7 - 38.6 ka, as well as uncalibrated ^{14}C ages between 11.7 - 43 ka (n=20, figure 6.2c) and is characterized by numerous unusually high B$_{atm}$ ages. In general, they range between 710-9500 a, 60 % of the results are exceeding 2000 a. The time span between 30 - 40 ka is notable. In this interval, only B$_{atm}$ ages between 3700-9500 a occur (n=3). In general, this core at 740 m water depth exhibits higher B$_{atm}$ ages than nearby cores at greater water depths (figure 5.1). A total of nine δ^{13}C measurements were conducted on corals with B$_{atm}$ ages between 740-9500 a. The resulting values ranged from -4.4 ‰ to 0.2 ‰. The depth profile contains numerous sections that are conspicuous for their low ^{14}C difference but large ^{230}Th/U difference. For instance, the corals from depths between 26-41 cm exhibit uncalibrated ^{14}C ages of 17.5-17.7 ka, whereas the ^{230}Th/U data vary between 17.5-18.8 ka. This yields B_{atm} ages between 2000-3700 a. A comparable situation is observed in the 87.5-114 cm section. Here, uncalibrated ^{14}C ages of 19.6-20.1 ka were measured, while ^{230}Th/U varied between 18.9-23 ka, also resulting in very high B_{atm} ages above 2000 a. Age-depth inversions in the ^{230}Th/U depth profile can be associated with anomalous ^{14}C ventilation ages in this core.

A total of two paired ^{230}Th/U and ^{14}C measurements were obtained from core GeoB 12725-1 (figure 6.2d). The ^{230}Th/U dating revealed ages between 37.5-39 ka, the ^{14}C dating between 40-41.4 ka. The combination of both yields anomalous B_{atm} ages above 7000 a. Additionally, δ^{13}C measurements were conducted on both samples, resulting in values between -2.4 ‰ and -3.1 ‰.

For the core GeoB 18139-1, 14 paired ^{230}Th/U and ^{14}C measurements are available (figure 6.2e). The ^{230}Th/U data indicates an age range between 17-35 ka, while the ^{14}C data range between 15.5-34 ka. The calculated B_{atm} ages vary between 370-3600 a. 21 % of the data exhibit ^{14}C ventilation anomalies. The two oldest samples, 30 ka and 35 ka, show B_{atm} ages above 3000 a. δ^{13}C measurements were conducted on both samples, resulting in values of -6.1 ‰ and -0.4 ‰. Moreover, the sediment core exhibits a greater prevalence of ^{230}Th/U age-depth inversions relative to ^{14}C age-depth inversions. One ^{230}Th/U age-depth inversion at a core depth of 108.5 cm leads to a calculated B_{atm} age of 2600a.

Core GeoB 18141-1 was analyzed in Hemsing (2017) and references therein, and Hemsing unpublished. Paired ^{230}Th/U and ^{14}C measurements in sufficient quality are available on 19 samples (figure 6.2f). The results show ^{230}Th/U ages between 17.8-40 ka and ^{14}C ages between 16.3-36.5 ka. Overall, ventilation ages between 160-1800 a were calculated. Moreover, this sediment core exhibited only a few ^{230}Th/U age-depth inversions. A pronounced inversion was observed at 66 cm core depth, resulting in a B_{atm} age of 1800 a (^{230}Th/U age 17.8 ka). Although the core was recovered on the same mound as GeoB 18139-1 (chapter 6.2.1, figure B.8), the calculated B_{atm} ages differ considerably at 17.8 ka and 34.8 ka.

In summary, age-depth inversions are more prevalent in the ^{230}Th/U depth profiles, if compared to the ^{14}C depth profiles. ^{230}Th/U age-depth inversions are associated with anomalous ^{14}C ventilation ages above 2000 a and calculated values above the atmosphere. The occurrence of high B_{atm} ages and age-depth inversions is particularly pronounced in GeoB 12740-1 and in the time span of 30-40 ka. In contrast, the core GeoB 18141-1 exhibits the fewest age-depth inversions and anomalous ^{14}C ventilation ages. ^{14}C ventilation ages above the atmosphere (negative B_{atm} ages) were only calculated for core MD08-3231 (n=4). The δ^{13}C measurements on samples with anomalous ^{14}C ventilation ages yielded values between -6.1 ‰ and 0.2 ‰, which is within the typical range for CWC.

6.3.2. Mauritania

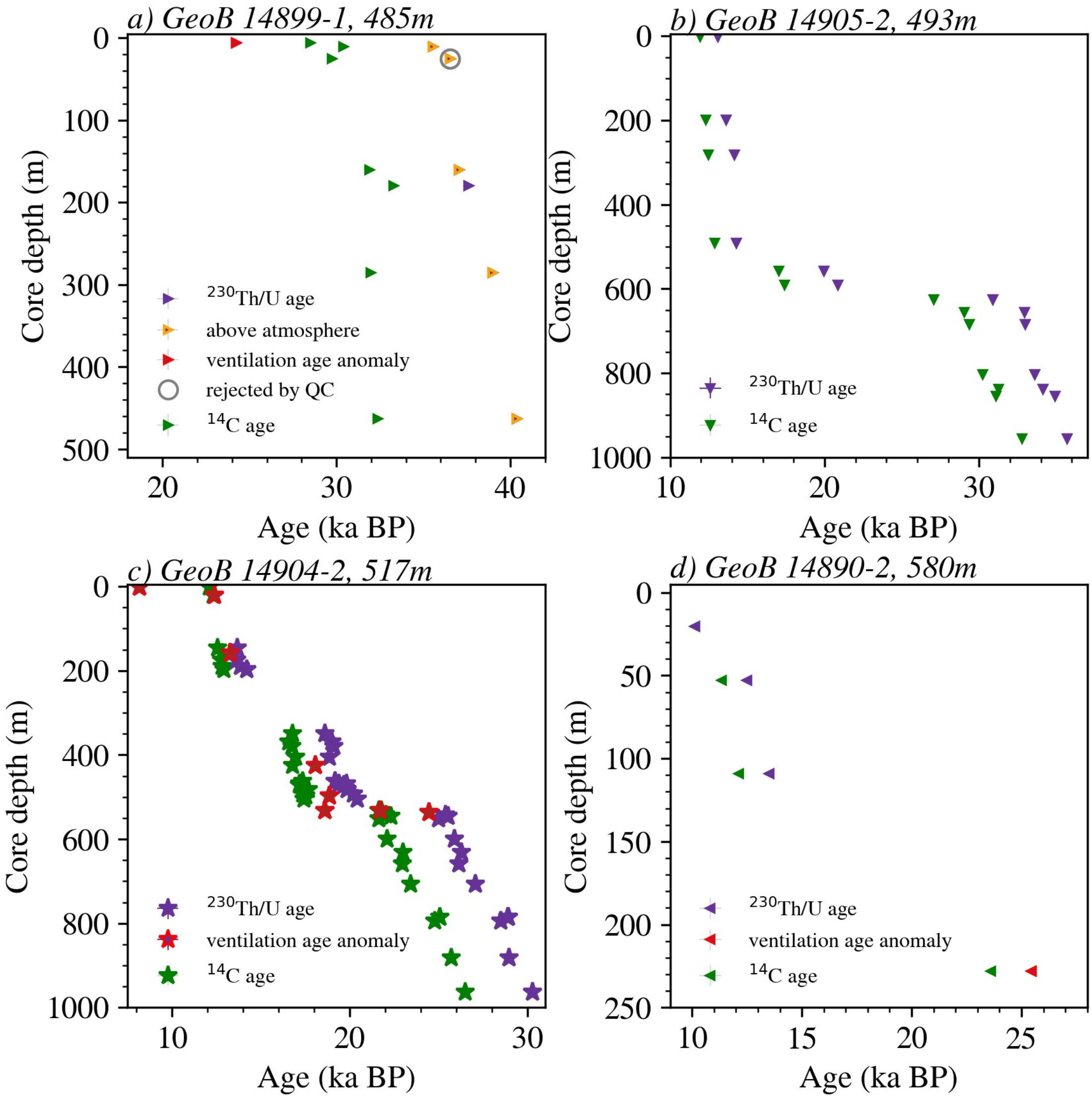

Figure 6.3.: Depth profiles of the four sediment cores investigated along the coast off Mauritania (Beisel (2021); Beisel et al. (2023); Schneider (2018); Stuhrmann (2023); Wienberg et al. (2018); this study). Coupled $^{230}Th/U$ ages (violet) and uncalibrated ^{14}C ages (green) are presented. $^{230}Th/U$ ages that lead to ^{14}C ventilation anomalies are highlighted in red. $^{230}Th/U$ ages associated with ^{14}C ventilation ages above the atmospheric reference (IntCal20, Reimer et al. (2020)) are highlighted in orange. Gray circles indicate data that did not pass the quality control (chapter 3.4.2).

Corals from the coast of Mauritania have been examined in Beisel (2021), Beisel et al. (2023), Schneider (2018), Stuhrmann (2023), Wienberg et al. (2018), and this study. The samples exhibit a $^{230}Th/U$ age range of 8-40 ka and ^{14}C ages between 10-33 ka (figure 6.3, B.10, table C.4). The ^{238}U concentrations range between 2.2-4 μg/g. The mean ^{232}Th concentration is 0.8 ± 0.4 ng/g, with a median of 0.7 ng/g. $\delta^{234}U_i$ shows an expected range between 138 ‰ and 150 ‰ (figure B.16). The calculated ^{14}C ventilation ages (B_{atm} ages) based on ^{230}Th/U and ^{14}C ages range from -2700 a to 8400 a, with ∼17 % of the values representing ^{14}C ventilation anomalies and 10 % representing values above the atmosphere (figure B.10). Moreover, repeated ^{230}Th/U measurements on new coral pieces of the same polyp demonstrate an age variance of up to 3.8 ka (figure B.17). As with the GoC, the depth profiles of the coupled ^{230}Th/U and ^{14}C measurements are analyzed below.

Core GeoB 14899-1 exhibits ^{230}Th/U ages between 24-40 ka and ^{14}C ages between 28.5-32.5 ka. ^{230}Th/U ages were part of the thesis of Schneider (2018) and Stuhrmann (2023). Two of the data points have already been published in Beisel et al. (2023). The B_{atm} ages vary between -2700 a and 8400 a. Consequently, 71 % of the data indicate values above the atmosphere and 14 % ^{14}C reveal ventilation anomalies. The pronounced ^{230}Th/U age-depth inversion in the upper part of the core (5.5 cm) is associated with a ^{14}C ventilation anomaly (B_{atm}=8400 a).

^{14}C data up to 21 ka from core GeoB 14905-2 have already been published in Beisel et al. (2023). ^{230}Th/U ages are part of Stuhrmann (2023) and Wienberg et al. (2018). In general, the ^{230}Th/U ages were determined to be between 13-35.7 ka and ^{14}C ages between 12-32.8 ka. The B_{atm} ages of this core range between 200-1500 a. Both the ^{230}Th/U and ^{14}C depth profiles are consistent. No ^{14}C ventilation anomalies or values above the atmosphere were calculated.

Core GeoB 14904-2 was presented in part in Beisel et al. (2023) and Wienberg et al. (2018). This study provides further data. The core exhibits ^{230}Th/U ages between 8-30 ka and ^{14}C ages between 12-26.5 ka. When combined, the B_{atm} ages fall within a range between 380-6500 a. ^{14}C ventilation anomalies account for 23 % of the data and occur in certain sections of the sediment. At core-depths between 530 – 540 cm, a wide range of values was obtained, with ^{230}Th/U ages between 18.5 – 24.4 ka, while ^{14}C remained constant (21.6 - 21.7 ka). This resulted in B_{atm} ages of up to 6500 a. A comparable situation occurred at core depth 425 cm. The calculated B_{atm} age from the outlier (18 ka) suggests a value of over 2000 a during the last deglaciation. Furthermore, ^{230}Th/U exhibits a considerable age variance in the upper part of the core, between 0 – 22 cm, resulting in B_{atm} ages of up to 4800 a. Thus, two out of these three ^{14}C ventilation anomaly cases occurred at the end of growth phases, with a pronounced hiatus visible in the depth profile. Additionally, δ^{13}C measurements were conducted on samples with B_{atm} ages between 720-6500 a. They range between -3.6 ‰ and -7.8 ‰.

The data from core GeoB 14890-2 were presented in Beisel et al. (2023), Beisel (2021) and Schneider (2018). The ^{230}Th/U ages range between 10-25 ka, while the ^{14}C ages range between 10-23.6 ka. The calculated B_{atm} ages vary between 460-2500 a. A ^{230}Th/U age-depth inversion is observed at a core depth of 228 cm. This results in a ^{14}C ventilation anomaly of 2500 a at 25.5 ka. Additionally, δ^{13}C was measured on this sample, resulting in a value of -1.8 ‰.

Additional ^{230}Th/U (Schneider (2018), published in Beisel et al. (2023)) and ^{14}C (Beisel et al., 2023) dating is available for the GeoB 14884-1 core. The respective B_{atm} age is negative, thus located above the atmosphere.

6.3.3. Brazil

The ^{230}Th/U and ^{14}C data from Brazil presented here were previously published (Mangini et al., 2010; Ruckelshausen, 2009, 2013). The data were analyzed with respect to the latest QC (chapter 3.4.2, gray circles in figure 6.4) and the B_{atm} ages were calculated using SHCal20 (Hogg et al. (2020), figure B.11). Furthermore, the correlation between ^{14}C ventilation anomalies / values above the atmosphere and the ^{230}Th/U and ^{14}C depth profile is analyzed. Prior to the QC, 30 % of the data exhibited ^{14}C ventilation anomalies and 13 % exhibited values above the atmosphere. The QC resulted in the rejection of 53 % of the total data set. Nevertheless, some ^{14}C ventilation anomalies and the values above atmosphere remain.

In core C1 (Mangini et al., 2010; Ruckelshausen, 2009, 2013), constant ^{14}C ages generally prevail during growth periods, while the ^{230}Th/U ages vary by several hundred to thousand years and exhibit pronounced age-depth inversions. This leads to Δ^{14}C results along the decay curve of ^{14}C (Mangini et al., 2010; Ruckelshausen, 2009). 63 % of the data are rejected by the more stringent QC. This concerns 75 % of the ^{14}C ventilation anomalies and the value above the atmosphere.

Only few data are available in core KGLC (Ruckelshausen, 2013). The more rigorous QC does not alter the original data set, and no ventilation anomalies or values above the atmosphere are observed.

In core C2 (Mangini et al., 2010; Ruckelshausen, 2009, 2013), the general situation is comparable to that observed in core C1. For each coral growth phase, the ^{14}C ages are nearly constant, while the ^{230}Th/U ages vary by several hundred to thousand years and exhibit pronounced age-depth inversions. 86 % of the ^{230}Th/U data causing ^{14}C ventilation anomalies can be discarded by the more rigorous QC (chapter 3.4.2). The same applies to one of the two values above the atmosphere. The oldest dating, at 37 ka, results in a B_{atm} age of approximately 5000 a, which is within in the range

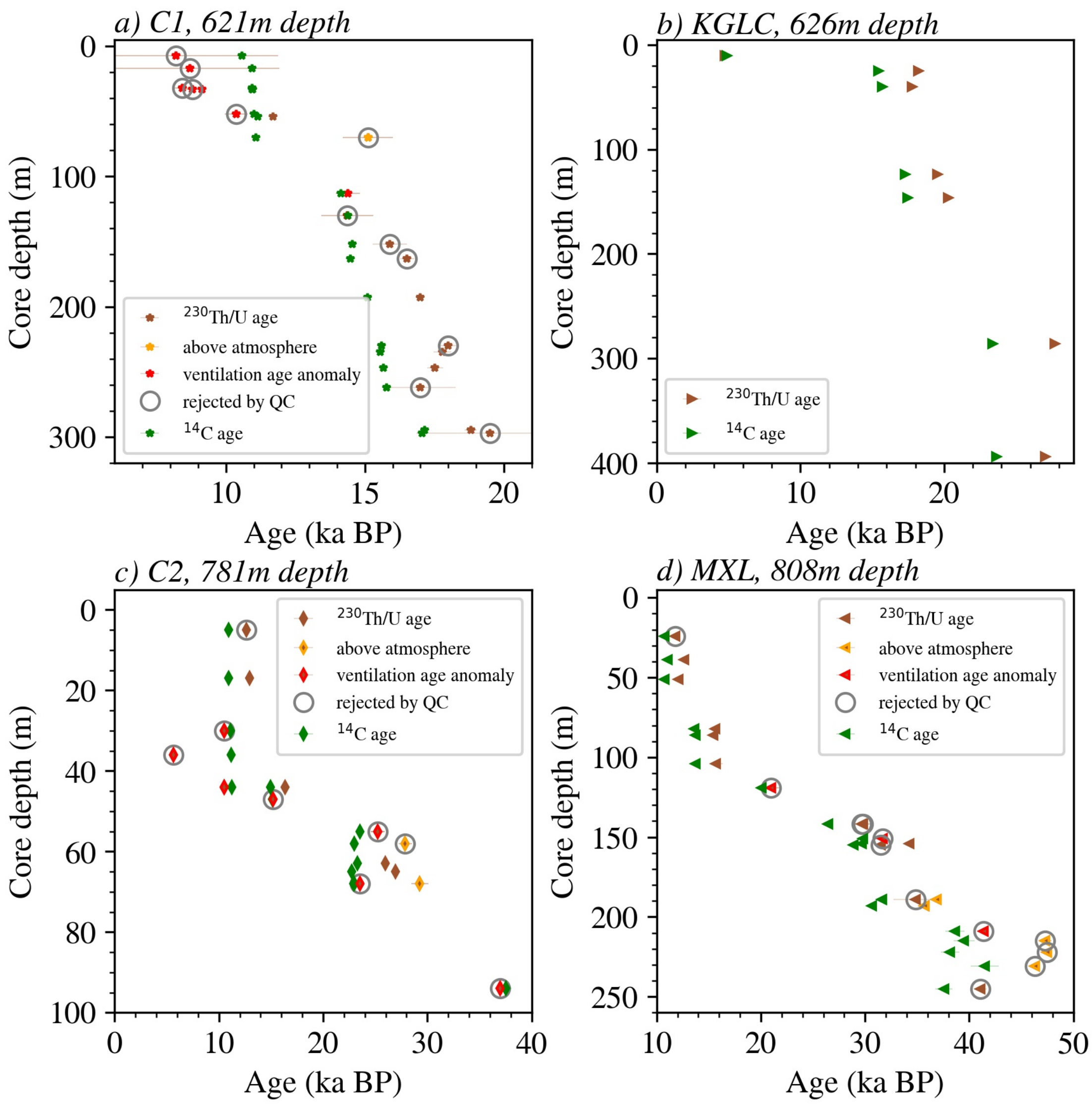

Figure 6.4.: Depth profiles of the four sediment cores investigated along the coast off Brazil (Mangini et al., 2010; Ruckelshausen, 2009, 2013). The ^{230}Th/U ages and uncalibrated ^{14}C ages are presented. The ^{230}Th/U ages that result in ^{14}C ventilation anomalies are highlighted in red. ^{230}Th/U ages associated with ventilation ages above the atmospheric reference (SHCal20, Hogg et al. (2020)) are highlighted in orange. Gray circles indicate data that did not pass quality control (chapter 3.4.2).

of the GoC B_{atm} ages observed during this time span (figure B.11, 6.1c).

A different picture emerges for the MXL core (Ruckelshausen, 2013). The occurrence of sectional constant ^{14}C ages, paired with almost constant ^{230}Th/U ages, only occur in the upper 100 cm. In the remaining part of the core, both ^{14}C ages and ^{230}Th/U ages vary section wise. All ^{14}C ventilation anomalies of this core can be identified and removed by the more stringent QC (chapter 3.4.2), as well as 60 % of the values above the atmosphere. Two of the samples were dated in two different laboratories (Ruckelshausen (2013), figure B.17). The ages agree within the error limits. In the case of sample M-189 (depth 189 cm), however, one dating result yielded in a ^{14}C ventilation age above the atmosphere.

6.4. Discussion

The following discussion is divided into three parts. The first part deals with the general concept of the origin of ^{14}C ventilation anomalies. These include perturbations or local carbon sources that may alter the original ^{14}C signal. The second part addresses the potential for a modification of the ^{230}Th/U age. The third part discusses possible U-series open system behavior and recommends the application of additional criteria to existing combined ^{230}Th/U and ^{14}C datasets.

6.4.1. Are The Observed ^{14}C Ventilation Signals Realistic?

As a basis for the calculation of ^{14}C ventilation ages in the ocean, an atmospheric reference curve, the IntCal20 (Reimer et al., 2020) for the Northern Hemisphere, and the SHCal20 for the Southern Hemisphere (Hogg et al., 2020), is used. While they are based exclusively on atmospheric tree-ring records up to 13.9 ka, various records from floating tree-rings, terrestrial macrofossils, speleothems, foraminifera, and corals are used for the remaining time span (Reimer et al., 2020). These data are statistically integrated and combined with a newly developed Bayesian spline approach (Reimer et al., 2020). The atmospheric reference curve is updated and improved on a regular basis. As this is a reconstructed curve derived from multiple archives, it is important to consider the associated uncertainties. It is essential to recognize that the IntCal curve represents an estimate of the atmospheric ^{14}C level, and that short-term fluctuations, particularly during the last glacial, may not be adequately reflected in the IntCal curve (Muscheler et al., 2020) (a more detailed discussion of this topic can be found in chapter 7). For instance, CWC ^{14}C ventilation ages calculated with the previous version, IntCal13 (Reimer et al., 2013), were found to be above the atmosphere, while recalculations with the current IntCal20 resulted in values below the atmosphere (e.g. data in Beisel et al. (2023) and Hines et al. (2019)). Consequently, it is possible that the marine $\Delta^{14}C$ data currently above IntCal reflect unbiased and realistic water mass signals. Nevertheless, in the presented data here, deviations of up to 660 ‰ from IntCal20 were identified (figure B.12). This order of magnitude cannot be explained by uncertainties in the IntCal20 or respective data. These values are therefore considered unrealistic, and an alternative explanation is required (chapter 6.4.2).

As for the values above the atmosphere, an explanation is required for ^{14}C ventilation anomalies, i.e. high B_{atm} age values. The new data presented in this study were obtained from CWCs in the GoC and Mauritania in the eastern Atlantic. The results of the GoC in water depths between 520-940 m, present a B_{atm} age record with values between 1000 – 4000 a during deglaciation, 0 – 3000 a during the Last Glacial Maximum (LGM), even up to 10000 a between 30 – 40 ka (figure 6.1). The high resolution of this record indicates high variations in B_{atm} ages, up to several thousand years in time spans of centuries, for example at 17.7 ka during deglaciation or multiple times during the LGM, for example at 20.4 ka, 20.8 ka, and 21.2 ka. On the other hand, analyzed sediment cores from Mauritania have yielded both punctual ^{14}C ventilation anomalies up to 8400 a (24 ka) and values far above the atmosphere, up to 660 ‰ offset (figure B.10). The question thus arises as to whether such high B_{atm} ages and pronounced variations are indeed feasible.

During the last glacial, a number of processes, including increasing sea ice cover, increased stratification, or reduced ventilation led to an aged Atlantic Ocean compared to the present day (e.g. Adkins, 2013; Rafter et al., 2022; Skinner and Bard, 2022). The growing number of ^{14}C compilation papers (Rafter et al., 2022; Skinner and Bard, 2022; Skinner et al., 2023; Zhao et al., 2018) provide an overview of the general development of ocean ^{14}C ventilation through time. With regard to the Atlantic, the most significant aging is anticipated to occur below a depth of 2 km, with B_{atm} ages reaching up to 2500 – 3000 a (Rafter et al., 2022; Skinner and Bard, 2022; Skinner et al., 2023). The CWC recovered from the GoC and Mauritania were obtained in depths between 523 and 944 m. In this depth range, it is plausible that B_{atm} ages between 0 – 2000 a are realistic. This is in strong contrast to the results, which demonstrate ventilation ages up to 8000 a during the LGM and following deglaciation. Following the criterion of regional consistency (Skinner et al., 2019), the results from the GoC are compared to the B_{atm} ages obtained from benthic foraminifera in the Iberian Margin, located to the north-west of the GoC (Skinner et al. (2017), figure 6.1). During the LGM, the benthic foraminifera exhibited B_{atm} ages up to 2000 a depth of 3.1 km. It is therefore challenging to postulate that the corals at a depth of only 900 m with B_{atm} ages above 2000 a display a true water mass signal. Similar to presumably locally influenced foraminifera ^{14}C records, local influences must have altered the CWC B_{atm} age.

What factors could have influenced the observed B_{atm} age signals, resulting in ^{14}C ventilation anomalies? The methods employed in this study are subject to rigorous quality procedures to ensure the reliability of the obtained results (Kerber et al. (2023), Kerber (2023), Therre et al. (2021), Wefing et al. (2017), and chapter 4). Consequently, analytical issues with the respective dating methods are ruled out here. There must have been a process that locally modified the $^{230}Th/U$ and/or ^{14}C dating in the CWCs without the samples being conspicuous, based on the rigorous QC (chapter 3.4.2).

Biases Through Local Carbon Sources?

It is possible that ventilation anomalies (very high B_{atm} ages) may be attributable to the presence of a local old carbon source, such as respired carbon or methane from gas hydrate seepage. Respired carbon could be a local source of highly ^{14}C-depleted signals. However, in the event that respired carbon played a predominant role, it would be expected that a far greater number of corals would be affected by ^{14}C ventilation anomalies. Moreover, Adkins et al. (2003) estimated the maximum amount of respired CO_2 to be less than 8 % of the coral skeleton. Furthermore, corals consistently reflect the ^{14}C composition of the surrounding seawater (Adkins, 1998; Adkins et al., 2002; Frank et al., 2004), and are therefore unlikely impacted by respired carbon.

Another potential local source of very old carbon is methane seepages. Such gases may contribute localized depleted $\Delta^{14}C$ signals up to -1000 ‰, disrupting the original carbon signal from the ocean. Such extremely depleted ^{14}C values would not be discernible in comprehensive compilations, as the old carbon is likely to dissipate rapidly (Hain et al., 2011). Nevertheless, corals situated in close proximity to these old carbon sources would incorporate some of it, resulting in a carbon signal that is overprinted by a local contribution.

The GoC is characterized by the occurrence of numerous mud volcanoes and seeps, which are associated with the outgassing of methane. Given that methane has a $\Delta^{14}C$ signature of -1000 ‰ (Sassen et al., 2003), even the smallest amounts would influence the observed $\Delta^{14}C$ signature and thus the B_{atm} age. A simple mixing model provides a rough estimate of the quantity of old carbon derived from methane that must be added to obtain strongly depleted $\Delta^{14}C$ values (high B_{atm} ages). To illustrate, the time span between 30 - 40 ka is selected, as the most pronounced depletion occurs during this time span. Assuming an initial seawater value of approximately 300 ‰ (Heaton et al., 2020), an added quantity of methane of 54 % is required for a $\Delta^{14}C$ signature of -400 ‰. Consequently, it can be deducted that 54 % of the carbon incorporated into the coral must not contain ^{14}C in order to produce the observed $\Delta^{14}C$ signals (B_{atm} age). This is a considerable amount, which should also be reflected in the $\delta^{13}C$ results.

Methane exhibits a $\delta^{13}C$ signature of approximately -120 ‰ to -20 ‰, depending on the source (e.g. Cherrier et al., 2014; Sassen et al., 2003; Whiticar, 1999). The $\delta^{13}C$ signature within a CWC exhibits considerable variability of up to 12 ‰, with typical values within a range of -10 ‰ to 2 ‰ (Blamart et al., 2005; Rollion-Bard et al., 2003; Smith et al., 2000). The final $\delta^{13}C$ signature of the coral with 54 % methane-derived CO_2 should therefore be between -69.4 ‰ and -9.9 ‰. A total of 17 CWCs from the GoC and six CWCs from Mauritania were subjected to $\delta^{13}C$ measurements (chapter 6.2.2, figure B.13). The corals show a $\delta^{13}C$ range from -9 ‰ to 0 ‰ (figure B.13). Consequently, there is no evidence for methane as a carbon source in the CWCs. This corroborates previous findings that strongly depleted ^{14}C signatures cannot be attributed to methane sources (Mangini et al., 2010; Ruckelshausen, 2013). Therefore, other explanations seem more likely.

The presence of ^{14}C signals above the atmosphere requires the existence of an additional, local carbon source, which would provide an additional source of in-situ produced ^{14}C. However, given that no such non-anthropogenic ^{14}C sources have yet been identified, this possibility has been ruled out.

6.4.2. Biased ^{230}Th/U Ages?

The second possible explanation for the observed anomalies is a modification of the ^{230}Th/U age, which could result in either an underestimation of the ^{230}Th/U ages (low $\Delta^{14}C$ values, high B_{atm} ages) or an overestimation of the ^{230}Th/U ages ($\Delta^{14}C$ values above the atmosphere, negative B_{atm} ages). But how could we quantify and recognize if such influence happened, when U-series results in closed system evolution?

Diagenetic changes can have an enormous influence on age determination using the ^{230}Th/U method. In CWCs, uranium is incorporated as a trace constituent in near equilibrium with the U/Ca ratio of seawater. Even the slightest alterations in the concentrations of uranium or thorium subsequent to the formation of the original skeleton can have profound effects on the isotopic composition and calculated age. In order to ensure the reliability of the ^{230}Th/U ages of CWCs, three criteria are met: the ^{232}Th concentration, the $\delta^{234}U_i$ value (chapter 3.4.2), and a ^{238}U concentration typical for CWCs. Nevertheless, ^{14}C ventilation anomalies and values above the atmosphere have been observed (figure 6.1, B.10, B.11, B.12). Therefore, either further in-depth geochemical studies would be required to infer changes in the uranium and thorium concentration through time, or one could explore the consistency of the coral mound chronology as an additional quality control criterion.

Stratigraphic Order as Additional Criterion

The stratigraphic order of a coral-bearing sediment core is generally not used as a quality control parameter, as deviations from a homogeneous chronology may be attributable to a range of processes. Firstly, it should be noted that coral reef growth itself is not necessarily a uniform process (chapter 2.3). In the presence of suitable environmental conditions, the coral larvae settle on a hard substrate (Roberts et al., 2006). The formation of CWC mounds occurs when the corals are able to keep pace with sediment deposition (Dorschel et al., 2005). Dead corals or coral fragments continuously form new, hard substrate on which the new coral generation grows. Active coral growth adapts to the prevailing conditions (Corbera et al., 2022). Locations with strong currents and the associated food source are preferred, which can result in a chaotic chronology on the mound. Furthermore, external factors such as landslides or the collapse/demolition of individual corals with subsequent displacement can also lead to irregularities in the stratigraphic order (e.g. De Haas et al., 2009; Douarin et al., 2013; Frank et al., 2009; Krengel, 2020; Ruckelshausen, 2013). The coalescence with older coral material results in a hiatus in the chronology, indicating periods when reef growth was not possible due to changing environmental conditions. Moreover, during the extraction of the sediment core and sampling, coral fragments may have been displaced, resulting in their appearance at a different core depth than initially. All of these processes result in age clusters within the sediment core, which are interrupted by hiatus. The clusters themselves may occur in a dischronological arrangement due to the aforementioned processes.

The combined ^{230}Th/U and ^{14}C analysis of corals obtained from sediment cores allows for the comparison of both respective chronologies. The ^{230}Th/U and the uncalibrated ^{14}C age of a coral should differ, as the ^{14}C content of the coral depends not only on its age, but also on the “age” of the water mass in which the coral has grown (Adkins et al., 1998; Mangini et al., 1998). Depending on the “age” of the water mass, the uncalibrated ^{14}C age may therefore be a few hundred to thousand years younger (reservoir effect). Given that the ^{14}C content in the ocean depends on variable factors, such as transport processes in the ocean, air-sea gas exchange, cosmogenic radiocarbon production, or local influences (Skinner and Bard, 2022), fluctuations in the corals’ ^{14}C content and, consequently, the ^{14}C depth profile can be anticipated within a range of a few hundred to thousand years. If the reservoir age is known, a calibration software (e.g. “calib.org”) can be utilized to convert the uncalibrated ^{14}C age into a calendar age. With an accurate reservoir age assumption, this age should be equivalent to the ^{230}Th/U age. However, the reservoir age varies through time (e.g. Rafter et al., 2022; Skinner and Bard, 2022; Skinner et al., 2023), and is typically not known for CWCs.

In general, with the exception for coral mound related reasons (see above), an uniform pattern can be anticipated in the ^{230}Th/U depth profile (e.g. Douarin et al., 2013; Wienberg et al., 2018, 2020). However, when the ^{230}Th/U chronologies of the respective coral-bearing sediment cores are analyzed, it becomes evident that ^{14}C ventilation anomalies and values above the atmosphere can be associated with ^{230}Th/U age-depth inversions (chapter 6.3, figure 6.5). In contrast, the ^{14}C depth profiles do not display such pronounced age-depth inversions as observed in the ^{230}Th/U chronologies, although the reservoir age may have varied over time. Given that fluctuations in the ^{14}C chronology are to be expected, but not in the ^{230}Th/U chronology, this feature is particularly intriguing. This further supports the hypothesis that the ventilation anomalies in CWC are likely to be related to modifications of the ^{230}Th/U ages.

Upon analysis of the sediment cores from GoC, Mauritania and Brazil, a number of cases are evident. First, (i) it is evident that not every sediment core and site seem to be affected. Thus far, no age-depth inversions, ^{14}C ventilation anomalies or values above the atmosphere have been detected at the Angola site (Beisel et al. (2023), figure B.18) as well as in the cores GeoB 18141-1 (GoC, Hemsing unpublished, Hemsing (2017) and references therein), GeoB 14905-2 (Mauritania, chapter 7) and KGLC (Brazil, Ruckelshausen (2013)). Age-depth inversions and associated ^{14}C ventilation anomalies / values above the atmosphere have been observed at the affected sites either (ii) in specific sections in the core, e.g. in certain sediment sections or hiatus (e.g. GeoB 18139-1, MD08-3231, GeoB 14904-2) or (iii) across almost the entire core (GeoB 12740-1, GeoB 14899-1, C1, C2, MXL). This could provide us with important insights into to the underlying processes. Given that not all sediment cores and CWCs seem to be affected, the phenomenon seems to depend strongly on specific local conditions. These occur either as in case (ii) only at certain times or (iii) over a longer period of time.

The aforementioned indications thus point to a modification of the ^{230}Th/U method. There must be at least two different processes influencing the ^{230}Th/U dating. One process shifts the actual ^{230}Th/U ages towards younger ages, which in turn leads to ^{14}C ventilation anomalies (figure 6.5c, d). The other process shifts the actual ^{230}Th/U ages towards older ages, resulting in values above the atmosphere (figure 6.5a, b). In some instances, both processes occur within a coral-bearing sediment core (GeoB 14899-1, C1, C2, MXL). Moreover, it cannot be excluded that other samples may also be affected. Possible reasons for such modifications remain elusive and yield results

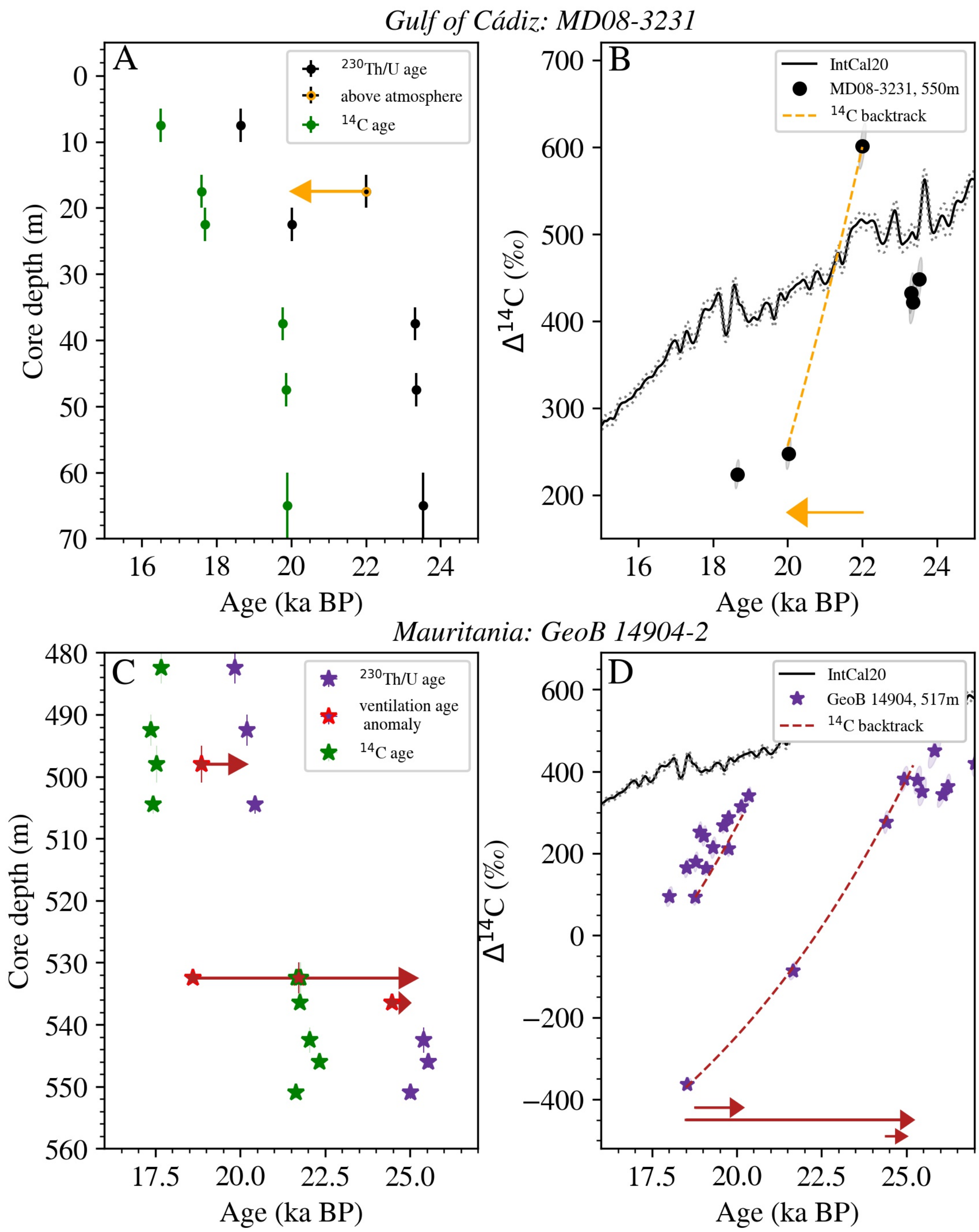

Figure 6.5.: Visual illustration of the effects of a ^{230}Th/U age modification at a constant ^{14}C age. (A) Excerpt through the depth profile of MD08-3231, Gulf of Cádiz (Hemsing, 2017). A shift of the ^{230}Th/U age-depth inversion at a depth of 17.5 cm by -2 ka results in (B) a shift of Δ^{14}C above the atmosphere (IntCal20, Reimer et al. (2020)) along the ^{14}C backtrack curve (constant ^{14}C age) to an expected range below. (C) Excerpt through the depth profile of GeoB 14904-2, Mauritania. Once more, a shift from the ^{230}Th/U age-depth inversions at 498 cm (+1.4 ka), 532.5 cm (+6.7 ka and +3.5 ka) and 536.5 cm (+0.6 ka) depth results in (D) a shift of the ^{14}C ventilation anomalies along the ^{14}C backtrack curve into an expected ventilation range.

consistent with the theoretical development (chapter 6.4.3).

Analysis of Diagenetic Indicators and Closed System Presumptions

The new and compiled data presented here have all been subjected to a rigorous quality control for the ^{238}U concentration, the ^{232}Th concentration and the $\delta^{234}U_i$ value to ensure reliable ages. It is a very surprising and important observation that nevertheless the ^{230}Th/U age seems to be modified in the order of several hundred to thousands of years (e.g. figure 6.5) in certain instances. However, diagenetic processes in CWCs still remain a field of active research (e.g. Wang et al., 2022). The following sections summarize the previous criteria, their respective strengths and limitations, and their impact on the compiled data set (table C.9).

^{238}U concentration Given that uranium is evenly distributed in the ocean and is assumed to be constant at a value of 3.3 μg/g, the ^{238}U concentration criterion is employed to identify CWCs that have been exposed to drastic uranium additions or removals and to ensure that they are excluded at an early stage. Bioerosion, such as endolithic sponge borings, has been observed to exhibit higher uranium concentrations of up to 15 μg/g (Robinson et al., 2006). However, the U/Ca ratio in CWCs is strongly correlated with temperature, alkalinity and the biomineralization process, which is assumed to change with the environment (Chen et al., 2021a). In fossil corals, the ^{238}U concentration exhibits fluctuations that are likely due to alpha-recoil diffusion, without any correlation to the calculated age (Robinson et al., 2006). Typical values are within the range of 2-6 μg/g (e.g. de Carvalho Ferreira et al., 2022; Robinson et al., 2006). The CWCs with probably biased ^{14}C ventilation ages, as compiled here (table C.9), exhibit ^{238}U concentrations between 2.2-7 μg/g (mean 3.4 ± 0.7 μg/g, median 3.3 μg/g) prior to the QC and 2.2-5.3 μg/g (mean 3.4 ± 0.6 μg/g, median 3.3 μg/g) following QC (figure B.14). No correlation can be established between anomalous ^{14}C ventilation ages and ^{238}U concentrations. Nevertheless, it is questionable whether this criterion is sufficient on its own. Diagenetically altered parts, such as chalk layers in CWCs, have been observed to have similar uranium contents (Wang et al., 2022). Given that the original ^{238}U concentration is unknown and that the value fluctuates within the coral, small additions or removals in the ppm range of uranium could go undetected but still affect the calculated ^{230}Th/U age.

^{232}Th concentration The ^{232}Th concentration is employed to evaluate and correct the contamination with ^{230}Th. Consequently, the ^{232}Th concentration is directly related to the ^{230}Th/U age uncertainty. Moreover, a high ^{232}Th concentration can be indicative of diagenetically altered parts of the coral skeleton, caused by microbial activity or coating on the surface. Recently, calcareous layers in the CWC *M. oculata* were investigated and revealed to be a diagenetically altered part of the coral skeleton, characterized by a very high ^{232}Th concentration, which increases the resulting age and age corrections (Wang et al., 2022). Thorough cleaning practices can reduce the total amount of ^{232}Th and associated contamination or diagenetically altered parts of the coral skeleton. Thresholds for the ^{232}Th concentrations exhibit considerable differences across studies. For instance, some accept ^{232}Th values <10 ng/g (Mangini et al., 2010), <6 ng/g (de Carvalho Ferreira et al., 2022), <5 ng/g (Cheng et al., 2000), others have utilized thresholds between 2-3.8 ng/g (Beisel et al., 2023; Chen et al., 2015; Chutcharavan et al., 2018; Hines et al., 2015, 2019; Li et al., 2020).

The new anomalous data presented here range from ^{232}Th concentrations of 0.03-1.3 ng/g for the GoC (n=23) and 0.16-2.3 ng/g for Mauritania (n=15). One data point could be excluded on the basis of the ^{232}Th threshold of 2 ng/g. However, the impact of a strict ^{232}Th criterion becomes evident when older data sets are included and rescreened. As the compiled data set (n=66, figure B.15) ranges between 0.03-98.2 ng/g, a threshold value of 2 ng/g leads to 31 % data rejection (n=20). Nevertheless, 69 % of the anomalous data remains. No correlation between the ^{232}Th concentration and anomalous ^{14}C ventilation ages can be established.

δ^{234}U$_i$ ratio The most commonly applied criterion for ensuring closed system behavior is the δ^{234}U$_i$ ratio. The δ^{234}U$_i$ ratio should be within error identical to the marine δ^{234}U$_i$ ratio: 146.8 ± 0.1 ‰ (Andersen et al., 2010). However, it is assumed that the marine δ^{234}U$_i$ ratio varies over time and location, and that it represents a potential tracer itself for continental weathering and subglacial discharge (e.g. Chen et al., 2016; Chutcharavan et al., 2018; Esat and Yokoyama, 2006; Li et al., 2023; Robinson et al., 2004; Yokoyama and Esat, 2004). Hence, a boundary around this value, between ± 7-15 ‰, is most commonly applied (e.g. Beisel et al., 2023; Chen et al., 2015; de Carvalho Ferreira et al., 2022; Hines et al., 2019; Raddatz et al., 2023). Some studies apply different boundaries depending on the assumed absolute age of the sample, like 141.7 ± 7.8 ‰ for samples older than 17 ka (e.g. Hines et al., 2015, 2019; Reimer et al., 2009), or individual thresholds for different climate stages (e.g. Li et al., 2020). Moreover, the δ^{234}U$_i$ ratio varies within the coral, likely due to alpha-recoil diffusion (Li et al., 2023; Robinson et al., 2006).

Figure 6.6 presents the compilation of data with ^{14}C ventilation ages anomalies, together with boundaries around the modern δ^{234}U$_i$ ratio (146.8 ± 7 ‰) and a glacial threshold of 141.7 ± 7.8 ‰ (Reimer et al., 2009), consistent with the glacial reduction of approximately -5 ‰ ± 2 ‰(Chutcharavan et al., 2018). As can be seen, 9 % of the

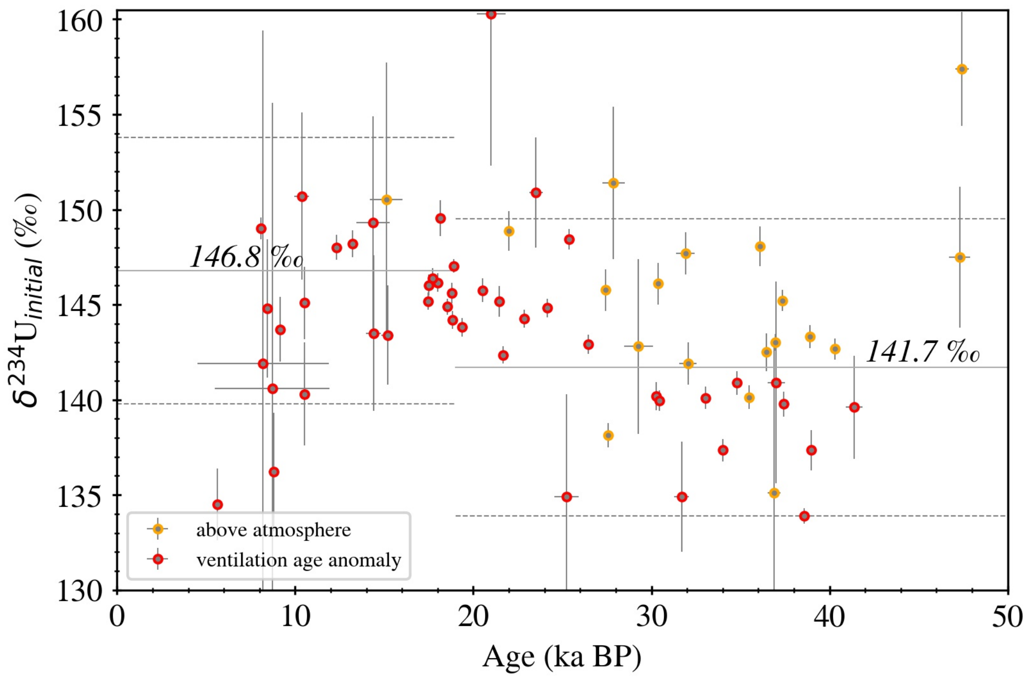

Figure 6.6.: The evolution of the initial activity ratio of $^{234}U/^{238}U$ ($\delta^{234}U_{initial}$) over time, based on the compiled ^{14}C ventilation anomalies (red) and the values above the atmosphere (orange) (table C.9). The horizontal lines show the thresholds 146.8 ± 7 ‰(Andersen et al., 2010) and 141.7 ± 7.8 ‰(Reimer et al., 2009) for the glacial. 91 % of the anomalous data fulfill the $\delta^{234}U_i$ criterion.

anomalous data can be rejected due to not fulfilling the current $\delta^{234}U_i$ criteria. It should be noted that these 9 % originate from older publications with more generous $\delta^{234}U_i$ limits. The majority of the data (91 %) meets the current closed system $\delta^{234}U_i$ criteria. In the case of ^{14}C ventilation anomalies, applying even more stringent boundaries would not resolve the issue. However, for values above the atmosphere, a trend towards higher $\delta^{234}U_i$ ratios can be observed (figure 6.6, B.16). This becomes particularly evident when values obtained from CWCs from Mauritania are compared with the CWCs from Angola, which so far show no signs of significantly modified $^{230}Th/U$ ages (Beisel et al. (2023), figure B.16). Restricting corals with ages >35 ka to values <141.7 ‰ would eliminate all data above the atmosphere in this time range. The introduction of a locally stronger temporal limitation of the $\delta^{234}U_i$ criterion could therefore lead to a higher reliability of the data. However, the potential use of $\delta^{234}U_i$ as a tracer is also being discussed (e.g. Chen et al., 2016; Chutcharavan et al., 2018; Esat and Yokoyama, 2006; Li et al., 2023). A more rigorous data selection based on $\delta^{234}U_i$ is only feasible if the local and temporal evolution of $\delta^{234}U_i$ has been identified.

It is a very important observation, that the majority of the potentially modified $^{230}Th/U$ ages assumed here cannot be recognized by the $\delta^{234}U_i$ ratio. Studies, particularly those on tropical corals, have already demonstrated that the fulfillment of the

$\delta^{234}U_i$ criterion does not necessarily indicate a reliable age, as indicated by insufficient age reproducibility (Andersen et al., 2008; Chutcharavan and Dutton, 2021; Gallup et al., 2002; Pons-Branchu et al., 2005; Robinson et al., 2006). However, tropical corals differ from CWCs in several ways. Due to their shallow location, they may have been exposed to meteoric water and subaerial weathering due to sea level fluctuations. Weathering, recrystallization and α-recoil processes result in U-series open system behavior (e.g. Frank et al., 2006; Henderson and Slowey, 2000; Robinson et al., 2006; Scholz et al., 2004; Thompson et al., 2003; Villemant and Feuillet, 2003). A number of models have been developed to correct $^{230}Th/U$ data from tropical corals with known diagenetic processes under certain circumstances (Scholz et al., 2004; Thompson et al., 2003; Villemant and Feuillet, 2003). However, in CWCs, the lack of a correlated ^{234}U and ^{230}Th deviation from the theoretical evolution precludes the application of such U-series open system models. Numerous factors that induce U-series open system behavior in tropical corals are not applicable to CWCs. Such corals are generally not exposed to meteoric water or subaerial weathering due to sea level fluctuations.

In summary, the understanding of U-series boundary conditions has evolved, and the present criteria for QC removes 35 % of the compiled anomalous ^{14}C ventilation ages due to discrepancies in the ^{238}U concentration, the ^{232}Th concentration, and $\delta^{234}U_i$ ratio. Even with the most recent QC, ^{14}C ventilation anomalies and values above the atmosphere persist. However, their occurrence is confined to specific locations and depths within sediment cores at these locations (chapter 6.3). This leads to the question of whether the criteria commonly used to date are sufficient to detect these diagenetically altered CWCs.

Reproducibility For tropical corals, it is recommended to measure several subsamples to obtain more reliable $^{230}Th/U$ ages (e.g. Chutcharavan and Dutton, 2021; Gallup et al., 2002; Scholz and Mangini, 2007). In practice, however, this is not always feasible, as sufficient sample material and financial resources must be available for repeated measurements. In CWC, replicate measurements are typically employed to reduce the age error due to ^{232}Th contamination (e.g. in Chen et al. (2015); Li et al. (2020, 2023)).

In order to assess age reproducibility, 44 corals were resampled from the GoC, Mauritania and Angola for $^{230}Th/U$ dating (chapter 6.2.2, table C.5 and C.6). Two samples were previously analyzed in another laboratory, the Laboratory for Climate and Environmental Sciences (LSCE) at GIF-sur-Yvette in France (Wienberg et al., 2010, 2018). In addition, three corals underwent a third and fourth $^{230}Th/U$ measurement. For this purpose, double the amount, approximately 120 mg, was collected and prepared. The solution was divided and measured on two different days. The two measurements of the split solutions yielded identical results within their uncertainty. In one case, the results align with an earlier measurement (LSCE), in the other two cases they do not. The results are presented in figure B.17, table C.5, and C.6. While the ages from the LSCE (n=2) and the ages from Angola (n=6) could be successfully reproduced, only 27 % of the ages from the Gulf of Cadiz (n=3 out of n=11) and 31 % of the ages from Mauritania (n=8 out of n=26) could be reproduced.

Additionally, duplicate measurements were conducted on the CWC from Brazil (Ruckelshausen, 2009, 2013). Ruckelshausen (2009) mentions a CWC from sediment core C1 (Brazil) that was measured three times due to a high ^{232}Th concentration with age differences of up to 3 ka. Due to the lack of reproducibility, it was removed from the data set (Ruckelshausen, 2009). Two further duplicate measurements are listed in Ruckelshausen (2013). One of each measurement was also conducted at LSCE. Both measurements are within 2σ error, although one of the samples has an extremely high age uncertainty of 6 % (figure B.17).

In terms of reproducibility, a site-dependent trend can be confirmed. In sediment cores where ^{14}C ventilation anomalies occur (table 6.1 and C.5), only 27 %-66 % of the ^{230}Th/U measurements could be successfully reproduced. In some cases, however, ^{230}Th/U age anomalies, and hence ^{14}C ventilation anomalies, could also be reproduced. Consequently, repeated measurements are not able to reliably determine ^{230}Th/U anomalies at certain locations. Moreover, no uniform isotope shift was observed between the repeated measurements. Accordingly, no model correction can be made as with tropical corals. Further options for data filtering are discussed in chapter 6.4.3.

In contrast, all measurements could be reproduced at sites and sediment cores in which no ^{14}C ventilation anomalies are known to date (Angola, Mauritania GeoB 14905-2 (with the exception of a sample contaminated with 7 ng/g ^{232}Th, which is assumed to originate from diagenetically altered material, see section 6.4.2)). This observation is consistent with other CWC studies where the duplicate measurements were always successful (e.g. equatorial Atlantic (Chen et al., 2015) and Drake Passage (Li et al., 2020, 2023), table 6.1). This clearly demonstrates the limitation of divergent ^{230}Th/U ages to certain locations.

Furthermore, there is no evidence to suggest that ^{14}C dating is affected. ^{14}C measurements not only demonstrate much more homogeneous depth profiles within the sediment cores (chapter 6.4.2), but they are also reproducible in all locations (chapter 4, table C.2). An alternative explanation would be the different sample size. For ^{14}C dating, only 15 mg are required (chapter 3.3), whereas for ^{230}Th/U dating ~50 mg are needed (Kerber et al., 2023; Wefing et al., 2017). If only small areas of the coral

Location	Anomalies	Reproducibility	No.
GoC (this study, Wienberg et al. (2010))	Yes	27 %	N=11
Mauritania (this study, Wienberg et al. (2018))	Yes	31 %	N=26
Equatorial Atlantic (Chen et al., 2015)	No	100 %	N=6
Angola (this study, Wefing et al. (2017))	No	100 %	N=6
Brazil (Ruckelshausen, 2009, 2013)	Yes	66 %	N=3*
Drake Passage (Li et al., 2020, 2023)	No	100 %	N>6**

Table 6.1.: Overview of the locations in which duplicate measurements on CWCs were carried out. A site-dependent trend is evident. At sites without known ^{14}C ventilation anomalies and values above the atmosphere, the reproducibility of the CWC samples is 100 %.
*very high age uncertainty (up to 6 % (2ka total), figure B.17)
** Li et al. (2020) does not mention the exact number

have been diagenetically modified, the probability of detecting modification increases with the sample size.

The following section presents a summary of possible mechanisms and recommended steps for filtering data.

6.4.3. Identifying Modified ^{230}Th/U Ages

What Could Cause Modified ^{230}Th/U Ages?

So far, the ^{14}C ventilation anomalies observed in CWC data appear to be related to a chronology modification rather than a local carbon influence. ^{14}C ventilation anomalies due to underestimated ^{230}Th/U ages (n=46, n=31 after QC) are present in the following locations: Gulf of Cádiz, Mauritania, and Brazil (this study, (Beisel, 2021; Hemsing, 2017; Mangini et al., 2010; Ruckelshausen, 2009, 2013)). All of the aforementioned studies have one thing in common: the corals were retrieved from sediment cores.

Negative ^{14}C ventilation ages, i.e. Δ^{14}C values above the atmosphere, with calculation of the current calibration curve IntCal20/SHCal20 (Hogg et al., 2020; Reimer et al., 2020), are known at the following locations: Gulf of Cadiz, Tropic Seamount, Mauritania, Brazil and south of Tasmania (this study, (Beisel, 2021; Beisel et al., 2023; de Carvalho Ferreira, 2022; Hemsing, 2017; Hines et al., 2015; Mangini et al., 2010; Ruckelshausen, 2009, 2013). It is important to note that not only corals from sediment cores are affected. In some studies, the corals were collected from the seafloor (n=4) (de Carvalho Ferreira et al., 2022; Hines et al., 2015). Nevertheless, more corals from sediment cores (n=16) are affected (this study, (Beisel, 2021; Beisel et al., 2023; Hemsing, 2017; Mangini et al., 2010; Ruckelshausen, 2009, 2013). Depending on the extent, these cases could also have been caused by an underestimated atmospheric ^{14}C reference curve.

Conversely, CWCs at other locations do not appear to be affected, or at least not to any noticeable extent. These include, for example, Angola, the equatorial Atlantic, and the Drake Passage (Beisel et al., 2023; Burke and Robinson, 2012; Chen et al., 2015, 2020; Li et al., 2020). In Angola, the corals were obtained from sediment cores as well (Beisel et al., 2023).

The question, thus, remains as to the cause of these divergent ages. As the affected data cannot be completely filtered out by the usual quality control parameters, the responsible processes must adjust the thorium and/or uranium isotopes in a way that they remain within the defined limits (chapter 6.4.2). ^{230}Th/U ages that are "too young" (high ^{14}C ventilation ages) may have been caused by the addition of uranium. ^{230}Th/U ages that are "too old" (^{14}C values above the atmosphere), on the other hand, may be attributed to the removal of uranium. Mobility of uranium is the more likely cause, given that thorium is a highly particle-reactive element that cannot be readily displaced in the matrix (Langmuir and Herman, 1980; Scholz et al., 2004). Furthermore, thorium impurities can be classified according to the ^{232}Th value and removed by cleaning, such as crusts, coatings, and calcareous layers. Consequently, it is more probable that uranium caused the observed deviations.

One possibility to explain shifted ^{230}Th/U ages (younger and older than the apparent age) is closed-system diagenesis, as the $\delta^{234}U_i$ criterion is fulfilled. Internal reorganization of thorium and uranium through alpha-recoil diffusion could result in age biases of up to thousands of years, if combined with a sampling bias (Robinson et al., 2006). Such a sampling bias could be reinforced if a greater degree of variable grain size and porosity is present in the aragonite. This would favor alpha-recoil diffusion (Robinson et al., 2006). The aragonite crystals of the CWC *D. pertusum* become smaller when the corals are exposed aragonite undersaturated conditions (Hennige et al., 2020), although it is assumed that the arrangement of the fibers does not change (Wall et al., 2015). Changing chemical conditions that shift the aragonite saturation horizon may therefore have led to changes in the corals aragonite lattice that favor alpha-recoil diffusion. Moreover, alpha-recoil diffusion is time-dependent. The more time elapsed, the stronger the observable effect. This could explain the increased extent of ^{14}C ventilation anomalies in the period 30-40ka (B_{atm} ages up to 10000 a, figure 6.1).

The addition of uranium may occur through precipitation or remineralization of secondary aragonitic fibers or by uranium migration from pore waters in the sediment (Frank and Hemsing, 2021; Pons-Branchu et al., 2005; Robinson et al., 2006). Secondary aragonitic fibers would have little effect on $\delta^{234}U_i$, as modeling predicts maximum changes of 2 ‰ after 20 ka (Robinson et al., 2006). Even a small quantity added to the coral skeleton at a later time would supply the system with additional uranium, still having the isotopic composition of seawater, but would result in a younger ^{230}Th/U age. This could explain why the recorded anomalies are still consistent with the theoretical evolution of $\delta^{234}U_i$ in seawater. Lazar et al. (2004) modelled that after 1000 a of continuous precipitation of secondary aragonite results in an apparent age rejuvenation effect of 7 % in the tropical coral species *Porites*. The precipitation of secondary aragonite could therefore easily explain the observed age shifts in the order of hundreds to thousands of years (figure 6.5). However, despite no measurable effect on $\delta^{234}U_i$, the ^{238}U concentration is expected to be significantly higher (Lazar et al., 2004). Although significantly elevated ^{238}U concentrations could not be identified in corals with ^{14}C ventilation anomalies, this could still be a possibility as the original ^{238}U concentration in the coral skeleton is not known. In the tropical coral species *Porites*, secondary aragonite can be identified by an elevated Sr/Ca and U/Ca ratio, a lower Mg/Ca ratio and a reduced skeletal density (Enmar et al., 2000; Hendy et al., 2007; Lazar et al., 2004; Quinn and Taylor, 2006; Rashid et al., 2020; Sayani et al., 2011). Furthermore, secondary aragonite cannot be detected by XRD measurements, as carried out by Mangini et al. (2010) and Ruckelshausen (2013), but only by SEM measurements (e.g. Frank et al., 2006). A recent study conducted at the Alpha Mound in the GoC demonstrated the presence of secondary aragonite within CWC fragments (Feenstra et al., 2020). Therefore, it seems likely that secondary aragonite plays an important role in CWC in certain locations, such as the GoC.

One can only speculate as to why U-series open system behavior occurs more frequently at certain locations in certain periods of time. Location-specific processes could play an important role, such as fluid venting activity which is expressed by the occurrence of seeps, pockmarks, diapiric ridges, or mud-volcanoes that would temporally and locally alter sea-water and pore water chemistry and might influence the chemistry of the CWC skeleton (Feenstra et al., 2020; Foubert et al., 2008), for example through the precipitation of secondary aragonite (Feenstra et al., 2020). In the GoC, off Mauritania and Brazil, those are well-known geological features (e.g. Davies et al., 2015, 2023; Foubert et al., 2008; Mangini et al., 2010; Ruckelshausen, 2013; Sanz et al., 2017; Somoza et al., 2003; Sumida et al., 2004; Westphal et al., 2014; Yang et al., 2013, 2021). Rather than an influence of ^{14}C via methane, which is unlikely given that

^{14}C indicates homogenous reef growth for these sites, and has been excluded via ^{13}C measurements (Mangini et al. (2010); Ruckelshausen (2013), this study, chapter 6.4.1), the $^{230}Th/U$ dating may have been modified through an alteration in the chemistry of the coral skeleton. Given that only specific sections in the sediment cores and only specific locations are affected, it seems plausible that the fossil coral skeletons were more susceptible to diagenetic processes due to a change in environmental conditions, such as seawater and/or pore water chemistry, at certain times. Coral mounds in the vicinity of mud volcanoes may be temporarily affected by diagenesis, resulting in the dissolution of aragonite and potential precipitation of carbonate (Foubert et al., 2008). Additionally, CWCs with secondary aragonite were discovered in direct vicinity of methane seepage in the GoC (Feenstra et al., 2020). Hydrothermal fluids could provide aragonite, enabling aragonite recrystallization or the precipitation of inorganic aragonitic pore-filling cements within the coral skeleton (Pederson et al., 2020) or the encrustation of dead coral fragments (Pichler and Veizer, 2004). The dissolution of aragonite could be induced by the degradation of organic matter or bacterial mediated sulphate reduction, which lowers the pH of the pore water (Frank et al., 2011b; Wang et al., 2022). Dissolution and re-precipitation may occur on a micro-scale, with the secondary aragonite forming only a few layers (Pederson et al., 2019). Therefore, no major textural changes would occur (Pederson et al., 2019). Nevertheless, the rigorous cleaning procedure (chapter 6.2.2) ensures that any potential secondary aragonite has been removed from the surface of the coral. Consequently, it can be assumed that some form of secondary aragonite must be present in the coral itself, such as in the CWC from the GoC studied by Feenstra et al. (2020). Since XRD measurements are not suitable for detecting secondary aragonite or dissolution, SEM measurements would provide detailed information on the microstructure and potential secondary aragonite. Further studies are necessary to determine the exact origin of the divergent $^{230}Th/U$ ages. Nevertheless, altered samples can be identified through the application of additional criteria. These include the criterion of regional consistency (Skinner et al., 2019) and consistent $^{230}Th/U$ and ^{14}C chronology.

Identifying Divergent Ages: Additional Criteria

Combined $^{230}Th/U$ and ^{14}C ages are used to calculate ^{14}C ventilation ages. An important prerequisite for this is the fulfillment of the closed system and the detection of local influences on the ^{14}C ventilation signal. Corals associated with "too old" $^{230}Th/U$ ages and associated ^{14}C ventilation ages above the reconstructed atmosphere can be easily identified and excluded from the scientific discussions. The situation is different for "too young" $^{230}Th/U$ ages that result in anomalous old ^{14}C ventilation ages. Although the current selection criteria are apparently not sufficient to identify all corals affected by U-series open system processes (chapter 6.4.2), several tools are available to validate data. These can be employed until the exact origin and mechanisms behind divergent ^{230}Th/U ages are known, and new selection criteria have been developed. The following criteria should be checked. These include (i) regional consistency or local ^{14}C curves and, in the case of analyzed sediment cores, (ii) consistent chronology of the ^{230}Th/U age-depth profile.

(i) Regional Consistency and Local ^{14}C Curves In general, the criterion of regional consistency (Skinner et al., 2019) should be employed to identify divergent ^{14}C ventilation ages through chronology inconsistencies and/or local influences. A true ^{14}C ventilation signal of a water mass must be capable of being recorded at multiple sites, considering the spatial proximity of the sites and the expected flow patterns. This can refer to cores of similar depth at a certain location as well as cores or samples from other locations where the same water mass is expected. The growing number of ^{14}C compilations for the ocean over time allows us to estimate a certain range for ^{14}C ventilation ages (Rafter et al., 2022; Skinner and Bard, 2022; Skinner et al., 2023; Zhao et al., 2018). If the results deviate significantly from the compilations, it is probable that local influences or chronology issues have occurred.

Local marine ^{14}C calibration curves reflect the ^{14}C content depending on location and depth as a function of time, thereby providing the optimal means of verifying the obtained ^{230}Th/U ages. If available, the uncalibrated ^{14}C age can be converted to a calendar age. Their development is currently a subject of research. For the sea surface, a calibration curve known as Marine20 has already been developed and requires adaptation to regional conditions (Heaton et al., 2020, 2023). Until local and reliable ^{14}C calibration curves are available for all regions of the ocean to accurately reconstruct local variations, the absolute ^{230}Th/U ages can be plotted against the uncalibrated ^{14}C ages for a given location and depth range for a first approximation (figure 6.7). While vertical movements, i.e. the variation of ^{14}C at a given time, are caused by changes in ^{14}C production, ocean circulation or alike, horizontal variations are usually not plausible. This also includes cases in which an uncalibrated ^{14}C age is assigned to several absolute ages. In ^{14}C ventilation records, this phenomenon is expressed by values along the ^{14}C decay curve, well-known cases are known from Brazil (Mangini et al., 2010; Ruckelshausen, 2013). From a physical point of view, the realization of a water mass with a constant ^{14}C age over hundreds or thousands of years, despite the decay of ^{14}C over time, would require a very unrealistic specific water mass mixture over an extended period of time. Consequently, a large scatter in the data set is likely indicative of local processes or influenced ages (figure 6.7a,b,e,f). However, further investigation is required in individual cases to ascertain whether the

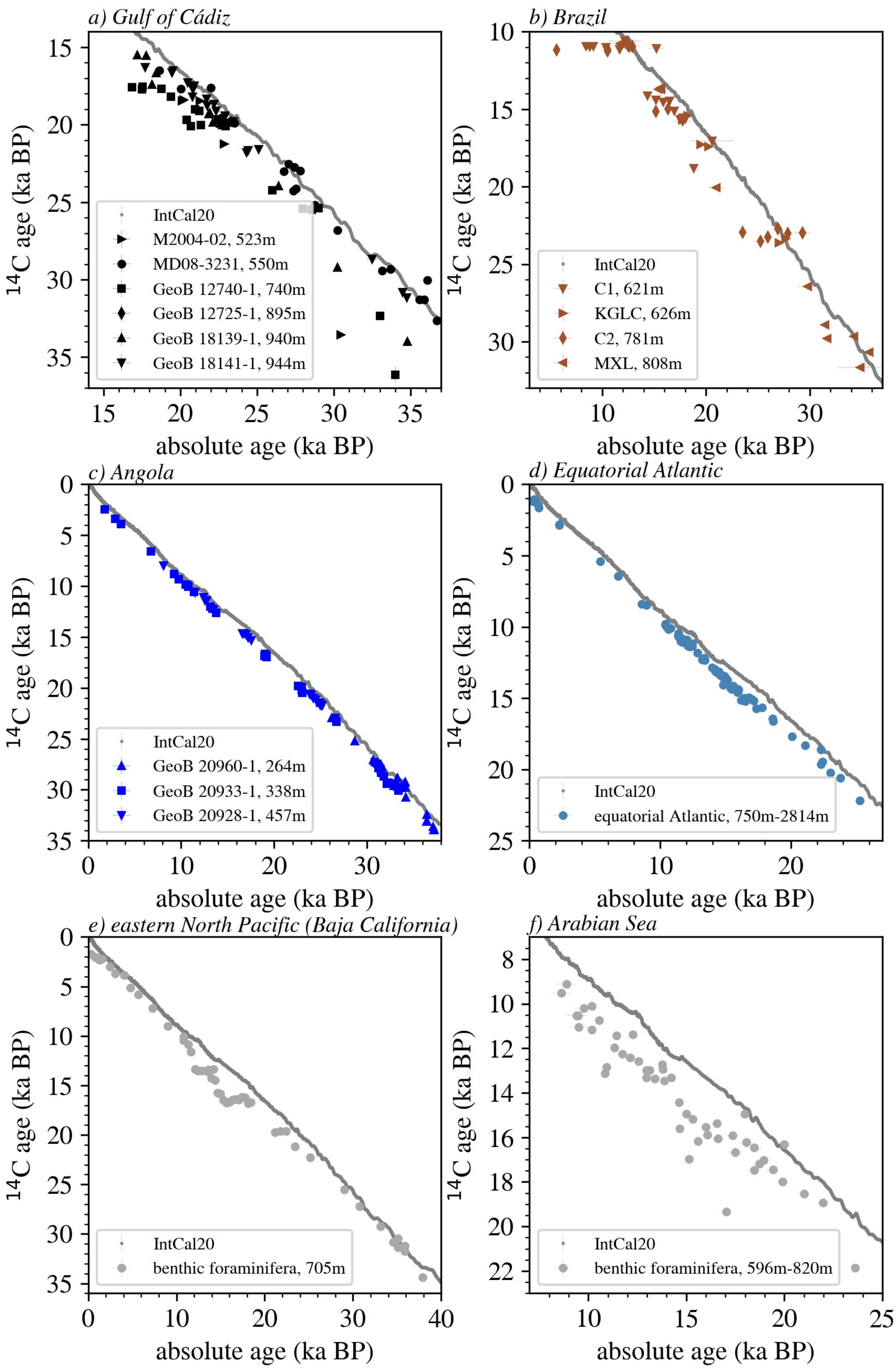

a) Gulf of Cádiz
b) Brazil
c) Angola
d) Equatorial Atlantic
e) eastern North Pacific (Baja California)
f) Arabian Sea
^{14}C age (ka BP)
absolute age (ka BP)
IntCal20
M2004-02, 523m
MD08-3231, 550m
GeoB 12740-1, 740m
GeoB 12725-1, 895m
GeoB 18139-1, 940m
GeoB 18141-1, 944m
C1, 621m
KGLC, 626m
C2, 781m
MXL, 808m
GeoB 20960-1, 264m
GeoB 20933-1, 338m
GeoB 20928-1, 457m
equatorial Atlantic, 750m-2814m
benthic foraminifera, 705m
benthic foraminifera, 596m-820m

Figure 6.7.

Figure 6.7.: Plotted absolute ages against uncalibrated ^{14}C ages for different locations, with IntCal20 (Reimer et al., 2020) as atmospheric reference. A wide scatter is indicative for modified or locally influenced ages. a) CWC record of the Gulf of Cádiz (Hemsing (2017), this study). b) CWC record from Brazil (Mangini et al., 2010; Ruckelshausen, 2009, 2013). c) CWC record off Angola (Beisel et al. (2023), chapter 7). d) CWC record of the equatorial Atlantic (Chen et al., 2015, 2020). e) Benthic foraminifera record from the eastern North Pacific (Marchitto et al., 2007). f) Benthic foraminifera record from the Arabian Sea (Bryan et al., 2010).

absolute age or the uncalibrated ^{14}C age of the sample has been falsified, e.g. by local processes or influences.

This criterion can be employed independently of the respective archive. In addition to the influenced CWC datasets, questionable datasets of foraminifera can also be examined. For instance, the plots of the widely discussed data sets of Marchitto et al. (2007) in the eastern North Pacific and Bryan et al. (2010) in the Arabian Sea demonstrate a wide scatter of uncalibrated ^{14}C ages in the age ranges in question. This supports the hypothesis of an altered signal (e.g. Skinner and Bard, 2022).

(ii) Consistent Chronology: Depth Profiles If the corals were recovered in sediment cores and sufficient data points are available, the consistent chronology criterion can be applied. In this instance, the ^{230}Th/U depth profile is analyzed. Age-depth inversions are most likely the result of U-series open or closed system processes (chapter 6.4.3). However, it should be noted that not all ^{230}Th/U age-depth inversions are due to U-series open or closed system behavior. If they occur simultaneously with ^{14}C age-depth inversions, they may be attributable to reef formation or external influences. In this instance, it is necessary to determine whether the ^{14}C ventilation age is plausible or if it should be excluded as a precautionary measure. A reliable assessment can only be achieved in conjunction with another dating method.

Sediment cores exhibiting pronounced scatter in the ^{230}Th/U ages or diffuse age trends should be excluded from further paleoceanography research, until the origin of divergent ^{230}Th/U ages is better understood (e.g. GeoB 14899-1 in Mauritania, C1, C2 and MXL in Brazil, GeoB 12740-1 in Cadiz). Nevertheless, they are optimal for elucidating the underlying causes of this phenomenon in further studies.

In summary, although the common selection criteria ^{232}Th, ^{238}U and $\delta^{234}U_i$ are likely insufficient for identifying all diagenetic alterations, additional criteria can be applied to ensure the reliability of the data. In addition to the criterion of regional consistency (Skinner et al., 2019) or the employment of local ^{14}C curves, the ^{230}Th/U chronology in the sediment cores should be examined.

Usability of Data Sets From the Gulf of Cádiz and Mauritania

Until the origin of divergent ^{230}Th/U ages is better understood, the question arises as to which of the new data presented from the Gulf of Cádiz and Mauritania can be utilized for palaeoceanographic research.

In the Gulf of Cadiz, it is recommended that cores M2004-02, GeoB 12740-1, GeoB 12725-1 be excluded from further discussions due to high scatter and/or low data resolution. The cores MD08-3231 and GeoB 18141-1 were previously discussed in Hemsing (2017), with the data checked for chronological consistency, and values above the atmosphere were excluded from the discussion. Core GeoB 18139-1 is situated on the same mound as GeoB 18141-1 (chapter 6.2.1). According to regional consistency, the same signal would be expected. However, the signals exhibit significant discrepancies ((i.e. same ^{14}C age, significantly different ^{230}Th/U age, figure 6.1, 6.7). These observations, when considered alongside the depth profiles, suggest that the chronology of GeoB 18139-1 may be compromised.

Alongside, no further investigations are recommended on the coast of Mauritania due to the high scatter / low data resolution for the sediment cores GeoB 14899-1, GeoB 14884-1 and GeoB 14890-2 (>15ka). The core GeoB 14904-2 may be analyzed with regard to regional consistency and the chronology criterion. Despite the observed age variations among some coral fragments (chapter 6.4.2), the current evaluation of the results according to regional consistency and the chronological criterion yields results that are consistent with those of previous research (e.g. Beisel et al., 2023; de Carvalho Ferreira, 2022). This underlines the effectiveness of the additional selection criteria. The GeoB 14905-2 core displays chronological consistency and is discussed in chapter 7.

6.5. Conclusion

Detailed and high-resolution ^{230}Th/U and ^{14}C studies of coral-bearing sediment cores permit the investigation of the underlying causes of ^{14}C ventilation anomalies and values above the atmosphere, which cannot be excluded with the usual quality criteria ^{238}U concentration, ^{232}Th concentration and $\delta^{234}U_i$ ratio. The presence of strong ^{14}C depletions, as well as certain values above the atmosphere, recorded in CWCs from sediment cores is associated with age-depth inversions in the ^{230}Th/U chronology. This occurrence is locally restricted to specific locations, such as the Gulf of Cádiz, the Mauritanian and Brazilian margins, and requires further investigation. At these locations, either entire coral-bearing sediment cores or only certain sections of these sediment cores are affected. Fluid venting activity may have played an important role, as the sites in question are affected by it.

The observed variance in ^{230}Th/U age within the coral skeletons may be related to the increased occurrence of alpha-recoil diffusion, possibly enhanced by variable grain sizes or porosity in the aragonite, and/or secondary aragonite. Secondary aragonite would not be noticeable by $\delta^{234}U_i$, as maximum changes are 2 ‰ after 20 ka (Robinson et al., 2006). However, a 1000 a long continuous precipitation of secondary aragonite would rejuvenate the age by 7 % (Lazar et al., 2004), and could thus easily explain observed ^{230}Th/U age modifications in the order of hundreds to thousands of years.

Affected locations can be easily identified through repeated measurements. Moreover, the additional quality criteria presented, regional and chronological consistency, are extremely effective in identifying affected samples. In this way, the modified data records can be reliably filtered.

It is important to note that the majority of CWC study areas not impacted by these modifications, including regions such as Angola, Drake Passage, the North and equatorial Atlantic, New England Seamount, and southwest Australia (Beisel et al., 2023; Chen et al., 2015, 2020; Frank et al., 2004; Hines et al., 2019; Li et al., 2020; Robinson et al., 2006; Trotter et al., 2022). CWCs from these sites still provide excellent means of reconstructing ocean ventilation and carbon cycling.

7. Eastern Atlantic Thermocline Marine Reservoir Age Variability Between 38,000 -30,000 Years Ago

7.1. Introduction

During the Last Glacial Maximum (LGM), a close coupling between the thermocline and intermediate waters of the South Atlantic and Southern Ocean was evident, as well as a shoaled thermocline off Angola and increased carbon storage (chapter 5, Beisel et al. (2023), Lausecker (2021)). However, it is still unclear when this development was initiated. Several centennial abrupt climatic events occurred during the last glacial. Between 38-30 ka, Antarctic Isotope Maxima (AIM) 8 to 4.1 occurred in the Southern Hemisphere, and subsequent Dansgaard-Oeschger (D/O) events 8 to 5 occurred in the Northern Hemisphere (e.g. Anderson et al., 2021; EPICA, 2006; Li and Born, 2019; Menviel et al., 2020; Rahmstorf, 2002; Zheng et al., 2021). AIM events are characterized by 1-3°C warming at Antarctica that preceded the onset of D/O events (EPICA, 2006). For D/O events, the warming ranged from 5 to 16.5°C in Northern Greenland over several decades (Kindler et al., 2014). AIM and D/O peak warming are shifted by several decades to hundreds of years (EPICA, 2006; Malmierca-Vallet et al., 2023). The causes and effects on the ocean are not yet fully understood (e.g. Li and Born, 2019; Malmierca-Vallet et al., 2023; Menviel et al., 2020). Much remains to be learned about the effects of D/O, and AIM events, on the carbon cycle and thus on ^{14}C in the ocean (Köhler et al., 2024). When was the shoaling of the thermocline and the increased carbon storage initiated?

Furthermore, between 36-30 ka, one or more geomagnetic field excursions are proposed (e.g. Cassata et al., 2008; Channell, 2006; Kissel et al., 2011; Korte et al., 2019; Laj et al., 2014). These are rapid, short-term reversals of the Earth's magnetic field. The weakened magnetic field leads to a significantly increased production rate and thus to increased $\Delta^{14}C$ values in the atmosphere. However, this is a highly controversial issue, with different temporal proposals (Korte et al., 2019; Laj et al., 2014). For example, Laj et al. (2014) propose 34.2 ± 1.2 ka as a time span. Due to the exchange between atmosphere and ocean, these events must also appear in oceanic records. In particular, records near the surface or in the upper part of the thermocline could provide further information.

In this study, cold-water corals (CWC) from the thermocline of Angola and Mauritania are analyzed using combined ^{230}Th/U, ^{14}C and Li/Mg measurements. Selected is one core off Mauritania with perfect chronology (GeoB 14905-2, n=7), and two cores off Angola (GeoB 20933-1, n=7, and GeoB 20960-1, n=18). A first Δ^{14}C and B_{atm} age record is established together with a thermocline temperature reconstruction from Angola between 38-30 ka. The aim is to assess the extent to which the changing atmospheric influence is visible, and to determine when the shoaling of the thermocline and thus close connection between the South Atlantic and Southern Hemisphere waters was first established.

7.2. Materials and Methods

In this study, CWC of the species *D. pertusum* were investigated at the sites Mauritania (GeoB 14905-2, 17°32.456'N, 16°39.999'W, 493m, Westphal et al. (2014)) and Angola (GeoB 20933-1, 9°49.331'S 12°46.565'E, 338m; GeoB 20960-1, 9°43.017'S, 12°45.997'E, 264m, Hebbeln et al. (2017)). The sites and their hydrography have already been described in chapters 5 and 6. Today, they show some similarities, such as the influence of the oxygen-poor and nutrient-rich South Atlantic Central Water (SACW) (Wienberg et al., 2023). Off Mauritania, the Cap Verde Frontal Zone (CVZF) separates the SACW from the North Atlantic Central Water, which extends to a depth of 600 m (Peña-Izquierdo et al., 2015; Zenk et al., 1991). Off Angola, the Angola-Benguela Front (ABF) separates the SACW coming from the north from the ESACW flowing towards the equator.

Sample preparation for ^{230}Th/U and ^{14}C measurements followed the procedure outlined in chapter 3. The refined selection criteria were applied (chapter 3.4.2). ^{230}Th/U and ^{14}C ages are reported in BP (before present).

The Li/Mg ratio in the CWC is primarily temperature dependent (e.g. Cuny-Guirriec et al., 2019; Montagna et al., 2014; Raddatz et al., 2013; Stewart et al., 2023) and can be used as a tool to reconstruct (past) thermocline seawater temperatures (ThWT). The empirical calibration curve from (Montagna et al., 2014) was used to translate Li/Mg ratios into ThWT.

The new ThWT reconstructions of GeoB 20960-1 were performed by two student interns, Dana Hoelkermann and Lucy Boyer, under the supervision of Prof. Dr. Norbert Frank. The ThWT reconstructions of GeoB 20933-1 are from the PhD thesis of Marleen Lausecker (2021), the Master thesis of Sina Schreiber (2023), and Bachelor thesis of Carla Roesch (2017). For further details on the methodology, including recent updates on the measurement protocol, mass spectrometric methods, and used reference material, please refer to the PhD thesis of Marleen Lausecker (2021), as well as Hessenthaler (2024), Rampmeier (2021), and Schreiber (2023). Lisa Hessenthaler (2024) determined the accuracy of ThWT to be within ± 1°C, which aligns with the findings of Cuny-Guirriec et al. (2019).

7.3. Results

7.3.1. ^{230}Th/U Dating

The ^{230}Th/U ages for Mauritania are between 30.8-35.6 ka (n=7, GeoB 14905-2) and for Angola between 26.21-37.3 ka (n=18, GeoB 20960-1) and between 31.56-33.4 (n=7, GeoB 20933-1). The 2σ age uncertainties are on average ± 0.1 ka and are not repeated in the following sections for better readability. In order to evaluate the quality of the data and to exclude open system behavior, the criteria outlined in chapter 3.4.2 (^{232}Th, $\delta^{234}U_i$) are used. The evaluation of the chronology criterion and regional consistency (chapter 6) are included in the discussion (chapter 7.4.1).

^{230}Th/U dating of two corals was rejected due to ^{232}Th concentrations between 2-3 ng/g. The remaining ^{232}Th concentrations between 0.3-1.7 ng/g, with a mean value of 0.8 ± 0.3 ng/g, demonstrate that residual contamination with non-carbonate material or coating is negligible. The initial $^{234}U/^{238}U$ ratio, $\delta^{234}U_i$, is between 138-145.4 ‰, which is consistent with a glacial reduction of $\delta^{234}U_i$ (Chen et al., 2016; Chutcharavan et al., 2018; Reimer et al., 2009). A total of four ^{230}Th/U measurements from Mauritania and six measurements from Angola were repeated (table C.6). Following the application of a ^{232}Th limit value of 2 ng/g, the respective measurements were found to be in agreement. The ages with the lowest ^{232}Th contamination were used for the calculation of ^{14}C ventilation ages.

7.3.2. ^{14}C Dating

The uncalibrated ^{14}C ages of the CWC of Mauritania range from 27.1-32.8 ka, those of Angola between 22.95-33.9 ka (GeoB 20960-1) and 28.7-30.1 ka (GeoB 20933-1). Seven ^{14}C measurements were duplicated and yielded identical results (table C.2 and C.11). The Δ^{14}C values exhibit fluctuations over time, sometimes the mean values of the ellipses of Angola are even identical to the current atmospheric calibration curve for the Southern Hemisphere, SHCal20 (Hogg et al., 2020) (figure 7.1). While $\Delta^{14}C$ off Mauritania fluctuates between 260-440 ‰ (mean value 360 ± 70 ‰), the fluctuations in $\Delta^{14}C$ values off Angola are much more pronounced, ranging from 260-620 ‰ (mean value 400 ± 90 ‰). This becomes particularly evident in the periods 34.2-34 ka and 33.4-33.3 ka, during which $\Delta^{14}C$ exhibited pronounced fluctuations of up to 250 ‰ within a few hundred years.

Between 37.3-36.4 ka, calculated B_{atm} ages of Angola yield a mean value of 910 a and thus, are within the average LGM value of 970 ± 260 a (chapter 5). This is followed by a rapid change to lower B_{atm} ages, between 34.2-34 ka, with the B_{atm} age decreasing from 1100 ± 400 a to -50 ± 260 a. A further rapid change in B_{atm} age occurs between 33.4-33.3 ka, from 1080 ± 330 a to -50 ± 320 a. The carbon system then returns to the mean LGM values, with B_{atm} ages of 890 ± 300 a to 1080 ± 320 a between 32.9-32.2 ka. Subsequently, from 31.8-26.2 ka, the B_{atm} age range of chapter 5 (Beisel et al., 2023) is confirmed. With the exception of one data point indicating radiocarbon levels closer to the atmosphere (0 ± 270 a B_{atm} age), the mean value is 800 ± 100 a.

Mauritanian B_{atm} ages vary between 560 ± 440 a and 1800 ± 500 a. With two exceptions, 35.6 ka and 34 ka, which at 1500 ± 450 a and 1800 ± 500 a indicate less equilibrated ("older") water, they represent the same range as the corals from Angola.

7.3.3. Temperature Reconstruction on Angola Cold-Water Corals

Whereas modern ThWT off Angola are between 13.5°-9°C (Hebbeln et al., 2020), the reconstructions of glacial ThWT from Angola yielded temperatures between 2°-9°C (figure 7.5, table C.12). The accuracy of the ThWT is ± 1°C (Cuny-Guirriec et al., 2019; Hessenthaler, 2024) and is not repeated in the following sections for better readability. Between 37.3-36.4 ka, ThWT were found between 7.4°-9.3°C. The pronounced $\Delta^{14}C$ increase and fluctuation at 34.2-34 ka is accompanied by a temperature drop of approximately 3°C (6.9°C to 4.2°C). This is followed by a warming to 6.8°C around 33.7 ka, and a renewed cooling to 4.1°-5.2°C between 33.4-33.1 ka. Subsequently, the CWCs documented 6.4°C at 32.9 ka and a subsequent cooling to 3.2°C at 32.3 ka. Between 32.3-26.2 ka, temperatures remain low, between 1.9°C and 3.4°C.

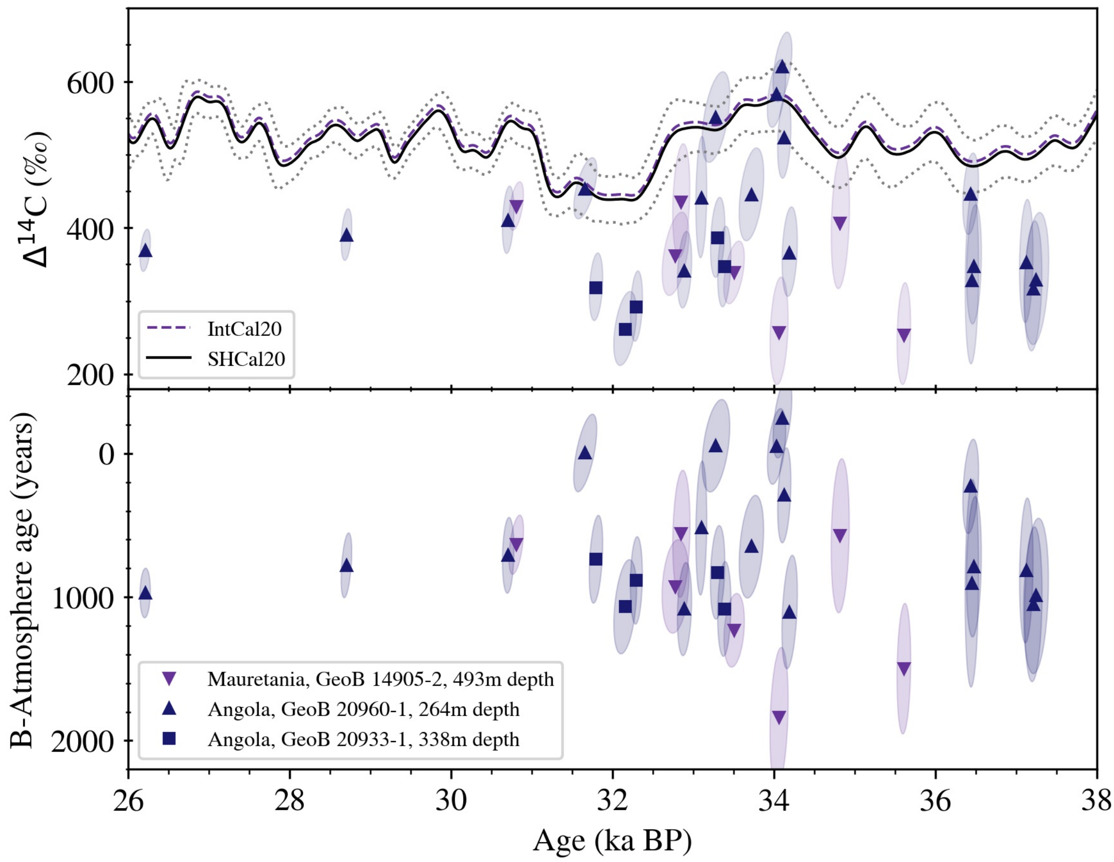

Figure 7.1.: Radiocarbon variability in the thermocline off Mauritania and Angola between 38-26 ka (this study). The upper panel shows $\Delta^{14}C$ values in comparison with the atmospheric $\Delta^{14}C$ estimate IntCal20 (dotted violet line, Reimer et al. (2020)) and SHCal20 (solid black line, Hogg et al. (2020)) and its 2σ uncertainty. The lower panel shows the B_{atm} age values.

7.4. Discussion

The ^{14}C records of corals, and thus their $\Delta^{14}C$ and B_{atm} age records, are influenced by a number of factors. First, in certain locations, such as Mauritania, the absolute age, determined by the $^{230}Th/U$ method, could have been modified by processes that are not yet fully understood, resulting in ^{14}C ventilation anomalies (chapter 6). Moreover, the ^{14}C record is subject to influences from various factors, such as ^{14}C production and the ^{14}C content of the atmosphere, gas exchange and transport and mixing processes, which in turn depend on the prevailing climate. In order to interpret the data set, all of these factors must be considered.

7.4.1. Regional and Chronological Consistency

Some locations in the Atlantic Ocean, including Mauritania, are affected by ^{14}C ventilation anomalies (chapter 6). These anomalies are attributed to modifications

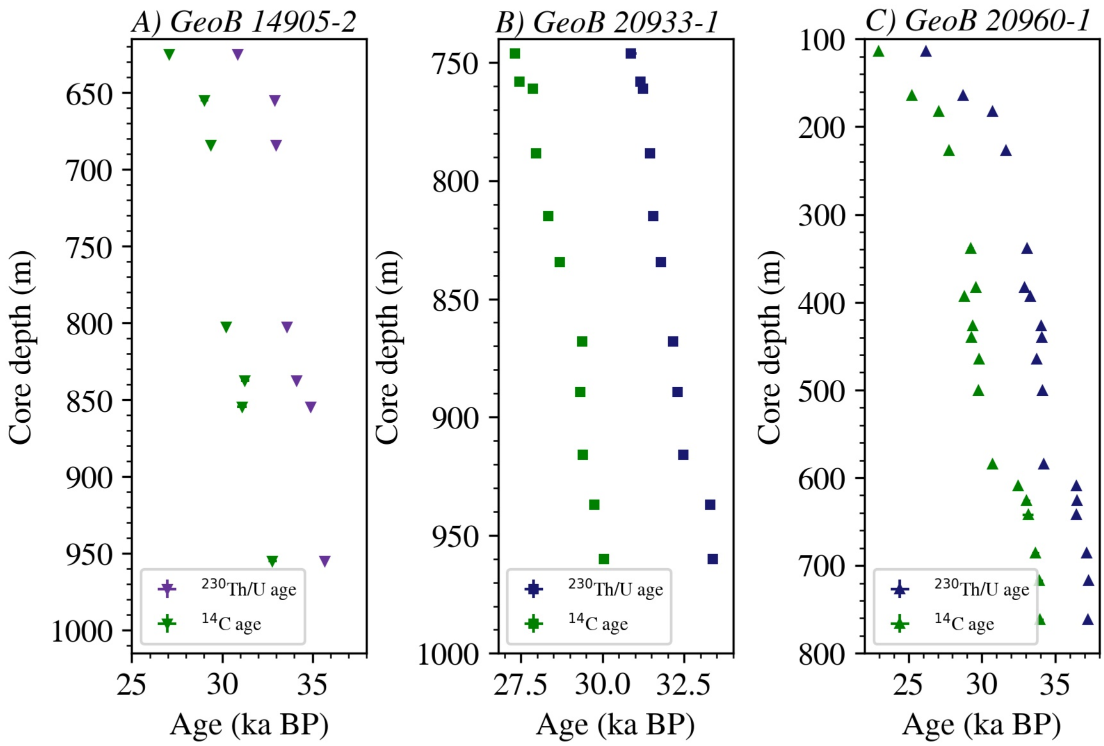

Figure 7.2.: Age-depth profiles from the investigated sediment cores from (A) GeoB 14905-2, Mauritania (this study), (B) GeoB 20933-1, Angola (Wefing et al. (2017) and this study) and (C) GeoB 20960-1, Angola (this study). Displayed are the ^{230}Th/U ages, as well as the uncalibrated ^{14}C ages. In most cases, the error bars are smaller than the symbols.

of the ^{230}Th/U ages in the order of a few hundred to thousands of years (chapter 6). The causes for these modified ^{230}Th/U ages remain unknown (chapter 6). Additional selection criteria, such as regional and chronological consistency, can effectively eliminate such age anomalies (chapter 6).

Only very few ^{14}C data are available for the period between 38-30 ka. The Atlantic thermocline was only investigated for the period 32-30 ka (chapter 5). As a consequence of the low data density, the criterion of regional consistency can only be applied to a very limited extent.

The two cores from Angola, GeoB 20933-1 and GeoB 20960-1, are generally expected to have the same ^{14}C signal due to their proximity. In general, the ^{14}C signals from GeoB 20933-1 and GeoB 20960-1 are consistent with each other (figure 7.5). An exception is the coral with an age of 33.3 ka and a ^{14}C value identical to that of the atmospheric reconstruction (Hogg et al., 2020). Applying the criterion of chronological consistency, this coral is chronologically consistent with its neighboring corals. Therefore, it represents merely a rapid and short-term ^{14}C fluctuation that is not yet visible in the record of GeoB 20933-1.

Considering only the criterion of chronological consistency, the core GeoB 14905-2 from Mauritania (figure 7.2a) and GeoB 20933-1 from Angola (figure 7.2b) both demonstrate a consistent chronological sequence of ^{230}Th/U ages within the depth profile. Under the current resolution, the data from GeoB 14905-2 and GeoB 20933-1 are therefore considered as reliable.

GeoB 20960-1 demonstrates chronological consistency between 100-300 cm, and 580-800 cm core depth. Between 300-580 cm core depth, both ^{230}Th/U age-depth inversions and ^{14}C age-depth inversions are evident. Therefore, the documented ^{230}Th/U age-depth inversions are attributed to reef formation or external influences (chapter 6). ^{14}C age-depth inversions may have been superimposed by variations in the ^{14}C content of the surrounding water. To date, no ^{14}C ventilation anomalies and associated ^{230}Th/U age anomalies have been confirmed for the Angola site (chapter 6). Consequently, in conjunction with the regional consistency criterion, it can be concluded that there is no compelling evidence for modified ^{230}Th/U ages. All presented ages are considered to be reliable.

7.4.2. The Atmospheric ^{14}C Influence

This section discusses the atmospheric contribution to the oceanic Δ^{14}C signal in the time range 40-30 ka, as well as the uncertainty due to the atmospheric reconstruction of ^{14}C (IntCal20 and SHCal20, (Hogg et al., 2020; Reimer et al., 2020)). SHCal20 has an average offset from IntCal20 of 36 ± 27 ^{14}C years (Hogg et al., 2020) and was constructed from the IntCal20 and Southern Hemisphere ^{14}C records using a statistical model of the north-south atmospheric radiocarbon offset (Hogg et al., 2020). Since the differences between IntCal20 and SHCal20 are small between 38-30 ka (figure 7.1), the discussion of the fundamental uncertainties of IntCal20 can be applied to SHCal20.

The atmospheric ^{14}C reference (IntCal20 for the Northern Hemisphere (Reimer et al., 2020) and SHCal20 for the Southern Hemisphere (Hogg et al., 2020)) has been reconstructed from a variety of archives, including tree rings, lacustrine and marine sediments, speleothems, and tropical corals (Reimer et al., 2020). The preferred archive for reconstructing atmospheric ^{14}C is tree rings, which not only provide a direct record of the ^{14}C content in the atmosphere but can also be precisely dated (e.g. Muscheler et al., 2020). Up until 13.9 ka BP, IntCal20 was reconstructed exclusively using tree rings (Reimer et al., 2020). Atmospheric ^{14}C reconstruction beyond that time employed a combination of the aforementioned archives (Reimer et al., 2020).

It is important to note that IntCal offers point-wise estimates of past ^{14}C levels, which

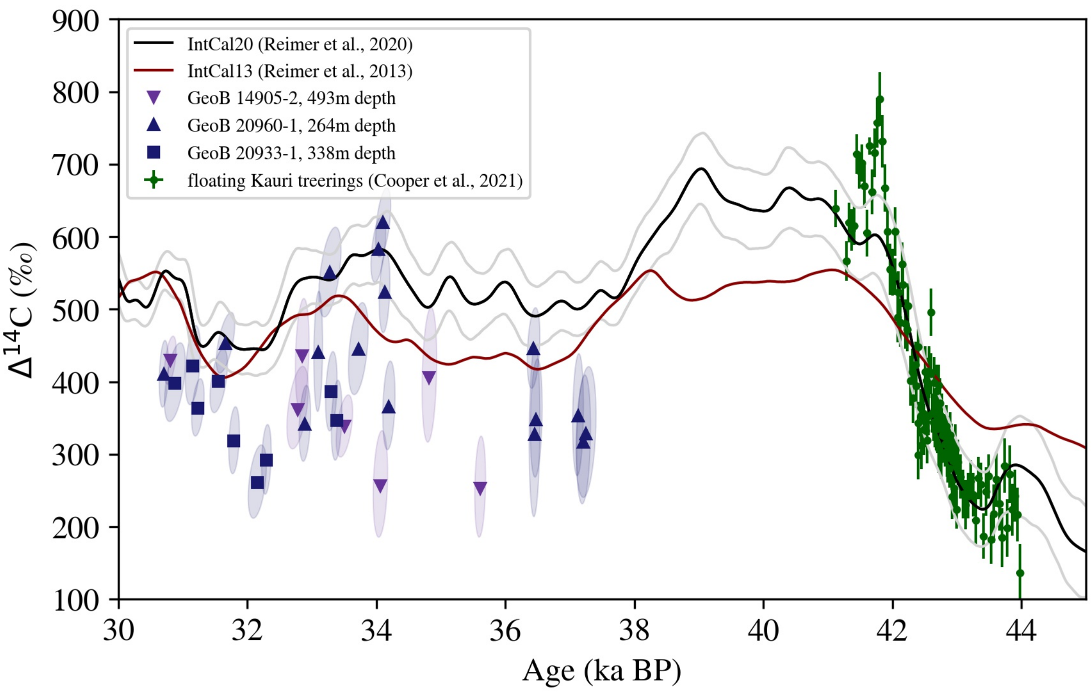

Figure 7.3.: Atmospheric $\Delta^{14}C$ comparison between IntCal20 with 2σ uncertainty (grey lines) (Reimer et al., 2020), IntCal13 (Reimer et al., 2013), and a new floating Kauri treering record from New Zealand (Cooper et al., 2021), as well as CWC data from Mauritania and Angola (this study and Beisel et al. (2023)).

may not reflect short-term atmospheric variation (Muscheler et al., 2020). This is of particular relevance during glacial periods (Muscheler et al., 2020). The lower data density on which IntCal20 is based, as well as the increased measurement uncertainty, increase the risk of increased smoothness of the atmospheric $\Delta^{14}C$ reconstruction (Muscheler et al., 2020). For example, between 42 and 33 ka, there is a notable discrepancy of up to 100 ‰ between IntCal20 and the previous version, IntCal13 (Reimer et al. (2020, 2013), figure 7.3). It is hypothesized that one or more geomagnetic field excursions occurred between 36-30 ka (e.g. Cassata et al., 2008; Channell, 2006; Kissel et al., 2011; Korte et al., 2019; Laj et al., 2014). A prominent example and very well-known field excursion took place around 42 ka, the Laschamp event (e.g. Channell et al., 2020; Laj et al., 2014; Nowaczyk et al., 2012). It was assumed that there was an increase in $\Delta^{14}C$ from 200 ‰ to 600 ‰, as demonstrated by IntCal20 (Reimer et al., 2020). However, a recent study on floating Kauri treerings estimates this value to be up to 800 ‰ (Cooper et al., 2021), up to ~200 ‰ larger than previously thought (figure 7.3). As demonstrated for the Laschamp event, low data density may result in underestimated $\Delta^{14}C$ values, particularly during periods of geomagnetic field excursions. This exemplifies the impact that the incorporation of additional data sets, and the implementation of enhanced methodologies can have on IntCal. For instance, rapid fluctuations or oceanic $\Delta^{14}C$ values identical to the current atmospheric curve could be misinterpreted if IntCal20 is not sufficiently resolved in the respective time period. Observed $\Delta^{14}C$ values off Angola, which are identical to the atmospheric $\Delta^{14}C$ reconstruction at 34 ka, 33.3 ka, and 31.6 ka could therefore indicate that the IntCal curve has been underestimated. Consequently, it must be carefully investigated whether rapid fluctuations are the consequence of ocean-related processes, or the result of an overly smooth atmospheric reference curve.

In addition to $\Delta^{14}C$, such events are also visible in other records of cosmogenic radionuclides, such as ^{10}Be and ^{36}Cl reconstructed from ice cores (e.g. Adolphi et al., 2018). These records are constrained only by the sampling method, as the individual ice-layers are merely "thinned out" over time by the pressure of the newly formed ice on top, while part flows off to the side. However, they can be distorted by a bias caused by atmospheric circulation and deposition (e.g. Adolphi et al., 2023; Elsässer et al., 2015; Muscheler et al., 2020). Identifying this bias and its extent is not always straightforward (e.g. Adolphi et al., 2023; Muscheler et al., 2020). For instance, the polar bias can result in a dampening of the signal intensity by 23 % to 37 % (Adolphi et al., 2023). Moreover, there persists a considerable discrepancy between the $\Delta^{14}C$ reconstruction by archives (IntCal) and a $\Delta^{14}C$ calculation with ^{10}Be and ^{36}Cl, after the production rate has been reconstructed and the carbon cycle incorporated (e.g. Dinauer et al., 2020; Köhler et al., 2022).

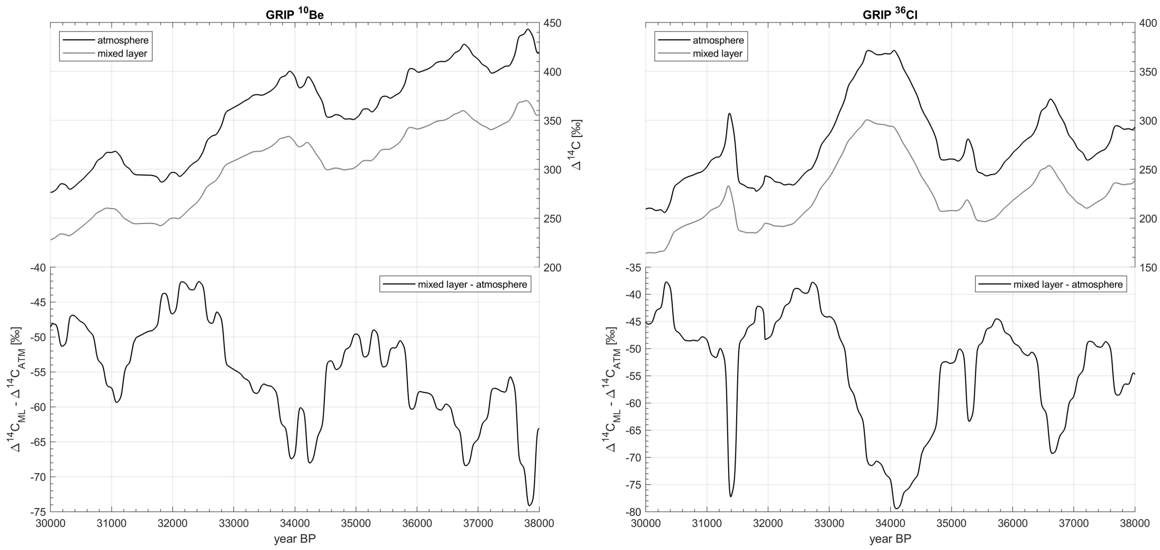

Figure 7.4.: *Courtesy of Dr. Florian Adolphi.* Based on ^{10}Be and ^{36}Cl, the production rate was estimated and the $\Delta^{14}C$ values of the atmosphere and the mixed layer of the ocean were estimated using a carbon cycle model. ^{10}Be and ^{36}Cl data presented in Adolphi et al. (2018) and references therein. The resolution is about 50 years for ^{10}Be and 200 years for ^{36}Cl. The lower figure shows the difference between the mixed layer and the atmosphere.

Reconstructions of the geomagnetic field strength demonstrate a peak around 34 ka towards lower values, indicating a weak geomagnetic field (Adolphi et al., 2018; Laj et al., 2014; Nowaczyk et al., 2012). This would result in an increased production rate of radionuclides, such as ^{14}C. Figure 7.4 shows the modeled $\Delta^{14}C$ content of the atmosphere and the mixed layer of the ocean, derived from ^{10}Be and ^{36}Cl data (courtesy of Dr. Florian Adolphi). Accordingly, the $\Delta^{14}C$ content in the atmosphere increases by 50-100 ‰. Due to the delayed transmission of the atmospheric $\Delta^{14}C$ signal into the ocean, the rapid increase in the production rate would initially manifest itself in an increase in reservoir ages (Butzin et al. (2017), lower panels in figure 7.4), as these are always considered relative to the atmosphere. This is followed by a decline in reservoir ages over approximately 1000 a until the previous level is reached again.

Variations in $\Delta^{14}C_{ocean}$, especially at 200 m paleodepth such as off Angola, between 38-30 ka could have been caused by geomagnetic excursions, depending on the magnitude and timing. In this context, it is important to note the smoothed and damped response of the ocean caused by the rate of gas exchange between the ocean and the atmosphere, and mixing with deeper, older water (Bard and Heaton, 2021), resulting in smoothing and phase-shifting of the $\Delta^{14}C$ signal (Heaton et al. (2023) and references therein).

The Mono Lake/Auckland excursion is hypothesized to have occurred around 34 ka (Laj et al., 2014). However, the rapid decline of B_{atm} ages off Angola between 34.2-34 ka would be too fast to have been solely influenced by the atmosphere. This magnitude could only be achieved by a subsequent rapid decline in production rates and thus $\Delta^{14}C$. However, this seems very unlikely given the resolution of the ^{10}Be and ^{36}Cl data (pers. comm. Dr. Florian Adolphi). Therefore, involvement of another component, such as gas exchange or mixing/upwelling, is necessary for the Angola record.

On the other hand, Mauritania CWCs record an increase in B_{atm} ages at 34 ka with a following decline in B_{atm} ages over 600 a. This decline is equivalent to a change in $\Delta^{14}C$ of approximately 50 ‰, and therefore consistent with an increase in reservoir ages through a rapid increase in the ^{14}C production rate.

In conclusion, the observed $\Delta^{14}C$ values, which are identical to the atmospheric $\Delta^{14}C$ reconstruction in the thermocline off Angola at 34 ka, 33.3 ka, and 31.6 ka, indicate that the IntCal curve has been underestimated. The rapid fluctuation in the thermocline off Angola are likely superimposed by atmospheric ^{14}C fluctuations, yet an oceanic component remains a necessary factor. The decline in reservoir ages off Mauritania between 34.1-33.5 ka reflects the incorporation of ^{14}C production rate changes due to the Mono Lake/Auckland excursion.

7.4.3. Ventilation and Temperature of the East Atlantic Thermocline During the Last Glacial

Core GeoB 20960-1 was collected at water depth of 264 m off Angola. During the Last Glacial Maximum (LGM), the sea level was approximately 120–130 meters lower than it is today (Lambeck et al., 2014), therefore core GeoB 20960-1 was located at an approximate paleo water depth of only 134 - 144 m. This shoaling could imply a greater influence of the atmosphere compared to the recently investigated corals at slightly greater paleo depth (chapter 5). During the LGM, the CWCs from the thermocline off Angola exhibit a homogeneous mean B_{atm} age of 970 ± 260 a, with partially high variability (chapter 5, light blue shading in figure 7.5d), which is corroborated by the new observations from shallower depth with B_{atm} ages of 970 ± 170 years at 26.2 ka and 780 ± 230 years at 28.7 ka (figure 7.1, 7.5). This finding supports the assumption of a homogeneously aged water throughout the entire upper thermocline and the surface water of the South Atlantic (Beisel et al., 2023; Skinner et al., 2023). Between 32-30 ka, the data corroborate the findings of Beisel et al. (2023) (chapter 5), regarding a well-ventilated thermocline off Angola.

Between 38-30 ka, the uncertainties of $\Delta^{14}C$ and B_{atm} age increase due to increased ^{14}C measurement uncertainties. During this period, the relative sea level is assumed to be 60 to 70 meters lower than today (Lambeck et al., 2014). Therefore, the paleo-depth of GeoB 20960-1 was approximately at 200 m, whereas that of GeoB 20933-1 was approximately 280 m. Hence, both were located within the upper thermocline. In general, the ^{14}C content of the thermocline off Angola in the period 38-30 ka varies between glacial conditions, comparable to the ^{14}C content of the LGM, and punctual close to the atmospheric reconstruction (figure 7.5d, SHCal20, Hogg et al. (2020)).

With two documented exceptions (34.8 ka and 35.6 ka), the growth of Mauritanian corals occurred at the same time as that of Angolan corals (figure 7.5d). At 34 ka, there is a more pronounced decline in the ^{14}C content off Mauritania, up to 1800 ± 490 a B_{atm} age, indicative of the incorporation of an atmospheric ^{14}C signal (chapter 7.4.2, figure 7.5d). At times 33.5 ka, 32.9 ka and 30.8 ka, identical ^{14}C signals were recorded within the error margins between Mauritania and Angola. This indicates a similar water mass influence and is consistent with previous observations that showed matching B_{atm} ages between Mauritania and Angola at the beginning of the LGM (chapter 5). The presence of different B_{atm} age signals between Mauritania and Angola indicates of frontal shifts, as the corals of Mauritania which are close to the CVFZ, are strongly influenced by frontal movements (chapter 5).

The period between 38-30 ka is one with many climatic upheavals, such as D/O and AIM events. The triggers of these events are still under discussion (e.g. Li and Born,

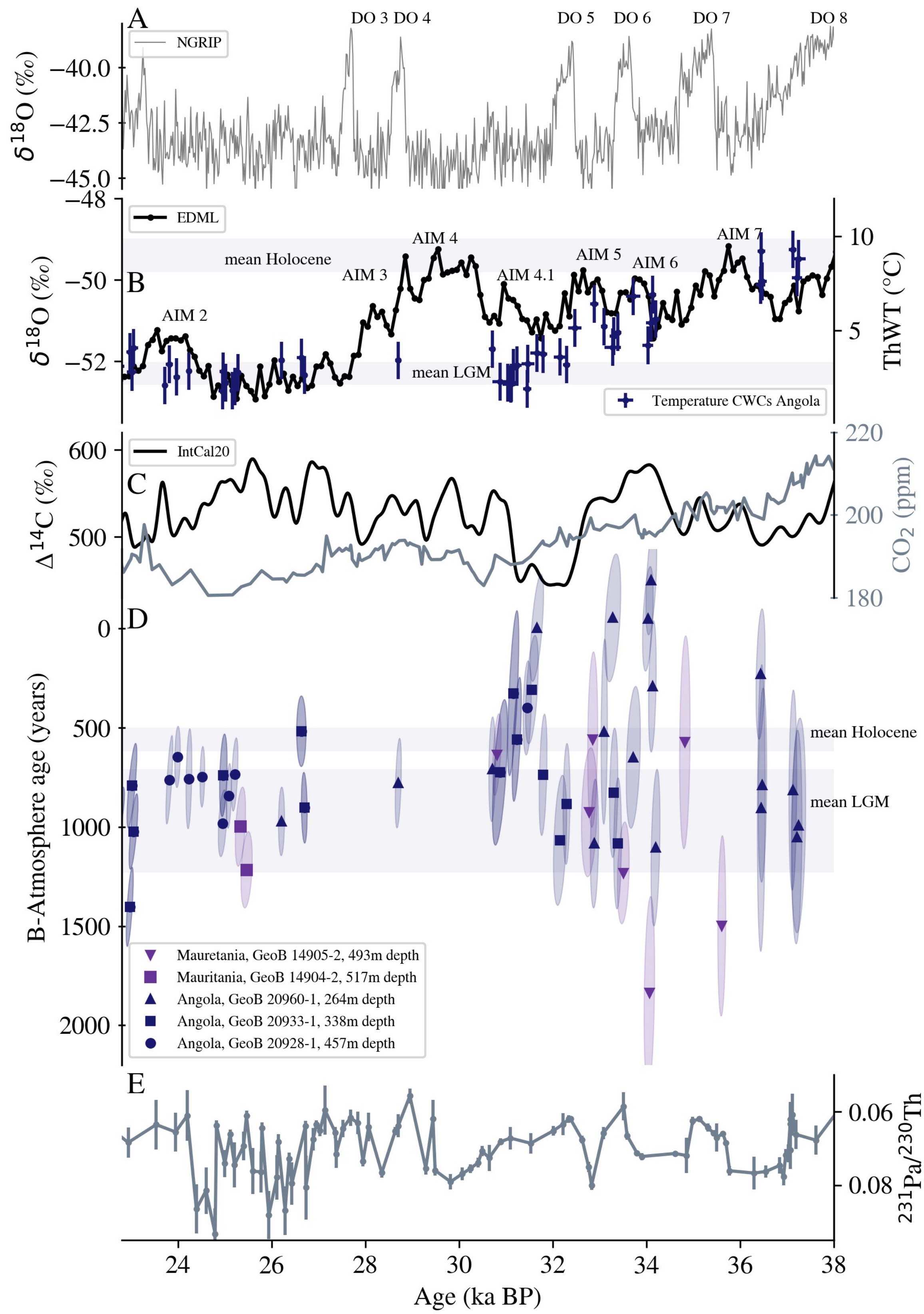
A
NGRIP
DO 3 DO 4
DO 5
DO 6
DO 7
DO 8
δ^{18}O (‰)
−40.0
−42.5
−45.0
−48
B
EDML
mean Holocene
AIM 2
AIM 3
AIM 4
AIM 4.1
AIM 5
AIM 6
AIM 7
mean LGM
Temperature CWCs Angola
δ^{18}O (‰)
−50
−52
ThWT (°C)
10
5
C
IntCal20
Δ^{14}C (‰)
600
500
CO_2 (ppm)
220
200
180
D
B-Atmosphere age (years)
0
500
1000
1500
2000
mean Holocene
mean LGM
Mauretania, GeoB 14905-2, 493m depth
Mauritania, GeoB 14904-2, 517m depth
Angola, GeoB 20960-1, 264m depth
Angola, GeoB 20933-1, 338m depth
Angola, GeoB 20928-1, 457m depth
E
^{231}Pa/^{230}Th
0.06
0.08
24
26
28
30
32
34
36
38
Age (ka BP)

Figure 7.5.

Figure 7.5.: Climate and radiocarbon age variability between 38-30 ka. (A) $\delta^{18}O$ record from NGRIP, Greenland (Bazin et al., 2013). (B) $\delta^{18}O$ record from EDML, Antarctica (EPICA, 2006), together with the reconstructed temperature from Angola CWCs (blue data points, Lausecker (2021); Roesch (2017); Schreiber (2023) and this study). Shaded area marks the mean temperature in the LGM (2.7 ± 0.6°C) and the Holocene (9 ± 0.9 °C) (Lausecker, 2021; Roesch, 2017; Schreiber, 2023). (C) Reconstructed $\Delta^{14}C$ record (IntCal20, Reimer et al. (2020) and CO_2 compilation record (Bereiter et al., 2015). (D) B-Atmosphere age record from Mauritania and Angola (Beisel et al. (2023) and this study). (E) $^{231}Pa/^{230}Th$ records of sediments from the Bermuda rise (Böhm et al., 2015; Henry et al., 2016; Lippold et al., 2019; McManus et al., 2004).

2019; Malmierca-Vallet et al., 2023; Menviel et al., 2020). With respect to ^{14}C in the ocean, these events are not well resolved nor understood. In the Southern Ocean, only two previously published measurements fall within the AIM6 time frame (Hines et al., 2015). They show a B_{atm} age variability of 160-1300 a at 33.7 ± 0.1 ka at 1700 m depth, but with a very large measurement uncertainty of ~500 a (Hines et al., 2015). Within the available data and their uncertainties, no correlation can be established between changes in the ^{14}C content of the thermocline off Angola and the general occurrence of AIM or D/O events (figure 7.5).

Variations between glacial and interglacial conditions are also reflected in the ThWT range, which lies between 2°-9°C (figure 7.5b). Consequently, the ThWT range falls between the mean glacial ThWT of the LGM (2.7 ± 0.6°C) and the mean ThWT of the Holocene (9 ± 0.9°C) (Lausecker, 2021; Roesch, 2017; Schreiber, 2023). Furthermore, it was below the modern water temperature of 13.5°-9°C (Hebbeln et al., 2020). There is no discernible correlation between B_{atm} age and the temperature in general (figure 7.6), which implies a decoupling of thermal and radiocarbon ventilation age structure.

Nevertheless, the cross-plot between B_{atm} age and ThWT from Angola (figure 7.6), and respective box-plot (figure 7.7), clearly demonstrate the transition between warm and cold thermocline water. Warm and in terms of ^{14}C relatively stable thermocline water was present between 37.2-36.4 ka (figure 7.6 and 7.7). This changed between 34.2-32 ka, where strong varations in both the ThWT and B_{atm} ages are present. Here, the ThWT fluctuations off Angola follow the temperature fluctuations of AIM6 and AIM5 (figure 7.5b, EPICA (2006)). Subsequently, since 32 ka, the situation has stabilized at cold ThWT levels characteristic of a glacial period, and less B_{atm} age varations (figure 7.6, 7.7).

A strong correlation between Southern Ocean sea surface temperatures and AIM events was found by Anderson et al. (2021). Fluctuations consistent with AIM6 and AIM5 can be observed in the thermocline off Angola (34.2-32 ka, marked red in figure 7.6), but not with AIM4.1 and AIM2 (figure 7.5b, this study and Lausecker (2021);

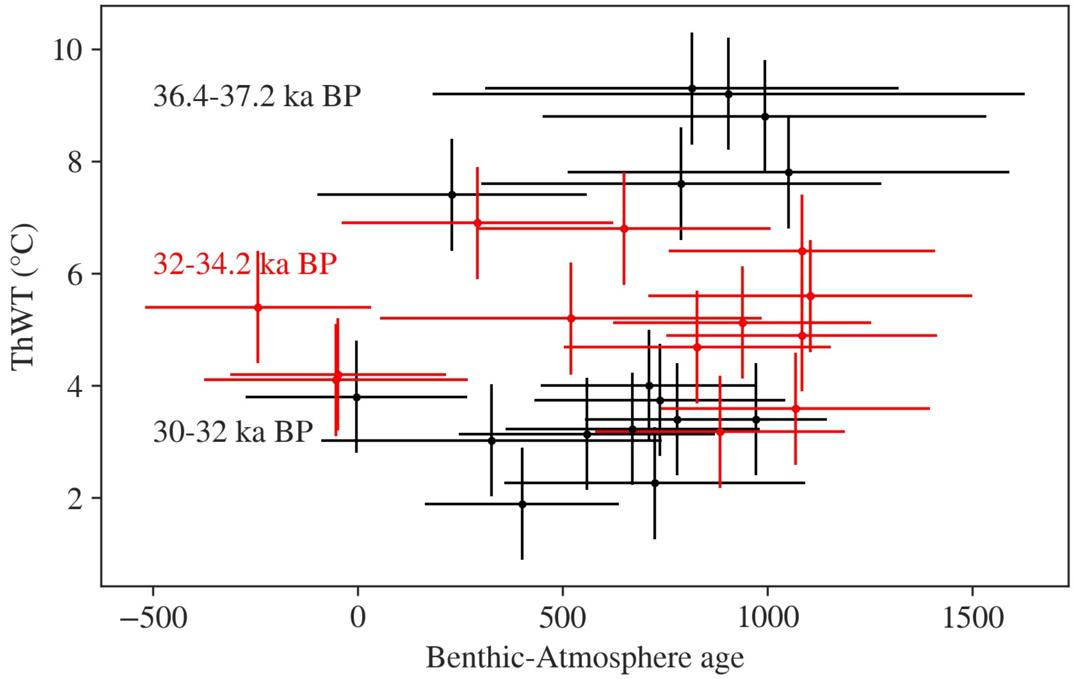

Figure 7.6.: Cross-plot B_{atm} age against temperature from Angola between 38-30 ka (this study, Beisel et al. (2023), Lausecker (2021); Roesch (2017); Schreiber (2023). Between 34.2-32 ka there was a close coupling between ThWT off Angola and AIM events.

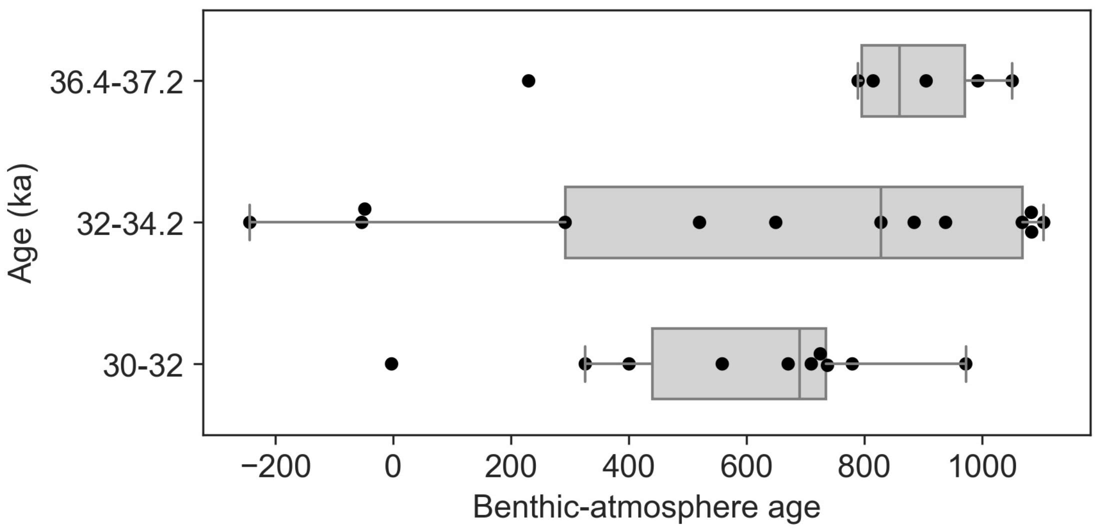

Figure 7.7.: Box-plots for B_{atm} between 38-30 ka (this study and Beisel et al. (2023)). A transitional period with high variability between 34.2-32 ka is evident.

Roesch (2017); Schreiber (2023)). Even if the ^{14}C ventilation ages are not significantly different for the most part due to measurement uncertainty, the thermocline off Angola seems to have behaved differently after AIM5. Instead of following the temperature fluctuation of the Southern Hemisphere, it remains at a cold, glacial temperature of approximately 3°C. No shifts in the ABF are known to have affected Angolan corals between 38-30 ka (Little et al., 1997). Therefore, there is no indication to suggest that the observed fluctuations are the result of differing water mass influences induced by local frontal shifts. The close coupling between the ThWT off Angola and the temperature fluctuations of AIM6 and AIM5 suggests a close coupling to processes in the Southern Hemisphere. Therefore, the ^{14}C ventilation signal off Angola reflects ventilation processes in the Southern Hemisphere and their fluctuations during AIM6 and AIM5. However, the ^{14}C signal is likely superimposed by atmospheric ^{14}C variations that are not yet reflected in IntCal20 (chapter 7.4.2), which makes it more difficult to estimate the magnitude of the oceanic ^{14}C signal without.

The decoupling between the Southern Hemisphere temperature fluctuations and ThWT off Angola between AIM5 and AIM4.1 indicates a shift in water mass provenance. While the ThWT fluctuations off Angola were closely linked to the temperature changes of the Southern Hemisphere, this changed around 32 ka. Persistent cold ThWT off Angola around 3°C and increasing B_{atm} ages indicate a shoaled thermocline.

The expansion of the Antarctic ice sheet led to a weakening of Antarctic Bottom Water production (Chadwick et al., 2022; Menviel et al., 2017; Shulmeister et al., 2019). In conjunction with an equatorward shift of the Southern Hemisphere westerly winds at 32 ka, which resulted in the weakening of the Antarctic Circumpolar Current, this enabled the advection of Glacial Pacific Deep Water (GPDW) into the South Atlantic (Venugopal et al., 2023; Yu et al., 2020). From thereon, the ThWT off Angola remained cold at approximately 3°C. This cold water has an initial radiocarbon signature close to the atmosphere, which then gradually decreased until glacial levels were achieved (figure 7.5, Beisel et al. (2023) and this study). At the same time, atmospheric CO_2 levels are declining (figure 7.5, Bereiter et al. (2015)). Thus, the shoaling of the thermocline, visible in increasing B_{atm} ages and cold ThWT, initiated increased carbon storage. Consequently, the close coupling observed in the LGM between the thermocline and intermediate water of the South Atlantic and the Southern Ocean, as observed in chapter 5 (Beisel et al., 2023), developed around 32 ka.

7.5. Summary and Conclusions

Combined ^{230}Th/U, ^{14}C and Li/Mg measurements allow a thorough investigation of the ^{14}C ventilation age and ThWT off Angola through time. In this study, the period between 38-30 ka was examined to determine when the close connection between the waters of the South Atlantic and the Southern Hemisphere was established.

The application of the new criteria for data selection, regional and chronological consistency, confirm the accuracy of the ^{14}C ventilation age reconstructions off Angola and one specific sediment core from Mauritania.

Oceanic ^{14}C values identical to those of the reconstructed atmosphere are indicative of an underestimated atmospheric reference curve, a consequence of the lower data density and greater smoothness of the atmospheric reconstruction. Moreover, geomagnetic field excursions lead to rapid changes in the ^{14}C production rate due to a weakening of the Earth's magnetic field. Notwithstanding the smoothed and damped response of the ocean to atmospheric changes, such events are also clearly reflected in the ocean's ^{14}C signature, as demonstrated by Mauritanian CWCs. However, the variations in the ^{14}C ventilation age off Angola cannot be attributed solely to changes in the ^{14}C production rate.

With the current data resolution and ^{14}C calibration curve, there is no correlation between the occurrence of AIM events and changes in B_{atm} age. Furthermore, the thermal and radiocarbon ventilation age structure are decoupled.

Temperature variations of the thermocline off Angola correlate with AIM6 and AIM5, but not with AIM4.1 and AIM2. The decoupling between temperature fluctuations of the Southern Hemisphere and the ThWT off Angola between AIM5 and AIM4.1 indicates the initiation of a shoaled thermocline.

At 32 ka, waters off Angola remained cold, with a glacial ThWT of 3°C, but well-equilibrated with the atmosphere. The following increase in ^{14}C ventilation ages while ThWT remained cold reflects an isolation, which enabled enhanced carbon storage during the LGM. Hence, the close coupling between the thermocline and intermediate water of the South Atlantic and Southern Ocean observed in chapter 5 (Beisel et al., 2023), developed around 32 ka.

8. Summary and Outlook

This thesis investigated the Eastern Atlantic thermocline ^{14}C ventilation age variability over the last 38,000 years through combined $^{230}Th/U$ and ^{14}C dating of cold-water corals (CWC). The aragonite skeleton of CWCs captures trace elements from the ocean, which enables, among other things, an absolute age determination by $^{230}Th/U$ dating. In conjunction with their global distribution over time, they represent an optimal archive for the reconstruction of past ocean processes. The combination of $^{230}Th/U$ and ^{14}C dating allows for the reconstruction of ^{14}C ventilation ages over time, thereby providing an excellent means of investigating past ocean circulation and carbon cycle interactions.

The evaluation of quality control parameters at the Heidelberg Radiocarbon Laboratory has demonstrated optimal conditions for precise ^{14}C measurements. The updated long-term blank value is (0.190 ± 0.064) pMC (n=138). The International Atomic Energy Agency (IAEA)-C2 Standard (41.14 ± 0.03 pMC, (Rozanski et al., 1992)) is excellently reproduced, with a value of (41.15 ± 0.16) pMC (n=75). Moreover, 33 CWC measurements have been duplicated. All agree within 2σ, 85% even in the 1σ range. This reflects slightly overestimated uncertainties of the ^{14}C ages reported by the AMS laboratory in Mannheim. Consistent high quality of ^{14}C measurements is testified, which is ensured by ongoing quality controls. This guarantees optimal conditions for the determination of ^{14}C in CWCs.

Radiocarbon Ventilation Anomalies in CWCs

Over the past two decades, apparent ^{14}C ventilation anomalies, i.e. unusual large ^{14}C ventilation ages of several thousands of years, or marine ^{14}C values larger than the ambient atmosphere, have been reported in certain locations. The interpretation of such anomalous values remains challenging. They do not align with the prevailing framework of oceanic ^{14}C ventilation over time, and subsequent studies have been unable to corroborate these observations. While the underlying mechanisms of ^{14}C ventilation anomalies reconstructed from foraminifera have been widely studied, the underlying causes of ventilation anomalies in CWCs remain unknown. To this end, coral-bearing sediment cores from the Gulf of Cádiz and Mauritania have been investigated, and anomalous ^{14}C ventilation values from the literature have been compiled.

The underlying cause behind these anomalies is not the carbon content itself. The strong correlation between $^{230}Th/U$ age-depth inversions in coral-bearing sediment cores and ventilation anomalies argues for a modification of the $^{230}Th/U$ age in the order of a few hundred to thousands of years. Such a behavior contrasts the overall excellent agreement of the $^{230}Th/U$ data with the theoretical evolution in a closed system.

At least two processes must be responsible for this behavior: (i) addition of uranium, shifting the $^{230}Th/U$ ages towards younger ages, resulting in ^{14}C ventilation anomalies and (ii) removal of uranium, shifting the $^{230}Th/U$ ages towards older ages, resulting in marine ^{14}C values above the atmospheric reference. Possible reasons behind these $^{230}Th/U$ modifications remain elusive, as they yield results consistent with the theoretical development.

These observations are strictly geographically and temporally constrained, with occurrences possibly linked to fluid venting. The impact is not widespread; rather, it is limited to specific regions, including the Gulf of Cádiz, Mauritania, and Brazil. Within these locations, most but not all sediment cores are affected. This implies the presence of a local influence that has resulted in modifications of the $^{230}Th/U$ ages of the CWCs. Local alterations to the chemistry of sea water and/or pore water, resulting from fluid venting activity, may have influenced the CWC skeletons. The observed variations in $^{230}Th/U$ ages may be attributed to changes in the aragonite lattice that could favor alpha-recoil diffusion, or secondary aragonite within the coral skeletons. As a 1000 year long continous precipitaion of secondary aragonite would rejuvinate the age by 7 % (Lazar et al., 2004), this could easily explain the observed $^{230}Th/U$ age modifications in the order of hundreds to thousands of years. Therefore, it is likely that secondary aragonite plays an important role in certain locations affected by fluid venting.

Consequently, at these locations, additional criteria are required to validate ^{14}C ventilation ages until the origins of altered $^{230}Th/U$ ages are fully explored. These include (i) regional ^{14}C ventilation age consistency and, in the case of analyzed sediment cores, (ii) consistent chronology of the $^{230}Th/U$ age-depth profile. Both are extremely effective in identifying affected samples.

As the majority of CWC study areas is not affected by modified $^{230}Th/U$ ages, this has no impact on the general reconstruction of ^{14}C ventilation ages through time.

Radiocarbon in Cold-Water Corals of the Eastern Atlantic Thermocline Over the Last 38,000 Years

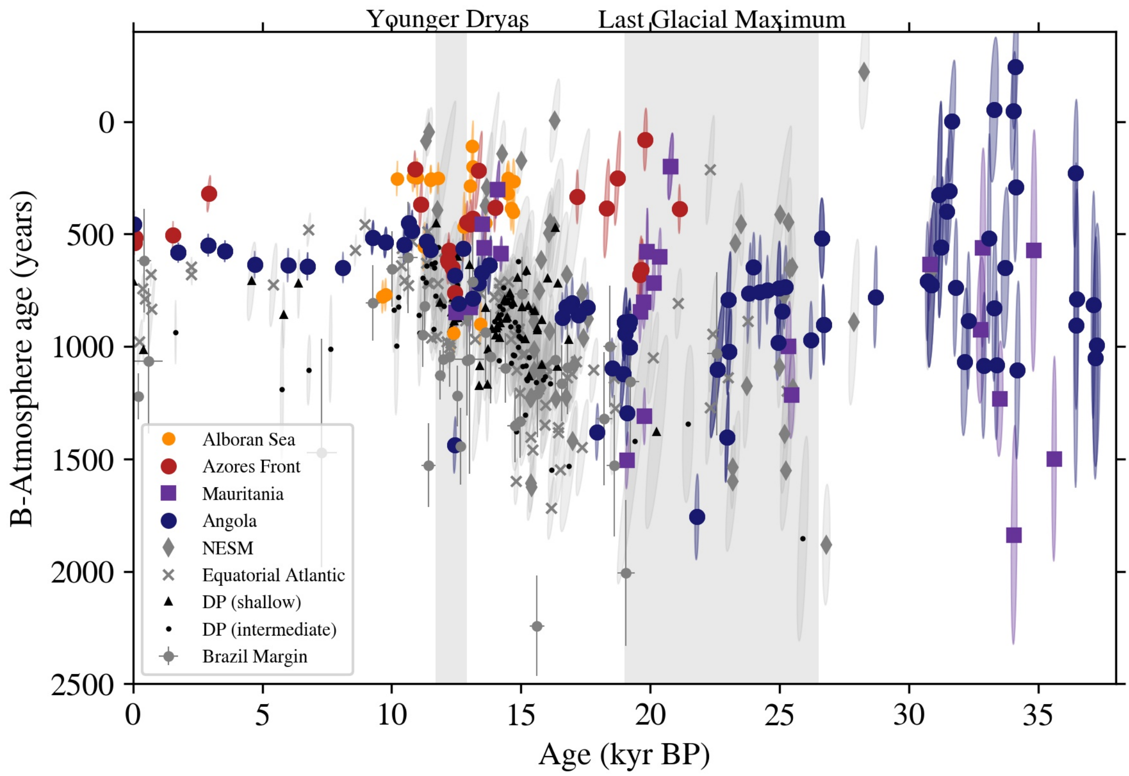

Figure 8.1.: Selected ^{14}C ventilation ages obtained from CWCs (~200-2000 m depth) and foraminifera (~1000-2500 m depth) in the Atlantic and Mediterranean Sea. CWC data shown with 2σ error ellipses, foraminifera data with 1σ error bars. Colored symbols: CWC data in 260-1000 m depth, discussed in this thesis (n=150), including Beisel et al. (2023). Not shown are new CWC data from the GoC (n=42) and Mauritania (n=35) from chapter 6. NESM: New England Seamount: (Adkins et al., 1998; Eltgroth et al., 2006; Hines et al., 2019; Robinson et al., 2006; Thiagarajan et al., 2014). Equatorial Atlantic: (Chen et al., 2015, 2020). DP: Drake Passage (Burke and Robinson, 2012; Chen et al., 2015; Li et al., 2020). Brazil Margin (foraminifera): Skinner et al. (2021).

Within this thesis, CWCs from the Alboran Sea (Mediterranean Sea), Azores, Great Meteor Seamount, Mauritania and Angola have been investigated over the last 32,000 years, together with ^{14}C simulations carried out with an Large Scale Geostrophic (LSG) Ocean General Circulation Model provided by Dr. Martin Butzin. The results are published under Beisel et al. (2023) and are in perfect agreement with the interpolation of ^{14}C ventilation ages through time by Skinner and Bard (2022) and Skinner et al. (2023).

The ^{14}C ventilation age records indicate that the North and South Atlantic thermocline waters operated as separate carbon reservoirs during the Last Glacial Maximum (LGM) and subsequent deglaciation until the modern circulation was established during the

Younger Dryas (YD). Angola corals inferred a connection between the mid-depth equatorial Atlantic and Southern Ocean. Simultaneous shifts in ^{14}C ventilation ages highlight a strong glacial dynamic range and could indicate short periods of injection of aged deep water, enabled through a strengthened intermediate layer exchange between the Pacific, South Atlantic and Indian Ocean. The ^{14}C ventilation age patterns provide evidence for a ^{14}C drawdown during the LGM, consistent with Southern Hemisphere ^{14}C aging below the wind-driven surface ocean, as well as significant variability through presumed influence of underlying, less equilibrated water. Hence, the Angola thermocline apparently represents the young envelop of the strong age depth gradients present during the last glacial. The results of the LSG model are in close agreement with the data from the Angola record. During deglaciation, the upper Southern Atlantic thermocline likely contributed to the increase in atmospheric CO_2 through the transfer of respired carbon.

In contrast, at the end of the LGM, corals from the Azores, Great Meteor Seamount and Mauritania trace well-equilibrated thermocline waters near the Azores Front and Cap Verde Frontal Zone. The mean age of $\sim$500 years demonstrates strong surface to thermocline ocean connectivity, likely attributable to processes such as Ekman pumping and a shallow overturning. This feature of wind-driven subsurface circulation is not captured by the LSG model results. Mauritania CWCs reveal multiple displacements of the Cap Verde Frontal Zone (CVFZ), as they punctually match the southern ^{14}C signal (Angola).

During the Bolling-Allerod, a well-ventilated state of the North and South Atlantic thermocline waters can be observed, corroborating the hypothesis of enhanced ocean ventilation. After a five-century in-situ aging period, ventilation resumes in the middle of the YD until the modern state of radiocarbon ventilation is initiated by the end of the YD.

Lastly, an investigation of ^{14}C ventilation ages off Angola and Mauritania, and reconstruction of thermocline seawater temperatures (ThWT) off Angola between 38-30 ka aimed to determine, when the coupling between the thermocline and intermediate waters of the South Atlantic and Southern Ocean was initiated. During this time period, however, the increased uncertainty in the atmospheric ^{14}C reference must be evaluated.

The lower data density on which the atmospheric ^{14}C calibration curve, IntCal20, is based during the glacial, increases the risk of smoothness of the atmospheric ^{14}C reconstruction (Muscheler et al., 2020; Reimer et al., 2020). In particular, at times of increased ^{14}C production rates, caused by a weakening of the Earth's magnetic field, atmospheric ^{14}C levels may have been severely underestimated. In the ocean, these events appear smoothed and phase-shifted due to the rate of gas exchange and mixing with older, deeper water (Bard and Heaton, 2021; Heaton et al., 2023). CWCs off Mauritania record an increase in $\Delta^{14}C$ of approximately 50 ‰, that is consistent with a rapid increase in the ^{14}C production rate through the Mono Lake / Auckland excursion around 34 ka. Since ^{14}C ventilation ages are always considered relative to the atmosphere, ocean-related ^{14}C ventilation ages are therefore superimposed by atmospheric variations. Observed ^{14}C values in the thermocline off Angola, which are close to the atmospheric reconstruction, indicate underestimated atmospheric ^{14}C values.

During AIM6 and AIM5, the investigation of ThWT off Angola indicates a close correlation to Southern Hemisphere temperature fluctuations, analogous to the link between Southern Ocean sea surface temperatures and AIM events as proposed by Anderson et al. (2021). Around 32 ka, the tight coupling between ThWT and AIM variation ceased. Cold ThWT and increasing B_{atm} ages indicate a shoaled thermal thermocline, and the initiation of carbon storage. Consequently, the coupling between the thermocline and intermediate waters of the South Atlantic and Southern Ocean developed around 32 ka.

Outlook

Further investigation of the Atlantic thermocline would provide information on regional differences, the extent of the well-equilibrated North Atlantic thermocline water, as well as the possibility of an east-west ventilation gradient (Beisel et al., 2023; Skinner et al., 2021). Moreover, research into the period preceding the Last Glacial Maximum remains a crucial endeavor. Currently, knowledge about this period is severely limited. The occurrence of changes in the ^{14}C production rate and abrupt climatic events characterize this period. While Chapter 7 provided first insights, additional studies at all water depths are essential to gain a comprehensive understanding of ^{14}C ventilation ages and carbon storage over time.

Globally, the Indian Ocean is sparsely studied in terms of ^{14}C ventilation ages (e.g. Rafter et al., 2022; Skinner et al., 2023). A preliminary investigation of the Indian Ocean thermocline by Raddatz et al. (2023) indicated the presence of variable ventilation ages in the range of the South Atlantic and Southern Ocean signal (chapter 5). This variability may be linked to elevated CO_2 storage and abyssal upward mixing of ^{14}C-depleted carbon towards the Indian Ocean thermocline (Raddatz et al., 2023). Further studies are required to gain a deeper understanding of the Indian Ocean's role in the global carbon cycle to make more reliable statements of ^{14}C ventilation over time (e.g. Rafter et al., 2022; Skinner et al., 2023).

Since cold-water corals serve as a very valuable climate archive, it is of paramount importance to ascertain the underlying cause of modified ^{230}Th/U ages at certain locations. Further investigations are required to elucidate diagenetic processes and potential effects that could alter the uranium and/or thorium concentration in the coral skeletons over time. Sediment cores from the Gulf of Cádiz and Mauritania are optimal for investigating the underlying causes of modified ^{230}Th/U ages. Further studies of the water-sediment interfaces in fluid-venting active regions are required in order to ascertain the causes and likelihood of altered isotopic composition. Are Holocene CWCs in fluid-venting active regions affected by modified isotopic compositions? Dating via calibrated ^{14}C ages compared to ^{230}Th/U ages would provide valuable insights. What are the local differences between affected and unaffected sediment cores at these sites? What are the differences to sites such as Angola, which are clearly not impacted? In order to exploit new CWC study areas, such as the Indian Ocean, it is important to recognize the influencing factors at an early stage. Is it possible to find a parameter in the sediment that would allow us to identify altered sections in advance? Furthermore, more detailed analyses of coral skeletons are required. Robinson et al. (2006) examined fission track maps of *Desmophyllum dianthus*. Comprehensive uranium distribution analyses should be conducted on more corals, such as *D. pertusum* or *M. oculata*, which were primarily utilized in this thesis. Scanning electron microscope measurements may elucidate whether secondary aragonite or a higher degree of variable grain size, which favors alpha-recoil diffusion, are relevant factors.

So far, cold-water corals from Angola are most promising for further studies of ocean circulation and carbon cycling. The sediment cores examined generally show well-preserved specimens from all ice ages and interglacial periods. Further sampling could enable the completion of the record, as has already been demonstrated. For example, GeoB 20933-1 and GeoB 20928-1 complement each other perfectly in time. Further sampling of sediment cores from Angola could therefore enable the establishment of a complete regional calibration curve for the thermocline water off Angola, as well as an investigation into the effects of rapid climatic variations and changes in ^{14}C production rates.

To corroborate the rapid Δ^{14}C fluctuations in the thermocline off Angola, core GeoB 20960-1 should be resampled at a high resolution between 300-600 cm. The observed fluctuations in chapter 7 indicate substantial alterations in the ^{14}C content of the thermocline. Besides possible oceanic processes, they could verify assumptions about an underestimated atmospheric ^{14}C calibration curve. Evidence of rapid Δ^{14}C fluctuations and values consistent with the atmospheric reconstruction would have major implications for further research. This core provides plenty of coral material for further research purposes (see figure 3.1).

Appendix

A. List of Publications of the Author

Raddatz, J., **Beisel, E.**, Butzin, M., Schröder-Ritzrau, A., Betzler, C., Friedrich, R., and Frank, N. (2023). Variable ventilation ages in the equatorial Indian Ocean thermocline during the LGM. *Scientific Reports*, 13(1), 11355. `https://doi.org/10.1038/s41598-023-38388-z`

used in this thesis:
Beisel, E., Frank, N., Robinson, L. F., Lausecker, M., Friedrich, R., Therre, S., Schröder-Ritzrau, A., and Butzin, M. (2023). Climate induced thermocline aging and ventilation in the eastern Atlantic over the last 32.000 years. *Paleoceanography and Paleoclimatology*, e2023PA004662. `https://doi.org/10.1029/2023PA004662`

B. Supplementary Information

B.1. Supporting Information for Chapter 5

The following section provides supplementary figures for chapter 5. It is published under Beisel et al. (2023).

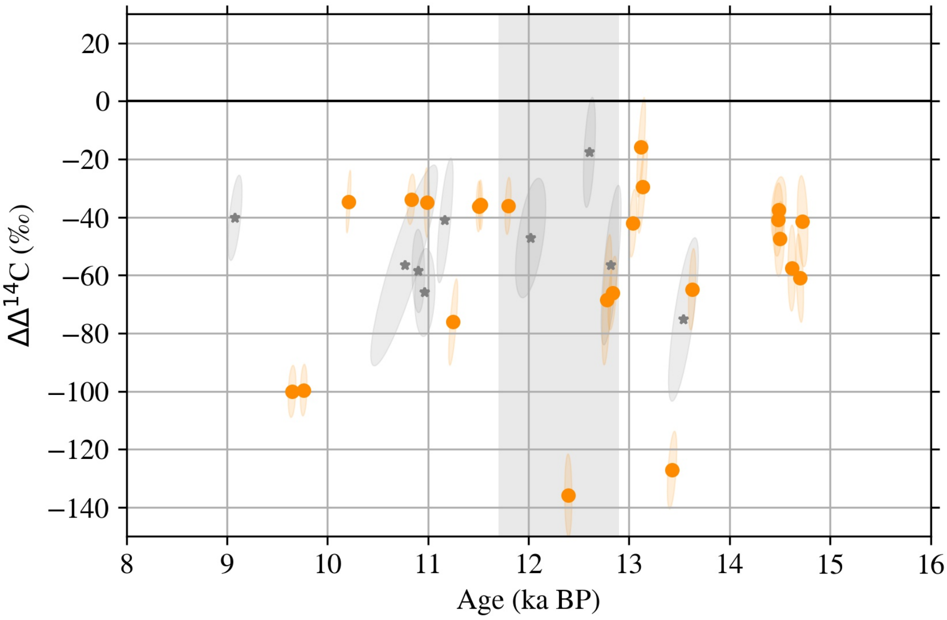

Figure B.1.: $\Delta\Delta^{14}$C evolution (Δ^{14}C offset) from the Alboran Sea (orange, this study) in 319 – 332 m depth. The Alboran Sea is not represented in the LSG ocean general circulation model, therefore no comparison can be shown. Grey dots represent previous results from the Alboran and Balearic Sea (McCulloch et al., 2010). One data point identical to the atmospheric reconstruction was excluded from the discussion.

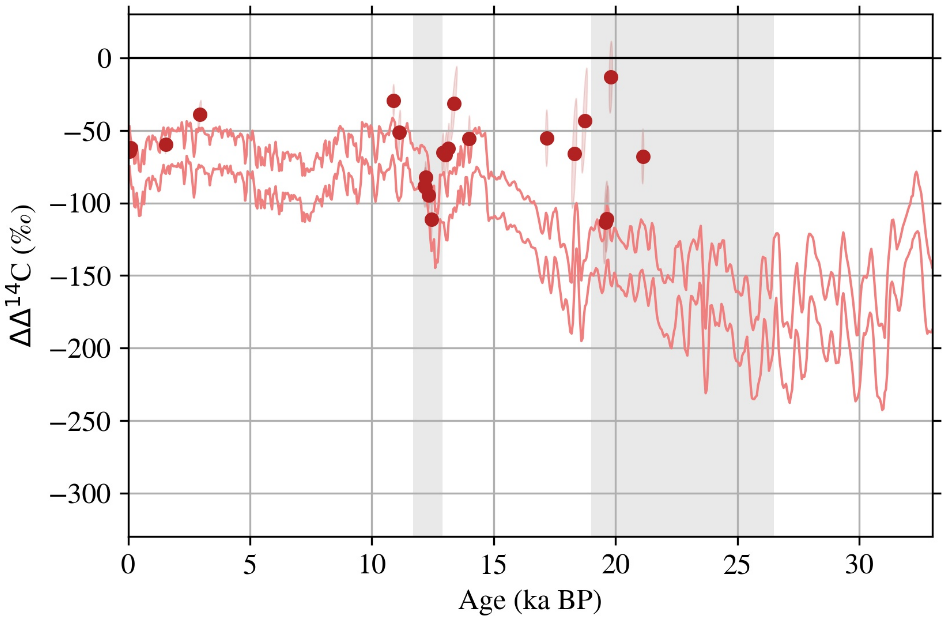

Figure B.2.: $\Delta\Delta^{14}C$ evolution ($\Delta^{14}C$ offset) in the Azores Front region in 560 – 970 m depth, including the LSG upper and lower bound of model prediction for the Azores (thin red lines). No depth dependence is evident in the data (see Supplementary Table). Since the onset of the YD, the model agrees well with the data. Earlier, the well-ventilated water mass, occurring during the LGM and subsequent deglaciation, is not represented by the LSG model.

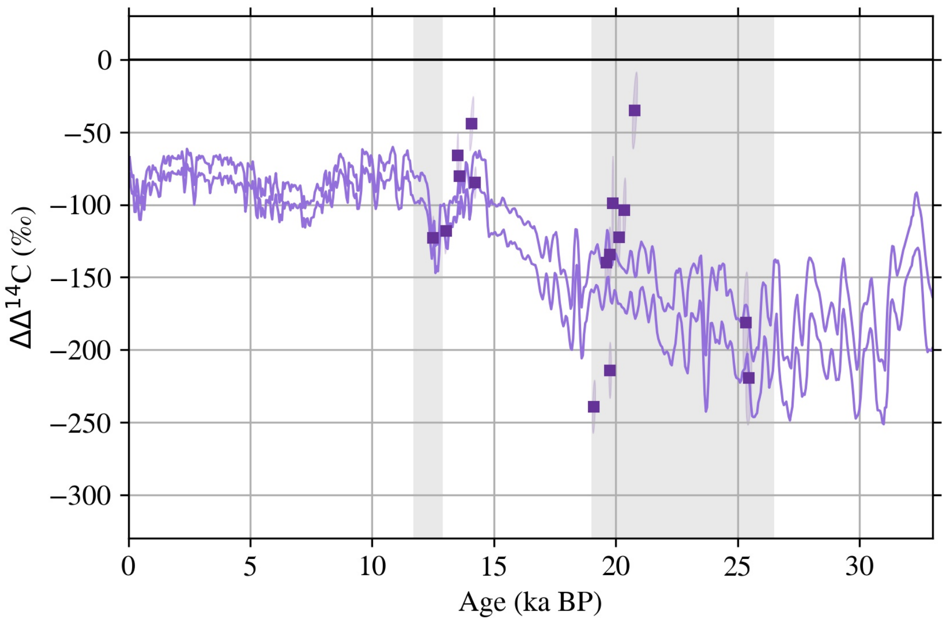

Figure B.3.: $\Delta\Delta^{14}C$ evolution ($\Delta^{14}C$ offset) off the coast of Mauritania in 485 – 580 m depth, including the LSG upper and lower bound of model prediction for Mauretania (thin grey lines). The LSG model agrees well within the southern-sourced water influence (for example section wise in the B/A, where Mauritania matches the results from Angola and equatorial Atlantic). Northern-sourced influence is not represented by the model. Note: excluded data not shown, see supplementary tables.

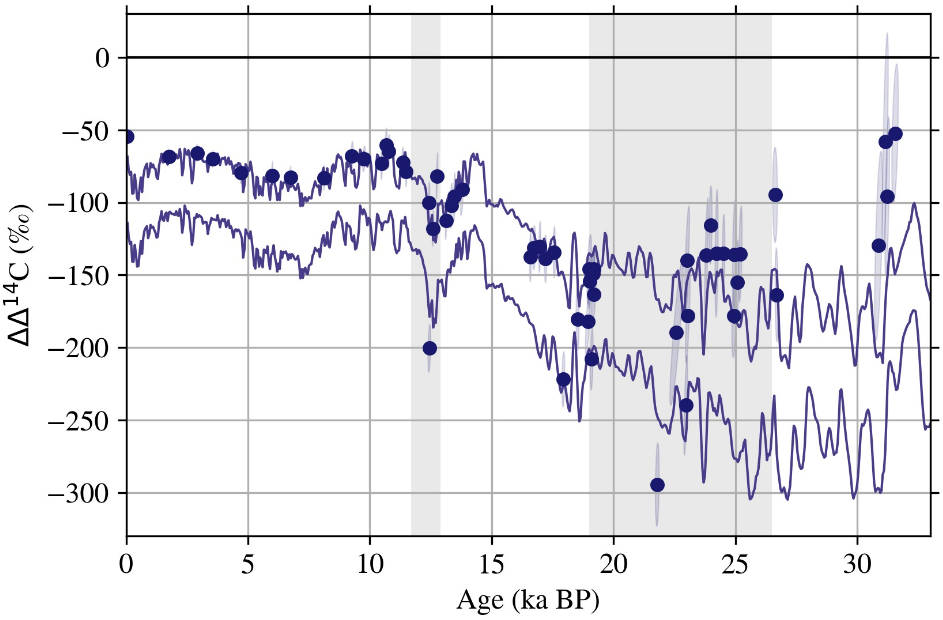

Figure B.4.: $\Delta\Delta^{14}C$ evolution ($\Delta^{14}C$ offset) off the coast of Angola in 260 – 460 m depth, including the LSG upper and lower bound of model prediction for Angola (thin blue lines). Model predication agrees well for the last 19 ka. Measured data tend to be at the upper limit of the LSG model.

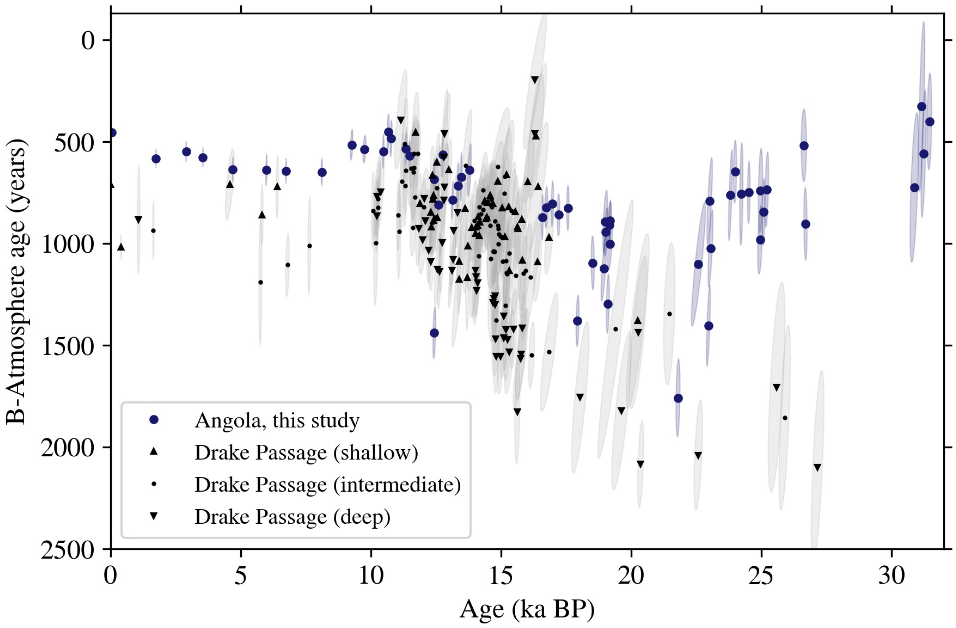

Figure B.5.: B_{atm} age reconstructed from CWC from Angola (this study) in direct comparison to the signal apparent in the Drake Passage (Burke and Robinson, 2012; Chen et al., 2015; Li et al., 2020).

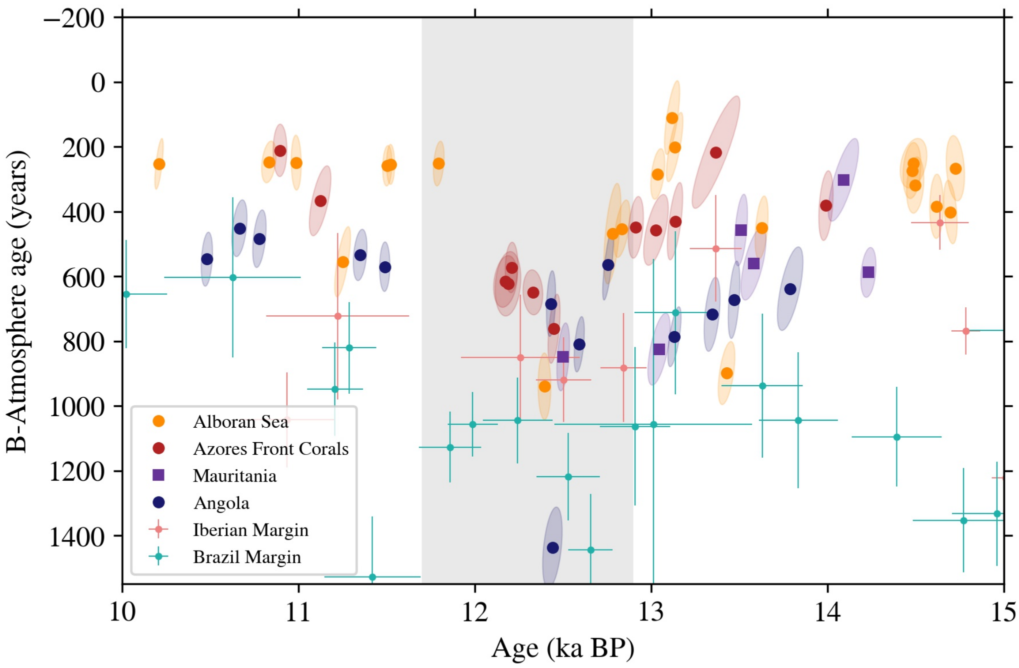

Figure B.6.: B_{atm} ages reconstructed in this study from CWC in various locations in comparison with B_{atm} ages obtained from foraminifera. CWCs: Alboran Sea (319 – 332 m depth); Azores (560 – 970 m depth); Mauritania (485 – 580 m depth); Angola (260 – 460 m depth). Foraminifera: (1σ error) Iberian Margin (2.1 km depth) and Brazil Margin (0.7 – 2.4 km depth), both from (Skinner et al., 2021).

B.2. Supporting Information for Chapter 6

The following section provides supplementary figures for chapter 6.

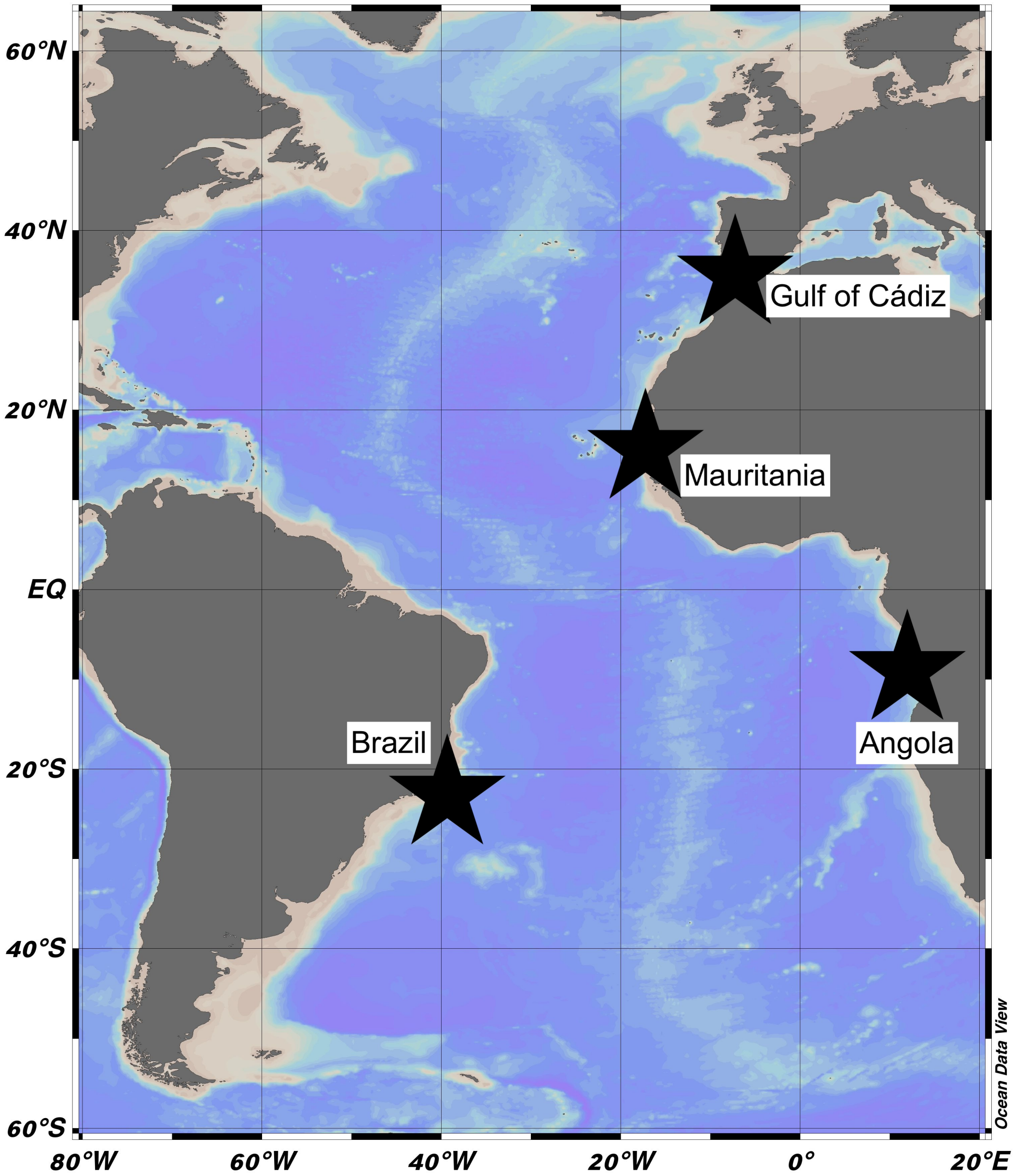

Figure B.7.: Overview of the investigated sediment core locations. Created with Ocean Data View (Schlitzer, 2023).

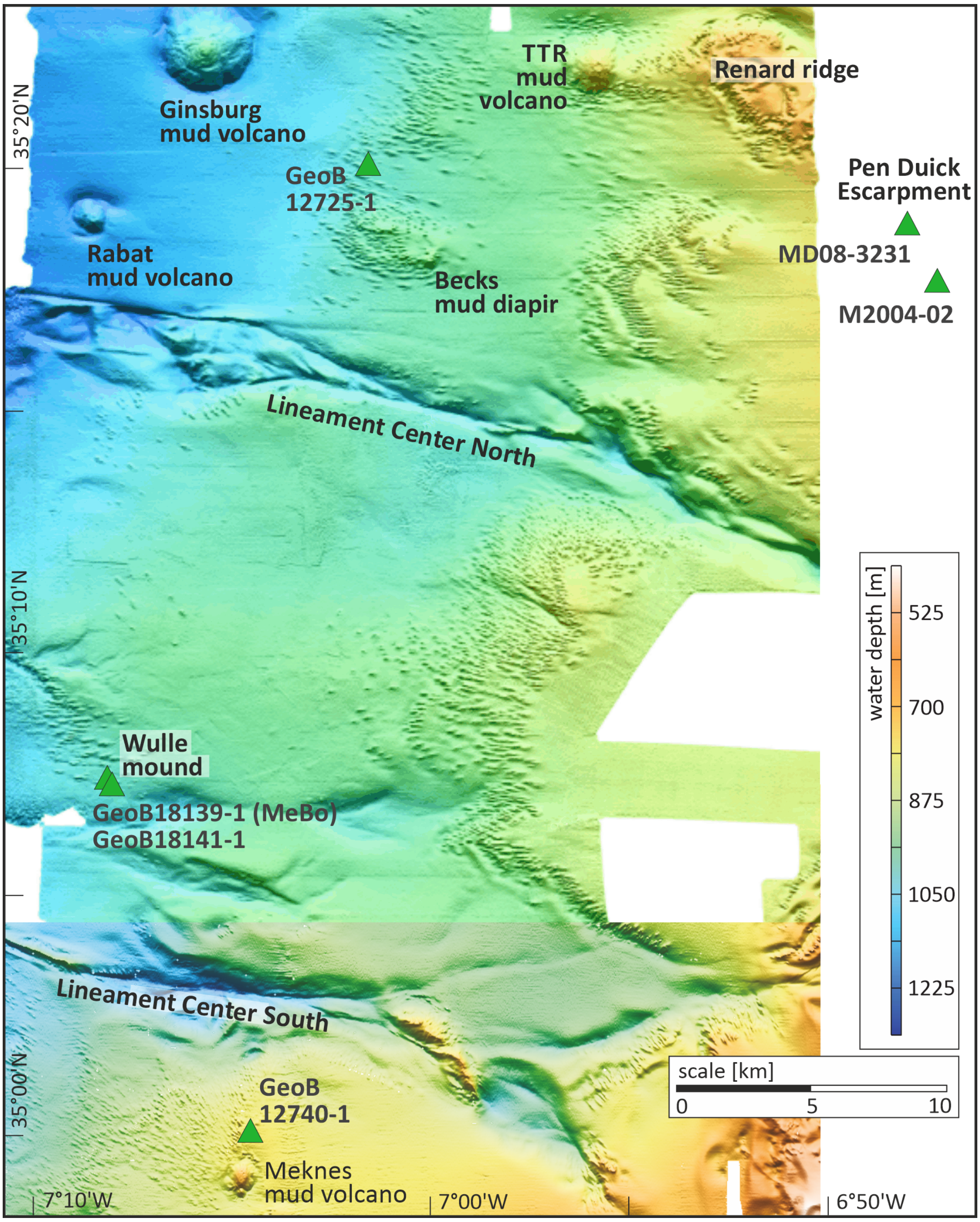

Figure B.8.: Positions of the investigated sediment cores in the Gulf of Cádiz. Several mud volcanoes are located in the immediate vicinity. Figure courtesy of Dr. Claudia Wienberg.

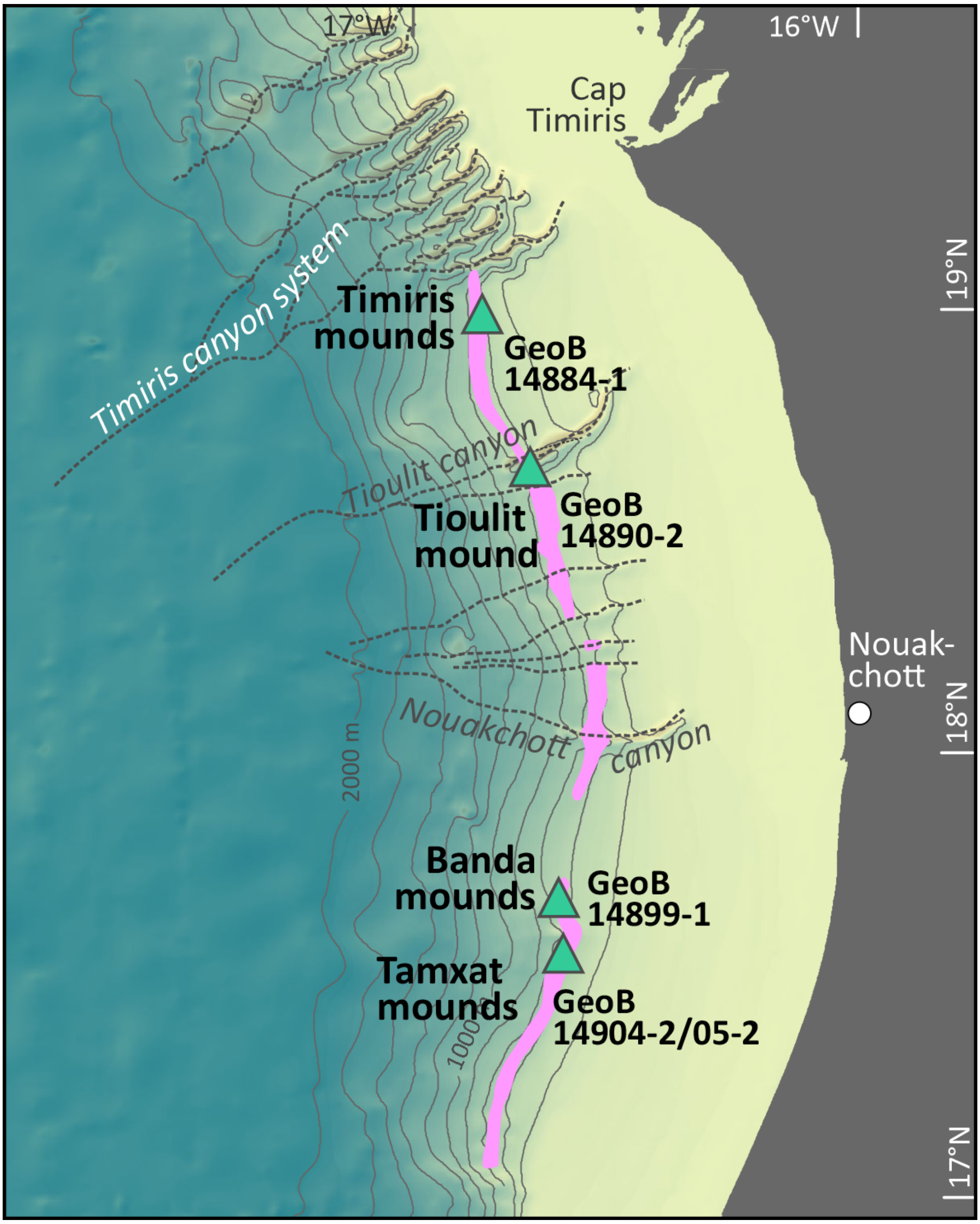

Figure B.9.: Positions of the investigated sediment cores offshore Mauritania. Figure courtesy of Dr. Claudia Wienberg.

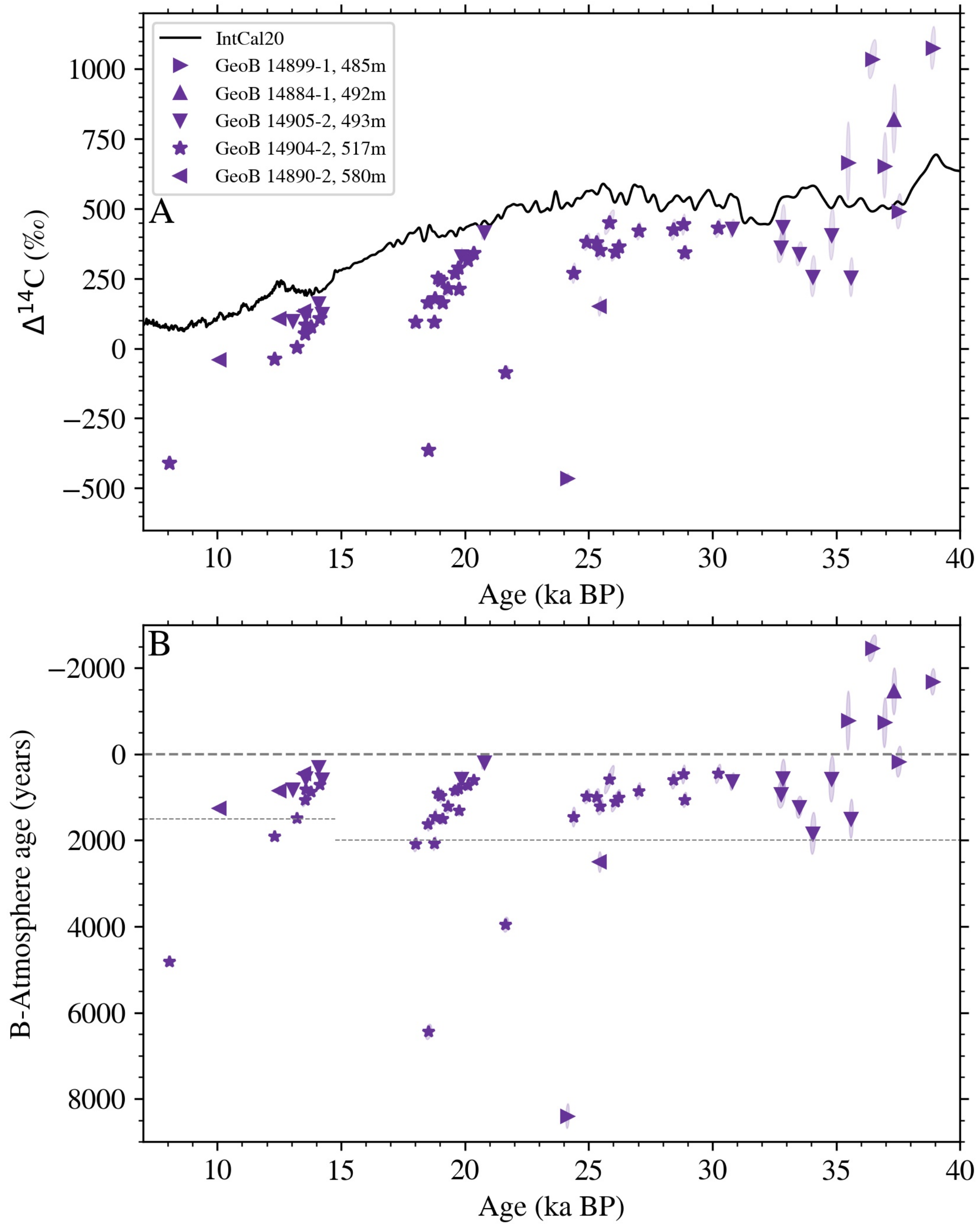

Figure B.10.: Radiocarbon records obtained from cold-water corals offshore Mauritania (this study, Beisel (2021); Beisel et al. (2023)). (A) $\Delta^{14}C$ record with IntCal20 (Reimer et al., 2020) as atmospheric reference. (B) Calculated B-Atmosphere age record. Horizontal lines mark the threshold values for the defined ventilation anomalies (chapter 6.2.3).

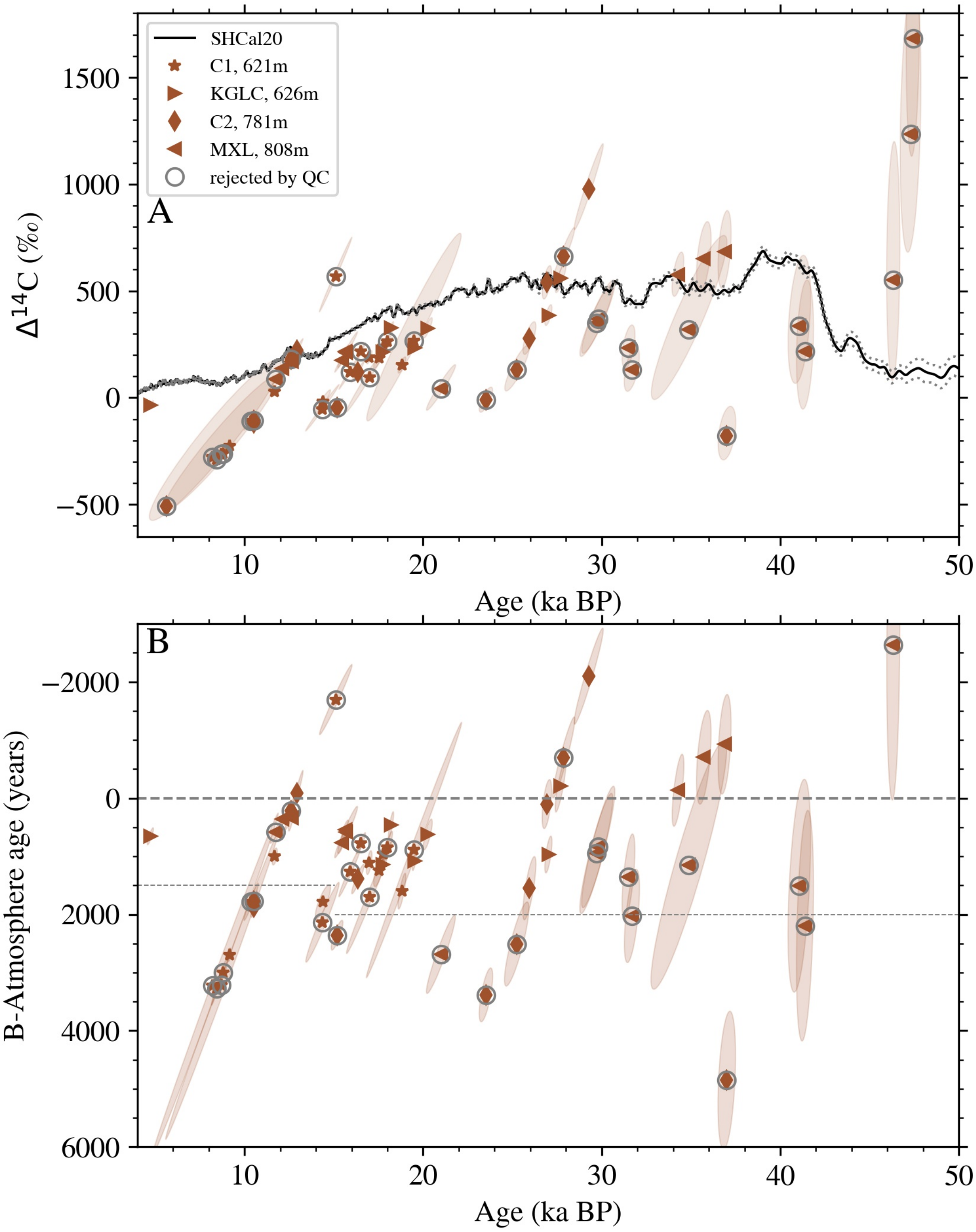

Figure B.11.: Radiocarbon records obtained from cold-water corals offshore Brazil (Mangini et al., 2010; Ruckelshausen, 2009, 2013). (A) $\Delta^{14}C$ record with SHCal20 (Hogg et al., 2020) as atmospheric reference. (B) Calculated B-Atmosphere age record. Horizontal lines mark the threshold values for the defined ventilation anomalies (chapter 6.2.3).

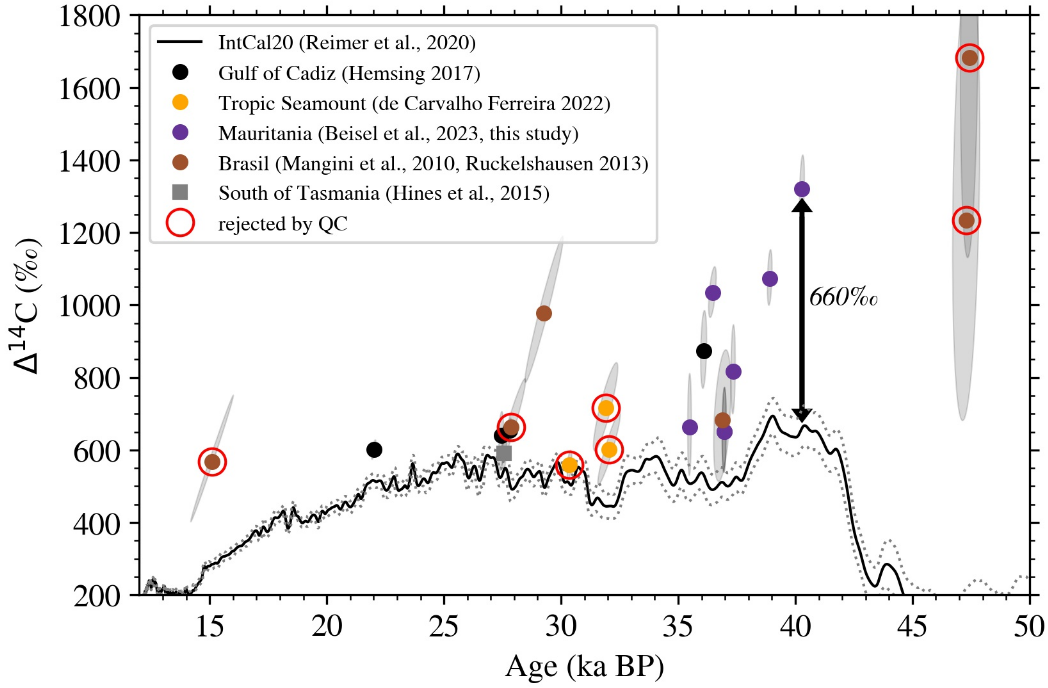

Figure B.12.: Compiled Δ^{14}C values (n=19) that exceed the current atmospheric calibration curve, IntCal20 (Reimer et al., 2020) (or SHCal20 for the Southern Hemisphere, (Hogg et al., 2020)). Red circles indicate data that did not meet the quality control criteria ^{232}Th and $\delta^{234}U_i$ (chapter 3.4.2, 37 %). It should be noted that the IntCal/SHCal represents an estimation of Δ^{14}C in the past. It is possible that certain sections have been underestimated.

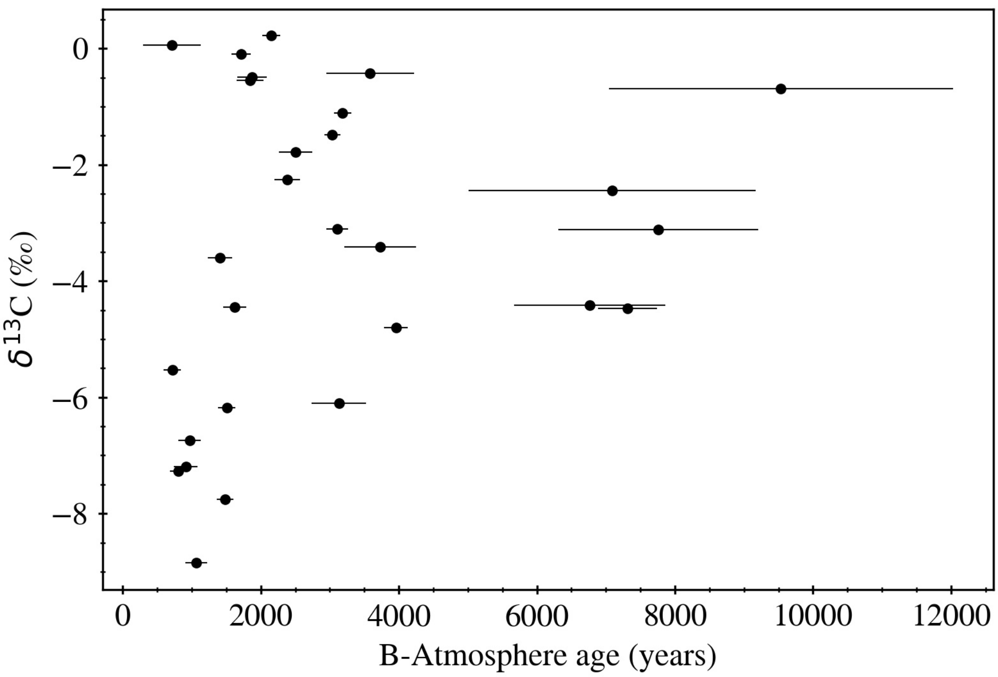

Figure B.13.: B-Atmosphere age against δ^{13}C for Mauritania and the Gulf of Cádiz (Stellbrink (2023), this study).

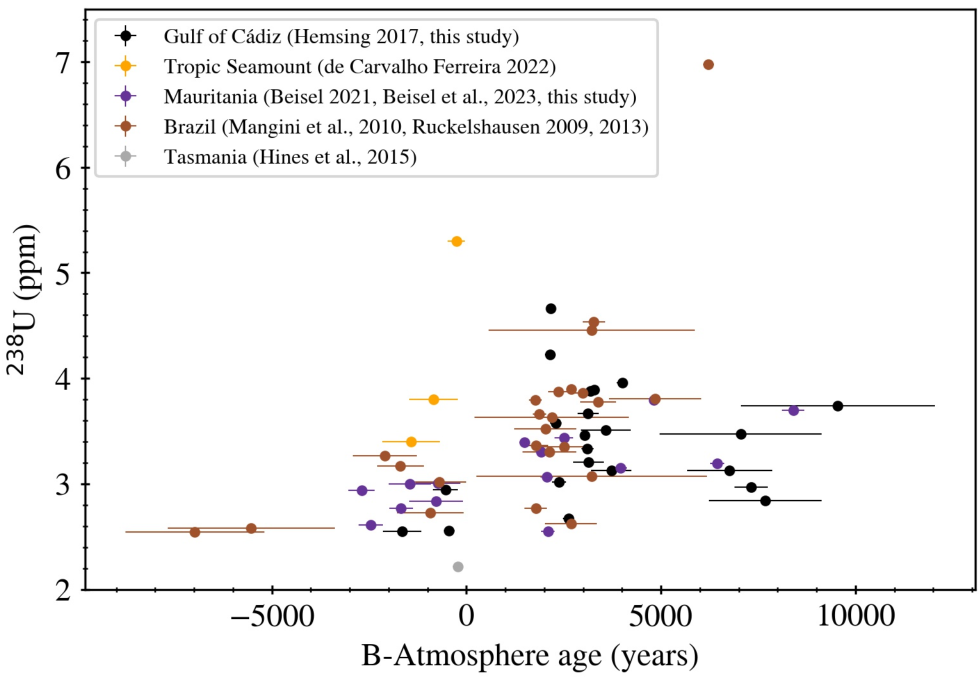

Figure B.14.: Compiled data with ventilation anomalies and values above the atmosphere, plotted as Benthic-atmosphere age (years) against ^{238}U concentration in ppm. Ventilation anomalies exhibit a mean ^{238}U concentration of 3.6 ± 0.7 ppm, while values above the atmosphere exhibit a mean of 3.0 ± 0.6 ppm. Only one coral from Brazil shows a high ^{238}U concentration of 7 ppm.

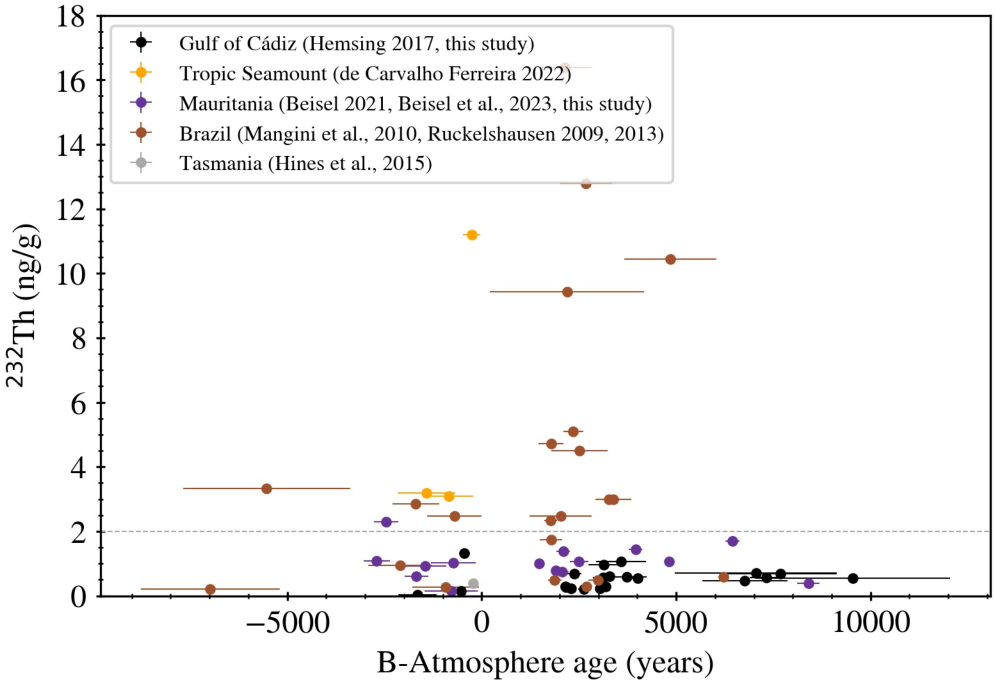

Figure B.15.: Compiled data with ventilation anomalies and values above the atmosphere, plotted as Benthic-atmosphere age (years) against ^{232}Th concentration in ng/g. Two data points from Brazil are not shown, as they exhibit exceptionally high ^{232}Th concentrations over 70 ng/g (Mangini et al., 2010; Ruckelshausen, 2009). These data points were not included in the discussion by Mangini et al. (2010). A threshold of 2 ng/g results in the rejection of to 31 % of the data.

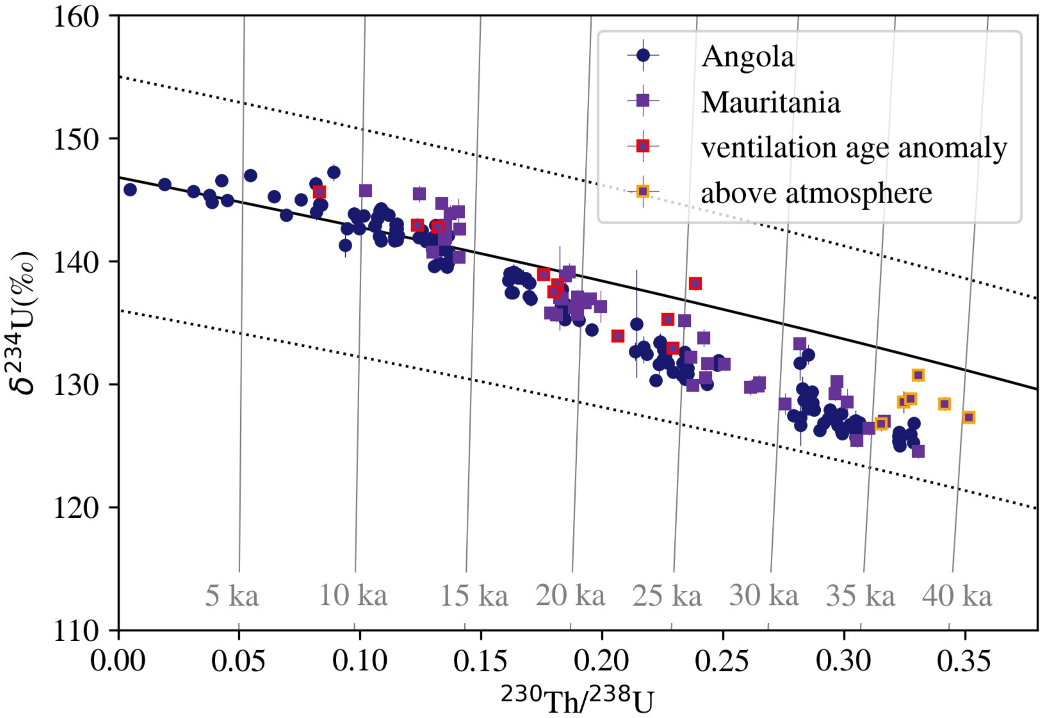

Figure B.16.: The evolution of the activity ratio of $^{234}U/^{238}U$ ($\delta^{234}U$) over time. Shown are ratios from Angola (Beisel et al. (2023) and chapter 7) and Mauritania (Beisel (2021); Beisel et al. (2023), this study). Values that are "above the atmosphere" (orange) and that are older than 35 ka differ significantly from the mean $\delta^{234}U$ values from Angola.

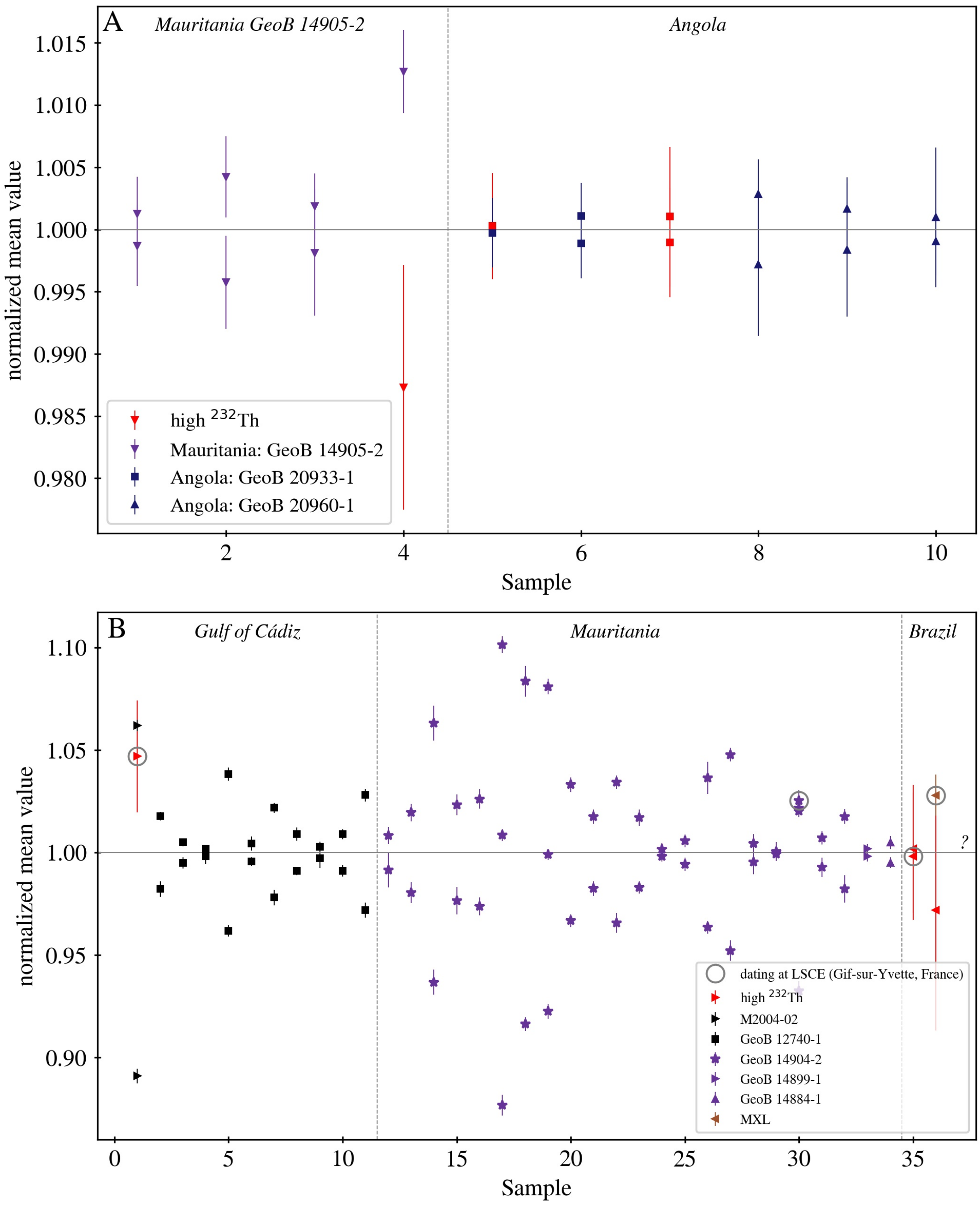

Figure B.17.: Duplicate ^{230}Th/U measurements, shown with 2σ error. (A) Duplicate measurements on sediment cores where no ventilation anomalies or values above the atmosphere could be detected so far. Except for one sample from GeoB 14905-2 with a very high ^{232}Th concentration (no. 4, ^{232}Th=7 ng/g), all ages could be reproduced. Sample no. 4 with a high ^{232}Th concentration consists probably of diagenetically altered material (see chapter 6.4.2). Angola CWC data this study, chapter 7 and Wefing et al. (2017). (B) Duplicate measurements on sediment cores where ventilation anomalies and values above the atmosphere are known. Data from GoC from this study and Wienberg et al. (2010), from Mauritania in part from (Beisel et al., 2023; Wienberg et al., 2018), and this study. The Brazil samples are obtained from Ruckelshausen (2013). Sample no. 37 ("?") was only mentioned in text form in Ruckelshausen (2009). It could not be reproduced in three measurements (Ruckelshausen, 2009). The data from the LSCE are published in Wienberg et al. (2010, 2018).

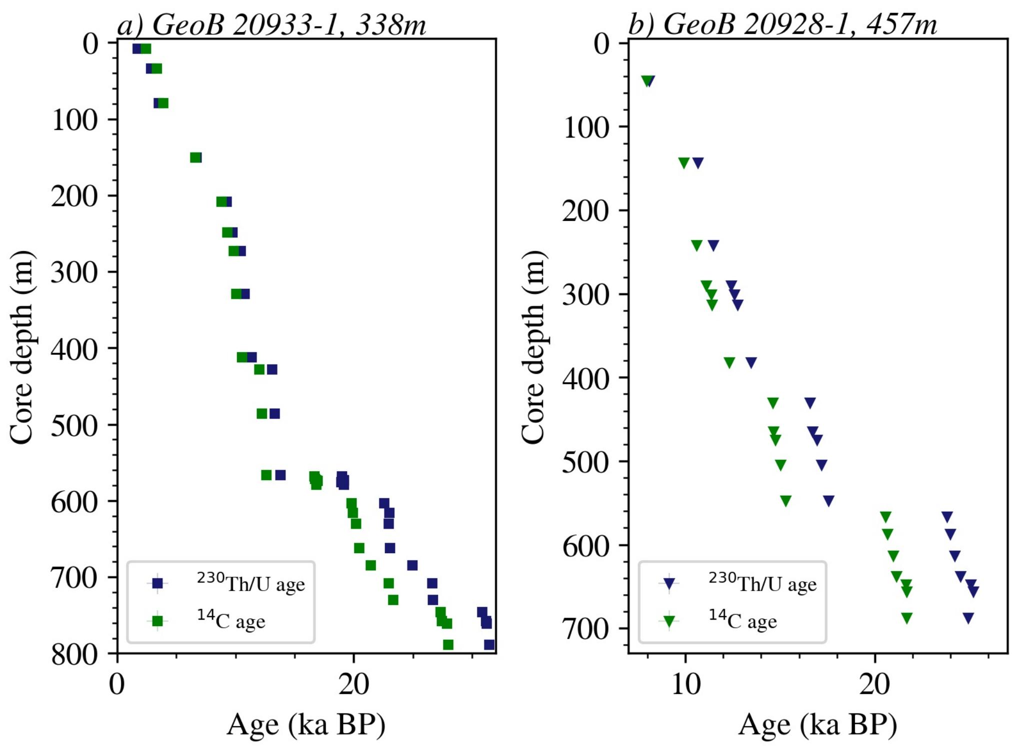

Figure B.18.: Depth profiles from sediment cores offshore Angola (chapter 5, Beisel et al. (2023)).

C. Supplementary Data

Supplementary data for each chapter are listed below. ^{230}Th/U ages of former publications were re-calculated according to Kerber et al. (2023). For the calculation of the B_{atm} age, IntCal20 (Reimer et al., 2020) was used for the Northern Hemisphere and SHCal20 (Hogg et al., 2020) for the Southern Hemisphere. Δ^{14}C and B_{atm} ages are given as the mean value of the ellipses with 2σ error. In the case of two ^{14}C measurements, the mean age was used.

Locations: table C.1

Chapter 4: table C.2

Chapter 5: `https://doi.org/10.1594/PANGAEA.959508`

Chapter 6: table C.3 - C.9

Chapter 7: table C.10 - C.12

Location	Core	Latitude °N	Longitude °E	Water Depth (m)	Research Cruise
Gulf of Cadiz	GeoB12725-1	35°21.410’	-6°59.440’	895	64PE284 (Hebbeln et al., 2008)
Gulf of Cadiz	GeoB12740-1	35°0.020’	-7°4.470’	739	64PE284 (Hebbeln et al., 2008)
Gulf of Cadiz	GeoB18139-1	35°7.143	-7°7.73’	940	MSM36 (Hebbeln et al., 2015)
Gulf of Cadiz	GeoB18141-1	35°7.15’	-7°7.74’	944	MSM36 (Hebbeln et al., 2015)
Gulf of Cadiz	MD08-3231	35°18.87’	-6°48.05’	550	MD169 (Van Rooij et al., 2008)
Gulf of Cadiz	M2004-02	35°17.68’	-6°47.25’	523	64PE229 (Mienis et al., 2004)
Mauritania	GeoB14884-1	18°57.803’	-16°52.123’	492	MSM16/3 (Westphal et al., 2014)
Mauritania	GeoB14890-2	18°38.792’	-16°43.698’	580	MSM16/3 (Westphal et al., 2014)
Mauritania	GeoB14899-1	17°40.191’	-16°40.329’	485	MSM16/3 (Westphal et al., 2014)
Mauritania	GeoB14904-2	17°32,558’	-16°39.806’	517	MSM16/3 (Westphal et al., 2014)
Mauritania	GeoB14905-2	17°32.456’	-16°39.999’	493	MSM16/3 (Westphal et al., 2014)
Angola	GeoB20933-1	-9°49.331’	12°46.565’	338	M122 ANNA (Hebbeln et al., 2017)
Angola	GeoB20960-1	-9°43.017’	12°45.997’	264	M122 ANNA (Hebbeln et al., 2017)

Table C.1.: Overview of the investigated locations.
Locations of chapter 5 (Beisel et al., 2023) are listed in PANGAEA.
Sample material from M2004-02 has been provided by Dr. Furu Mienis.
Remaining sample material from the sediment cores has been provided by the GeoB Core Repository at the MARUM – Center for Marine Environmental Sciences, University of Bremen, Germany.

Table C.2.: Duplicate ^{14}C measurements from the Heidelberg ^{14}C Laboratory. Compiled from [1] Beisel (2021),[2] Beisel et al. (2023),[3] Raddatz et al. (2023), and this study.

Lab No IUP	Lab No MAMS	Location	^{14}C Age (a BP)	1σ (a)
8372[1]	47329	Alboran Sea	9.518	27
	47322		9.572	27
7617[2]	47327	Alboran Sea	9.832	27
	47324		9.790	28
9154[1]	48633	Mauritania	10.146	34
	48622		10.141	31
11542	57608	Galicia Bank	10.768	41
	59318		10.679	32
10086[2]	47336	Azores	10.980	30
	42193		11.004	36
10701[2]	48631	Angola	11.088	33
	48638		11.122	34
8377[2]	48632	Alboran Sea	11.256	37
	48630		11.363	33
8378[2]	48634	Alboran Sea	11.277	39
	48620		11.389	46
10402[2]	46597	Angola	11.870	40
	47315		11.920	32
7611[2]	47325	Alboran Sea	12.847	33
	47326		12.855	33
10080[2]	47333	Azores	15.416	41
	42189		15.500	47
8814[2]	46862	Mauritania	17.074	65
	46859		16.997	64
11593	64380	Mauritania	17.474	45
	64379		17.602	46
11619	63007	Gulf of Cádiz	17.513	54
	63008		17.612	55
11647	62332	Gulf of Cádiz	17.606	66
	63012		17.560	56
10924[3]	51108	Maldives	18.715	60
	51109		18.743	59

Continued on next page

Table C.2 – *continued from previous page*

Lab No IUP	Lab No MAMS	Location	^{14}C Age (a BP)	1σ (a)
10406[2]	46601	Angola	19.624	71
	47316		19.719	53
10534[2]	46602	Angola	20.992	78
	46609		21.007	82
7939[2]	48640	Angola	21.437	72
	31382		21.469	63
11597	59335	Mauritania	21.754	80
	63004		21.849	74
8407[1]	46613	Gulf of Cádiz	25.096	115
	46615		25.246	115
12074	67223	Angola	28.803	98
	67210		28.841	99
12070	67218	Mauritania	28.978	152
	68125		29.070	146
10949	63561	Angola	29.201	161
	63567		29.271	161
8929[2]	46867	Mauritania	30.350	238
	46868		30.436	234
12078	67226	Angola	30.581	120
	67206		30.877	125
12062	67214	Mauritania	30.990	179
	68124		31.215	182
12055	67227	Mauritania	31.183	132
	68123		31.358	185
12053	67213	Mauritania	32.777	151
	67219		32.812	157
11582	57616	Gulf of Cádiz	32.922	437
	59323		32.341	249
10953	63559	Angola	33.173	251
	63568		33.126	251
11583	59324	Gulf of Cádiz	35.975	375
	59325		36.307	388
11584	59326	Gulf of Cádiz	42.584	829
	59327		43.576	932

Table C.3.: ^{230}Th/U results of the Gulf of Cádiz from chapter 6. 'AR': Activity Ratio.
Sample denoted with * did not pass the quality control (chapter 3.4.2) due to a ^{232}Th concentration > 2 ng/g.
[1] Hemsing (2017) and references therein. Recalculated according to Kerber et al. (2023).

Lab No IUP	Core	Depth (cm)	σ (cm)	^{238}U (μg/g)	2σ (μg/g)	^{232}Th (ng/g)	2σ (ng/g)	^{230}Th/^{238}U AR	2σ AR	^{230}Th/^{232}Th AR	2σ AR	δ^{234}U ‰	2σ ‰	Age uncor (ka)	2σ ka	Age (ka BP)	2σ (‰)	δ^{234}U$_i$ (‰)	2σ (‰)
11662	M2004-02	41	0,5	3,66045	0,00099	0,7710	0,0019	0,11102	0,00062	1614	10	145,14	0,47	11,10	0,07	10,97	0,07	149,74	0,49
11665	M2004-02	131	0,5	3,64972	0,00010	0,9237	0,0020	0,19384	0,00069	2337	10	135,52	0,52	20,34	0,08	20,20	0,08	143,50	0,55
11666	M2004-02	140	0,5	3,53125	0,00011	0,4339	0,0010	0,19294	0,00055	4788	17	136,26	0,42	20,22	0,06	20,11	0,07	144,25	0,44
11649	M2004-02	140,5	0,5	3,64658	0,00015	0,1517	0,0003	0,20282	0,00045	14908	48	136,38	0,53	21,35	0,05	21,27	0,05	144,84	0,57
11667	M2004-02	200	0,5	3,01525	0,00010	0,6796	0,0020	0,21657	0,00068	2932	13	135,21	0,44	22,99	0,08	22,86	0,09	144,25	0,47
11668	M2004-02	301	0,5	2,96871	0,00011	0,5706	0,0017	0,27727	0,00102	4399	21	128,39	0,50	30,58	0,13	30,46	0,13	139,95	0,55
8400[1]	MD08-3231	7,5	2,5	4,42590	0,00020	0,1524	0,0006	0,18060	0,00052	15951	80	141,30	0,70	18,72	0,06	18,65	0,06	148,92	0,78
8401[1]	MD08-3231	17,5	2,5	2,55520	0,00010	1,3272	0,0032	0,21080	0,00060	1232	5	139,90	1,00	22,20	0,07	22,01	0,10	148,88	1,04
8411[1]	MD08-3231	22,5	2,5	3,56550	0,00020	0,2208	0,0009	0,19220	0,00057	9472	48	137,40	1,00	20,11	0,07	20,02	0,07	145,45	1,01
6577[1]	MD08-3231	37,5	2,5	3,15340	0,00010	0,3048	0,0007	0,22050	0,00055	6950	24	137,20	0,50	23,40	0,07	23,31	0,07	146,53	0,49
8402[1]	MD08-3231	47,5	2,5	3,70350	0,00020	0,2339	0,0008	0,22040	0,00077	10603	51	135,40	0,90	23,44	0,09	23,35	0,09	144,60	0,94
8403[1]	MD08-3231	65	5	3,37060	0,00020	0,1909	0,0010	0,22180	0,00063	11903	68	134,70	0,90	23,61	0,08	23,53	0,08	143,98	0,92
8404[1]	MD08-3231	95	5	3,32500	0,00020	0,4595	0,0015	0,25130	0,00075	5535	25	134,50	1,00	27,16	0,10	27,06	0,10	145,16	1,09
8405[1]	MD08-3231	105	5	4,57610	0,00020	0,3689	0,0010	0,24780	0,00074	9372	38	130,70	0,60	26,85	0,09	26,76	0,09	140,99	0,66
8406[1]	MD08-3231	115	5	2,94370	0,00010	0,1467	0,0005	0,25430	0,00079	15543	70	134,90	1,00	27,52	0,10	27,44	0,10	145,77	1,09
6584[1]	MD08-3231	155	5	3,70670	0,00020	0,3712	0,0009	0,25690	0,00064	7816	27	133,00	0,50	27,90	0,08	27,81	0,08	143,85	0,56
7009[1]	MD08-3231	175	5	3,53200	0,00010	0,4567	0,0008	0,25320	0,00052	5968	16	131,70	0,60	27,48	0,07	27,38	0,07	142,33	0,62
8407[1]	MD08-3231	185	5	4,52790	0,00020	0,4898	0,0014	0,26390	0,00073	7425	29	129,90	0,60	28,85	0,09	28,76	0,09	140,86	0,70
8306[1]	MD08-3231	195	5	4,84630	0,00020	0,4182	0,0015	0,27620	0,00090	9740	46	131,70	0,60	30,34	0,11	30,25	0,12	143,43	0,61
7020[1]	MD08-3231	215	5	3,46840	0,00010	0,3243	0,0006	0,25470	0,00067	8320	27	133,10	0,60	27,62	0,08	27,53	0,09	143,91	0,63
7019[1]	MD08-3231	225	5	4,19360	0,00010	1,1292	0,0018	0,29840	0,00063	3383	9	128,60	0,60	33,28	0,09	33,15	0,09	141,18	0,64
7018[1]	MD08-3231	235	5	3,68070	0,00020	0,0951	0,0002	0,30230	0,00060	35630	105	129,20	0,50	33,77	0,08	33,70	0,08	142,15	0,54
8408[1]	MD08-3231	255	5	2,54980	0,00010	0,0258	0,0001	0,32180	0,00093	96765	606	133,70	0,90	36,16	0,13	36,09	0,13	148,06	1,04
7015[1]	MD08-3231	265	5	4,25490	0,00020	1,4097	0,0028	0,31710	0,00080	2917	9	128,50	0,80	35,73	0,11	35,59	0,12	142,06	0,94
7014[1]	MD08-3231	275	5	3,44950	0,00010	0,8680	0,0018	0,31990	0,00079	3871	13	130,80	0,70	36,02	0,11	35,90	0,11	144,74	0,72
7012[1]	MD08-3231	295	5	3,53650	0,00010	1,9952	0,0032	0,32610	0,00063	1759	4	128,30	0,50	36,94	0,09	36,73	0,11	142,31	0,55
7021[1]	MD08-3231	305	5	3,35250	0,00010	1,4628	0,0028	0,33110	0,00080	2319	7	130,10	0,70	37,54	0,11	37,37	0,12	144,64	0,75
11612	GeoB 12740-1	5,5	1,5	3,71256	0,00012	0,9039	0,0022	0,12733	0,00038	1596	6	144,18	0,43	12,83	0,04	12,70	0,05	149,47	0,44
11613	GeoB 12740-1	26	1	3,88929	0,00014	0,6148	0,0013	0,17047	0,00058	3294	13	138,95	0,53	17,62	0,06	17,51	0,07	146,02	0,55
11617	GeoB 12740-1	29,5	0,5	3,88264	0,00013	0,2841	0,0006	0,16971	0,00031	7072	19	138,17	0,42	17,55	0,04	17,46	0,04	145,18	0,45
11618	GeoB 12740-1	35	1	4,22290	0,00015	0,2897	0,0004	0,18167	0,00027	8065	16	136,71	0,45	18,92	0,03	18,83	0,03	144,20	0,47
11619	GeoB 12740-1	41	1	3,45843	0,00011	0,2375	0,0004	0,17230	0,00029	7670	19	139,21	0,51	17,82	0,03	17,73	0,04	146,39	0,53
11620	GeoB 12740-1	46	1	4,66589	0,00017	0,2769	0,0004	0,18639	0,00032	9609	21	136,13	0,46	19,47	0,04	19,38	0,04	143,81	0,49
11621	GeoB 12740-1	58,5	1,5	3,05534	0,00010	0,5852	0,0011	0,20855	0,00038	3337	9	136,53	0,48	22,02	0,05	21,90	0,05	145,26	0,51
11622	GeoB 12740-1	62	1	3,91062	0,00016	0,1400	0,0003	0,19923	0,00036	17031	46	136,39	0,42	20,94	0,04	20,86	0,04	144,69	0,45
11614	GeoB 12740-1	87,5	1,5	3,95734	0,00012	0,5416	0,0010	0,18299	0,00047	4085	13	139,36	0,33	19,02	0,05	18,92	0,06	147,04	0,35
11623	GeoB 12740-1	94,5	1,5	3,57572	0,00016	0,2364	0,0005	0,20441	0,00047	9469	29	136,63	0,76	21,53	0,06	21,44	0,06	145,18	0,81

Continued on next page

Table C.3 – *continued from previous page*

Lab No IUP	Core	Depth (cm)	σ (cm)	^{238}U (μg/g)	2σ (μg/g)	^{232}Th (ng/g)	2σ (ng/g)	^{230}Th/^{238}U AR	2σ AR	^{230}Th/^{232}Th AR	2σ AR	δ^{234}U ‰	2σ ‰	Age uncor (ka)	2σ ka	Age (ka BP)	2σ (‰)	$\delta^{234}U_i$ (‰)	2σ (‰)
11624	GeoB 12740-1	99,5	1,5	3,33066	0,00013	0,3280	0,0005	0,19659	0,00033	6120	14	137,53	0,58	20,61	0,04	20,51	0,04	145,75	0,61
11625	GeoB 12740-1	105	1	3,09668	0,00010	0,1353	0,0003	0,21367	0,00049	14995	50	138,57	0,44	22,57	0,06	22,49	0,06	147,68	0,47
11626	GeoB 12740-1	114	1	3,38204	0,00015	0,9829	0,0036	0,21771	0,00087	2393	13	136,92	0,91	23,08	0,11	22,94	0,11	146,10	0,97
11627	GeoB 12740-1	158	2	4,11436	0,00018	0,3281	0,0007	0,24574	0,00049	9889	28	131,62	0,63	26,57	0,06	26,48	0,06	141,86	0,68
11628	GeoB 12740-1	169	1	4,09877	0,00017	0,3106	0,0008	0,26613	0,00052	11010	34	130,66	0,61	29,11	0,07	29,02	0,07	141,84	0,67
11629	GeoB 12740-1	182,5	1,5	4,68220	0,00023	0,3281	0,0007	0,26247	0,00051	11467	33	130,85	0,61	28,65	0,06	28,56	0,07	141,86	0,66
11615	GeoB 12740-1	188,5	1,5	3,66566	0,00013	0,5595	0,0016	0,24596	0,00080	4926	22	132,61	0,48	26,57	0,10	26,46	0,10	142,92	0,51
11582	GeoB 12740-1	291,5	1,5	3,13002	0,00013	0,5832	0,0022	0,29710	0,00093	4902	24	127,61	0,54	33,15	0,12	33,03	0,12	140,10	0,60
11583	GeoB 12740-1	386	1	3,12969	0,00010	0,4641	0,0009	0,30381	0,00091	6306	23	124,76	0,53	34,12	0,12	34,02	0,12	137,36	0,59
11584	GeoB 12740-1	472	1	3,74309	0,00011	0,5521	0,0013	0,33650	0,00087	6958	24	120,06	0,35	38,70	0,12	38,59	0,12	133,90	0,40
11580	GeoB 12725-1	321	5	3,47575	0,00022	0,7138	0,0030	0,32986	0,00145	4920	30	125,73	0,58	37,55	0,20	37,43	0,20	139,77	0,65
11581	GeoB 12725-1	370,5	0,5	2,84439	0,00016	0,6810	0,0034	0,34037	0,00147	4365	29	123,02	0,95	39,10	0,21	38,97	0,21	137,34	1,07
11573	GeoB 18139-1	87,5	2,5	5,08869	0,00021	1,4117	0,0056	0,16772	0,00115	1858	15	138,32	0,57	17,33	0,13	17,19	0,13	145,23	0,61
11877	GeoB 18139-1	87,5	2,5	4,01233	0,00040	0,6438	0,0012	0,17278	0,00047	3303	11	138,19	0,46	17,89	0,05	17,78	0,06	145,33	0,49
11878	GeoB 18139-1	96,5	0,5	3,38426	0,00019	1,1522	0,0020	0,17915	0,00041	1614	5	138,84	0,53	18,60	0,05	18,44	0,06	146,28	0,56
11879	GeoB 18139-1	108,5	0,5	2,67282	0,00014	0,2073	0,0005	0,17655	0,00048	6986	24	142,05	0,90	18,25	0,06	18,16	0,06	149,55	0,95
11881	GeoB 18139-1	121,5	0,5	2,24447	0,00017	0,3727	0,0008	0,20875	0,00058	3852	14	139,12	0,88	21,98	0,07	21,87	0,07	148,01	0,93
11882	GeoB 18139-1	125,5	0,5	2,78655	0,00018	0,3241	0,0004	0,20869	0,00041	5497	13	136,38	0,63	22,04	0,05	21,93	0,05	145,12	0,67
11884	GeoB 18139-1	136	2	2,62176	0,00020	0,6849	0,0016	0,21419	0,00066	2508	10	136,56	1,11	22,68	0,08	22,54	0,09	145,55	1,18
11885	GeoB 18139-1	145,5	2,5	2,91193	0,00022	0,9215	0,0020	0,21556	0,00057	2082	7	133,79	0,95	22,90	0,07	22,75	0,08	142,69	1,01
11886	GeoB 18139-1	150,5	2,5	2,98604	0,00018	0,9787	0,0022	0,21060	0,00068	1963	8	135,83	0,76	22,27	0,08	22,12	0,09	144,61	0,81
11887	GeoB 18139-1	155,5	2,5	2,78564	0,00019	0,8505	0,0016	0,22088	0,00053	2219	7	135,63	0,78	23,48	0,07	23,33	0,08	144,89	0,84
11890	GeoB 18139-1	173	2	2,70690	0,00017	0,7135	0,0015	0,21477	0,00068	2493	9	135,69	0,60	22,76	0,08	22,62	0,09	144,67	0,65
11891	GeoB 18139-1	178,5	1,5	3,40677	0,00024	0,2697	0,0011	0,24542	0,00082	9470	51	132,53	0,61	26,50	0,10	26,41	0,10	142,81	0,65
11575	GeoB 18139-1	251,5	0,5	3,20816	0,00016	0,9676	0,0024	0,27597	0,00109	2820	13	128,69	0,69	30,41	0,14	30,26	0,14	140,19	0,75
11576	GeoB 18139-1	348,5	1,5	3,51138	0,00017	1,0721	0,0046	0,31095	0,00149	3119	20	127,68	0,56	34,95	0,20	34,81	0,20	140,88	0,62
7507[1]	GeoB 18141-1	17	3	5,02220	0,00040	1,4543	0,0130	0,03630	0,00043	383	6	145,60	2,40	3,51	0,04	3,37	0,06	146,98	2,45
7545[1]	GeoB 18141-1	66	3	2,55806	0,00021	0,7169	0,0030	0,17235	0,00082	1930	12	139,82	1,86	17,84	0,10	17,71	0,10	147,02	1,96
7508*[1]	GeoB 18141-1	70,0	3	3,07297	0,00013	3,0616	0,0107	0,18941	0,00077	583	3	138,45	0,73	19,77	0,09	19,46	0,15	146,29	0,78
7547[1]	GeoB 18141-1	83	3	2,94815	0,00035	0,5184	0,0058	0,18805	0,00162	3332	47	138,07	3,03	19,65	0,19	19,54	0,20	145,94	3,21
7509[1]	GeoB 18141-1	95	3	2,96943	0,00015	1,3934	0,0085	0,20066	0,00159	1311	13	138,50	2,32	21,06	0,19	20,88	0,20	146,93	2,47
7548[1]	GeoB 18141-1	107	3	2,61189	0,00030	0,4948	0,0041	0,19680	0,00179	3248	40	140,56	3,39	20,60	0,21	20,49	0,22	148,97	3,59
7510[1]	GeoB 18141-1	127	3	3,07317	0,00014	1,8662	0,0079	0,20022	0,00094	1011	6	136,53	0,85	21,05	0,11	20,83	0,13	144,83	0,90
7551[1]	GeoB 18141-1	138	3	2,57017	0,00020	0,4083	0,0023	0,19894	0,00127	3921	33	137,22	2,36	20,92	0,16	20,81	0,16	145,56	2,51
7552[1]	GeoB 18141-1	156	3	2,62764	0,00022	0,2175	0,0016	0,19926	0,00191	7540	91	135,36	2,24	20,99	0,22	20,91	0,22	143,63	2,38
7512[1]	GeoB 18141-1	184	3	3,18643	0,00014	0,7044	0,0021	0,20701	0,00068	2877	13	135,88	0,71	21,85	0,08	21,73	0,09	144,50	0,76
7554[1]	GeoB 18141-1	275	3	2,83057	0,00025	0,7517	0,0033	0,19908	0,00108	2346	16	137,28	1,57	20,93	0,13	20,80	0,14	145,62	1,66
7514*[1]	GeoB 18141-1	282	3	3,50572	0,00015	2,4572	0,0065	0,21179	0,00067	927	4	135,02	0,54	22,43	0,08	22,19	0,12	143,77	0,58
7556[1]	GeoB 18141-1	291	3	3,39066	0,00029	1,1116	0,0063	0,20667	0,00115	1977	16	132,74	2,10	21,91	0,15	21,76	0,14	141,19	2,24
7515[1]	GeoB 18141-1	310	3	3,89433	0,00015	0,8330	0,0238	0,21231	0,00193	3048	92	137,06	5,32	22,44	0,25	22,32	0,26	146,00	5,67
7513[1]	GeoB 18141-1	328	3	3,69742	0,00018	0,8792	0,0035	0,21632	0,00096	2793	17	134,87	2,15	22,96	0,12	22,84	0,13	143,87	2,29
7516[1]	GeoB 18141-1	518	3	2,42210	0,00040	0,1418	0,0040	0,21740	0,00194	11330	332	139,30	3,80	22,98	0,24	22,90	0,24	148,63	4,07
7557[1]	GeoB 18141-1	535	3	2,54302	0,00018	0,8867	0,0042	0,21566	0,00101	1941	13	136,82	1,78	22,87	0,11	22,72	0,14	145,92	1,90

Continued on next page

Table C.3 – *continued from previous page*

Lab No IUP	Core	Depth (cm)	σ (cm)	^{238}U (μg/g)	2σ (μg/g)	^{232}Th (ng/g)	2σ (ng/g)	^{230}Th/^{238}U AR	2σ AR	^{230}Th/^{232}Th AR	2σ AR	δ^{234}U ‰	2σ ‰	Age uncor (ka)	2σ ka	Age (ka BP)	2σ (‰)	δ^{234}U$_i$ (‰)	2σ (‰)
7517[1]	GeoB 18141-1	549	3	2,61608	0,00013	0,4057	0,0009	0,22158	0,00064	4375	16	135,95	0,92	23,56	0,08	23,45	0,08	145,28	0,98
7559[1]	GeoB 18141-1	561	3	2,73535	0,00021	0,7844	0,0034	0,21827	0,00107	2379	16	135,35	2,09	23,21	0,14	23,08	0,15	144,50	2,23
7518*[1]	GeoB 18141-1	568	3	3,36706	0,00016	2,6038	0,0114	0,22980	0,00118	910	6	134,14	0,84	24,58	0,14	24,32	0,17	143,70	0,90
7562[1]	GeoB 18141-1	578	3	2,93567	0,00027	1,1329	0,0066	0,23007	0,00152	1875	16	135,93	2,11	24,60	0,19	24,44	0,19	145,68	2,27
7519[1]	GeoB 18141-1	584	3	2,73663	0,00024	0,4418	0,0026	0,23579	0,00132	4466	36	137,07	1,75	25,22	0,16	25,12	0,17	147,16	1,88
7563*[1]	GeoB 18141-1	593	3	4,19409	0,00047	10,5427	0,0609	0,29747	0,00201	373	3	129,01	1,86	33,19	0,29	32,49	0,37	141,44	2,05
7522[1]	GeoB 18141-1	805	3	3,21593	0,00014	1,2964	0,0023	0,30851	0,00072	2346	7	127,39	0,57	34,64	0,10	34,48	0,11	140,43	0,63
7523[1]	GeoB 18141-1	810	3	4,27876	0,00016	0,3644	0,0008	0,30990	0,00075	11153	37	126,52	0,56	34,86	0,10	34,77	0,10	139,59	0,62
7567[1]	GeoB 18141-1	870	3	3,86533	0,00030	0,1405	0,0012	0,34945	0,00249	30042	336	126,17	3,69	40,26	0,39	40,19	0,36	141,37	4,14

Table C.4.: ^{230}Th/U results of Mauritania from chapter 6. 'AR': Activity Ratio.
Sample denoted with * did not pass the quality control (chapter 3.4.2) due to a ^{232}Th concentration > 2 ng/g.
[1] Beisel et al. (2023); [2] Stuhrmann (2023); [3] Wienberg et al. (2018), recalculated according to Kerber et al. (2023); [4] Schneider (2018), recalculated according to Kerber et al. (2023)

Lab No IUP	Core	Depth (cm)	σ (cm)	^{238}U (μg/g)	2σ (μg/g)	^{232}Th (ng/g)	2σ (ng/g)	^{230}Th/^{238}U AR	2σ AR	^{230}Th/^{232}Th AR	2σ AR	δ^{234}U ‰	2σ ‰	Age uncor (ka)	2σ ka	Age (ka BP)	2σ (‰)	δ^{234}U$_i$ (‰)	2σ (‰)
8928[4]	GeoB 14899-1	5,5	1,5	3,69708	0,00016	0,39181	0,00074	0,22722	0,00057	6595	21	135,25	0,47	24,24	0,07	24,15	0,07	144,82	0,50
8929[1,4]	GeoB 14899-1	10,5	1,5	2,83590	0,00012	0,15695	0,00036	0,31531	0,00058	17520	52	126,76	0,55	35,57	0,08	35,48	0,08	140,13	0,61
12066*[2]	GeoB 14899-1	25	1	2,61282	0,00017	2,28888	0,00470	0,32477	0,00089	1131	4	128,54	0,89	36,75	0,13	36,46	0,16	142,50	0,99
8935[1,4]	GeoB 14899-1	160,5	1,5	3,00520	0,00010	1,02560	0,00170	0,32760	0,00056	2938	7	128,80	0,40	37,12	0,08	36,96	0,09	143,02	0,44
12067[2]	GeoB 14899-1	179,25	1	2,83689	0,00010	1,25315	0,00256	0,33072	0,00072	2297	7	124,49	0,54	37,72	0,10	37,54	0,12	138,43	0,60
12061[2]	GeoB 14899-1	285,25	1	2,77127	0,00015	0,61142	0,00111	0,34163	0,00069	4728	13	128,39	0,54	39,04	0,10	38,91	0,10	143,32	0,60
12063[2]	GeoB 14899-1	463	2	2,93746	0,00013	1,09363	0,00210	0,35159	0,00063	2884	8	127,30	0,49	40,45	0,09	40,29	0,10	142,66	0,55
8230[1,3]	GeoB 14905-2	1	1	3,19650	0,00020	0,75220	0,00210	0,13010	0,00051	1670	8	140,70	0,90	13,17	0,06	13,05	0,06	145,97	0,92
8231[1,3]	GeoB 14905-2	199	1	3,08920	0,00010	1,10840	0,00270	0,13550	0,00050	1141	5	141,90	1,00	13,74	0,05	13,58	0,07	147,48	1,02
8232[1,3]	GeoB 14905-2	281	1	2,43120	0,00010	1,14830	0,00330	0,14070	0,00056	897	4	144,00	1,10	14,28	0,06	14,09	0,09	149,83	1,18
8813[1]	GeoB 14905-2	491,5	1,5	3,39200	0,00010	0,68590	0,00090	0,14100	0,00032	2122	6	140,30	0,40	14,35	0,04	14,23	0,04	146,12	0,39
8814[1]	GeoB 14905-2	557,5	1,5	2,71650	0,00010	0,28360	0,00030	0,19090	0,00027	5572	10	136,60	0,60	19,97	0,03	19,88	0,04	144,49	0,59
8235[1,3]	GeoB 14905-2	590,5	1,5	2,79750	0,00010	1,14550	0,00390	0,19940	0,00076	1473	8	136,30	1,30	20,96	0,09	20,79	0,11	144,52	1,41
12060[2]	GeoB 14905-2	625	5	2,53857	0,00014	1,10145	0,00194	0,28175	0,00056	1987	5	133,25	0,46	30,99	0,07	30,81	0,09	145,39	0,51
12070[2]	GeoB 14905-2	655	5	2,79560	0,00015	0,72562	0,00158	0,29634	0,00077	3534	12	129,20	0,58	32,99	0,10	32,85	0,11	141,78	0,64
12054[2]	GeoB 14905-2	684	2	2,39596	0,00076	1,34786	0,00303	0,29684	0,00111	1628	7	130,95	1,11	33,00	0,15	32,78	0,17	143,67	1,22
12058[2]	GeoB 14905-2	802,5	2,5	2,61335	0,00015	0,90591	0,00163	0,30136	0,00086	2661	9	128,52	1,11	33,67	0,12	33,51	0,13	141,30	1,22
12055[2]	GeoB 14905-2	837,5	2,5	2,82544	0,00008	1,73155	0,00267	0,30526	0,00060	1522	4	125,39	0,55	34,29	0,08	34,06	0,11	138,07	0,61
12062[2]	GeoB 14905-2	854,5	0,5	2,70505	0,00010	0,37701	0,00080	0,31039	0,00081	6800	23	126,38	0,56	34,93	0,11	34,82	0,11	139,45	0,62
12053[2]	GeoB 14905-2	955	3	2,83388	0,00010	0,60576	0,00097	0,31668	0,00059	4527	11	126,98	0,56	35,74	0,08	35,61	0,08	140,44	0,62
11763	GeoB14904-2	1	1	3,79625	0,00011	1,07142	0,00416	0,08330	0,00057	906	7	145,61	0,56	8,22	0,06	8,08	0,07	149,00	0,57
11764	GeoB14904-2	21,5	1,5	3,30369	0,00013	0,78389	0,00191	0,12363	0,00038	1602	6	142,92	0,62	12,46	0,04	12,32	0,05	148,01	0,65
11601	GeoB14904-2	145,5	1,5	2,68580	0,00011	0,69915	0,00153	0,13546	0,00055	1602	7	142,89	0,62	13,72	0,06	13,58	0,07	148,51	0,65
11602	GeoB14904-2	159	1	3,39481	0,00012	1,00510	0,00224	0,13210	0,00038	1374	5	142,76	0,68	13,36	0,04	13,22	0,06	148,21	0,71
11603	GeoB14904-2	175	1	2,20281	0,00020	0,52348	0,00279	0,13493	0,00096	1751	16	141,77	1,00	13,68	0,10	13,55	0,11	147,32	1,04
11604	GeoB14904-2	190,5	2,5	2,50295	0,00010	0,56549	0,00099	0,13736	0,00051	1877	8	143,85	0,66	13,91	0,06	13,78	0,06	149,58	0,69
11769	GeoB14904-2	198	2	2,59071	0,00007	1,32250	0,00390	0,14113	0,00087	848	6	142,57	0,52	14,34	0,09	14,14	0,11	148,40	0,54
11606	GeoB14904-2	349,5	1,5	2,81216	0,00019	0,30994	0,00083	0,17889	0,00060	4992	21	135,78	0,47	18,63	0,07	18,52	0,07	143,10	0,50
11607	GeoB14904-2	369,5	1,5	2,43193	0,00012	0,35867	0,00064	0,18259	0,00049	3800	12	137,04	0,47	19,02	0,06	18,91	0,06	144,58	0,50
11608	GeoB14904-2	379,5	2,5	2,65760	0,00010	0,32713	0,00100	0,18363	0,00055	4580	20	136,91	0,59	19,14	0,06	19,04	0,07	144,50	0,62
11609	GeoB14904-2	406	6	2,83432	0,00010	0,33378	0,00064	0,18130	0,00053	4751	17	135,61	0,55	18,90	0,06	18,80	0,06	143,03	0,58
11610	GeoB14904-2	425	1	2,55037	0,00009	1,39261	0,00210	0,17581	0,00055	983	3	138,88	0,45	18,22	0,06	18,01	0,09	146,16	0,48
11587[1]	GeoB14904-2	463,5	2,5	2,71910	0,00011	0,69581	0,00116	0,18482	0,00048	2203	7	138,79	0,69	19,24	0,06	19,11	0,06	146,50	0,73
11588[1]	GeoB14904-2	469,5	2,5	2,59461	0,00008	0,38425	0,00075	0,19001	0,00054	3914	13	137,07	0,64	19,87	0,06	19,76	0,06	144,96	0,68
11589	GeoB14904-2	469,5	2,5	2,79677	0,00013	0,58370	0,00151	0,18657	0,00062	2748	12	139,10	0,73	19,43	0,07	19,31	0,08	146,92	0,78
11590[1]	GeoB14904-2	471,5	2,5	3,05596	0,00010	0,50106	0,00092	0,18868	0,00045	3504	10	136,20	0,48	19,73	0,05	19,62	0,06	143,99	0,50

Continued on next page

Table C.4 – *continued from previous page*

Lab No IUP	Core	Depth (cm)	σ (cm)	^{238}U (μg/g)	2σ (μg/g)	^{232}Th (ng/g)	2σ (ng/g)	^{230}Th/^{238}U AR	2σ AR	^{230}Th/^{232}Th AR	2σ AR	δ^{234}U ‰	2σ ‰	Age uncor (ka)	2σ ka	Age (ka BP)	2σ (‰)	$\delta^{234}U_i$ (‰)	2σ (‰)
11591[1]	GeoB14904-2	482,5	2,5	3,47633	0,00010	0,53503	0,00071	0,18991	0,00040	3757	9	135,69	0,39	19,88	0,05	19,77	0,05	143,50	0,42
11592[1]	GeoB14904-2	492,5	2,5	2,58617	0,00009	0,42765	0,00074	0,19324	0,00048	3557	11	136,62	0,45	20,24	0,06	20,13	0,06	144,63	0,48
11593	GeoB14904-2	498	3	3,06420	0,00015	0,75436	0,00142	0,18183	0,00049	2285	8	138,06	0,50	18,92	0,06	18,78	0,06	145,61	0,53
11594[1]	GeoB14904-2	504,5	1,5	2,16394	0,00008	0,31685	0,00054	0,19524	0,00050	4068	12	136,90	0,51	20,47	0,06	20,36	0,06	145,03	0,54
11596	GeoB14904-2	532,5	2,5	3,15229	0,00010	1,44190	0,00465	0,20658	0,00088	1377	7	133,88	0,42	21,84	0,10	21,66	0,12	142,35	0,45
11595	GeoB14904-2	532,5	2,5	3,19221	0,00011	1,69639	0,00477	0,18018	0,00096	1034	6	137,48	0,41	18,74	0,11	18,54	0,13	144,89	0,43
11597	GeoB14904-2	536,5	1,5	2,92634	0,00015	0,93119	0,00171	0,22933	0,00054	2216	7	132,88	0,46	24,55	0,07	24,40	0,08	142,39	0,49
11598[1]	GeoB14904-2	542,5	2	2,92535	0,00012	0,76325	0,00389	0,23680	0,00087	2769	17	132,19	0,49	25,47	0,11	25,33	0,11	142,01	0,53
11599[1]	GeoB14904-2	546	1	3,33681	0,00010	0,98376	0,00257	0,23746	0,00094	2461	12	129,89	0,44	25,61	0,11	25,46	0,12	139,60	0,48
11770	GeoB14904-2	551	1	2,82850	0,00020	0,79505	0,00203	0,23418	0,00088	2550	12	135,13	0,68	25,08	0,11	24,93	0,11	145,01	0,73
11771	GeoB14904-2	600	1	2,21044	0,00006	1,42864	0,00626	0,24212	0,00145	1145	9	133,74	0,73	26,07	0,18	25,84	0,19	143,88	0,79
11772	GeoB14904-2	632	2	3,15420	0,00020	0,39502	0,00114	0,24373	0,00068	5938	24	131,67	0,44	26,32	0,08	26,22	0,08	141,81	0,47
11773	GeoB14904-2	658,5	1,5	3,11017	0,00010	1,34601	0,00469	0,24294	0,00122	1722	11	130,53	0,63	26,26	0,15	26,08	0,16	140,53	0,68
11774	GeoB14904-2	707	2	3,27221	0,00018	0,59943	0,00126	0,25045	0,00068	4165	14	131,59	0,41	27,14	0,08	27,02	0,09	142,05	0,44
11611	GeoB14904-2	785	0,5	2,28198	0,00010	0,30596	0,00054	0,26463	0,00058	6094	17	129,83	0,51	28,95	0,07	28,84	0,07	140,86	0,55
11775	GeoB14904-2	794	1	2,62851	0,00010	0,54990	0,00159	0,26144	0,00075	3845	16	129,73	0,62	28,55	0,10	28,43	0,10	140,60	0,67
12231	GeoB14904-2	882,5	2,5	3,47827	0,00015	0,52397	0,00118	0,26509	0,00065	5378	18	130,07	0,64	29,00	0,08	28,89	0,09	141,15	0,70
12233	GeoB14904-2	963	4	2,90957	0,00015	0,87774	0,00179	0,27569	0,00078	2809	10	128,37	0,89	30,38	0,10	30,23	0,11	139,83	0,97
9154[1,4]	GeoB14890-2	20,5	1,5	3,77306	0,00018	0,71856	0,00118	0,10223	0,00025	1650	5	145,74	0,53	10,17	0,03	10,06	0,04	149,96	0,55
9155[1,4]	GeoB14890-2	53	3	3,96033	0,00017	0,21000	0,00048	0,12453	0,00032	7208	25	145,46	0,66	12,52	0,03	12,44	0,04	150,69	0,69
9156[1,4]	GeoB14890-2	109	1	2,89741	0,00010	0,22985	0,00047	0,13392	0,00033	5173	17	144,68	0,50	13,53	0,04	13,45	0,04	150,30	0,52
9158[4]	GeoB14890-2	228	1	3,43779	0,00012	1,07238	0,00158	0,23863	0,00049	2352	6	138,14	0,50	25,54	0,06	25,39	0,07	148,43	0,54
8801[1,4]	GeoB 14884-1	228	1	2,99850	0,00010	0,92440	0,00120	0,33090	0,00061	3259	7	130,70	0,50	37,49	0,09	37,34	0,09	145,21	0,55

Table C.5.: Duplicate ^{230}Th/U measurements from the Gulf of Cádiz and Mauritania (chapter 6). 'AR': Activity Ratio.
** same solution, measured on different days
[1] Wienberg et al. (2018); [2] Beisel et al. (2023); [3] Schneider (2018), recalculated according to Kerber et al. (2023). ; [4] Wienberg et al. (2010)

Lab No IUP	Core	^{238}U (μg/g)	2σ (μg/g)	^{232}Th (ng/g)	2σ (ng/g)	^{230}Th/^{238}U AR	2σ AR	^{230}Th/^{232}Th AR	2σ AR	δ^{234}U ‰	2σ ‰	Age uncor (ka)	2σ ka	Age (ka BP)	2σ (‰)	δ^{234}U$_i$ (‰)	2σ (‰)
8801	GeoB 14884-1	2,68359	0,00012	0,7491	0,0015	0,33295	0,00084	3676	12	128,44	0,60	37,86	0,12	37,71	0,12	142,89	0,67
8801[2,3]	GeoB 14884-1	2,99847	0,00012	0,9270	0,0012	0,33090	0,00061	3254	7	130,66	0,49	37,54	0,08	37,34	0,10	145,26	0,55
8929	GeoB 14899-1	2,77398	0,00011	0,2643	0,0006	0,31432	0,00061	10169	29	126,41	0,44	35,45	0,08	35,35	0,08	139,70	0,49
8929[2,3]	GeoB 14899-1	2,83590	0,00012	0,1570	0,0004	0,31531	0,00058	17520	52	126,76	0,55	35,57	0,08	35,48	0,08	140,13	0,61
11611	GeoB14904-2	2,51387	0,00010	0,7040	0,0026	0,24436	0,00109	2663	15	129,15	0,69	26,47	0,13	26,32	0,14	139,14	0,74
GIF-2805[1]	GeoB14904-2	2,52300	0,00590	0,3898	0,0007					131,30	1,90			28,95	0,14	142,55	2,10
11611*	GeoB14904-2	2,28193	0,00012	0,3075	0,0007	0,26420	0,00066	6078	20	129,35	0,45	28,91	0,08	28,80	0,08	140,34	0,49
11611*	GeoB14904-2	2,28198	0,00010	0,3060	0,0005	0,26463	0,00058	6094	17	129,83	0,51	28,95	0,07	28,84	0,07	140,86	0,55
11606	GeoB14904-2	3,78242	0,00016	1,4813	0,0032	0,14613	0,00062	1143	5	140,31	0,59	14,91	0,07	14,74	0,08	146,30	0,61
11606	GeoB14904-2	2,81216	0,00019	0,3099	0,0008	0,17889	0,00060	4992	21	135,78	0,47	18,63	0,07	18,52	0,07	143,10	0,50
11606*	GeoB14904-2	2,66942	0,00016	0,4198	0,0008	0,16548	0,00041	3269	10	138,48	0,44	17,07	0,05	16,96	0,05	145,30	0,46
11606*	GeoB14904-2	2,66939	0,00013	0,4188	0,0012	0,16622	0,00036	3269	12	138,92	0,72	17,15	0,04	17,04	0,05	145,79	0,75
11608	GeoB14904-2	2,62425	0,00011	0,4788	0,0013	0,15903	0,00052	2657	11	138,05	0,63	16,36	0,06	16,25	0,06	144,56	0,66
11608	GeoB14904-2	2,65760	0,00010	0,3271	0,0010	0,18363	0,00055	4580	20	136,91	0,59	19,14	0,06	19,04	0,07	144,50	0,62
11608*	GeoB14904-2	2,63468	0,00012	0,3524	0,0008	0,17103	0,00039	3970	13	138,07	0,43	17,70	0,05	17,59	0,05	145,13	0,45
11608*	GeoB14904-2	2,63503	0,00015	0,3508	0,0008	0,17083	0,00054	3965	15	138,43	0,61	17,67	0,06	17,57	0,06	145,50	0,64
11603	GeoB14904-2	2,20281	0,00020	0,5235	0,0028	0,13493	0,00096	1751	16	141,77	1,00	13,68	0,10	13,55	0,11	147,32	1,04
11603	GeoB14904-2	2,52867	0,00010	1,2380	0,0018	0,12082	0,00046	754	3	145,24	0,43	12,13	0,05	11,94	0,08	150,24	0,44
11607	GeoB14904-2	2,43193	0,00012	0,3587	0,0006	0,18259	0,00049	3800	12	137,04	0,47	19,02	0,06	18,91	0,06	144,58	0,50
11607	GeoB14904-2	2,56852	0,00010	0,8084	0,0017	0,17214	0,00070	1671	8	139,02	0,59	17,81	0,08	17,66	0,09	146,16	0,62
11597	GeoB14904-2	2,92634	0,00015	0,9312	0,0017	0,22933	0,00054	2216	7	132,88	0,46	24,55	0,07	24,40	0,08	142,39	0,49
11597	GeoB14904-2	3,25450	0,00009	1,1781	0,0053	0,21065	0,00089	1772	11	133,16	0,46	22,34	0,10	22,17	0,12	141,79	0,49
11588	GeoB14904-2	2,37378	0,00011	0,3154	0,0007	0,19198	0,00053	4444	16	137,12	0,47	20,09	0,06	19,98	0,06	145,10	0,50
11588[2]	GeoB14904-2	2,59461	0,00008	0,3843	0,0008	0,19001	0,00054	3914	13	137,07	0,64	19,87	0,06	19,76	0,06	144,96	0,68
11589	GeoB14904-2	2,79677	0,00013	0,5837	0,0015	0,18657	0,00062	2748	12	139,10	0,73	19,43	0,07	19,31	0,08	146,92	0,78
11589	GeoB14904-2	2,80040	0,00008	0,7542	0,0010	0,18086	0,00040	2047	5	138,38	0,40	18,80	0,05	18,66	0,06	145,89	0,42
11591	GeoB14904-2	3,11920	0,00012	0,3823	0,0008	0,19037	0,00048	4779	15	135,25	0,45	19,94	0,05	19,84	0,06	143,07	0,48
11591[2]	GeoB14904-2	3,47633	0,00010	0,5350	0,0007	0,18991	0,00040	3757	9	135,69	0,39	19,88	0,05	19,77	0,05	143,50	0,42
11593	GeoB14904-2	3,06420	0,00015	0,7544	0,0014	0,18183	0,00049	2285	8	138,06	0,50	18,92	0,06	18,78	0,06	145,61	0,53
11593	GeoB14904-2	3,38060	0,00008	1,3085	0,0017	0,17156	0,00027	1351	3	138,93	0,35	17,75	0,03	17,58	0,06	146,03	0,37
11595	GeoB14904-2	3,97940	0,00018	0,9267	0,0020	0,15374	0,00045	2038	7	136,43	0,47	15,81	0,05	15,67	0,06	142,63	0,49
11595	GeoB14904-2	3,19221	0,00011	1,6964	0,0048	0,18018	0,00096	1034	6	137,48	0,41	18,74	0,11	18,54	0,13	144,89	0,43
11601	GeoB14904-2	2,68580	0,00011	0,6992	0,0015	0,13546	0,00055	1602	7	142,89	0,62	13,72	0,06	13,58	0,07	148,51	0,65
11601	GeoB14904-2	2,83456	0,00010	1,6045	0,0028	0,13040	0,00052	704	3	143,03	0,45	13,18	0,06	12,96	0,09	148,39	0,47
11602	GeoB14904-2	3,39481	0,00012	1,0051	0,0022	0,13210	0,00038	1374	5	142,76	0,68	13,36	0,04	13,22	0,06	148,21	0,71
11602	GeoB14904-2	3,02551	0,00009	1,2744	0,0019	0,12759	0,00038	927	3	142,27	0,38	12,89	0,04	12,71	0,07	147,49	0,40
11604	GeoB14904-2	2,50295	0,00010	0,5655	0,0010	0,13736	0,00051	1877	8	143,85	0,66	13,91	0,06	13,78	0,06	149,58	0,69

Continued on next page

Table C.5 – *continued from previous page*

Lab No IUP	Core	^{238}U (μg/g)	2σ (μg/g)	^{232}Th (ng/g)	2σ (ng/g)	^{230}Th/^{238}U AR	2σ AR	^{230}Th/^{232}Th AR	2σ AR	δ^{234}U ‰	2σ ‰	Age uncor (ka)	2σ ka	Age (ka BP)	2σ (‰)	δ^{234}U$_i$ (‰)	2σ (‰)
11604	GeoB14904-2	2,62590	0,00011	0,7662	0,0010	0,13104	0,00043	1374	5	144,63	0,55	13,23	0,05	13,08	0,06	150,10	0,57
11609	GeoB14904-2	2,83432	0,00010	0,3338	0,0006	0,18130	0,00053	4751	17	135,61	0,55	18,90	0,06	18,80	0,06	143,03	0,58
11609	GeoB14904-2	2,91532	0,00009	0,6800	0,0014	0,17627	0,00051	2303	8	138,45	0,56	18,28	0,06	18,15	0,07	145,76	0,59
11764	GeoB14904-2	3,30369	0,00013	0,7839	0,0019	0,12363	0,00038	1602	6	142,92	0,62	12,46	0,04	12,32	0,05	148,01	0,65
11764	GeoB14904-2	2,67013	0,00011	1,1847	0,0046	0,12225	0,00084	846	7	143,53	0,60	12,30	0,09	12,12	0,10	148,55	0,62
11771	GeoB14904-2	2,67341	0,00012	1,1863	0,0021	0,22694	0,00046	1572	4	135,47	0,63	24,21	0,06	24,02	0,08	145,00	0,67
11771	GeoB14904-2	2,21044	0,00006	1,4286	0,0063	0,24212	0,00145	1145	9	133,74	0,73	26,07	0,18	25,84	0,19	143,88	0,79
11775	GeoB14904-2	2,62851	0,00010	0,5499	0,0016	0,26144	0,00075	3845	16	129,73	0,62	28,55	0,10	28,43	0,10	140,60	0,67
11775	GeoB14904-2	2,28005	0,00009	1,7307	0,0076	0,25485	0,00129	1031	7	130,95	0,85	27,70	0,16	27,44	0,19	141,52	0,92
11770	GeoB14904-2	2,82850	0,00020	0,7950	0,0020	0,23418	0,00088	2550	12	135,13	0,68	25,08	0,11	24,93	0,11	145,01	0,73
11770	GeoB14904-2	2,48467	0,00007	1,5853	0,0058	0,23298	0,00108	1118	7	134,69	0,66	24,95	0,13	24,71	0,15	144,45	0,71
11772	GeoB14904-2	3,15420	0,00020	0,3950	0,0011	0,24373	0,00068	5938	24	131,67	0,44	26,32	0,08	26,22	0,08	141,81	0,47
11772	GeoB14904-2	3,34631	0,00011	0,8401	0,0029	0,24350	0,00096	2971	16	128,44	0,51	26,38	0,12	26,25	0,12	138,34	0,55
11774	GeoB14904-2	3,27221	0,00018	0,5994	0,0013	0,25045	0,00068	4165	14	131,59	0,41	27,14	0,08	27,02	0,09	142,05	0,44
11774	GeoB14904-2	3,19245	0,00008	1,1347	0,0029	0,24765	0,00094	2141	10	131,65	0,54	26,80	0,12	26,64	0,12	141,95	0,59
11619	GeoB 12740-1	3,87354	0,00014	0,2664	0,0006	0,17049	0,00043	7607	26	137,80	0,54	17,64	0,05	17,55	0,05	144,83	0,57
11619	GeoB 12740-1	3,45843	0,00011	0,2375	0,0004	0,17230	0,00029	7670	19	139,21	0,51	17,82	0,03	17,73	0,04	146,39	0,53
11624	GeoB 12740-1	3,21978	0,00015	0,1589	0,0005	0,19838	0,00061	12369	54	139,42	0,62	20,78	0,07	20,69	0,07	147,84	0,66
11624	GeoB 12740-1	3,33066	0,00013	0,3280	0,0005	0,19659	0,00033	6120	14	137,53	0,58	20,61	0,04	20,51	0,04	145,75	0,61
11614	GeoB 12740-1	3,52093	0,00015	0,4746	0,0014	0,19619	0,00053	4490	18	139,37	0,38	20,53	0,06	20,42	0,06	147,67	0,40
11614	GeoB 12740-1	3,95734	0,00012	0,5416	0,0010	0,18299	0,00047	4085	13	139,36	0,33	19,02	0,05	18,92	0,06	147,04	0,35
11615	GeoB 12740-1	3,74068	0,00017	0,3407	0,0009	0,25843	0,00067	8751	33	133,09	0,53	28,08	0,08	27,99	0,09	144,06	0,58
11615	GeoB 12740-1	3,66566	0,00013	0,5595	0,0016	0,24596	0,00080	4926	22	132,61	0,48	26,57	0,10	26,46	0,10	142,92	0,51
11617	GeoB 12740-1	3,95953	0,00021	0,3767	0,0012	0,16426	0,00057	5320	25	137,85	0,47	16,95	0,06	16,85	0,06	144,59	0,50
11617	GeoB 12740-1	3,88264	0,00013	0,2841	0,0006	0,16971	0,00031	7072	19	138,17	0,42	17,55	0,04	17,46	0,04	145,18	0,45
11618	GeoB 12740-1	4,35727	0,00024	0,3716	0,0015	0,18102	0,00061	6534	34	136,11	0,51	18,86	0,07	18,77	0,07	143,54	0,54
11618	GeoB 12740-1	4,22290	0,00015	0,2897	0,0004	0,18167	0,00027	8065	16	136,71	0,45	18,92	0,03	18,83	0,03	144,20	0,47
11621	GeoB 12740-1	3,20334	0,00028	0,6427	0,0020	0,20117	0,00065	3085	14	140,29	0,70	21,08	0,08	20,96	0,08	148,87	0,74
11621	GeoB 12740-1	3,05534	0,00010	0,5852	0,0011	0,20855	0,00038	3337	9	136,53	0,48	22,02	0,05	21,90	0,05	145,26	0,51
11622	GeoB 12740-1	3,90684	0,00020	0,4019	0,0011	0,20301	0,00055	6072	23	138,26	0,49	21,34	0,07	21,24	0,07	146,83	0,52
11622	GeoB 12740-1	3,91062	0,00016	0,1400	0,0003	0,19923	0,00036	17031	46	136,39	0,42	20,94	0,04	20,86	0,04	144,69	0,45
11623	GeoB 12740-1	3,70589	0,00024	0,4345	0,0021	0,20346	0,00088	5326	34	136,35	0,48	21,43	0,10	21,33	0,10	144,84	0,52
11623	GeoB 12740-1	3,57572	0,00016	0,2364	0,0005	0,20441	0,00047	9469	29	136,63	0,76	21,53	0,06	21,44	0,06	145,18	0,81
11627	GeoB 12740-1	4,10809	0,00020	0,2824	0,0009	0,24180	0,00059	10784	43	131,42	0,37	26,09	0,07	26,00	0,07	141,46	0,40
11627	GeoB 12740-1	4,11436	0,00018	0,3281	0,0007	0,24574	0,00049	9889	28	131,62	0,63	26,57	0,06	26,48	0,06	141,86	0,68
11649	M2004-02	3,64658	0,00015	0,1517	0,0003	0,20282	0,00045	14908	48	136,38	0,53	21,35	0,05	21,27	0,05	144,84	0,57
11649	M2004-02	3,74053	0,00014	0,3386	0,0010	0,17279	0,00062	5841	28	135,63	0,61	17,94	0,07	17,85	0,07	142,66	0,64
GIF-1634[4]	M2004-02	3,86170	0,00694	4,6657	0,0129	0,20272	0,00322	513	8	136,49	2,30	21,37	0,42	20,97	0,55	144,98	2,30

Table C.6.: Duplicate $^{230}Th/U$ measurements from GeoB 20933-1 and GeoB 20960-1 (Angola) and GeoB 14905-2 (Mauritania) (chapter 6 and 7). 'AR': Activity Ratio.
* rejected due to very high ^{232}Th concentration
[1] Wefing et al. (2017), recalculated according to Kerber et al. (2023); [2] Stuhrmann (2023)

Lab No IUP	Core	^{238}U ($\mu g/g$)	2σ ($\mu g/g$)	^{232}Th (ng/g)	2σ (ng/g)	$^{230}Th/^{238}U$ AR	2σ AR	$^{230}Th/^{232}Th$ AR	2σ AR	$\delta^{234}U$ ‰	2σ ‰	Age uncor (ka)	2σ ka	Age (ka BP)	2σ (‰)	$\delta^{234}U_i$ (‰)	2σ (‰)
7943[1]	GeoB 29033-1	3,51787	0,00009	2,8083	0,0057	0,28645	0,00065	1096	3	128,71	0,57	31,74	0,09	31,47	0,13	140,70	0,63
7943	GeoB 29033-1	3,86683	0,00100	1,1163	0,0030	0,28519	0,00063	3054	11	127,99	0,41	31,60	0,08	31,45	0,09	139,90	0,44
7945[1]	GeoB 29033-1	3,58454	0,00010	1,3689	0,0025	0,28722	0,00058	2299	6	127,19	0,45	31,89	0,07	31,73	0,09	139,13	0,49
7945	GeoB 29033-1	3,33799	0,00036	0,6546	0,0013	0,28765	0,00060	4544	13	127,89	0,53	31,92	0,08	31,80	0,08	139,93	0,58
7948[1]	GeoB 29033-1	3,07680	0,00009	2,9195	0,0053	0,29435	0,00061	949	3	127,88	0,45	32,78	0,08	32,48	0,14	140,18	0,50
7948	GeoB 29033-1	2,77560	0,00031	3,2406	0,0065	0,29574	0,00081	787	3	129,33	0,64	32,91	0,11	32,54	0,18	141,80	0,70
12078	GeoB20960-1	3,15793	0,00020	1,4764	0,0052	0,30498	0,00140	2018	12	127,04	0,82	34,19	0,19	34,00	0,19	139,86	0,91
12078	GeoB20960-1	3,20853	0,00014	1,3607	0,0021	0,30632	0,00060	2236	6	126,85	0,39	34,38	0,08	34,20	0,10	139,73	0,43
12079	GeoB20960-1	3,87601	0,00028	1,1055	0,0035	0,32314	0,00148	3492	20	125,56	0,71	36,66	0,20	36,51	0,20	139,21	0,79
12079	GeoB20960-1	3,26415	0,00017	0,9389	0,0016	0,32277	0,00065	3475	9	126,07	0,48	36,59	0,09	36,44	0,10	139,76	0,53
12080	GeoB20960-1	2,94852	0,00017	2,2395	0,0064	0,32296	0,00127	1308	6	125,81	0,63	36,62	0,17	36,36	0,20	139,43	0,70
12080	GeoB20960-1	2,74472	0,00013	0,5472	0,0009	0,32269	0,00067	5012	13	125,37	0,45	36,60	0,09	36,48	0,09	138,99	0,50
12054	GeoB14905-2	2,81063	0,00015	1,1663	0,0017	0,29729	0,00054	2192	5	130,21	0,45	33,08	0,07	32,90	0,09	142,91	0,50
12054[2]	GeoB14905-2	2,39596	0,00076	1,3479	0,0030	0,29684	0,00111	1628	7	130,95	1,11	33,00	0,15	32,78	0,17	143,67	1,22
12060[2]	GeoB14905-2	2,53857	0,00014	1,1014	0,0019	0,28175	0,00056	1987	5	133,25	0,46	30,99	0,07	30,81	0,09	145,39	0,51
12060	GeoB14905-2	2,79976	0,00021	1,3027	0,0020	0,28068	0,00062	1865	5	131,27	0,58	30,92	0,08	30,73	0,10	143,19	0,63
12070	GeoB14905-2	2,76319	0,00012	1,3820	0,0032	0,29462	0,00081	1808	7	129,07	0,59	32,77	0,11	32,58	0,12	141,53	0,65
12070[2]	GeoB14905-2	2,79560	0,00015	0,7256	0,0016	0,29634	0,00077	3534	12	129,20	0,58	32,99	0,10	32,85	0,11	141,78	0,64
12055[2]	GeoB14905-2	2,82544	0,00008	1,7315	0,0027	0,30526	0,00060	1522	4	125,39	0,55	34,29	0,08	34,06	0,11	138,07	0,61
12055*	GeoB14905-2	2,98740	0,00025	7,4021	0,0151	0,30285	0,00072	377	1	127,28	0,63	33,91	0,10	33,21	0,33	139,81	0,70

Table C.7.: ^{14}C and $\delta^{13}C$ results of the Gulf of Cádiz from chapter 6.
Samples denoted with * did not pass the quality control (chapter 3.4.2) due to an ^{232}Th concentration > 2 ng/g.
$\delta^{13}C$ measurement: Stellbrink (2023)
[1] Hemsing (2017) and references therein; [2] Beisel (2021); [3] Hemsing unpublished.

Lab No IUP	Lab No MAMS	Core	Depth (cm)	σ (cm)	Age (ka BP)	2σ (ka)	^{14}C Age (ka BP)	1σ (ka)	$\Delta^{14}C$ (‰)	2σ (‰)	B_{atm} age (a)	2σ (a)	$\delta^{13}C$ (‰)	σ (‰)
11662	62343	M2004-02	41	0	10,9732	0,07	9,95	0,03	93	12	367	74		
11665	63013	M2004-02	131	0	20,2	0,0848	18,41	0,06	163	21	1713	140	-0,095	0,009
11666	62341	M2004-02	140	0	20,1142	0,0661	18,48	0,09	142	27	1843	192	-0,545	0,004
11649	62333	M2004-02	140,5	0	21,2705	0,0548	18,47	0,07	315	24	893	146		
11667	63014	M2004-02	200	0	22,8574	0,0867	21,24	0,07	128	23	2380	185	-2,259	0,009
11668	63015	M2004-02	301	0	30,4603	0,1331	33,58	0,21	-389	33	7318	427	-4,468	0,073
8400[1]	31379	MD08-3231	7,5	2,5	18,646	0,06	16,50	0,05	223	17	1249	146		
8401[1]	31376	MD08-3231	17,5	2,5	22,005	0,097	17,60	0,05	601	27	-445	143		
8411[1]	31369	MD08-3231	22,5	2,5	20,024	0,068	17,68	0,05	248	18	1105	117		
6577[1]	21744	MD08-3231	37,5	2,5	23,314	0,067	19,77	0,06	432	23	365	138		
8402[1]	31368	MD08-3231	47,5	2,5	23,353	0,094	19,87	0,05	422	25	426	146		
8403[1]	31377	MD08-3231	65	5	23,529	0,077	19,89	0,06	448	24	381	139		
8404[2]	46611	MD08-3231	95	5	27,062	0,098	22,54	0,10	598	43	-99	238		
8405[1]	31375	MD08-3231	105	5	26,761	0,092	23,02	0,07	451	30	624	172		
8406[2]	46610	MD08-3231	115	5	27,443	0,102	22,74	0,10	632	44	-496	233		
6584[1]	21750	MD08-3231	155	5	27,806	0,081	22,98	0,07	654	33	-717	243		
7009[1]	24543	MD08-3231	175	5	27,378	0,067	24,26	0,08	339	28	1077	197		

Continued on next page

Table C.7 – *continued from previous page*

Lab No IUP	Lab No MAMS	Core	Depth (cm)	σ (cm)	Age (ka BP)	2σ (ka)	^{14}C Age (ka BP)	1σ (ka)	Δ^{14}C (‰)	2σ (‰)	B_{atm} age (a)	2σ (a)	δ^{13}C (‰)	σ (‰)
8407[2]	46613 / 46615	MD08-3231	185	5	28,759	0,094	25,17	0,16	414	60	663	354		
8306[2]	46616	MD08-3231	195	5	30,254	0,115	26,83	0,14	379	50	750	318		
7020[2]	46612	MD08-3231	215	5	27,533	0,085	24,13	0,10	388	39	828	230		
7019[2]	47737	MD08-3231	225	5	33,147	0,091	29,44	0,15	413	54	709	323		
7018[3]	34012	MD08-3231	235	5	33,695	0,08	29,33	0,24	535	95	229	503		
8408[2]	46845	MD08-3231	255	5	36,087	0,129	30,02	0,22	877	107	-1647	493		
7015[2]	47745	MD08-3231	265	5	35,585	0,119	31,29	0,17	508	69	30	380		
7014[1]	24548	MD08-3231	275	5	35,895	0,112	31,30	0,12	563	51	-168	276		
7012[1]	24546	MD08-3231	295	5	36,729	0,112	32,65	0,14	460	55	239	311		
7021[2]	46618	MD08-3231	305	5	37,366	0,124	32,85	0,25	543	97	-124	509		
11612	63562	GeoB 12740-1	5,5	1,5	12,7014	0,0495	11,69	0,03	85	10	999	128		
11613	64375	GeoB 12740-1	26	1	17,5107	0,0689	17,72	0,05	-84	13	3291	111		
11617	63005	GeoB 12740-1	29,5	0,5	17,4608	0,0368	17,59	0,06	-74	13	3185	126	-1,112	0,006
11618	63006	GeoB 12740-1	35	1	18,8348	0,0323	17,70	0,06	78	16	2152	129	0,217	0,007
11619	63007 / 63008	GeoB 12740-1	41	1	17,7341	0,035	17,56	0,08	-40	19	3086	163	-1,487	0,007
11620	63563	GeoB 12740-1	46	1	19,384	0,0382	18,19	0,05	85	14	2162	110		
11621	59338	GeoB 12740-1	58,5	1,5	21,8966	0,0521	19,00	0,06	328	22	1055	138		
11622	62344	GeoB 12740-1	62	1	20,8577	0,0415	19,11	0,08	156	23	1841	169	-0,489	0,005
11614	64381	GeoB 12740-1	87,5	1,5	18,9173	0,0551	19,67	0,05	-148	13	4005	136		
11623	63564	GeoB 12740-1	94,5	1,5	21,4445	0,0572	20,03	0,06	106	18	2292	147		
11624	63009	GeoB 12740-1	99,5	1,5	20,5141	0,0411	20,10	0,07	-20	18	3106	157	-3,102	0,005

Continued on next page

Table C.7 – *continued from previous page*

Lab No IUP	Lab No MAMS	Core	Depth (cm)	σ (cm)	Age (ka BP)	2σ (ka)	^{14}C Age (ka BP)	1σ (ka)	Δ^{14}C (‰)	2σ (‰)	B_{atm} age (a)	2σ (a)	δ^{13}C (‰)	σ (‰)
11625	59339	GeoB 12740-1	105	1	22,4852	0,0585	19,64	0,06	317	23	1016	168		
11626	59340	GeoB 12740-1	114	1	22,935	0,1115	20,09	0,07	315	28	1112	226		
11627	63010	GeoB 12740-1	158	2	26,4757	0,0634	24,22	0,09	207	29	1886	237		
11628	62345	GeoB 12740-1	169	1	29,0181	0,0684	25,38	0,15	421	55	640	315	0,054	0,012
11629	63011	GeoB 12740-1	182,5	1,5	28,5584	0,066	25,49	0,10	326	35	1236	221		
11615	64366	GeoB 12740-1	188,5	1,5	26,4573	0,0997	25,41	0,10	39	28	3127	270		
11582	59323	GeoB 12740-1	291,5	1,5	33,0283	0,1238	32,34	0,25	-28	62	3727	518	-3,418	0,006
11583	59324 / 59325	GeoB 12740-1	386	1	34,0156	0,1213	36,14	0,54	-312	95	6764	1092	-4,419	0,004
11584	59326 / 59327	GeoB 12740-1	472	1	38,5867	0,1215	43,08	1,25	-476	168	9548	2493	-0,691	0,004
11580	57614	GeoB 12725-1	321	5	37,4286	0,2002	40,08	1,04	-345	172	7053	2083	-2,445	0,009
11581	59322	GeoB 12725-1	370,5	0,5	38,9654	0,2086	41,41	0,72	-345	120	7688	1448	-3,113	0,008
11573	63003	GeoB 18139-1	87,5	2,5	17,1852	0,131	15,53	0,05	157	23	1393	154		
11877	64373	GeoB 18139-1	87,5	2,5	17,7817	0,0576	15,53	0,04	243	14	1022	101		
11878	63021	GeoB 18139-1	96,5	0,5	18,4415	0,0631	16,68	0,05	167	18	1487	121		
11879	64374	GeoB 18139-1	108,5	0,5	18,1578	0,0577	17,41	0,04	29	13	2621	137		
11881	63565	GeoB 18139-1	121,5	0,5	21,868	0,0739	19,32	0,06	271	21	1397	133		
11882	63566	GeoB 18139-1	125,5	0,5	21,9339	0,0516	19,25	0,05	294	19	1271	125		
11884	64382	GeoB 18139-1	136	2	22,537	0,0875	19,70	0,06	315	23	1027	160		
11885	63022	GeoB 18139-1	145,5	2,5	22,7465	0,0818	20,02	0,06	297	24	1230	140		
11886	63558	GeoB 18139-1	150,5	2,5	22,1167	0,0917	19,87	0,06	223	22	1713	155		
11887	64372	GeoB 18139-1	155,5	2,5	23,3343	0,0762	19,80	0,06	430	24	374	143		

Continued on next page

Table C.7 – *continued from previous page*

Lab No IUP	Lab No MAMS	Core	Depth (cm)	σ (cm)	Age (ka BP)	2σ (ka)	^{14}C Age (ka BP)	1σ (ka)	Δ^{14}C (‰)	2σ (‰)	B_{atm} age (a)	2σ (a)	δ^{13}C (‰)	σ (‰)
11890	64367	GeoB 18139-1	173	2	22,6238	0,0895	19,92	0,06	294	23	1174	138		
11891	64377	GeoB 18139-1	178,5	1,5	26,4111	0,1037	23,97	0,09	236	30	1754	257		
11575	59320	GeoB 18139-1	251,5	0,5	30,2589	0,1432	29,20	0,17	26	47	3131	394	-6,107	0,013
11576	59321	GeoB 18139-1	348,5	1,5	34,8061	0,1989	34,02	0,30	-20	76	3584	639	-0,427	0,005
7507[1]	32093	GeoB 18141-1	17	3	3,37	0,06	3,70	0,08	-51	19	551	169		
7545[1]	32100	GeoB 18141-1	66	3	17,71	0,10	16,30	0,05	120	20	1817	124		
7508*[1]	31371	GeoB 18141-1	70	3	19,46	0,15	16,65	0,05	325	30	528	185		
7547[3]	34016	GeoB 18141-1	83	3	19,54	0,20	16,51	0,06	362	39	319	219		
7509[1]	32092	GeoB 18141-1	95	3	20,88	0,20	17,47	0,06	422	40	160	219		
7548[3]	34017	GeoB 18141-1	107	3	20,49	0,22	17,28	0,07	388	44	322	246		
7510[1]	31373	GeoB 18141-1	127	3	20,83	0,13	17,72	0,06	369	30	462	181		
7551[3]	34018	GeoB 18141-1	138	3	20,81	0,16	17,51	0,07	402	36	268	208		
7552[3]	34019	GeoB 18141-1	156	3	20,91	0,22	17,52	0,07	417	45	193	241		
7512[1]	31370	GeoB 18141-1	184	3	21,73	0,09	18,34	0,05	414	23	496	116		
7554[3]	34020	GeoB 18141-1	275	3	20,80	0,14	18,19	0,07	287	33	961	205		
7514*[1]	31367	GeoB 18141-1	282	3	22,19	0,12	18,66	0,05	436	27	425	167		
7556[3]	34022	GeoB 18141-1	291	3	21,76	0,14	18,76	0,08	347	34	887	179		
7515[3]	34013	GeoB 18141-1	310	3	22,32	0,26	19,09	0,08	383	51	696	324		
7513[1]	32095	GeoB 18141-1	328	3	22,84	0,13	19,58	0,07	385	32	708	207		
7516[3]	34014	GeoB 18141-1	518	3	22,90	0,24	19,41	0,09	427	53	429	321		
7557[3]	34023	GeoB 18141-1	535	3	22,72	0,14	19,79	0,08	331	35	999	204		

Continued on next page

Table C.7 – *continued from previous page*

Lab No IUP	Lab No MAMS	Core	Depth (cm)	σ (cm)	Age (ka BP)	2σ (ka)	^{14}C Age (ka BP)	1σ (ka)	Δ^{14}C (‰)	2σ (‰)	B_{atm} age (a)	2σ (a)	δ^{13}C (‰)	σ (‰)
7517[1]	31374	GeoB 18141-1	549	3	23,45	0,08	19,77	0,07	456	29	260	163		
7559[3]	34024	GeoB 18141-1	561	3	23,08	0,15	19,90	0,09	371	39	722	265		
7518*[1]	31372	GeoB 18141-1	568	3	24,32	0,17	21,79	0,06	259	33	1516	198		
7562[3]	34025	GeoB 18141-1	578	3	24,44	0,19	21,66	0,10	298	45	1314	253		
7519[1]	32096	GeoB 18141-1	584	3	25,12	0,17	21,57	0,09	424	42	743	248		
7563*[3]	34027	GeoB 18141-1	593	3	32,49	0,37	28,69	0,23	436	104	307	508		
7522[3]	34015	GeoB 18141-1	805	3	34,48	0,11	30,81	0,29	402	103	759	625		
7523[1]	32099	GeoB 18141-1	810	3	34,77	0,10	31,16	0,25	390	90	673	536		
7567[1]	32098	GeoB 18141-1	870	3	40,19	0,36	36,52	0,47	384	173	1486	1006		

Table C.8.: ^{14}C and $\delta^{13}C$ results from Mauritania from chapter 6.
Samples denoted with * did not pass the quality control (chapter 3.4.2) due to an ^{232}Th concentration > 2 ng/g.
$\delta^{13}C$ measurement: Stellbrink (2023)
[1] Beisel et al. (2023); [2] $^{230}Th/U$ dating Stuhrmann (2023); [3] $^{230}Th/U$ dating Wienberg et al. (2018), recalculated according to Kerber et al. (2023); [4] $^{230}Th/U$ dating Schneider (2018), recalculated according to Kerber et al. (2023); [5] Beisel (2021) .

Lab No IUP	Lab No MAMS	Core	Depth (cm)	σ (cm)	Age (ka BP)	2σ (ka)	^{14}C Age (ka BP)	1σ (ka)	$\Delta^{14}C$ (‰)	2σ (‰)	B_{atm} age (a)	2σ (a)	$\delta^{13}C$ (‰)	σ (‰)
8928[4,5]	48628	GeoB 14899-1	5,5	1,5	24,15	0,07	28,52	0,14	-466	19	8402	287		
8929[1,4]	46867 / 46868	GeoB 14899-1	10,5	1,5	35,48	0,08	30,39	0,33	670	140	-781	684		
12066[2]	67220	GeoB 14899-1	25	1	36,46	0,16	29,73	0,11	1036	69	-2461	310		
8935[1,4]	46865	GeoB 14899-1	160,5	1,5	36,96	0,09	31,90	0,28	655	117	-732	579		
12067[2]	67225	GeoB 14899-1	179,25	1	37,54	0,12	33,28	0,16	490	63	172	358		
12061[2]	67222	GeoB 14899-1	285,25	1	38,91	0,10	31,95	0,14	1076	77	-1681	307		
12063[2]	67215	GeoB 14899-1	463	2	40,29	0,10	32,39	0,15	1324	92	-2697	334		
8230[1,3]	48615	GeoB 14905-2	1	1	13,05	0,06	11,93	0,04	98	13	825	111		
8231[1,3]	48617	GeoB 14905-2	199	1	13,58	0,07	12,30	0,04	118	14	561	112		
8232[1,3]	48624	GeoB 14905-2	281	1	14,09	0,09	12,49	0,04	162	16	302	128		
8813[1]	47313	GeoB 14905-2	491,5	1,5	14,23	0,04	12,90	0,03	123	11	588	77		
8814[1]	46862 / 46859	GeoB 14905-2	557,5	1,5	19,88	0,04	17,04	0,09	329	31	580	195		
8235[1,3]	48616	GeoB 14905-2	590,5	1,5	20,79	0,11	17,41	0,05	416	26	199	148		
12060[2]	67205	GeoB 14905-2	625	5	30,81	0,09	27,07	0,08	430	33	636	206		
12070[2]	68125	GeoB 14905-2	655	5	32,85	0,11	29,02	0,21	438	78	560	442		
12054[2]	68122	GeoB 14905-2	684	2	32,78	0,17	29,38	0,15	365	57	926	325		

Continued on next page

Table C.8 – *continued from previous page*

Lab No IUP	Lab No MAMS	Core	Depth (cm)	σ (cm)	Age (ka BP)	2σ (ka)	^{14}C Age (ka BP)	1σ (ka)	Δ^{14}C (‰)	2σ (‰)	B_{atm} age (a)	2σ (a)	δ^{13}C (‰)	σ (‰)
12058[2]	67216	GeoB 14905-2	802,5	2,5	33,51	0,13	30,22	0,11	340	43	1232	257		
12055[2]	67227 / 68123	GeoB 14905-2	837,5	2,5	34,06	0,11	31,27	0,23	259	73	1837	487		
12062[2]	68124 / 67214	GeoB 14905-2	854,5	0,5	34,82	0,11	31,10	0,26	410	91	573	537		
12053[2]	67213 / 67219	GeoB 14905-2	955	3	35,61	0,08	32,79	0,22	254	68	1499	455		
11763	67204	GeoB14904-2	1	1	8,08	0,07	12,10	0,02	-411	6	4823	89		
11764	64369	GeoB14904-2	21,5	1,5	12,32	0,05	12,30	0,03	-39	9	1911	65		
11601	64368	GeoB14904-2	145,5	1,5	13,58	0,07	12,56	0,03	83	12	819	103		
11602	62336	GeoB14904-2	159	1	13,22	0,06	12,82	0,05	3	14	1485	119	-7,754	0,004
11603	62334	GeoB14904-2	175	1	13,55	0,11	12,76	0,05	52	19	1063	158	-8,848	0,003
11604	64371	GeoB14904-2	190,5	2,5	13,78	0,06	12,80	0,03	77	11	877	109		
11769	64370	GeoB14904-2	198	2	14,14	0,11	12,93	0,03	106	17	705	128		
11606	62338	GeoB14904-2	349,5	1,5	18,52	0,07	16,78	0,07	165	24	1620	166	-4,447	0,012
11607	62339	GeoB14904-2	369,5	1,5	18,91	0,06	16,57	0,07	252	25	914	171	-7,188	0,015
11608	62342	GeoB14904-2	379,5	2,5	19,04	0,07	16,76	0,07	243	25	970	164	-6,746	0,018
11609	62340	GeoB14904-2	406	6	18,80	0,06	16,95	0,08	179	25	1457	186		
11610	62335	GeoB14904-2	425	1	18,01	0,09	16,78	0,08	95	24	2095	169		
11587[1]	59328	GeoB14904-2	463,5	2,5	19,11	0,06	17,35	0,05	163	17	1506	126	-6,174	0,015
11588[1]	59329	GeoB14904-2	469,5	2,5	19,76	0,06	17,17	0,05	287	20	803	119	-7,267	0,014
11589	62337	GeoB14904-2	469,5	2,5	19,31	0,08	17,21	0,08	214	26	1216	166		
11590[1]	59330	GeoB14904-2	471,5	2,5	19,62	0,06	17,16	0,05	268	19	845	138		
11591[1]	59331	GeoB14904-2	482,5	2,5	19,77	0,05	17,68	0,06	211	19	1310	126		

Continued on next page

Table C.8 – *continued from previous page*

Lab No IUP	Lab No MAMS	Core	Depth (cm)	σ (cm)	Age (ka BP)	2σ (ka)	^{14}C Age (ka BP)	1σ (ka)	Δ^{14}C (‰)	2σ (‰)	B_{atm} age (a)	2σ (a)	δ^{13}C (‰)	σ (‰)
11592[1]	59332	GeoB14904-2	492,5	2,5	20,13	0,06	17,37	0,05	314	20	718	124	-5,528	0,021
11593	64380 / 64379	GeoB14904-2	498	3	18,78	0,06	17,54	0,06	93	19	2074	164		
11594[1]	59333	GeoB14904-2	504,5	1,5	20,36	0,06	17,43	0,06	341	21	602	129		
11596	59334	GeoB14904-2	532,5	2,5	21,66	0,12	21,77	0,08	-87	22	3958	174	-4,800	0,012
11595	64376	GeoB14904-2	532,5	2,5	18,54	0,13	21,65	0,07	-364	15	6447	179		
11597	59335 / 63004	GeoB14904-2	536,5	1,5	24,40	0,08	21,80	0,11	269	36	1458	230	-3,606	0,012
11598[1]	59336	GeoB14904-2	542,5	2	25,33	0,11	22,04	0,08	379	34	999	199		
11599[1]	59337	GeoB14904-2	546	1	25,46	0,12	22,33	0,09	352	35	1216	193		
11770	63016	GeoB14904-2	551	1	24,93	0,11	21,64	0,07	381	30	979	173		
11771	63017	GeoB14904-2	600	1	25,84	0,19	22,12	0,07	451	43	590	329		
11772	63018	GeoB14904-2	632	2	26,22	0,08	22,99	0,08	363	30	1006	183		
11773	67203	GeoB14904-2	658,5	1,5	26,08	0,16	22,97	0,05	345	32	1102	238		
11774	63019	GeoB14904-2	707	2	27,02	0,09	23,45	0,08	421	32	858	198		
11611	64378	GeoB14904-2	785	0,5	28,84	0,07	25,08	0,10	443	38	470	220		
11775	63020	GeoB14904-2	794	1	28,43	0,10	24,78	0,10	425	38	600	209		
12231	67209	GeoB14904-2	882,5	2,5	28,89	0,09	25,71	0,07	342	29	1061	178		
12233	67207	GeoB14904-2	963	4	30,23	0,11	26,51	0,08	430	33	457	223		
9154[1,4]	48633 / 48622	GeoB14890-2	20,5	1,5	10,06	0,04	10,14	0,05	-45	12	1261	98		
9155[1,4]	46861	GeoB14890-2	53	3	12,44	0,04	11,34	0,04	98	12	849	105		
9156[1,4]	46863	GeoB14890-2	109	1	13,45	0,04	12,13	0,04	124	13	457	111		

Continued on next page

Table C.8 – *continued from previous page*

Lab No IUP	Lab No MAMS	Core	Depth (cm)	σ (cm)	Age (ka BP)	2σ (ka)	^{14}C Age (ka BP)	1σ (ka)	Δ^{14}C (‰)	2σ (‰)	B_{atm} age (a)	2σ (a)	δ^{13}C (‰)	σ (‰)
9158[4,5]	46860	GeoB14890-2	228	1	25,39	0,07	23,62	0,12	141	34	2505	240	-1,788	0,008
8801[1,4]	46866	GeoB 14884-1	228	1	37,34	0,09	31,49	0,27	821	122	-1459	544		

Table C.9.: Compiled ^{14}C anomalies from chapter 6. QC: Quality Control: (1) ^{238}U, (2) ^{232}Th, (3) $\delta^{234}U_i$
Ref: Reference: (1) Ruckelshausen (2009), (2) Mangini et al. (2010), (3) Hemsing (2017), (4) Beisel (2021), (5) Hines et al. (2015) (6) de Carvalho Ferreira (2022) (7) Stuhrmann (2023), this study (8) Beisel et al. (2023) (9) Ruckelshausen (2013)
∗old series: cleaned only with water (Mangini et al., 2010; Ruckelshausen, 2009)

Lab No	Label/Core	Ref.	Location	Water depth (m)	^{238}U (μg/g)	2σ (μg/g)	^{232}Th (ng/g)	2σ (ng/g)	Age (ka BP)	2σ (ka)	^{14}C Age (ka)	1σ (ka)	$\delta^{234}U_i$ ‰	2σ ‰	QC	B_{atm} age (a)	2σ (a)
	C1-70*	1,2	Brazil	621	3,1680	0,0030	2,8510	0,0370	15,11	0,91	11,07	0,03	150,54	7,20	(2)	-1696	603
8401	MD08-3231	3	Gulf of Cadiz	550	2,5552	0,0001	1,3272	0,0032	22,01	0,10	17,60	0,05	148,88	1,04		-445	143
8406	MD08-3231	5	Gulf of Cadiz	550	2,9437	0,0001	0,1467	0,0005	27,44	0,10	22,74	0,10	145,77	1,09		-496	233
	C2-68	1,2	Brazil	781	3,2690	0,0030	0,9400	0,0100	29,27	0,82	22,97	0,09	142,80	4,60		-2098	826
6584	MD08-3231	3	Gulf of Cadiz	550	3,7067	0,0002	0,3712	0,0009	27,81	0,08	22,98	0,07	143,85	0,56		-717	243
UCIAMS35362	C2-58	1,2	Brazil	781	3,0170	0,0030	2,4700	0,0200	27,87	0,63	23,00	0,09	151,40	4,00	(2,3)	-700	697
SH_SOI_A05		5	South of Tasmania	1575	2,2142	0,0016	0,3940	0,0116	27,58	0,09	23,07	0,11	138,13	0,65		-223	130
JC142-047-006-c-col-001		6	Tropic Seamount	995	5,3000	0,0120	11,200	0,048	30,36	0,10	25,94	0,09	146,10	1,10	(2)	-257	220
JC142-113-007-cl-001		6	Tropic Seamount	1797	3,4000	0,0070	3,2000	0,0140	31,91	0,52	26,67	0,13	147,70	1,10	(2)	-1262	590
JC142-113-007-Cl-002		6	Tropic Seamount	1797	3,8000	0,0100	3,1000	0,0140	32,05	0,48	27,37	0,09	141,90	1,10	(2)	-703	474
12066	GeoB 14899-1	7	Mauritania	485	2,6128	0,0002	2,2889	0,0047	36,46	0,16	29,73	0,11	142,50	0,99	(2)	-2461	310
8408	MD08-3231	4	Gulf of Cadiz	550	2,5498	0,0001	0,0258	0,0001	36,09	0,13	30,02	0,22	148,06	1,04		-1647	493
8929	GeoB 14899-1	8	Mauritania	485	2,8359	0,0001	0,1570	0,0004	35,48	0,08	30,39	0,33	140,13	0,61		-781	684
8801	GeoB14884-1	8	Mauritania	492	2,9985	0,0001	0,9244	0,0012	37,34	0,09	31,49	0,27	145,21	0,55		-1459	544
GIF-2475	M-189	9	Brazil	808	2,7273	0,0003	0,2723	0,0006	36,88	0,36	31,66	0,39	135,10	8,10		-927	856
8935	GeoB14899-1	8	Mauritania	485	3,0052	0,0001	1,0256	0,0017	36,96	0,09	31,90	0,28	143,02	0,44		-732	579
12061	GeoB 14899-1	7	Mauritania	485	2,7713	0,0001	0,6114	0,0011	38,91	0,10	31,95	0,14	143,32	0,60		-1681	307
12063	GeoB 14899-1	7	Mauritania	485	2,9375	0,0001	1,0936	0,0021	40,29	0,10	32,39	0,15	142,66	0,55		-2697	334
5446	M-222	9	Brazil	808	2,5430	0,0031	0,2057	0,0010	47,43	0,38	38,17	0,87	157,40	3,00	(3)	-6981	1786
5451	M-215	9	Brazil	808	2,5826	0,0026	3,3307	0,0167	47,30	0,58	39,51	1,03	147,50	3,70	(2)	-5531	2145
	C1-7*	1,2	Brazil	621	3,0740	0,0030	73,100	1,000	8,20	3,69	10,59	0,02	141,90	17,50	(2)	3220	2962
HD-5244	C1-33	9	Brazil	621	3,8972	0,0039	0,2935	0,0012	9,15	0,08	10,93	0,05	143,70	1,70		2694	114
	C1-17*	1,2	Brazil	621	4,4540	0,0040	98,200	1,200	8,71	3,21	10,94	0,02	140,60	15,00	(2)	3219	2648
UCIAMS27015	C1-32*	1,2	Brazil	621	4,5330	0,0050	3,0010	0,0150	8,44	0,29	10,94	0,02	144,81	3,63	(2)	3272	288
HD-5136	C1-33	9	Brazil	621	3,8609	0,0054	0,4941	0,0085	8,79	0,29	10,97	0,04	136,20	3,10		2997	249
UCIAMS27016	C1-52*	1,2	Brazil	621	3,3640	0,0030	4,7310	0,0250	10,37	0,41	11,01	0,03	150,70	4,40	(2)	1785	320
UCIAMS35359	C2-30	1,2	Brazil	781	3,7970	0,0040	2,3400	0,0100	10,53	0,19	11,14	0,03	145,10	1,90	(2)	1771	170
HD-4679	C2-36	9	Brazil	781	6,9776	0,0070	0,5909	0,0040	5,64	0,07	11,17	0,05	134,50	1,90	(1,3)	6223	134
ETH-35224	C2-44	1,2	Brazil	781	3,6590	0,0040	0,4990	0,0030	10,52	0,17	11,23	0,05	140,30	2,70		1876	176
11763	GeoB 14904-2		Mauritania	517	3,7963	0,0001	1,0714	0,0042	8,08	0,07	12,10	0,02	149,00	0,57		4823	89
11764N	GeoB 14904-2		Mauritania	517	3,3037	0,0001	0,7839	0,0019	12,32	0,05	12,30	0,03	148,01	0,65		1911	65
11602N	GeoB 14904-2		Mauritania	517	3,3948	0,0001	1,0051	0,0022	13,22	0,06	12,82	0,05	148,21	0,71		1485	119
ETH-35225	C1-113	1,2	Brazil	621	2,7670	0,0050	1,7500	0,0200	14,39	0,43	14,14	0,07	143,50	4,10		1782	292
	C1-130*	1,2	Brazil	621	3,3010	0,0030	16,380	0,070	14,36	0,93	14,40	0,03	149,30	5,60	(2)	2135	686
HD-4502	C2-47	1,2,9	Brazil	781	3,8710	0,0040	5,1000	0,0200	15,18	0,33	15,13	0,06	143,40	2,60	(2)	2357	256
11610	GeoB 14904-2		Mauritania	517	2,5504	0,0001	1,3926	0,0021	18,01	0,09	16,78	0,08	146,16	0,48		2095	169

Continued on next page

Table C.9 – *continued from previous page*

Lab No	Label/Core	Ref.	Location	Water depth (m)	^{238}U (μg/g)	2σ (μg/g)	^{232}Th (ng/g)	2σ (ng/g)	Age (ka BP)	2σ (ka)	^{14}C Age (ka)	1σ (ka)	$\delta^{234}U_i$ ‰	2σ ‰	QC	B_{atm} age (a)	2σ (a)
11879	GeoB 18139-1		Gulf of Cadiz	940	2,6728	0,0001	0,2073	0,0005	18,16	0,06	17,41	0,04	149,55	0,95		2621	137
11593N	GeoB 14904-2		Mauritania	517	3,0642	0,0001	0,7544	0,0014	18,78	0,06	17,54	0,06	145,61	0,53		2074	164
11619	GeoB 12740-1		Gulf of Cadiz	739	3,4584	0,0001	0,2375	0,0004	17,73	0,04	17,56	0,08	146,39	0,53		3086	163
11617	GeoB 12740-1		Gulf of Cadiz	739	3,8826	0,0001	0,2841	0,0006	17,46	0,04	17,59	0,06	145,18	0,45		3185	126
11618	GeoB 12740-1		Gulf of Cadiz	739	4,2229	0,0001	0,2897	0,0004	18,83	0,03	17,70	0,06	144,20	0,47		2152	129
11613	GeoB 12740-1		Gulf of Cadiz	739	3,8893	0,0001	0,6148	0,0013	17,51	0,07	17,72	0,05	146,02	0,55		3291	111
11620	GeoB 12740-1		Gulf of Cadiz	739	4,6659	0,0002	0,2769	0,0004	19,38	0,04	18,19	0,05	143,81	0,49		2162	110
11614	GeoB 12740-1		Gulf of Cadiz	739	3,9573	0,0001	0,5416	0,0010	18,92	0,06	19,67	0,05	147,04	0,35		4005	136
11623	GeoB 12740-1		Gulf of Cadiz	739	3,5757	0,0002	0,2364	0,0005	21,44	0,06	20,03	0,06	145,18	0,81		2292	147
5462	M-119	9	Brazil	808	2,6254	0,0089	12,784	0,147	21,00	0,81	20,08	0,10	160,30	8,00	(2,3)	2686	672
11624	GeoB 12740-1		Gulf of Cadiz	739	3,3307	0,0001	0,3280	0,0005	20,51	0,04	20,10	0,07	145,75	0,61		3106	157
11667	M2004-02		Gulf of Cadiz	523	3,0153	0,0001	0,6796	0,0020	22,86	0,09	21,24	0,07	144,25	0,47		2380	185
11595	GeoB 14904-2		Mauritania	517	3,1922	0,0001	1,6964	0,0048	18,54	0,13	21,65	0,07	144,89	0,43		6447	179
11596	GeoB 14904-2		Mauritania	517	3,1523	0,0001	1,4419	0,0046	21,66	0,12	21,77	0,08	142,35	0,45		3958	174
ETH-35223	C2-68	1,2	Brazil	781	3,7750	0,0040	3,0000	0,0100	23,52	0,38	22,95	0,16	150,90	2,90	(2,3)	3384	463
ETH-35222	C2-55	1,2	Brazil	781	3,3540	0,0050	4,5000	0,0500	25,24	0,69	23,54	0,18	134,90	5,40	(2)	2509	724
9158	GeoB 14890-2	4	Mauritania	580	3,4378	0,0001	1,0724	0,0016	25,39	0,07	23,62	0,12	148,43	0,54		2505	240
11615	GeoB 12740-1		Gulf of Cadiz	739	3,6657	0,0001	0,5595	0,0016	26,46	0,10	25,41	0,10	142,92	0,51		3127	270
8928	GeoB 14899-1	4	Mauritania	485	3,6971	0,0002	0,3918	0,0007	24,15	0,07	28,52	0,14	144,82	0,50		8402	287
11575	GeoB 18139-1		Gulf of Cadiz	940	3,2082	0,0002	0,9676	0,0024	30,26	0,14	29,20	0,17	140,19	0,75		3131	394
5460	M-151	9	Brazil	808	3,5192	0,0039	2,4678	0,0155	31,69	0,42	29,81	0,31	134,90	2,90	(2)	2028	800
11582	GeoB 12740-1		Gulf of Cadiz	739	3,1300	0,0001	0,5832	0,0022	33,03	0,12	32,34	0,25	140,10	0,60		3727	518
11668	M2004-02		Gulf of Cadiz	523	2,9687	0,0001	0,5706	0,0017	30,46	0,13	33,58	0,21	139,95	0,55		7318	427
11576	GeoB 18139-1		Gulf of Cadiz	940	3,5114	0,0002	1,0721	0,0046	34,81	0,20	34,02	0,30	140,88	0,62		3584	639
11583	GeoB 12740-1		Gulf of Cadiz	739	3,1297	0,0001	0,4641	0,0009	34,02	0,12	36,14	0,54	137,36	0,59		6764	1092
HD-5183	C2-94	9	Brazil	781	3,8076	0,0103	10,435	0,045	37,00	0,49	37,53	0,55	140,90	5,30	(2)	4853	1187
5452	M-209	9	Brazil	808	3,6308	0,0022	9,4387	0,0425	41,39	0,48	38,64	0,93	139,60	2,70	(2)	2193	1983
11580	GeoB 12725-1		Gulf of Cadiz	895	3,4758	0,0002	0,7138	0,0030	37,43	0,20	40,08	1,04	139,77	0,65		7053	2083
11581	GeoB 12725-1		Gulf of Cadiz	895	2,8444	0,0002	0,6810	0,0034	38,97	0,21	41,41	0,72	137,34	1,07		7688	1448
11584	GeoB 12740-1		Gulf of Cadiz	739	3,7431	0,0001	0,5521	0,0013	38,59	0,12	43,08	1,25	133,90	0,40		9548	2493

Table C.10.: ^{230}Th/U dating results from Mauritania (GeoB 14905-2) and Angola (GeoB 20933-1 and GeoB 20960-1) from chapter 7. 'AR': Activity Ratio. Sample denoted with * did not pass the quality control (chapter 3.4.2) due to a ^{232}Th concentration between 2-3 ng/g. Sample denoted with _2: different coral polyp.
[1] Stuhrmann (2023); [2] courtesy of Dr. Claudia Wienberg; [3] Wefing et al. (2017), recalculated according to Kerber et al. (2023)

Lab No IUP	Core	Depth (cm)	σ (cm)	^{238}U (μg/g)	2σ (μg/g)	^{232}Th (ng/g)	2σ (ng/g)	^{230}Th/^{238}U AR	2σ AR	^{230}Th/^{232}Th AR	2σ AR	δ^{234}U ‰	2σ ‰	Age uncor (ka)	2σ (ka BP)	Age (ka)	2σ (‰)	δ^{234}U$_i$ (‰)	2σ (‰)
12060[1]	GeoB14905-2	625	5	2,53857	0,00014	1,1014	0,0019	0,28175	0,00056	1987	5	133,25	0,46	30,99	0,07	30,81	0,09	145,39	0,51
12070[1]	GeoB14905-2	655	5	2,7956	0,00015	0,7256	0,0016	0,29634	0,00077	3534	12	129,2	0,58	32,99	0,1	32,85	0,11	141,78	0,64
12054[1]	GeoB14905-2	684	2	2,81063	0,00015	1,1663	0,0017	0,29729	0,00054	2192	5	130,21	0,45	33,08	0,07	32,9	0,09	142,91	0,5
12058[1]	GeoB14905-2	802,5	2,5	2,61335	0,00015	0,9059	0,0016	0,30136	0,00086	2661	9	128,52	1,11	33,67	0,12	33,51	0,13	141,3	1,22
12055[1]	GeoB14905-2	837,5	2,5	2,82544	0,00008	1,7315	0,0027	0,30526	0,0006	1522	4	125,39	0,55	34,29	0,08	34,06	0,11	138,07	0,61
12062[1]	GeoB14905-2	854,5	0,5	2,70505	0,0001	0,37701	0,0008	0,31039	0,00081	6800	23	126,38	0,56	34,93	0,11	34,82	0,11	139,45	0,62
12053[1]	GeoB14905-2	955	3	2,83388	0,0001	0,60576	0,00097	0,31668	0,00059	4527	11	126,98	0,56	35,74	0,08	35,61	0,08	140,44	0,62
7944*[3]	GeoB20933-1	815	0,5	3,92136	0,00013	1,9857	0,0067	0,28671	0,00091	1732	8	129,34	0,48	31,75	0,12	31,56	0,14	141,42	0,53
7945	GeoB20933-1	834,5	0,5	3,33799	0,00036	0,6546	0,0013	0,28765	0,0006	4544	13	127,89	0,53	31,92	0,08	31,8	0,08	139,93	0,58
7946[3]	GeoB20933-1	868	1	3,76462	0,00011	0,9028	0,0023	0,29005	0,00106	3703	16	126,25	0,41	32,28	0,14	32,16	0,14	138,27	0,45
7947[3]	GeoB20933-1	889,5	1,5	3,81176	0,0001	1,3176	0,002	0,29148	0,00046	2583	6	126,81	0,39	32,45	0,06	32,3	0,07	138,94	0,43
7948*	GeoB20933-1	916	1	3,0768	0,00009	2,9195	0,0053	0,29435	0,00061	949	3	127,88	0,45	32,78	0,08	32,48	0,14	140,18	0,5
7949[3]	GeoB20933-1	937	2	3,4563	0,00011	0,8697	0,0016	0,29889	0,00063	3634	10	126,14	0,42	33,43	0,08	33,3	0,09	138,6	0,46
7950[3]	GeoB20933-1	960	1	4,1953	0,00012	0,4644	0,0008	0,29921	0,00062	8277	22	125,98	0,4	33,48	0,08	33,39	0,08	138,45	0,44
10947[2]	GeoB20960-1	114,5	1,5	3,4738	0,0001	0,5971	0,0008	0,2434	0,00049	4325	10	129,98	0,5	26,32	0,07	26,21	0,06	139,99	0,54
12072	GeoB20960-1	165	5	3,90726	0,00018	0,5647	0,001	0,26356	0,0005	5584	14	129,88	0,38	28,81	0,06	28,7	0,07	140,86	0,42
10948[2]	GeoB20960-1	183	2	3,3821	0,0001	0,8898	0,0015	0,2791	0,00048	3238	8	127,44	0,56	30,84	0,07	30,71	0,07	139,01	0,61
12073	GeoB20960-1	227,5	2,5	2,7468	0,00016	0,8752	0,0026	0,287	0,0011	2762	13	128,48	0,72	31,81	0,13	31,66	0,14	140,52	0,79
10949[2]	GeoB20960-1	339	1	3,796	0,0001	0,687	0,0008	0,2974	0,00047	5021	10	126,66	0,55	33,22	0,06	33,1	0,07	139,09	0,61
10950_2	GeoB20960-1	383,5	2,5	3,76129	0,0003	0,655	0,0013	0,29595	0,00065	5256	15	127,27	0,48	33,01	0,08	32,89	0,09	139,68	0,53
12074	GeoB20960-1	393,5	1,5	3,23281	0,00022	0,6965	0,0031	0,29912	0,00128	4257	26	127,59	1,04	33,41	0,17	33,28	0,17	140,19	1,14
12075	GeoB20960-1	427,5	2,5	3,65867	0,00022	0,8701	0,0019	0,30454	0,00081	3923	13	126,24	0,69	34,17	0,11	34,03	0,11	138,99	0,76
12076	GeoB20960-1	440,5	2,5	2,99029	0,00017	0,7246	0,0018	0,30503	0,00082	3860	14	125,95	0,71	34,24	0,11	34,11	0,12	138,7	0,78
12077	GeoB20960-1	465	1	3,7537	0,00018	1,0477	0,0035	0,3024	0,0011	3344	17	126,72	0,73	33,86	0,15	33,72	0,15	139,4	0,8
10951[2]	GeoB20960-1	500,5	1,5	2,841	0,0001	0,3163	0,0006	0,3049	0,0006	8354	23	125,66	0,43	34,23	0,08	34,13	0,08	138,39	0,48
12078	GeoB20960-1	584,5	2,5	3,20853	0,00014	1,3607	0,0021	0,30632	0,0006	2236	6	126,85	0,39	34,38	0,08	34,2	0,1	139,73	0,43
12079	GeoB20960-1	609,5	2,5	3,26415	0,00017	0,9389	0,0016	0,32277	0,00065	3475	9	126,07	0,48	36,59	0,09	36,44	0,1	139,76	0,53
12080	GeoB20960-1	626	4	2,74472	0,00013	0,54716	0,00088	0,32269	0,00067	5012	13	125,37	0,45	36,6	0,09	36,48	0,09	138,99	0,5
10953[2]	GeoB20960-1	642	1	4,1059	0,0001	0,6916	0,0011	0,3225	0,00059	5853	14	125,79	0,41	36,57	0,08	36,45	0,08	139,45	0,45
10954_2	GeoB20960-1	686	0,5	2,45072	0,00027	0,4658	0,0007	0,32768	0,00059	5320	12	125,94	0,47	37,25	0,08	37,13	0,08	139,88	0,53
12081	GeoB20960-1	717	2	3,24889	0,00021	0,9564	0,0028	0,3286	0,0011	3433	15	125,24	0,64	37,4	0,15	37,25	0,15	139,15	0,71
12082	GeoB20960-1	761,5	1,5	3,02195	0,00015	1,0756	0,0019	0,32888	0,00072	2831	8	126,79	0,56	37,38	0,1	37,21	0,11	140,86	0,62

Table C.11.: ^{14}C dating results from Mauritania (GeoB 14905-2) and Angola (GeoB 20933-1 and GeoB 20960-1) from chapter 7. Sample denoted with * did not pass the quality control (chapter 3.4.2) due to an ^{232}Th concentration between 2-3 ng/g.
[1] ^{230}Th/U dating Stuhrmann (2023)
[2] ^{230}Th/U dating courtesy of Dr. Claudia Wienberg
[3] ^{230}Th/U dating Wefing et al. (2017), recalculated according to Kerber et al. (2023)

Lab No IUP	Lab No MAMS	Core	Depth (cm)	σ (cm)	Age (ka BP)	2σ (ka)	^{14}C Age (ka BP)	1σ (ka)	Δ^{14}C (‰)	2σ (‰)	B_{atm} age (a)	2σ (a)
12060[1]	67205	GeoB14905-2	625	5	30,81	0,09	27,07	0,08	430	33	636	206
12070[1]	68125	GeoB14905-2	655	5	32,85	0,11	29,02	0,21	437	78	560	442
12054[1]	68122	GeoB14905-2	684	2	32,9	0,09	29,38	0,15	364	57	926	325
12058[1]	67216	GeoB14905-2	802,5	2,5	33,51	0,13	30,22	0,11	339	43	1232	257
12055[1]	67227 / 68123	GeoB14905-2	837,5	2,5	34,06	0,11	31,27	0,23	259	74	1837	487
12062[1]	68124 / 67214	GeoB14905-2	854,5	0,5	34,82	0,11	31,1	0,26	410	93	573	537
12053[1]	67213 / 67219	GeoB14905-2	955	3	35,61	0,08	32,79	0,22	255	70	1499	455
7944*[3]	68113	GeoB20933-1	815	0,5	31,56	0,14	28,33	0,13	340	49	671	310
7945	68114	GeoB20933-1	834,5	0,5	31,8	0,08	28,68	0,13	319	46	737	306
7946[3]	68115	GeoB20933-1	868	1	32,16	0,14	29,39	0,14	262	51	1068	328
7947[3]	68116	GeoB20933-1	889,5	1,5	32,3	0,07	29,33	0,14	293	48	885	304
7948*	68117	GeoB20933-1	916	1	32,48	0,14	29,39	0,15	312	54	938	315
7949[3]	68118	GeoB20933-1	937	2	33,3	0,09	29,74	0,15	387	55	828	326
7950[3]	68119	GeoB20933-1	960	1	33,39	0,08	30,05	0,16	347	55	1083	330

Continued on next page

Table C.11 – *continued from previous page*

Lab No IUP	Lab No MAMS	Core	Depth (cm)	σ (cm)	Age (ka BP)	2σ (ka)	^{14}C Age (ka BP)	1σ (ka)	Δ^{14}C (‰)	2σ (‰)	B_{atm} age (a)	2σ (a)
10947[2]	63001	GeoB20960-1	114,5	1,5	26,21	0,06	22,95	0,08	369	29	972	173
12072	64361	GeoB20960-1	165	5	28,7	0,07	25,25	0,1	391	35	780	226
10948[2]	63560	GeoB20960-1	183	2	30,71	0,07	27,08	0,13	411	46	710	264
12073	67224	GeoB20960-1	227,5	2,5	31,66	0,14	27,77	0,09	454	42	-3	270
10949[2]	63561 / 63567	GeoB20960-1	339	1	33,1	0,07	29,24	0,23	442	83	520	466
10950_2	68120	GeoB20960-1	383,5	2,5	32,89	0,09	29,61	0,15	343	52	1084	324
12074	67223 / 67210	GeoB20960-1	393,5	1,5	33,28	0,17	28,82	0,14	551	62	-53	322
12075	67221	GeoB20960-1	427,5	2,5	34,03	0,11	29,39	0,1	583	46	-48	263
12076	67217	GeoB20960-1	440,5	2,5	34,11	0,12	29,27	0,1	620	48	-244	276
12077	64362	GeoB20960-1	465	1	33,72	0,15	29,82	0,16	446	63	650	358
10951[2]	63002	GeoB20960-1	500,5	1,5	34,13	0,08	29,79	0,14	524	56	292	331
12078	67226 / 67206	GeoB20960-1	584,5	2,5	34,2	0,1	30,73	0,17	367	61	1104	395
12079	67212	GeoB20960-1	609,5	2,5	36,44	0,1	32,45	0,15	447	56	230	328
12080	64363	GeoB20960-1	626	4	36,48	0,09	33,06	0,24	350	82	789	489
10953[2]	63559 / 63568	GeoB20960-1	642	1	36,45	0,08	33,15	0,36	333	119	905	722
10954_2	68121	GeoB20960-1	686	0,5	37,13	0,08	33,66	0,25	355	84	815	504
12081	64364	GeoB20960-1	717	2	37,25	0,15	33,92	0,26	331	90	993	541
12082	64365	GeoB20960-1	761,5	1,5	37,21	0,11	33,96	0,26	320	89	1051	539

Lab No IUP	Age (ka BP)	2σ (ka)	Temperature °C $\pm$ 1°C
10947	26,21	0,06	3,4
12072	28,70	0,07	3,4
10948	30,71	0,07	4
12073	31,66	0,14	3,8
10950_2	32,89	0,09	6,4
10949	33,10	0,07	5,2
12074	33,28	0,17	4,1
12077	33,72	0,15	6,8
12075	34,03	0,11	4,2
12076	34,11	0,12	5,4
10951	34,13	0,08	6,9
12078	34,20	0,10	5,6
12079	36,44	0,10	7,4
10953	36,45	0,08	9,2
12080	36,48	0,09	7,6
10954_2	37,13	0,08	9,3
12082	37,21	0,11	7,8
12081	37,25	0,15	8,8

Table C.12.: Temperature reconstruction from GeoB 20960-1.

List of Figures

List of Tables

Bibliography

Addamo, A. M., Vertino, A., Stolarski, J., García-Jiménez, R., Taviani, M., and Machordom, A. (2016). Merging scleractinian genera: the overwhelming genetic similarity between solitary desmophyllum and colonial lophelia. *BMC evolutionary biology*, 16:1–17.

Adkins, J. F. (1998). *Deep-sea corals: a new oceanic archive*. Dissertation, massachusetts institute of technology.

Adkins, J. F. (2013). The role of deep ocean circulation in setting glacial climates. *Paleoceanography*, 28(3):539–561.

Adkins, J. F. and Boyle, E. A. (1997). Changing atmospheric $\Delta^{14}C$ and the record of deep water paleoventilation ages. *Paleoceanography*, 12(3):337–344.

Adkins, J. F., Boyle, E. A., Curry, W. B., and Lutringer, A. (2003). Stable isotopes in deep-sea corals and a new mechanism for "vital effects". *Geochim. Cosmochim. Acta*, 67.

Adkins, J. F., Cheng, H., Boyle, E. A., Druffel, E. R. M., and Edwards, R. L. (1998). Deep-sea coral evidence for rapid change in ventilation of the deep north atlantic 15,400 years ago. *Science*, 280(5364):725–728.

Adkins, J. F., Griffin, S., Kashgarian, M., Cheng, H., Druffel, E., Boyle, E., Edwards, R. L., and Shen, C.-C. (2002). Radiocarbon dating of deep-sea corals. *Radiocarbon*, 44(2):567–580.

Adolphi, F., Bronk Ramsey, C., Erhardt, T., Edwards, R. L., Cheng, H., Turney, C. S., Cooper, A., Svensson, A., Rasmussen, S. O., and Fischer, H. (2018). Connecting the Greenland ice-core and UTh timescales via cosmogenic radionuclides: testing the synchroneity of Dansgaard–Oeschger events. *Climate of the Past*, 14(11):1755–1781.

Adolphi, F., Herbst, K., Nilsson, A., and Panovska, S. (2023). On the polar bias in ice core ^{10}Be data. *Journal of Geophysical Research: Atmospheres*, 128(4):e2022JD038203.

Andersen, M., Stirling, C., Zimmermann, B., and Halliday, A. (2010). Precise determination of the open ocean $^{234}U/^{238}U$ composition. *Geochemistry, Geophysics, Geosystems*, 11(12).

Andersen, M. B., Stirling, C. H., Potter, E.-K., Halliday, A. N., Blake, S. G., McCulloch, M. T., Ayling, B. F., and O'Leary, M. (2008). High-precision U-series measurements of more than 500,000 year old fossil corals. *Earth and Planetary Science Letters*, 265(1-2):229–245.

Anderson, H., Pedro, J., Bostock, H., Chase, Z., and Noble, T. (2021). Compiled southern ocean sea surface temperatures correlate with antarctic isotope maxima. *Quaternary Science Reviews*, 255:106821.

Antobreh, A. A. and Krastel, S. (2007). Mauritania slide complex: morphology, seismic characterisation and processes of formation. *International Journal of Earth Sciences*, 96:451–472.

Ausín, B., Haghipour, N., Wacker, L., Voelker, A. H., Hodell, D., Magill, C., Looser, N., Bernasconi, S. M., and Eglinton, T. I. (2019). Radiocarbon age offsets between two surface dwelling planktonic foraminifera species during abrupt climate events in the SW Iberian margin. *Paleoceanography and Paleoclimatology*, 34(1):63–78.

Balogh, V., Fragkopoulou, E., Serrão, E. A., and Assis, J. (2023). A dataset of cold-water coral distribution records. *Data in Brief*, 48:109223.

Bard, E. and Heaton, T. J. (2021). On the tuning of plateaus in atmospheric and oceanic ^{14}C records to derive calendar chronologies of deep-sea cores and records of ^{14}C marine reservoir age changes. *Climate of the Past*, 17(4):1701–1725.

Baringer, M. O. and Price, J. F. (1997). Mixing and spreading of the Mediterranean outflow. *Journal of Physical Oceanography*, 27(8):1654–1677.

Barker, S., Chen, J., Gong, X., Jonkers, L., Knorr, G., and Thornalley, D. (2015). Icebergs not the trigger for North Atlantic cold events. *Nature*, 520(7547):333–336.

Barker, S., Knorr, G., Vautravers, M. J., Diz, P., and Skinner, L. C. (2010). Extreme deepening of the Atlantic overturning circulation during deglaciation. *Nature Geoscience*, 3(8):567–571.

Barnola, J. M., Raynaud, D., Korotkevich, Y. S., and Lorius, C. (1987). Vostok ice core provides 160,000-year record of atmospheric CO_2. *Nature*, 329(6138):408–414.

Bazin, L., Landais, A., Lemieux-Dudon, B., Toyé Mahamadou Kele, H., Veres, D., Parrenin, F., Martinerie, P., Ritz, C., Capron, E., Lipenkov, V. Y., Loutre, M. F., Raynaud, D., Vinther, B. M., Svensson, A. M., Rasmussen, S. O., Severi, M., Blunier, T., Leuenberger, M. C., Fischer, H., Masson-Delmotte, V., Chappellaz, J. A., and Wolff, E. W. (2013). δ^{18}O measured on ice core NGRIP on AICC2012 chronology.

Beisel, E. (2017). Radiokohlenstoff-Alter von eiszeitlichem Zwischenwasser im NO-Atlantik. *Bachelorarbeit, Heidelberg University, Germany.*

Beisel, E. (2021). Interhemisphärische Gradienten von Radiokohlenstoff im Zwischenwasser des Atlantiks seit der letzten Eiszeit. *Masterarbeit, Heidelberg University, Germany.*

Beisel, E., Frank, N., Robinson, L. F., Lausecker, M., Friedrich, R., Therre, S., Schröder-Ritzrau, A., and Butzin, M. (2023). Climate induced thermocline aging and ventilation in the eastern Atlantic over the last 32.000 years. *Paleoceanography and Paleoclimatology*, page e2023PA004662.

Bereiter, B., Eggleston, S., Schmitt, J., Nehrbass-Ahles, C., Stocker, T. F., Fischer, H., Kipfstuhl, S., and Chappellaz, J. (2015). Revision of the EPICA Dome C CO_2 record from 800 to 600 kyr before present. *Geophysical Research Letters*, 42(2):542–549.

Blamart, D., Rollion-Bard, C., Cuif, J.-P., Juillet-Leclerc, A., Lutringer, A., van Weering, T. C., and Henriet, J.-P. (2005). C and O isotopes in a deep-sea coral (Lophelia pertusa) related to skeletal microstructure. *Cold-water corals and ecosystems*, pages 1005–1020.

Blunier, T., Schwander, J., Stauffer, B., Stocker, T., Dällenbach, A., Indermühle, A., Tschumi, J., Chappellaz, J., Raynaud, D., and Barnola, J. (1997). Timing of the Antarctic Cold Reversal and the atmospheric CO_2 increase with respect to the Younger Dryas event. *Geophysical Research Letters*, 24(21):2683–2686.

Bradtmiller, L. I., McManus, J. F., and Robinson, L. F. (2014). ^{231}Pa/^{230}Th evidence for a weakened but persistent Atlantic meridional overturning circulation during Heinrich Stadial 1. *Nature Communications*, 5:5817.

Broecker, W. (1991). The Great Ocean Conveyor. *Oceanography*, 4:79–89.

Broecker, W. S., Denton, G. H., Edwards, R. L., Cheng, H., Alley, R. B., and Putnam, A. E. (2010). Putting the Younger Dryas cold event into context. *Quaternary Science Reviews*, 29(9-10):1078–1081.

Bryan, S. P., Marchitto, T. M., and Lehman, S. J. (2010). The release of ^{14}C-depleted carbon from the deep ocean during the last deglaciation: Evidence from the Arabian Sea. *Earth and Planetary Science Letters*, 298(1-2):244–254.

Buhl-Mortensen, L., Houssa, R., M'bengue, B., Nyadjro, E., Cervantes, D., Idrissi, M., Mahu, E., Dia, A., Olsen, M., and Mas, C. (2024). Lophelia reefs off North and West Africa–Comparing environment and health. *Marine Biology*, 171(1):29.

Buizert, C. and Schmittner, A. (2015). Southern Ocean control of glacial AMOC stability and Dansgaard-Oeschger interstadial duration. *Paleoceanography*, 30(12):1595–1612.

Burke, A. and Robinson, L. F. (2012). The Southern Ocean's role in carbon exchange during the last deglaciation. *Science*, 335.

Burke, A., Stewart, A. L., Adkins, J. F., Ferrari, R., Jansen, M. F., and Thompson, A. F. (2015). The glacial mid-depth radiocarbon bulge and its implications for the overturning circulation. *Paleoceanography and Paleoclimatology*, 30.

Butzin, M., Köhler, P., and Lohmann, G. (2017). Marine radiocarbon reservoir age simulations for the past 50,000 years. *Geophysical Research Letters*, 44(16):8473–8480.

Butzin, M., Prange, M., and Lohmann, G. (2005). Radiocarbon simulations for the glacial ocean: the effects of wind stress, Southern Ocean sea ice and Heinrich events. *Earth and planetary science letters*, 235(1-2):45–61.

Böhm, E., Lippold, J., Gutjahr, M., Frank, M., Blaser, P., Antz, B., Fohlmeister, J., Frank, N., Andersen, M., and Deininger, M. (2015). Strong and deep Atlantic meridional overturning circulation during the last glacial cycle. *Nature*, 517(7532):73–76.

Büscher, J. V., Form, A. U., Wisshak, M., Kiko, R., and Riebesell, U. (2022). Cold-water coral ecosystems under future ocean change: Live coral performance vs. framework dissolution and bioerosion. *Limnology and Oceanography*, 67(11):2497–2515.

Büscher, J. V., Wisshak, M., Form, A. U., Titschack, J., Nachtigall, K., and Riebesell, U. (2019). In situ growth and bioerosion rates of Lophelia pertusa in a Norwegian fjord and open shelf cold-water coral habitat. *PeerJ*, 7:e7586.

Cairns, S. D. (2007). Deep-water corals: an overview with special reference to diversity and distribution of deep-water scleractinian corals. *Bulletin of marine Science*, 81(3):311–322.

Carlson, A. E. and Clark, P. U. (2012). Ice sheet sources of sea level rise and freshwater discharge during the last deglaciation. *Reviews of Geophysics*, 50(4).

Case, D. H., Robinson, L. F., Auro, M. E., and Gagnon, A. C. (2010). Environmental and biological controls on Mg and Li in deep-sea scleractinian corals. *Earth and Planetary Science Letters*, 300(3-4):215–225.

Cassata, W. S., Singer, B. S., and Cassidy, J. (2008). Laschamp and Mono Lake geomagnetic excursions recorded in New Zealand. *Earth and Planetary Science Letters*, 268(1-2):76–88.

Chadwick, M., Crosta, X., Esper, O., Thöle, L., and Kohfeld, K. E. (2022). Compilation of Southern Ocean sea-ice records covering the last glacial-interglacial cycle (12–130 ka). *Climate of the Past*, 18(8):1815–1829.

Channell, J. (2006). Late Brunhes polarity excursions (Mono Lake, Laschamp, Iceland Basin and Pringle Falls) recorded at ODP Site 919 (Irminger Basin). *Earth and Planetary Science Letters*, 244(1-2):378–393.

Channell, J. E., Singer, B. S., and Jicha, B. R. (2020). Timing of quaternary geomagnetic reversals and excursions in volcanic and sedimentary archives. *Quaternary Science Reviews*, 228:106114.

Chen, S., Littley, E. F., Rae, J. W., Charles, C. D., and Adkins, J. F. (2021a). Uranium Distribution and Incorporation Mechanism in Deep-Sea Corals: Implications for Seawater ${CO_3}^{2-}$ Proxies. *Frontiers in Earth Science*, 9:641327.

Chen, T., Robinson, L. F., Beasley, M. P., Claxton, L. M., Andersen, M. B., Gregoire, L. J., Wadham, J., Fornari, D. J., and Harpp, K. S. (2016). Ocean mixing and ice-sheet control of seawater $^{234}U/^{238}U$ during the last deglaciation. *Science*, 354(6312):626–629.

Chen, T., Robinson, L. F., Burke, A., Claxton, L., Hain, M. P., Li, T., Rae, J. W., Stewart, J., Knowles, T. D., and Fornari, D. J. (2020). Persistently well-ventilated intermediate-depth ocean through the last deglaciation. *Nature Geoscience*, 13(11):733–738.

Chen, T., Robinson, L. F., Burke, A., Southon, J., Spooner, P., Morris, P. J., and Ng, H. C. (2015). Synchronous centennial abrupt events in the ocean and atmosphere during the last deglaciation. *Science*, 349(6255):1537–41.

Chen, X., Tissot, F., Jansen, M., Bekker, A., Liu, C., Nie, N., Halverson, G., Veizer, J., and Dauphas, N. (2021b). The uranium isotopic record of shales and carbonates through geologic time. *Geochimica et cosmochimica acta*, 300:164–191.

Cheng, H., Adkins, J., Edwards, R. L., and Boyle, E. A. (2000). U-Th dating of deep-sea corals. *Geochimica et Cosmochimica Acta*, 64(14):2401–2416.

Cheng, H., Edwards, R. L., Shen, C.-C., Polyak, V. J., Asmerom, Y., Woodhead, J., Hellstrom, J., Wang, Y., Kong, X., and Spötl, C. (2013). Improvements in ^{230}Th dating, ^{230}Th and ^{234}U half-life values, and U–Th isotopic measurements by multi-collector inductively coupled plasma mass spectrometry. *Earth and Planetary Science Letters*, 371:82–91.

Cherrier, J., Sarkodee-Adoo, J., Guilderson, T., and Chanton, J. (2014). Fossil carbon in particulate organic matter in the gulf of mexico following the deepwater horizon event. *Environmental Science and Technology Letters*, 1(1):108–112.

Chutcharavan, P. M. and Dutton, A. (2021). A global compilation of U-series-dated fossil coral sea-level indicators for the Last Interglacial period (Marine Isotope Stage 5e). *Earth System Science Data*, 13(7).

Chutcharavan, P. M., Dutton, A., and Ellwood, M. (2018). Seawater ^{234}U/^{238}U recorded by modern and fossil corals. *Geochimica et Cosmochimia Acta*, 224:1–17.

Clark, P. U., Dyke, A. S., Shakun, J. D., Carlson, A. E., Clark, J., Wohlfarth, B., Mitrovica, J. X., Hostetler, S. W., and McCabe, A. M. (2009). The last glacial maximum. *science*, 325(5941):710–714.

Clark, P. U., Shakun, J. D., Baker, P. A., Bartlein, P. J., Brewer, S., Brook, E., Carlson, A. E., Cheng, H., Kaufman, D. S., and Liu, Z. (2012). Global climate evolution during the last deglaciation. *Proceedings of the National Academy of Sciences*, 109(19):E1134–E1142.

Clauzet, G., Wainer, I., Lazar, A., Brady, E., and Otto-Bliesner, B. (2007). A numerical study of the South Atlantic circulation at the Last Glacial Maximum. *Palaeogeography, Palaeoclimatology, Palaeoecology*, 253(3-4):509–528.

Cléroux, C., deMenocal, P., and Guilderson, T. (2011). Deglacial radiocarbon history of tropical Atlantic thermocline waters: absence of CO_2 reservoir purging signal. *Quaternary Science Reviews*, 30(15-16):1875–1882.

Colin, C., Frank, N., Copard, K., and Douville, E. (2010). Neodymium isotopic composition of deep-sea corals from the NE Atlantic: implications for past hydrological changes during the Holocene. *Quaternary Science Reviews*, 29(19-20):2509–2517.

Colin, C., Tisnérat-Laborde, N., Mienis, F., Collart, T., Pons-Branchu, E., Dubois-Dauphin, Q., Frank, N., Dapoigny, A., Ayache, M., and Swingedouw, D. (2019). Millennial-scale variations of the Holocene North Atlantic mid-depth gyre inferred from radiocarbon and neodymium isotopes in cold water corals. *Quaternary Science Reviews*, 211:93–106.

Cook, M. S. and Keigwin, L. D. (2015). Radiocarbon profiles of the NW Pacific from the LGM and deglaciation: Evaluating ventilation metrics and the effect of uncertain surface reservoir ages. *Paleoceanography*, 30(3):174–195.

Cooper, A., Turney, C. S., Palmer, J., Hogg, A., McGlone, M., Wilmshurst, J., Lorrey, A. M., Heaton, T. J., Russell, J. M., and McCracken, K. (2021). A global environmental crisis 42,000 years ago. *Science*, 371(6531):811–818.

Corbera, G., Lo Iacono, C., Simarro, G., Grinyó, J., Ambroso, S., Huvenne, V. A., Mienis, F., Carreiro-Silva, M., Martins, I., and Mano, B. (2022). Local-scale feedbacks influencing cold-water coral growth and subsequent reef formation. *Scientific Reports*, 12(1):20389.

Cordes, E. E., Mienis, F., Gasbarro, R., Davies, A., Baco, A. R., Bernardino, A. F., Clark, M. R., Freiwald, A., Hennige, S. J., and Huvenne, V. A. (2023). *A Global View of the Cold-Water Coral Reefs of the World*, pages 1–30. In: Cold-Water Coral Reefs of the World, Springer.

Cuny-Guirriec, K., Douville, E., Reynaud, S., Allemand, D., Bordier, L., Canesi, M., Mazzoli, C., Taviani, M., Canese, S., McCulloch, M., et al. (2019). Coral Li/Mg thermometry: caveats and constraints. *Chemical Geology*, 523:162–178.

Dansgaard, W., Clausen, H. B., Gundestrup, N., Hammer, C. U., Johnsen, S. F., Kristinsdottir, P., and Reeh, N. (1982). A new Greenland deep ice core. *Science*, 218(4579):1273–1277.

Dansgaard, W., Johnsen, S. J., Clausen, H. B., Dahl-Jensen, D., Gundestrup, N. S., Hammer, C. U., Hvidberg, C. S., Steffensen, J. P., Sveinbjörnsdottir, A., and Jouzel, J. (1993). Evidence for general instability of past climate from a 250-kyr ice-core record. *nature*, 364(6434):218–220.

Dansgaard, W., White, J. W., and Johnsen, S. J. (1989). The abrupt termination of the Younger Dryas climate event. *Nature*, 339(6225):532–534.

Davies, A. J., Wisshak, M., Orr, J. C., and Roberts, J. M. (2008). Predicting suitable habitat for the cold-water coral Lophelia pertusa (Scleractinia). *Deep Sea Research Part I: Oceanographic Research Papers*, 55(8):1048–1062.

Davies, R., Yang, J., Ireland, M., Berndt, C., Huuse, M., and Morales-Maqueda, M. (2023). Long-distance migration and venting of methane after marine hydrate dissociation. *Research Square preprint deposition service*.

Davies, R. J. and Clarke, A. L. (2010). Methane recycling between hydrate and critically pressured stratigraphic traps, offshore Mauritania. *Geology*, 38(11):963–966.

Davies, R. J., Yang, J., Li, A., Mathias, S., and Hobbs, R. (2015). An irregular feather-edge and potential outcrop of marine gas hydrate along the Mauritanian margin. *Earth and Planetary Science Letters*, 423:202–209.

de Carvalho Ferreira, M. L. (2022). *Deep-sea coral records of the intermediate Atlantic Ocean during the last glacial cycle.* Dissertation, University of Bristol.

de Carvalho Ferreira, M. L., Robinson, L. F., Stewart, J. A., Li, T., Chen, T., Burke, A., Kitahara, M. V., and White, N. J. (2022). Spatial and temporal distribution of cold-water corals in the Northeast Atlantic Ocean over the last 150 thousand years. *Deep Sea Research Part I: Oceanographic Research Papers*, 190:103892.

De Haas, H., Mienis, F., Frank, N., Richter, T. O., Steinacher, R., De Stigter, H., van Der Land, C., and Van Weering, T. C. (2009). Morphology and sedimentology of (clustered) cold-water coral mounds at the south Rockall Trough margins, NE Atlantic Ocean. *Facies*, 55:1–26.

De Pol-Holz, R., Keigwin, L., Southon, J., Hebbeln, D., and Mohtadi, M. (2010). No signature of abyssal carbon in intermediate waters off Chile during deglaciation. *Nature Geoscience*, 3(3):192–195.

Dinauer, A., Adolphi, F., and Joos, F. (2020). Mysteriously high $\Delta^{14}C$ of the glacial atmosphere: influence of ^{14}C production and carbon cycle changes. *Climate of the Past*, 16(4):1159–1185.

Dorschel, B., Hebbeln, D., Rüggeberg, A., Dullo, W.-C., and Freiwald, A. (2005). Growth and erosion of a cold-water coral covered carbonate mound in the Northeast Atlantic during the Late Pleistocene and Holocene. *Earth and Planetary Science Letters*, 233(1-2):33–44.

Douarin, M., Elliot, M., Noble, S. R., Sinclair, D., Henry, L.-A., Long, D., Moreton, S. G., and Roberts, J. M. (2013). Growth of north-east Atlantic cold-water coral reefs and mounds during the Holocene: A high resolution U-series and ^{14}C chronology. *Earth and Planetary Science Letters*, 375:176–187.

Dullo, W.-C., Flögel, S., and Rüggeberg, A. (2008). Cold-water coral growth in relation to the hydrography of the Celtic and Nordic European continental margin. *Marine Ecology Progress Series*, 371:165–176.

Dumoulin, J., Comby-Zerbino, C., Delqué-Količ, E., Moreau, C., Caffy, I., Hain, S., Perron, M., Thellier, B., Setti, V., and Berthier, B. (2017). Status report on sample preparation protocols developed at the LMC14 Laboratory, Saclay, France: from sample collection to ^{14}C AMS measurement. *Radiocarbon*, 59(3):713–726.

Eisele, M., Frank, N., Wienberg, C., Hebbeln, D., Correa, M. L., Douville, E., and Freiwald, A. (2011). Productivity controlled cold-water coral growth periods during the last glacial off Mauritania. *Marine Geology*, 280(1-4):143–149.

Elsässer, C., Wagenbach, D., Levin, I., Stanzick, A., Christl, M., Wallner, A., Kipfstuhl, S., Seierstad, I., Wershofen, H., and Dibb, J. (2015). Simulating ice core ^{10}Be on the glacial–interglacial timescale. *Climate of the Past*, 11(2):115–133.

Eltgroth, S. F., Adkins, J. F., Robinson, L. F., Southon, J., and Kashgarian, M. (2006). A deep-sea coral record of North Atlantic radiocarbon through the Younger Dryas: Evidence for intermediate water/deepwater reorganization. *Paleoceanography*, 21(4).

Enmar, R., Stein, M., Bar-Matthews, M., Sass, E., Katz, A., and Lazar, B. (2000). Diagenesis in live corals from the Gulf of Aqaba. I. The effect on paleo-oceanography tracers. *Geochimica et Cosmochimica Acta*, 64(18):3123–3132.

EPICA, C. M. (2006). One-to-one coupling of glacial climate variability in Greenland and Antarctica. *Nature*, 444(7116):195–198.

Esat, T. M. and Yokoyama, Y. (2006). Variability in the uranium isotopic composition of the oceans over glacial–interglacial timescales. *Geochimica et Cosmochimica Acta*, 70(16):4140–4150.

Ezat, M. M., Rasmussen, T. L., Thornalley, D. J., Olsen, J., Skinner, L. C., Hönisch, B., and Groeneveld, J. (2017). Ventilation history of Nordic Seas overflows during the last (de)glacial period revealed by species-specific benthic foraminiferal ^{14}C dates. *Paleoceanography*, 32(2):172–181.

Feenstra, E. J., Birgel, D., Heindel, K., Wehrmann, L. M., Jaramillo-Vogel, D., Grobéty, B., Frank, N., Hancock, L. G., Van Rooij, D., and Peckmann, J. (2020). Constraining the formation of authigenic carbonates in a seepage-affected cold-water coral mound by lipid biomarkers. *Geobiology*, 18(2):185–206.

Fentimen, R., Feenstra, E., Rüggeberg, A., Vennemann, T., Hajdas, I., Adatte, T., Van Rooij, D., and Foubert, A. (2020). Cold-water coral mound archive provides unique insights into intermediate water mass dynamics in the Alboran Sea during the last deglaciation. *Frontiers in Marine Science*, 7:354.

Fentimen, R., Feenstra, E. J., Rüggeberg, A., Hall, E., Rosso, A., Hajdas, I., Jaramillo-Vogel, D., Grobéty, B., Adatte, T., Van Rooij, D., Frank, N., and Foubert, A. (2023).

Staggered cold-water coral mound build-up on an Alboran ridge during the last deglacial (East Melilla Mound Field, western Mediterranean). *Marine Geology*, 457:106994.

Foubert, A., Depreiter, D., Beck, T., Maignien, L., Pannemans, B., Frank, N., Blamart, D., and Henriet, J.-P. (2008). Carbonate mounds in a mud volcano province off north-west Morocco: key to processes and controls. *Marine Geology*, 248(1-2):74–96.

Frank, N., Freiwald, A., Lopez-Correa, M., Eisele, F., Hebbeln, D., Wienberg, C., van Rooij, D., Henriet, J., Colin, C., and van Weering, T. (2011a). Northeast Atlantic cold-water coral reefs and climate. *Geological Society of America*.

Frank, N., Hebbeln, D., Blaser, P., Carreiro-Silva, M., Diekamp, V., Eichstädter, R., Freiwald, A., Gaide, S., Günther, B., Hemsing, F., Hoffman, L., Krengel, T., Lausecker, M., Leymann, T., Link, J., Linnemann, U., Matos, L., Nowald, N., Raddatz, J., Schade, T., Schröder, M., Schröder-Ritzrau, A., Seiter, C., Speicher, R., Stelzner, M., Tamborrino, L., Wefing, A.-M., Wenzel, J., and Wienberg, C. (2023). Atlantic Thermocline Ocean and Ecosystems Dynamic during Natural Climate Change - ATHENA, Cruise No. M151, October 06, 2018 - October 31, 2018, Ponta Delgada *Portugal* - Funchal *Portugal*.

Frank, N. and Hemsing, F. (2021). Dating of corals and other geological samples via the radioactive disequilibrium of uranium and thorium isotopes. *Paleoclimatology*, pages 89–100.

Frank, N., Paterne, M., Ayliffe, L., van Weering, T., Henriet, J.-P., and Blamart, D. (2004). Eastern North Atlantic deep-sea corals: tracing upper intermediate water $\Delta^{14}C$ during the Holocene. *Earth and Planetary Science Letters*, 219(3-4):297–309.

Frank, N., Ricard, E., Lutringer-Paquet, A., van Der Land, C., Colin, C., Blamart, D., Foubert, A., Van Rooij, D., Henriet, J.-P., and de Haas, H. (2009). The Holocene occurrence of cold water corals in the NE Atlantic: implications for coral carbonate mound evolution. *Marine Geology*, 266(1-4):129–142.

Frank, N., Turpin, L., Cabioch, G., Blamart, D., Tressens-Fedou, M., Colin, C., and Jean-Baptiste, P. (2006). Open system U-series ages of corals from a subsiding reef in New Caledonia: Implications for sea level changes, and subsidence rate. *Earth and Planetary Science Letters*, 249(3-4):274–289.

Frank, T. D., Titschack, J., and Thierens, M. (2011b). Aragonite loss in a cold-water coral mound: mechanisms and implications. *Sedimentology*, 58(3):670–690.

Franzese, A. M., Hemming, S. R., Goldstein, S. L., and Anderson, R. F. (2006).

Reduced Agulhas Leakage during the Last Glacial Maximum inferred from an integrated provenance and flux study. *Earth and Planetary Science Letters*, 250(1-2):72–88.

Freeman, E., Skinner, L., Tisserand, A., Dokken, T., Timmermann, A., Menviel, L., and Friedrich, T. (2015). An Atlantic–Pacific ventilation seesaw across the last deglaciation. *Earth and Planetary Science Letters*, 424:237–244.

Freeman, E., Skinner, L. C., Waelbroeck, C., and Hodell, D. (2016). Radiocarbon evidence for enhanced respired carbon storage in the Atlantic at the Last Glacial Maximum. *Nature Communications*, 7(1):1–8.

Freiwald, A., Fosså, J. H., Grehan, A., Koslow, T., and Roberts, J. M. (2004). *Cold-water coral reefs: out of sight-no longer out of mind*. UNEP-WCMC.

Freiwald, A., Rogers, A., Hall-Spencer, J., Guinotte, J., Davies, A., Yesson, C., Martin, C., and LV, W. (2017). Global distribution of cold-water corals (version 4.0). third update to the dataset in freiwald et al. (2004) by unep-wcmc, in collaboration with andre freiwald and john guinotte. *Cambridge (UK): UN Environment World Conservation Monitoring Centre.*

Friedman, I., O'NEIL, J., and Cebula, G. (1982). Two new carbonate stable-isotope standards. *Geostandards Newsletter*, 6(1):11–12.

Gallup, C. D., Cheng, H., Taylor, F., and Edwards, R. (2002). Direct determination of the timing of sea level change during termination ii. *Science*, 295(5553):310–313.

Godwin, H. (1962). Half-life of radiocarbon. *Nature*, 195(4845):984–984.

Gori, A., Orejas, C., Mienis, F., Ferrier-Pagès, C., Bilan, M., Flöter, S., Reynaud, S., Sweetman, A. K., Roberts, J. M., Wienberg, C., et al. (2023). Natural hypoxic conditions do not affect the respiration rates of the cold-water coral desmophyllum pertusum (lophelia pertusa) living in the angola margin (southeastern atlantic ocean). *Deep Sea Research Part I: Oceanographic Research Papers*, 197:104052.

Griffin, S. and Druffel, E. R. (1989). Sources of carbon to deep-sea corals. *Radiocarbon*, 31(3):533–543.

Hain, M. P., Sigman, D. M., and Haug, G. H. (2011). Shortcomings of the isolated abyssal reservoir model for deglacial radiocarbon changes in the mid-depth Indo-Pacific Ocean. *Geophys. Res. Lett.*, 38.

Hain, M. P., Sigman, D. M., and Haug, G. H. (2014). Distinct roles of the Southern

Ocean and North Atlantic in the deglacial atmospheric radiocarbon decline. *Earth and Planetary Science Letters*, 394:198–208.

Hanz, U., Wienberg, C., Hebbeln, D., Duineveld, G., Lavaleye, M., Juva, K., Dullo, W.-C., Freiwald, A., Tamborrino, L., and Reichart, G.-J. (2019). Environmental factors influencing benthic communities in the oxygen minimum zones on the Angolan and Namibian margins. *Biogeosciences*, 16(22):4337–4356.

Heaton, T. J., Bard, E., Ramsey, C. B., Butzin, M., Hatté, C., Hughen, K. A., Köhler, P., and Reimer, P. J. (2023). A response to community questions on the Marine20 radiocarbon age calibration curve: Marine reservoir ages and the calibration of ^{14}C samples from the oceans. *Radiocarbon*, 65(1):247–273.

Heaton, T. J., Köhler, P., Butzin, M., Bard, E., Reimer, R. W., Austin, W. E., Ramsey, C. B., Grootes, P. M., Hughen, K. A., and Kromer, B. (2020). Marine20—the marine radiocarbon age calibration curve (0–55,000 cal BP). *Radiocarbon*, 62(4):779–820.

Hebbeln, D., Bender, M., Gaide, S., Titschack, J., Vandorpe, T., Van Rooij, D., Wintersteller, P., and Wienberg, C. (2019). Thousands of cold-water coral mounds along the Moroccan Atlantic continental margin: distribution and morphometry. *Marine Geology*, 411:51–61.

Hebbeln, D., Van Rooij, D., and Wienberg, C. (2016). Good neighbours shaped by vigorous currents: Cold-water coral mounds and contourites in the North Atlantic. *Marine Geology*, 378:171–185.

Hebbeln, D., Wienberg, C., Bartels, M., Bergenthal, M., Frank, N., Gaide, S., Henriet, J.-P., Kaszemeik, K., Klar, S., Klein, T., Krengel, T., Kuhnert, M., Meyer-Schack, B., Noorlander, C., Reuter, M., Rosiak, U., Schmidt, W., Seeba, H., Seiter, C., Stange, N., Terhzaz, L., and Rooij, D. V. (2015). MoccoMeBo Climate-driven development of Moroccan cold-water coral mounds revealed by MeBo-drilling: Atlantic vs. Mediterranean settings - Cruise MSM36 – February 18 – March 17, 2014 – Malaga (Spain) – Las Palmas (Spain). *MARIA S. MERIAN-Berichte, MSM36*.

Hebbeln, D., Wienberg, C., Bender, M., Bergmann, F., Dehning, K., Dullo, W.-C., Eichstädter, R., Flöter, S., Freiwald, A., Gori, A., Haberkern, J., Hoffmann, L., João, F. M., Lavaleye, M., Leymann, T., Matsuyama, K., Meyer-Schack, B., Mienis, F., Nowald, I. B. M. N., Valle, C. O. S. d., Cordova, C. R., Saturov, D., Seiter, C., Titschack, J., Vittori, V., Wefing, A.-M., Wilsenack, M., and Wintersteller, P. (2017). ANNA - Cold-Water Coral Ecosystems off Angola and Namibia. Cruise

M122 - December 30, 2015 - January 31, 2016 - Walvisbay (Namibia) - Walvisbay (Namibia). *Meteor-Berichte*.

Hebbeln, D., Wienberg, C., Beuck, L., Boom, L., Cunha, W., Dimmler, W., Eisele, M., El Frihmat, Y., Fink, H., Groenewegen, R., Löffler, S.-B., López, N., Lutz, M., Meyer-Schack, B., and Nowald, N. (2008). Report and preliminary results of RV Pelagia Cruise 64PE284. Cold-water Corals in the Gulf of Cádiz and on Coral Patch Seamount (NE Atlantic). Portimão - Portimão, 18.02. - 09.03.2008. Report, Universität Bremen.

Hebbeln, D., Wienberg, C., Dullo, W.-C., Freiwald, A., Mienis, F., Orejas, C., and Titschack, J. (2020). Cold-water coral reefs thriving under hypoxia. *Coral Reefs*, 39:853–859.

Heinrich, H. (1988). Origin and consequences of cyclic ice rafting in the northeast Atlantic Ocean during the past 130,000 years. *Quaternary research*, 29(2):142–152.

Hemming, S. R. (2004). Heinrich events: Massive late Pleistocene detritus layers of the North Atlantic and their global climate imprint. *Reviews of Geophysics*, 42(1).

Hemsing, F. (2017). *Cold-Water Corals as Archives for Ocean Dynamics, Environmental Conditions and Glacial Reef Accumulation*. Dissertation, Heidelberg University, Germany.

Henderson, G. M. and Slowey, N. C. (2000). Evidence from U–Th dating against Northern Hemisphere forcing of the penultimate deglaciation. *Nature*, 404(6773):61–66.

Hendy, E., Gagan, M., Lough, J., McCulloch, M., and DeMenocal, P. (2007). Impact of skeletal dissolution and secondary aragonite on trace element and isotopic climate proxies in Porites corals. *Paleoceanography*, 22(4).

Hennige, S. J., Wolfram, U., Wickes, L., Murray, F., Roberts, J. M., Kamenos, N. A., Schofield, S., Groetsch, A., Spiesz, E. M., and Aubin-Tam, M.-E. (2020). Crumbling reefs and cold-water coral habitat loss in a future ocean: evidence of "Coralporosis" as an indicator of habitat integrity. *Frontiers in Marine Science*, 7:668.

Henry, L., McManus, J., Curry, W., Roberts, N., Piotrowski, A., and Keigwin, L. (2016). North Atlantic ocean circulation and abrupt climate change during the last glaciation. *Science*, 353(6298):470–474.

Hesse, T., Butzin, M., Bickert, T., and Lohmann, G. (2011). A model-data comparison of δ^{13}C in the glacial Atlantic Ocean. *Paleoceanography*, 26(3).

Hessenthaler, L. (2024). Optimierung der ICP-MS-Messsequenz für die Li/Mg-Temperaturrekonstruktion bei Kaltwasserkorallen nahe der Azorenfront. *Bachelorarbeit, Heidelberg University, Germany.*

Hines, S. K., Eiler, J. M., Southon, J. R., and Adkins, J. F. (2019). Dynamic intermediate waters across the late glacial revealed by paired radiocarbon and clumped isotope temperature records. *Paleoceanography and Paleoclimatology*, 34(7):1074–1091.

Hines, S. K., Southon, J. R., and Adkins, J. F. (2015). A high-resolution record of Southern Ocean intermediate water radiocarbon over the past 30,000 years. *Earth and Planetary Science Letters*, 432.

Hogg, A. G., Heaton, T. J., Hua, Q., Palmer, J. G., Turney, C. S., Southon, J., Bayliss, A., Blackwell, P. G., Boswijk, G., and Ramsey, C. B. (2020). SHCal20 Southern Hemisphere calibration, 0–55,000 years cal BP. *Radiocarbon*, 62(4):759–778.

Howe, J. N., Piotrowski, A. M., Noble, T. L., Mulitza, S., Chiessi, C. M., and Bayon, G. (2016). North Atlantic deep water production during the Last Glacial Maximum. *Nature Communications*, 7(1):1–8.

Huang, E., Mulitza, S., Paul, A., Groeneveld, J., Steinke, S., and Schulz, M. (2012). Response of eastern tropical Atlantic central waters to Atlantic meridional overturning circulation changes during the Last Glacial Maximum and Heinrich Stadial 1. *Paleoceanography*, 27(3).

Ivanovich, M. and Harmon, R. S. (1982). *Uranium series disequilibrium: applications to environmental problems*. Clarendon Press.

Kano, A., Ferdelman, T. G., Williams, T., Henriet, J.-P., Ishikawa, T., Kawagoe, N., Takashima, C., Kakizaki, Y., Abe, K., and Sakai, S. (2007). Age constraints on the origin and growth history of a deep-water coral mound in the northeast Atlantic drilled during Integrated Ocean Drilling Program Expedition 307. *Geology*, 35(11):1051–1054.

Keigwin, L. and Schlegel, M. (2002). Ocean ventilation and sedimentation since the glacial maximum at 3 km in the western North Atlantic. *Geochemistry, Geophysics, Geosystems*, 3(6):1–14.

Kerber, I. K. (2023). *Precision, timing and frequency distribution of Th/U dated secondary carbonates*. Dissertation, Heidelberg University, Germany.

Kerber, I. K., Arps, J., Eichstädter, R., Kontor, F., Dornick, C., Schröder-Ritzrau, A., Babu, A., Warken, S., and Frank, N. (2023). Simultaneous U and Th isotope measurements for U-series dating using MCICPMS. *Nuclear Instruments and Methods in Physics Research Section B: Beam Interactions with Materials and Atoms*, 539:169–178.

Kindler, P., Guillevic, M., Baumgartner, M., Schwander, J., Landais, A., and Leuenberger, M. (2014). Temperature reconstruction from 10 to 120 kyr b2k from the NGRIP ice core. *Climate of the Past*, 10(2):887–902.

Kipp, M. A., Li, H., Ellwood, M. J., John, S. G., Middag, R., Adkins, J. F., and Tissot, F. L. (2022). ^{238}U, ^{235}U and ^{234}U in seawater and deep-sea corals: A high-precision reappraisal. *Geochimica et Cosmochimica Acta*, 336:231–248.

Kissel, C., Guillou, H., Laj, C., Carracedo, J., Nomade, S., Perez-Torrado, F., and Wandres, C. (2011). The Mono Lake excursion recorded in phonolitic lavas from Tenerife (Canary Islands): Paleomagnetic analyses and coupled K/Ar and Ar/Ar dating. *Physics of the Earth and Planetary Interiors*, 187(3-4):232–244.

Korte, M., Brown, M. C., Panovska, S., and Wardinski, I. (2019). Robust characteristics of the laschamp and mono lake geomagnetic excursions: Results from global field models. *Frontiers in Earth Science*, 7:86.

Krengel, T. (2020). *550,000 years of marine climate variability in the western Mediterranean Sea revealed by cold-water corals.* Dissertation, Heidelberg University, Germany.

Kromer, B., Lindauer, S., Synal, H.-A., and Wacker, L. (2013). MAMS–a new AMS facility at the Curt-Engelhorn-Centre for Achaeometry, Mannheim, Germany. *Nuclear instruments and methods in physics research Section B: beam interactions with materials and atoms*, 294:11–13.

Kuhlbrodt, T., Griesel, A., Montoya, M., Levermann, A., Hofmann, M., and Rahmstorf, S. (2007). On the driving processes of the Atlantic meridional overturning circulation. *Reviews of Geophysics*, 45(2).

Kurie, F. N. (1934). A new mode of disintegration induced by neutrons. *Physical Review*, 45(12):904.

Köhler, P., Adolphi, F., Butzin, M., and Muscheler, R. (2022). Toward reconciling radiocarbon production rates with carbon cycle changes of the last 55,000 years. *Paleoceanography and Paleoclimatology*, 37(2):e2021PA004314.

Köhler, P., Nehrbass-Ahles, C., Schmitt, J., Stocker, T. F., and Fischer, H. (2017). A 156 kyr smoothed history of the atmospheric greenhouse gases CO_2, CO_4, and N_2O and their radiative forcing. *Earth System Science Data*, 9(1):363–387.

Köhler, P., Skinner, L. C., and Adolphi, F. (2024). Simulated radiocarbon cycle revisited by considering the bipolar seesaw and benthic ^{14}C data. *Earth and Planetary Science Letters*, 640:118801.

Laj, C., Guillou, H., and Kissel, C. (2014). Dynamics of the earth magnetic field in the 10–75 kyr period comprising the Laschamp and Mono Lake excursions: New results from the French Chaîne des Puys in a global perspective. *Earth and Planetary Science Letters*, 387:184–197.

Lambeck, K., Rouby, H., Purcell, A., Sun, Y., and Sambridge, M. (2014). Sea level and global ice volumes from the Last Glacial Maximum to the Holocene. *Proceedings of the National Academy of Sciences*, 111(43):15296–15303.

Langmuir, D. and Herman, J. S. (1980). The mobility of thorium in natural waters at low temperatures. *Geochimica et Cosmochimica Acta*, 44(11):1753–1766.

Lausecker, M. (2021). *Insights into Atlantic thermocline seawater temperatures from cold-water corals since the last glacial*. Dissertation, Heidelberg University, Germany.

Lauvset, S. K., Lange, N., Tanhua, T., Bittig, H. C., Olsen, A., Kozyr, A., Álvarez, M., Becker, S., Brown, P. J., and Carter, B. R. (2021). An updated version of the global interior ocean biogeochemical data product, GLODAPv2. 2021. *Earth System Science Data*, 13(12):5565–5589.

Lazar, B., Enmar, R., Schossberger, M., Bar-Matthews, M., Halicz, L., and Stein, M. (2004). Diagenetic effects on the distribution of uranium in live and Holocene corals from the Gulf of Aqaba. *Geochimica et Cosmochimica Acta*, 68(22):4583–4593.

León, R., Somoza, L., Medialdea, T., González, F., Díaz-del Río, V., Fernández-Puga, M., Maestro, A., and Mata, M. (2007). Sea-floor features related to hydrocarbon seeps in deepwater carbonate-mud mounds of the Gulf of Cádiz: from mud flows to carbonate precipitates. *Geo-Marine Letters*, 27:237–247.

Li, C. and Born, A. (2019). Coupled atmosphere-ice-ocean dynamics in Dansgaard-Oeschger events. *Quaternary Science Reviews*, 203:1–20.

Li, T., Robinson, L. F., Chen, T., Wang, X. T., Burke, A., Rae, J. W., Pegrum-Haram, A., Knowles, T. D., Li, G., and Chen, J. (2020). Rapid shifts in circulation and biogeochemistry of the Southern Ocean during deglacial carbon cycle events. *Science advances*, 6(42).

Li, T., Robinson, L. F., MacGilchrist, G. A., Chen, T., Stewart, J. A., Burke, A., Wang, M., Li, G., Chen, J., and Rae, J. W. (2023). Enhanced subglacial discharge from antarctica during meltwater pulse 1a. *Nature Communications*, 14(1):7327.

Libby, W. F. (1946). Atmospheric helium three and radiocarbon from cosmic radiation. *Physical Review*, 69(11-12):671.

Libby, W. F., Anderson, E. C., and Arnold, J. R. (1949). Age determination by radiocarbon content: world-wide assay of natural radiocarbon. *Science*, 109(2827):227–228.

Libby, W. F. and Johnson, F. (1955). *Radiocarbon dating*, volume 2. University of Chicago Press Chicago.

Lindsay, C. M., Lehman, S. J., Marchitto, T. M., and Ortiz, J. D. (2015). The surface expression of radiocarbon anomalies near baja california during deglaciation. *Earth and Planetary Science Letters*, 422:67–74.

Lippold, J., Luo, Y., Francois, R., Allen, S. E., Gherardi, J., Pichat, S., Hickey, B., and Schulz, H. (2012). Strength and geometry of the glacial Atlantic Meridional Overturning Circulation. *Nature Geoscience*, 5(11):813–816.

Lippold, J., Pöppelmeier, F., Süfke, F., Gutjahr, M., Goepfert, T. J., Blaser, P., Friedrich, O., Link, J. M., Wacker, L., and Rheinberger, S. (2019). Constraining the variability of the Atlantic meridional overturning circulation during the Holocene. *Geophysical Research Letters*, 46(20):11338–11346.

Little, M., Schneider, R., Kroon, D., Price, B., Bickert, T., and Wefer, G. (1997). Rapid palaeoceanographic changes in the Benguela Upwelling System for the last 160,000 years as indicated by abundances of planktonic foraminifera. *Palaeogeography, Palaeoclimatology, Palaeoecology*, 130(1-4):135–161.

Liu, M. and Tanhua, T. (2021). Water masses in the Atlantic Ocean: characteristics and distributions. *Ocean Science*, 17:463–486.

Lohmann, G. and Lorenz, S. (2000). On the hydrological cycle under paleoclimatic conditions as derived from AGCM simulations. *Journal of Geophysical Research: Atmospheres*, 105(D13):17417–17436.

Lomitschka, M. and Mangini, A. (1999). Precise Th/U-dating of small and heavily coated samples of deep sea corals. *Earth and Planetary Science Letters*, 170(4):391–401.

Lozier, M. S. (1997). Evidence for large-scale eddy-driven gyres in the North Atlantic. *Science*, 277(5324):361–364.

Lund, D., Adkins, J., and Ferrari, R. (2011). Abyssal Atlantic circulation during the Last Glacial Maximum: Constraining the ratio between transport and vertical mixing. *Paleoceanography*, 26(1).

Magana, A. L., Southon, J. R., Kennett, J. P., Roark, E. B., Sarnthein, M., and Stott, L. D. (2010). Resolving the cause of large differences between deglacial benthic foraminifera radiocarbon measurements in Santa Barbara Basin. *Paleoceanography*, 25(4).

Maier-Reimer, E., Mikolajewicz, U., and Hasselmann, K. (1993). Mean circulation of the Hamburg LSG OGCM and its sensitivity to the thermohaline surface forcing. *Journal of Physical Oceanography*, 23(4):731–757.

Malmierca-Vallet, I., Sime, L. C., and the D-O community members (2023). Dansgaard–Oeschger events in climate models: review and baseline Marine Isotope Stage 3 (MIS3) protocol. *Climate of the Past*, 19(5):915–942.

Mangini, A., Godoy, J. M., Godoy, M. L., Kowsmann, R., Santos, G. M., Ruckelshausen, M., Schroeder-Ritzrau, A., and Wacker, L. (2010). Deep sea corals off Brazil verify a poorly ventilated Southern Pacific Ocean during H2, H1 and the Younger Dryas. *Earth and Planetary Science Letters*, 293(3):269–276.

Mangini, A., Lomitschka, M., Eichstädter, R., Frank, N., Vogler, S., Bonani, G., Hajdas, I., and Patzold, J. (1998). Coral provides way to age deep water. *Nature*, 392(6674):347–348.

Marchal, O. and Zhao, N. (2021). On the estimation of deep Atlantic ventilation from fossil radiocarbon records. Part I: Modern reference estimates. *Journal of Physical Oceanography*, 51(6):1843–1873.

Marchitto, T. M., Lehman, S. J., Ortiz, J. D., Fluckiger, J., and Geen, A. (2007). Marine radiocarbon evidence for the mechanism of deglacial atmospheric CO_2 rise. *Science*, 316.

Marcott, S. A., Bauska, T. K., Buizert, C., Steig, E. J., Rosen, J. L., Cuffey, K. M., Fudge, T., Severinghaus, J. P., Ahn, J., and Kalk, M. L. (2014). Centennial-scale changes in the global carbon cycle during the last deglaciation. *Nature*, 514(7524):616–619.

McCulloch, M., Taviani, M., Montagna, P., Correa, M. L., Remia, A., and Mortimer, G. (2010). Proliferation and demise of deep-sea corals in the Mediterranean during the Younger Dryas. *Earth and Planetary Science Letters*, 298(1-2):143–152.

McManus, J. F., Francois, R., Gherardi, J. M., Keigwin, L. D., and Brown-Leger, S.

(2004). Collapse and rapid resumption of Atlantic meridional circulation linked to deglacial climate changes. *Nature*, 428.

Menviel, L., Yu, J., Joos, F., Mouchet, A., Meissner, K., and England, M. H. (2017). Poorly ventilated deep ocean at the Last Glacial Maximum inferred from carbon isotopes: A data-model comparison study. *Paleoceanography*, 32(1):2–17.

Menviel, L. C., Skinner, L. C., Tarasov, L., and Tzedakis, P. C. (2020). An ice–climate oscillatory framework for Dansgaard–Oeschger cycles. *Nature Reviews Earth and Environment*, 1(12):677–693.

Mienis, F., de Haas, H., and Party, S. S. (2004). Report of cruise Moundforce 2004. The distribution, morphology, sedimentology and watermass characteristics of and around mounds in the Gulf of Cadiz and at the SW Rockall Trough margin. Report, NIOZ.

Mienis, F., De Stigter, H., De Haas, H., Van der Land, C., and Van Weering, T. (2012). Hydrodynamic conditions in a cold-water coral mound area on the Renard Ridge, southern Gulf of Cadiz. *Journal of Marine Systems*, 96:61–71.

Moctar, S. M., Buhl-Mortensen, L., El Vadhel, H., Kide, S. O., Kutti, T., Sarre, A., Mahmoud, M. E. K. M., Chierici, M., Niang, M., and Johansen, Y. (2024). Lophelia reefs (Desmophyllum pertusum (Linnaeus, 1758)) in the oxygen minimum zone of the Mauritania/Senegal region–Distribution and health status. *Deep Sea Research Part I: Oceanographic Research Papers*, 208:104322.

Montagna, P., McCulloch, M., Douville, E., Correa, M. L., Trotter, J., Rodolfo-Metalpa, R., Dissard, D., Ferrier-Pages, C., Frank, N., and Freiwald, A. (2014). Li/Mg systematics in scleractinian corals: Calibration of the thermometer. *Geochimica et Cosmochimica Acta*, 132:288–310.

Mueller, C., Larsson, A., Veuger, B., Middelburg, J., and Van Oevelen, D. (2014). Opportunistic feeding on various organic food sources by the cold-water coral Lophelia pertusa. *Biogeosciences*, 11(1):123–133.

Muscheler, R., Adolphi, F., Heaton, T. J., Ramsey, C. B., Svensson, A., Van Der Plicht, J., and Reimer, P. J. (2020). Testing and improving the IntCal20 calibration curve with independent records. *Radiocarbon*, 62(4):1079–1094.

Naughton, F., Sánchez-Goñi, M. F., Landais, A., Rodrigues, T., Riveiros, N. V., and Toucanne, S. (2023). *The Bølling–Allerød Interstadial*, pages 45–50. Elsevier.

Naumann, M. S., Orejas, C., and Ferrier-Pagès, C. (2014). Species-specific physiological response by the cold-water corals Lophelia pertusa and Madrepora oculata to variations within their natural temperature range. *Deep Sea Research Part II: Topical Studies in Oceanography*, 99:36–41.

NIST (1983). Standard Reference Material 4990C Oxalic acid - International Standard Reference Material for Contemporary Carbon-14. *National Institute of Standards & Technology.*

Nowaczyk, N. R., Arz, H. W., Frank, U., Kind, J., and Plessen, B. (2012). Dynamics of the Laschamp geomagnetic excursion from Black Sea sediments. *Earth and Planetary Science Letters*, 351:54–69.

Palma, C., Lillebø, A. I., Borges, C., Souto, M., Pereira, E., Duarte, A. C., and de Abreu, M. P. (2012). Water column characterisation on the Azores platform and at the sea mounts south of the archipelago. *Marine pollution bulletin*, 64(9):1884–1894.

Paul, A. and Schäfer-Neth, C. (2003). Modeling the water masses of the Atlantic Ocean at the Last Glacial Maximum. *Paleoceanography*, 18(3).

Pederson, C., Mavromatis, V., Dietzel, M., Rollion-Bard, C., Breitenbach, S., Yu, D., Nehrke, G., and Immenhauser, A. (2020). Variation in the diagenetic response of aragonite archives to hydrothermal alteration. *Sedimentary geology*, 406:105716.

Pederson, C. L., Weiss, L., Mavromatis, V., Rollion-Bard, C., Dietzel, M., Neuser, R., and Immenhauser, A. (2019). Significance of fluid chemistry throughout diagenesis of aragonitic Porites corals–An experimental approach. *The Depositional Record*, 5(3):592–612.

Pedro, J., Andersson, C., Vettoretti, G., Voelker, A., Waelbroeck, C., Dokken, T. M., Jensen, M. F., Rasmussen, S., Sessford, E., and Jochum, M. (2022). Dansgaard-Oeschger and Heinrich event temperature anomalies in the North Atlantic set by sea ice, frontal position and thermocline structure. *Quaternary Science Reviews*, 289:107599.

Pedro, J. B., Bostock, H. C., Bitz, C. M., He, F., Vandergoes, M. J., Steig, E. J., Chase, B. M., Krause, C. E., Rasmussen, S. O., and Markle, B. R. (2016). The spatial extent and dynamics of the Antarctic Cold Reversal. *Nature Geoscience*, 9(1):51–55.

Petit, J. R., Jouzel, J., Raynaud, D., Barkov, N. I., Barnola, J. M., Basile, I., Bender, M., Chappellaz, J., Davis, M., Delaygue, G., Delmotte, M., Kotlyakov, V. M., Legrand, M., Lipenkov, V. Y., Lorius, C., PÉpin, L., Ritz, C., Saltzman, E., and

Stievenard, M. (1999). Climate and atmospheric history of the past 420,000 years from the Vostok ice core, Antarctica. *Nature*, 399(6735):429–436.

Peña-Izquierdo, J., van Sebille, E., Pelegrí, J. L., Sprintall, J., Mason, E., Llanillo, P. J., and Machín, F. (2015). Water mass pathways to the North Atlantic oxygen minimum zone. *Journal of Geophysical Research: Oceans*, 120(5):3350–3372.

Pichler, T. and Veizer, J. (2004). The precipitation of aragonite from shallow-water hydrothermal fluids in a coral reef, Tutum Bay, Ambitle Island, Papua New Guinea. *Chemical Geology*, 207(1-2):31–45.

Pons-Branchu, E., Hillaire-Marcel, C., Deschamps, P., Ghaleb, B., and Sinclair, D. J. (2005). Early diagenesis impact on precise U-series dating of deep-sea corals: Example of a 100–200-year old Lophelia pertusa sample from the northeast Atlantic. *Geochimica et Cosmochimica Acta*, 69(20):4865–4879.

Prange, M., Lohmann, G., Romanova, V., and Butzin, M. (2004). Modelling tempo-spatial signatures of Heinrich Events: influence of the climatic background state. *Quaternary Science Reviews*, 23(5-6):521–527.

Quinn, T. M. and Taylor, F. W. (2006). SST artifacts in coral proxy records produced by early marine diagenesis in a modern coral from Rabaul, Papua New Guinea. *Geophysical Research Letters*, 33(4).

Raddatz, J., Beisel, E., Butzin, M., Schröder-Ritzrau, A., Betzler, C., Friedrich, R., and Frank, N. (2023). Variable ventilation ages in the equatorial Indian Ocean thermocline during the LGM. *Scientific Reports*, 13(1):11355.

Raddatz, J., Liebetrau, V., Rüggeberg, A., Hathorne, E., Krabbenhöft, A., Eisenhauer, A., Böhm, F., Vollstaedt, H., Fietzke, J., Correa, M. L., et al. (2013). Stable Sr-isotope, Sr/Ca, Mg/Ca, Li/Ca and Mg/Li ratios in the scleractinian cold-water coral lophelia pertusa. *Chemical Geology*, 352:143–152.

Raddatz, J., Liebetrau, V., Trotter, J., Rüggeberg, A., Flögel, S., Dullo, W., Eisenhauer, A., Voigt, S., and McCulloch, M. (2016). Environmental constraints on Holocene cold-water coral reef growth off Norway: Insights from a multiproxy approach. *Paleoceanography*, 31(10):1350–1367.

Raddatz, J., Titschack, J., Frank, N., Freiwald, A., Conforti, A., Osborne, A., Skornitzke, S., Stiller, W., Rüggeberg, A., and Voigt, S. (2020). Solenosmilia variabilis-bearing cold-water coral mounds off Brazil. *Coral Reefs*, 39:69–83.

Rafter, P. A., Carriquiry, J. D., Herguera, J., Hain, M. P., Solomon, E. A., and Southon, J. R. (2019). Anomalous > 2000-year-old surface ocean radiocarbon age as evidence for deglacial geologic carbon release. *Geophysical Research Letters*, 46(23):13950–13960.

Rafter, P. A., Gray, W. R., Hines, S. K., Burke, A., Costa, K. M., Gottschalk, J., Hain, M. P., Rae, J. W., Southon, J. R., and Walczak, M. H. (2022). Global reorganization of deep-sea circulation and carbon storage after the last ice age. *Science Advances*, 8(46).

Rafter, P. A., Herguera, J.-C., and Southon, J. R. (2018). Extreme lowering of deglacial seawater radiocarbon recorded by both epifaunal and infaunal benthic foraminifera in a wood-dated sediment core. *Climate of the Past*, 14(12):1977–1989.

Rahmstorf, S. (2002). Ocean circulation and climate during the past 120,000 years. *Nature*, 419(6903):207–214.

Rahmstorf, S. (2006). Thermohaline ocean circulation. *Encyclopedia of quaternary sciences*, 5(18):191.

Rampmeier, J. L. (2021). Glaziale Zwischenwassertemperaturen nahe der Azorenfront: Li/Mg-Verhältnis in Kaltwasserkorallen unter dem Einfluss hydrothermaler Aktivität. *Bachelorarbeit, Heidelberg University, Germany.*

Rashid, R., Eisenhauer, A., Liebetrau, V., Fietzke, J., Böhm, F., Wall, M., Krause, S., Rüggeberg, A., Dullo, W.-C., and Jurikova, H. (2020). Early diagenetic imprint on temperature proxies in holocene corals: a case study from french polynesia. *Frontiers in Earth Science*, 8:301.

Rasmussen, S. O., Bigler, M., Blockley, S. P., Blunier, T., Buchardt, S. L., Clausen, H. B., Cvijanovic, I., Dahl-Jensen, D., Johnsen, S. J., and Fischer, H. (2014). A stratigraphic framework for abrupt climatic changes during the Last Glacial period based on three synchronized Greenland ice-core records: refining and extending the INTIMATE event stratigraphy. *Quaternary science reviews*, 106:14–28.

Reimer, P. J., Austin, W. E., Bard, E., Bayliss, A., Blackwell, P. G., Ramsey, C. B., Butzin, M., Cheng, H., Edwards, R. L., and Friedrich, M. (2020). The IntCal20 Northern Hemisphere radiocarbon age calibration curve (0–55 cal kBP). *Radiocarbon*, 62(4):725–757.

Reimer, P. J., Baillie, M. G. L., Bard, E., Bayliss, A., Beck, J. W., Blackwell, P. G., Bronk Ramsey, C., Buck, C. E., Burr, G. S., Edwards, R. L., Friedrich, M., Grootes, P. M., Guilderson, T. P., Hajdas, I., Heaton, T. J., Hogg, A. G., Hughen, K. A., Kaiser, K. F., Kromer, B., McCormac, F. G., Manning, S. W., Reimer, R. W., Richards, D. A., Southon, J. R., Talamo, S., Turney, C. S. M., van der Plicht, J., and Weyhenmeyer, C. E. (2009). IntCal09 and Marine09 Radiocarbon Age Calibration Curves, 0–50,000 Years cal BP. *Radiocarbon*, 51(4):1111–1150.

Reimer, P. J., Bard, E., Bayliss, A., Beck, J. W., Blackwell, P. G., Ramsey, C. B., Buck, C. E., Cheng, H., Edwards, R. L., and Friedrich, M. (2013). IntCal13 and Marine13 radiocarbon age calibration curves 0–50,000 years cal BP. *Radiocarbon*, 55(4):1869–1887.

Reißig, S., Nürnberg, D., Bahr, A., Poggemann, D., and Hoffmann, J. (2019). Southward displacement of the North Atlantic subtropical gyre circulation system during North Atlantic cold spells. *Paleoceanography and Paleoclimatology*, 34(5):866–885.

Roberts, J. M. (2009). *Cold-water corals: the biology and geology of deep-sea coral habitats*. Cambridge University Press.

Roberts, J. M., Wheeler, A. J., and Freiwald, A. (2006). Reefs of the deep: the biology and geology of cold-water coral ecosystems. *Science*, 312(5773):543–547.

Roberts, M. L. and Southon, J. R. (2007). A preliminary determination of the absolute $^{14}C/^{12}C$ ratio of OX-I. *Radiocarbon*, 49(2):441–445.

Robinson, L. F., Adkins, J. F., Fernandez, D. P., Burnett, D. S., Wang, S., Gagnon, A. C., and Krakauer, N. (2006). Primary U distribution in scleractinian corals and its implications for U series dating. *Geochemistry, Geophysics, Geosystems*, 7(5).

Robinson, L. F., Adkins, J. F., Frank, N., Gagnon, A. C., Prouty, N. G., Roark, E. B., and Van de Flierdt, T. (2014). The geochemistry of deep-sea coral skeletons: a review of vital effects and applications for palaeoceanography. *Deep Sea Research Part II: Topical Studies in Oceanography*, 99:184–198.

Robinson, L. F., Adkins, J. F., Keigwin, L. D., Southon, J., Fernandez, D. P., Wang, S.-L., and Scheirer, D. S. (2005). Radiocarbon variability in the western North Atlantic during the last deglaciation. *Science*, 310(5753):1469–1473.

Robinson, L. F., Adkins, J. F., Scheirer, D. S., Fernandez, D. P., Gagnon, A., and Waller, R. G. (2007). Deep-sea scleractinian coral age and depth distributions in the northwest Atlantic for the last 225,000 years. *Bulletin of Marine Science*, 81(3):371–391.

Robinson, L. F., Henderson, G. M., Hall, L., and Matthews, I. (2004). Climatic control of riverine and seawater uranium-isotope ratios. *Science*, 305(5685):851–854.

Roesch, C. (2017). Tiefseekorallen vor Angola: Archive der tropischen Zwischenwasserdynamik seit der letzten Eiszeit. *Bachelorarbeit, Heidelberg University, Germany.*

Rollion-Bard, C., Blamart, D., Cuif, J.-P., and Juillet-Leclerc, A. (2003). Microanalysis of C and O isotopes of azooxanthellate and zooxanthellate corals by ion microprobe. *Coral Reefs*, 22:405–415.

Romero, O. E., Kim, J., and Donner, B. (2008). Submillennial-to-millennial variability of diatom production off Mauritania, NW Africa, during the last glacial cycle. *Paleoceanography*, 23(3).

Ronge, T. A., Prange, M., Mollenhauer, G., Ellinghausen, M., Kuhn, G., and Tiedemann, R. (2020). Radiocarbon evidence for the contribution of the Southern Indian Ocean to the evolution of atmospheric CO_2 over the last 32,000 years. *Paleoceanography and Paleoclimatology*, 35(3):e2019PA003733.

Ronge, T. A., Sarnthein, M., Roberts, J., Lamy, F., and Tiedemann, R. (2019). East Pacific Rise core PS75/059-2: Glacial-to-deglacial stratigraphy revisited. *Paleoceanography and Paleoclimatology*, 34(4):432–435.

Ronge, T. A., Tiedemann, R., Lamy, F., Köhler, P., Alloway, B. V., De Pol-Holz, R., Pahnke, K., Southon, J., and Wacker, L. (2016). Radiocarbon constraints on the extent and evolution of the South Pacific glacial carbon pool. *Nature communications*, 7(1):11487.

Rozanski, K., Stichler, W., Gonfiantini, R., Scott, E., Beukens, R., Kromer, B., and Van Der Plicht, J. (1992). The IAEA ^{14}C intercomparison exercise 1990. *Radiocarbon*, 34(3):506–519.

Ruckelshausen, M. (2009). *Rekonstruktion von Tiefenwasseraltern während der Heinrich-Ereignisse H1 und H2 anhand von Tiefseekorallen vor Brasilien*. Diplomarbeit, Heidelberg University, Germany.

Ruckelshausen, M. (2013). *Cold-water corals: A paleoceanographic archive; Tracing past ocean circulation changes in the mid-depth subtropical western South Atlantic off Brazil for the last 40 ka BP*. Dissertation, Heidelberg University, Germany.

Sabatier, P., Reyss, J.-L., Hall-Spencer, J. M., Colin, C., Frank, N., Tisnerat-Laborde, N., Bordier, L., and Douville, E. (2012). ^{210}Pb-^{226}Ra chronology reveals rapid growth rate of Madrepora oculata and Lophelia pertusa on world's largest cold-water coral reef. *Biogeosciences*, 9(3):1253–1265.

Sanz, J. L., Maestro, A., and Agudo, L. M. (2017). The Mauritanian margin. Bathymetric and geomorphological characteristics. *Deep-sea ecosystems off Mauritania: research of marine biodiversity and habitats in the Northwest African margin*, pages 53–117.

Sassen, R., Milkov, A. V., Ozgul, E., Roberts, H. H., Hunt, J. L., Beeunas, M. A., Chanton, J. P., DeFreitas, D. A., and Sweet, S. T. (2003). Gas venting and subsurface charge in the Green Canyon area, Gulf of Mexico continental slope: evidence of a deep bacterial methane source? *Organic Geochemistry*, 34(10):1455–1464.

Sayani, H. R., Cobb, K. M., Cohen, A. L., Elliott, W. C., Nurhati, I. S., Dunbar, R. B., Rose, K. A., and Zaunbrecher, L. K. (2011). Effects of diagenesis on paleoclimate reconstructions from modern and young fossil corals. *Geochimica et Cosmochimica Acta*, 75(21):6361–6373.

Schiebel, R., Schmuker, B., Alves, M., and Hemleben, C. (2002). Tracking the Recent and late Pleistocene Azores front by the distribution of planktic foraminifers. *Journal of marine systems*, 37(1-3):213–227.

Schlitzer, R. (2023). Ocean data view.

Schmittner, A. (2003). Southern Ocean sea ice and radiocarbon ages of glacial bottom waters. *Earth and Planetary Science Letters*, 213(1-2):53–62.

Schneider, H. S. (2018). Cold-water corals Reconstruction of paleoenvironmental history off Mauritania. *Masterarbeit, Heidelberg University, Germany.*

Scholz, D. and Mangini, A. (2007). How precise are U-series coral ages? *Geochimica et cosmochimica acta*, 71(8):1935–1948.

Scholz, D., Mangini, A., and Felis, T. (2004). U-series dating of diagenetically altered fossil reef corals. *Earth and Planetary Science Letters*, 218(1-2):163–178.

Schreiber, S. J. (2023). Cold-water coral Ba/Ca and multi-element tracers of thermocline water temperature and nutrients of Angola since the LGM. *Masterarbeit, Heidelberg University, Germany.*

Schröder-Ritzrau, A., Freiwald, A., and Mangini, A. (2005). U/Th-dating of deep-water corals from the eastern North Atlantic and the western Mediterranean Sea. *Cold-water corals and ecosystems*, pages 157–172.

Schröder-Ritzrau, A., Mangini, A., and Lomitschka, M. (2003). Deep-sea corals evidence periodic reduced ventilation in the North Atlantic during the LGM/Holocene transition. *Earth and Planetary Science Letters*, 216(3):399–410.

Shulmeister, J., Thackray, G. D., Rittenour, T. M., Fink, D., and Patton, N. R. (2019). The timing and nature of the last glacial cycle in New Zealand. *Quaternary Science Reviews*, 206:1–20.

Sigman, D. M. and Boyle, E. A. (2000). Glacial/interglacial variations in atmospheric carbon dioxide. *Nature*, 407(6806):859–869.

Singer, B. S. (2014). A quaternary geomagnetic instability time scale. *Quaternary Geochronology*, 21:29–52.

Skinner, L. and Bard, E. (2022). Radiocarbon as a dating tool and tracer in paleoceanography. *Reviews of Geophysics*, 60(1).

Skinner, L., Freeman, E., Hodell, D., Waelbroeck, C., Vazquez Riveiros, N., and Scrivner, A. (2021). Atlantic ocean ventilation changes across the last deglaciation and their carbon cycle implications. *Paleoceanography and Paleoclimatology*, 36(2):e2020PA004074.

Skinner, L., Muschitiello, F., and Scrivner, A. (2019). Marine reservoir age variability over the last deglaciation: implications for marine carboncycling and prospects for regional radiocarbon calibrations. *Paleoceanography and Paleoclimatology*, 34(11):1807–1815.

Skinner, L., Primeau, F., Freeman, E., de la Fuente, M., Goodwin, P., Gottschalk, J., Huang, E., McCave, I. N., Noble, T., and Scrivner, A. (2017). Radiocarbon constraints on the glacial ocean circulation and its impact on atmospheric CO_2. *Nature Communications*, 8(1):1–10.

Skinner, L. and Shackleton, N. (2004). Rapid transient changes in northeast Atlantic deep water ventilation age across Termination I. *Paleoceanography*, 19(2).

Skinner, L. C., Fallon, S., Waelbroeck, C., Michel, E., and Barker, S. (2010). Ventilation of the deep Southern Ocean and deglacial CO_2 rise. *science*, 328(5982):1147–1151.

Skinner, L. C., Primeau, F., Jeltsch-Thömmes, A., Joos, F., Köhler, P., and Bard, E. (2023). Rejuvenating the ocean: mean ocean radiocarbon, CO_2 release, and radiocarbon budget closure across the last deglaciation. *Climate of the Past Discussions*, 2023:1–45.

Skinner, L. C., Waelbroeck, C., Scrivner, A. E., and Fallon, S. J. (2014). Radiocarbon evidence for alternating northern and southern sources of ventilation of the deep Atlantic carbon pool during the last deglaciation. *Proceedings of the National Academy of Sciences*, 111(15):5480–5484.

Slowey, N. C. and Curry, W. B. (1992). Enhanced ventilation of the North Atlantic subtropical gyre thermocline during the last glaciation. *Nature*, 358(6388):665–668.

Smith, J. E., Risk, M. J., Schwarcz, H. P., and McConnaughey, T. A. (1997). Rapid climate change in the North Atlantic during the Younger Dryas recorded by deep-sea corals. *Nature*, 386(6627):818–820.

Smith, J. E., Schwarcz, H. P., Risk, M. J., McCONNAUGHEY, T. A., and Keller, N. (2000). Paleotemperatures from deep-sea corals: overcoming 'vital effects'. *Palaios*, 15(1):25–32.

Somoza, L., Dıaz-del Rıo, V., León, R., Ivanov, M., Fernández-Puga, M., Gardner, J., Hernández-Molina, F., Pinheiro, L., Rodero, J., and Lobato, A. (2003). Seabed morphology and hydrocarbon seepage in the Gulf of Cadiz mud volcano area: Acoustic imagery, multibeam and ultra-high resolution seismic data. *Marine geology*, 195(1-4):153–176.

Soulet, G., Skinner, L. C., Beaupré, S. R., and Galy, V. (2016). A note on reporting of reservoir ^{14}C disequilibria and age offsets. *Radiocarbon*, 58(1):205–211.

Stanford, J. D., Rohling, E. J., Hunter, S. E., Roberts, A. P., Rasmussen, S. O., Bard, E., McManus, J., and Fairbanks, R. G. (2006). Timing of meltwater pulse 1a and climate responses to meltwater injections. *Paleoceanography*, 21(4).

Steinhof, A., Altenburg, M., and Machts, H. (2017). Sample preparation at the Jena ^{14}C laboratory. *Radiocarbon*, 59(3):815–830.

Stellbrink, M. (2023). Diagenesis of Corals and its Impact on U-Th Dating. *Bachelorarbeit, Heidelberg University, Germany.*

Stenström, K., Skog, G., Georgiadou, E., Genberg, J., and Mellström, A. (2011). A guide to radiocarbon units and calculations.

Stewart, J. A., Robinson, L. F., Rae, J. W., Burke, A., Chen, T., Li, T., de Carvalho Ferreira, M. L., and Fornari, D. J. (2023). Arctic and Antarctic forcing of ocean interior warming during the last deglaciation. *Scientific Reports*, 13(1):22410.

Stott, L., Davy, B., Shao, J., Coffin, R., Pecher, I., Neil, H., Rose, P., and Bialas, J. (2019). CO_2 release from pockmarks on the Chatham Rise-Bounty Trough at the glacial termination. *Paleoceanography and Paleoclimatology*, 34(11):1726–1743.

Stott, L., Southon, J., Timmermann, A., and Koutavas, A. (2009). Radiocarbon age anomaly at intermediate water depth in the Pacific Ocean during the last deglaciation. *Paleoceanography*, 24(2).

Stott, L. D. (2023). How old is too old? Implications of averaging ^{14}C-based estimates of ventilation age to assess the Pacific Ocean's role in sequestering CO_2 in the past. *Quaternary Science Reviews*, 310:108122.

Struve, T., Wilson, D. J., Hines, S. K., Adkins, J. F., and van de Flierdt, T. (2022). A deep Tasman outflow of Pacific waters during the last glacial period. *Nature Communications*, 13(1):3763.

Stuhrmann, L. A. K. (2023). U isotopic composition of seawater and corals. *Bachelorarbeit, Heidelberg University, Germany.*

Stuiver, M. (1983). International agreements and the use of the new oxalic acid standard. *Radiocarbon*, 25(2):793–795.

Stuiver, M., Pearson, G. W., and Braziunas, T. (1986). Radiocarbon age calibration of marine samples back to 9000 cal yr BP. *Radiocarbon*, 28(2B):980–1021.

Stuiver, M. and Polach, H. A. (1977). Discussion reporting of ^{14}C data. *Radiocarbon*, 19(3):355–363.

Stuiver, M. and Robinson, S. W. (1974). University of Washington GEOSECS north Atlantic carbon-14 results. *Earth and Planetary Science Letters*, 23(1):87–90.

Stuiver, M. and Suess, H. E. (1966). On the relationship between radiocarbon dates and true sample ages. *Radiocarbon*, 8:534–540.

Sumida, P. Y. G., Yoshinaga, M. Y., Madureira, L. A. S.-P., and Hovland, M. (2004). Seabed pockmarks associated with deepwater corals off SE Brazilian continental slope, Santos Basin. *Marine Geology*, 207(1-4):159–167.

Sweeney, C., Gloor, E., Jacobson, A. R., Key, R. M., McKinley, G., Sarmiento, J. L., and Wanninkhof, R. (2007). Constraining global air-sea gas exchange for CO_2 with recent bomb 14C measurements. *Global biogeochemical cycles*, 21(2).

Synal, H.-A., Stocker, M., and Suter, M. (2007). MICADAS: A new compact radiocarbon AMS system. *Nuclear Instruments and Methods in Physics Research Section B: Beam Interactions with Materials and Atoms*, 259(1):7–13.

Talley, L. D. (2013). Closure of the global overturning circulation through the Indian, Pacific, and Southern Oceans: schematics and transports. *Oceanography*, 26.

Therre, S. (2020). *Radiocarbon in Stalagmites: Indicator of Climate Variability and Key to Atmospheric Radiocarbon Reconstruction.* Dissertation, Heidelberg University, Germany.

Therre, S., Fohlmeister, J., Fleitmann, D., Matter, A., Burns, S. J., Arps, J., Schröder-Ritzrau, A., Friedrich, R., and Frank, N. (2020). Climate-induced speleothem radiocarbon variability on Socotra Island from the Last Glacial Maximum to the Younger Dryas. *Climate of the Past*, 16(1):409–421.

Therre, S., Proß, L., Friedrich, R., Trüssel, M., and Frank, N. (2021). Heidelberg radiocarbon lab – establishing a new carbon dioxide extraction line for carbonate samples. *Radiocarbon*, 63:1–10.

Thiagarajan, N., Subhas, A. V., Southon, J. R., Eiler, J. M., and Adkins, J. F. (2014). Abrupt pre-Bølling–Allerød warming and circulation changes in the deep ocean. *Nature*, 511(7507):75–78.

Thierens, M., Browning, E., Pirlet, H., Loutre, M.-F., Dorschel, B., Huvenne, V. A., Titschack, J., Colin, C., Foubert, A., and Wheeler, A. (2013). Cold-water coral carbonate mounds as unique palaeo-archives: the Plio-Pleistocene Challenger Mound record (NE Atlantic). *Quaternary Science Reviews*, 73:14–30.

Thompson, W. G., Spiegelman, M. W., Goldstein, S. L., and Speed, R. C. (2003). An open-system model for U-series age determinations of fossil corals. *Earth and Planetary Science Letters*, 210(1-2):365–381.

Thornalley, D. J., Barker, S., Broecker, W. S., Elderfield, H., and McCave, I. N. (2011). The deglacial evolution of North Atlantic deep convection. *science*, 331(6014):202–205.

Tisnérat-Laborde, N., Poupeau, J., Tannau, J., and Paterne, M. (2001). Development of a semi-automated system for routine preparation of carbonate samples. *Radiocarbon*, 43(2A):299–304.

Titschack, J., Baum, D., De Pol-Holz, R., Lopez Correa, M., Forster, N., Flögel, S., Hebbeln, D., and Freiwald, A. (2015). Aggradation and carbonate accumulation of Holocene Norwegian cold-water coral reefs. *Sedimentology*, 62(7):1873–1898.

Toggweiler, J., Dixon, K., and Bryan, K. (1989). Simulations of radiocarbon in a coarse-resolution world ocean model: 1. Steady state prebomb distributions. *Journal of Geophysical Research: Oceans*, 94(C6):8217–8242.

Trotter, J. A., McCulloch, M. T., D'Olivo, J. P., Scott, P., Tisnérat-Laborde, N., Taviani, M., and Montagna, P. (2022). Deep-water coral records of glacial and recent ocean-atmosphere dynamics from the Perth Canyon in the southeast Indian Ocean. *Quaternary Science Advances*, page 100052.

Unkel, I. (2006). *AMS-14C-Analysen zur Rekonstruktion der Landschafts- und Kulturgeschichte in der Region Palpa (S-Peru).* Dissertation, Heidelberg University, Germany.

Van Rooij, D., Blamart, D., scientists, and the Microsystem shipboard (2008). Cruise report MD169 MiCROSYSTEMS Brest (FR) - Algeciras (SP) 15 - 25 July 2008 ESF Eurodiversity MiCROSYSTEMS Internal Report. Report.

Van Rooij, D., Depreiter, D., Bouimetarhan, I., De Boever, E., De Rycker, K., Foubert, A., Huvenne, V., Réveillaud, J., Staelens, P., and Vercruysse, J. (2005). First sighting of active fluid venting in the Gulf of Cadiz. *Eos, Transactions American Geophysical Union*, 86(49):509–511.

Van Rooij, D., Hebbeln, D., Comas, M., Vandorpe, T., Delivet, S., and the MD194 shipboard scientists (2013). EuroFLEETS Cruise Summary Report „MD194 GATEWAY“, Cádiz (ES) - Lissabon (PT), 10-21 June 2013. Report.

Veitch, J., Penven, P., and Shillington, F. (2010). Modeling equilibrium dynamics of the Benguela Current System. *Journal of Physical Oceanography*, 40(9):1942–1964.

Venugopal, A. U., Bertler, N. A., Severinghaus, J. P., Brook, E. J., Cortese, G., Lee, J. E., Blunier, T., Mayewski, P. A., Kjær, H. A., Carter, L., et al. (2023). Antarctic evidence for an abrupt northward shift of the Southern Hemisphere westerlies at 32 ka BP. *Nature Communications*, 14(1):5432.

Villemant, B. and Feuillet, N. (2003). Dating open systems by the ^{238}U–^{234}U–^{230}Th method: application to Quaternary reef terraces. *Earth and Planetary Science Letters*, 210(1-2):105–118.

Voarintsoa, N. R. G. and Therre, S. (2022). Using the triple proxy δ^{13}C–radiocarbon–major and trace elements to understand stalagmite stable carbon composition in madagascar. *Chemical Geology*, 608:121044.

Waelbroeck, C., Duplessy, J.-C., Michel, E., Labeyrie, L., Paillard, D., and Duprat, J. (2001). The timing of the last deglaciation in North Atlantic climate records. *Nature*, 412(6848):724–727.

WAIS (2013). Onset of deglacial warming in West Antarctica driven by local orbital forcing. *Nature*, 500(7463):440–444.

WAIS (2015). Precise interpolar phasing of abrupt climate change during the last ice age. *Nature*, 520(7549):661–665.

Walker, M., Johnsen, S., Rasmussen, S. O., Popp, T., Steffensen, J., Gibbard, P., Hoek, W., Lowe, J., Andrews, J., and Björck, S. (2009). Formal definition and dating of the GSSP (Global Stratotype Section and Point) for the base of the Holocene using the Greenland NGRIP ice core, and selected auxiliary records. *Journal of Quaternary Science: Published for the Quaternary Research Association*, 24(1):3–17.

Wall, M., Ragazzola, F., Foster, L. C., Form, A., and Schmidt, D. N. (2015). pH up-regulation as a potential mechanism for the cold-water coral Lophelia pertusa to sustain growth in aragonite undersaturated conditions. *Biogeosciences*, 12(23):6869–6880.

Wang, M., Xu, K., Li, T., Robinson, L. F., Liu, Y., Shao, Q., Li, G., and Chen, T. (2022). The mineralization and early diagenesis of deep-sea coral Madrepora oculata. *Chemical Geology*, 606:120966.

Wefing, A.-M., Arps, J., Blaser, P., Wienberg, C., Hebbeln, D., and Frank, N. (2017). High precision U-series dating of scleractinian cold-water corals using an automated chromatographic U and Th extraction. *Chemical Geology*, 475:140–148.

Westphal, H., Beuck, L., Braun, S., Freiwald, A., Hanebuth, T., Hetzinger, S., Klicpera, A., Kudrass, H., Lantzsch, H., Lundälv, T., Vicens, G. M., Preto, N., Reumont, J. v., Schilling, S., Taviani, M., and Wienberg, C. (2014). Phaeton - Paleoceanographic and paleo-climatic record on the Mauritanian Shelf – Cruise No. MSM16/3 - October 13 – November 20, 2010 - Bremerhaven (Germany) – Mindelo (Cap Verde). MARIA S. MERIAN-Berichte, MSM16/3. *DFG-Senatskommission für Ozeanographie*.

Whiticar, M. J. (1999). Carbon and hydrogen isotope systematics of bacterial formation and oxidation of methane. *Chemical Geology*, 161(1-3):291–314.

Wienberg, C., Frank, N., Mertens, K. N., Stuut, J.-B., Marchant, M., Fietzke, J., Mienis, F., and Hebbeln, D. (2010). Glacial cold-water coral growth in the Gulf of Cádiz: Implications of increased palaeo-productivity. *Earth and Planetary Science Letters*, 298(3-4):405–416.

Wienberg, C., Freiwald, A., Frank, N., Mienis, F., Titschack, J., Orejas, C., and Hebbeln, D. (2023). Cold-water coral reefs in the oxygen minimum zones off west africa. In *Cold-Water Coral Reefs of the World*, pages 199–235. Springer.

Wienberg, C., Hebbeln, D., Fink, H. G., Mienis, F., Dorschel, B., Vertino, A., Correa, M. L., and Freiwald, A. (2009). Scleractinian cold-water corals in the Gulf of Cádiz—first clues about their spatial and temporal distribution. *Deep Sea Research Part I: Oceanographic Research Papers*, 56(10):1873–1893.

Wienberg, C., Krengel, T., Frank, N., Wang, H., Van Rooij, D., and Hebbeln, D. (2022). Cold-water coral mounds in the western Mediterranean Sea: New insights into their initiation and development since the Mid-Pleistocene in response to changes of African hydroclimate. *Quaternary Science Reviews*, 293:107723.

Wienberg, C. and Titschack, J. (2016). Framework-forming scleractinian cold-water corals through space and time: a late Quaternary North Atlantic perspective. *In: Marine Animal Forests, Springer.*

Wienberg, C., Titschack, J., Frank, N., De Pol-Holz, R., Fietzke, J., Eisele, M., Kremer, A., and Hebbeln, D. (2020). Deglacial upslope shift of NE Atlantic intermediate waters controlled slope erosion and cold-water coral mound formation (Porcupine Seabight, Irish margin). *Quaternary Science Reviews*, 237:106310.

Wienberg, C., Titschack, J., Freiwald, A., Frank, N., Lundälv, T., Taviani, M., Beuck, L., Schröder-Ritzrau, A., Krengel, T., and Hebbeln, D. (2018). The giant Mauritanian cold-water coral mound province: Oxygen control on coral mound formation. *Quaternary Science Reviews*, 185:135–152.

Williams, T. J., Martin, E. E., Sikes, E., Starr, A., Umling, N. E., and Glaubke, R. (2021). Neodymium isotope evidence for coupled Southern Ocean circulation and Antarctic climate throughout the last 118,000 years. *Quaternary Science Reviews*, 260:106915.

Yang, J., Davies, R. J., and Huuse, M. (2013). Gas migration below gas hydrates controlled by mass transport complexes, offshore Mauritania. *Marine and Petroleum Geology*, 48:366–378.

Yang, J., Lu, M., Yao, Z., Wang, M., Lu, S., Qi, N., and Xia, Y. (2021). A geophysical review of the Seabed Methane Seepage features and their relationship with gas hydrate systems. *Geofluids*, 2021:1–26.

Yokoyama, Y. and Esat, T. (2004). Long term variations of uranium isotopes and radiocarbon in the surface seawater recorded in corals. *Global environmental change in the ocean and on land*, 1:279–309.

Yokoyama, Y., Lambeck, K., De Deckker, P., Johnston, P., and Fifield, L. K. (2000). Timing of the Last Glacial Maximum from observed sea-level minima. *Nature*, 406(6797):713–716.

Yu, J., Menviel, L., Jin, Z., Anderson, R., Jian, Z., Piotrowski, A., Ma, X., Rohling, E., Zhang, F., and Marino, G. (2020). Last glacial atmospheric CO_2 decline due to widespread Pacific deep-water expansion. *Nature Geoscience*, 13(9):628–633.

Zenk, W., Klein, B., and Schroder, M. (1991). Cape Verde frontal zone. *Deep Sea Research Part A. Oceanographic Research Papers*, 38:S505–S530.

Zhao, N., Marchal, O., Keigwin, L., Amrhein, D., and Gebbie, G. (2018). A synthesis of deglacial deep-sea radiocarbon records and their (in)consistency with modern ocean ventilation. *Paleoceanogr. Paleoclimatol.*, 33.

Zheng, P., Pedro, J. B., Jochum, M., Rasmussen, S. O., and Lai, Z. (2021). Different trends in Antarctic temperature and atmospheric CO_2 during the last glacial. *Geophysical Research Letters*, 48(14):e2021GL093868.

Danksagung

An dieser Stelle möchte ich die Gelegenheit nutzen all jenen zu danken, ohne die diese Doktorarbeit nicht möglich gewesen wäre.

Ein ganz besonderer Dank geht an Prof. Norbert Frank, für die Ermöglichung und Betreuung dieser Doktorarbeit. Dein Enthusiasmus und die zahlreichen wissenschaftlichen Diskussionen haben maßgeblich zur Entwicklung dieser Doktorarbeit beigetragen!

Prof. Werner Aeschbach möchte ich dafür danken, dass er sich bereit erklärt hat, das Zweitgutachten dieser Dissertation zu übernehmen. Vielen Dank auch an Prof. Monika Dunford und Prof. Malte Schäfer, die sich bereit erklärt haben, Teil meines Prüfungskomitees zu sein.

Vielen Dank an Steffen Therre, für die Einführung ins ^{14}C-Labor und die stete Beantwortung von Fragen. Ein großes Dankeschön an Carl Kindermann, für seine hervorragende Arbeit im ^{14}C-Labor. Und natürlich Danke an Ronny Friedrich für das Durchführen der ^{14}C Messungen am AMS in Mannheim.

Ein herzliches Danke an Andrea Schröder-Ritzrau, für die vielen Gespräche rund um Korallen und die stete Unterstützung! Danke an alle Studierenden und HiWis, welche am Korallen putzen, Aufbereiten und Messen von Proben beteiligt waren, insbesondere Athulya Babu, Louisa Brückner, Julia Meissner, Max Stellbrink, Luisa Stuhrmann und Maren Zeleny. Danke an die beiden Projektpraktikantinnen, Dana Hoelkermann und Lucy Boyer, welche zusammen mit Prof. Norbert Frank die Li/Mg Messung und Temperaturrekonstruktion durchgeführt haben. Ein ganz großer Dank geht an René Eichstädter, fürs Durchführen der MC-ICPMS Messung, Auswertung und das Beantworten zahlreicher Fragen. Danke auch an Inga Kerber, welche stehts für Rückfragen bereitstand.

Vielen Dank an Furu Mienis für das Zusenden von Korallenproben und natürlich allen Leitern und Teilnehmern der Forschungsfahrten, die für die Bergung der in dieser Arbeit untersuchten Korallen verantwortlich waren. Die Fahrten wurden von Norbert Frank, Dierk Hebbeln, Hildegard Westphal, Furu Mienis und David Van Rooji organisiert. Vielen Dank, dass ich die Korallen analysieren durfte! Vielen Dank auch an die Arbeitsgruppe Marine Sedimentologie am MARUM und das GeoB Core Repository, welche mir die Beprobung der Sedimentkerne ermöglichten. Ganz besonderer Dank geht hier an Claudia Wienberg, für den herzlichen Empfang, die Beantwortung allerlei Fragen und die Zusammenarbeit! Vielen Dank an Andrea Schröder-Ritzrau und Marleen Lausecker, die mir bei der Beprobung der Sedimentkerne halfen.

Ein großes Dankeschön auch an die zahlreichen Wissenschaftler, mit welchen ich über die Jahre diskutieren und/oder zusammenarbeiten durfte. Dazu gehören neben Norbert Frank auch Andrea Schröder-Ritzrau, Marleen Lausecker, Claudia Wienberg, Martin Butzin, Jacek Raddatz, Ronny Friedrich, Laura Robinson, Florian Adolphi. Vielen Dank auch an Sophie Hines und zwei anonyme Reviewer, welche durch ihre Kommentare zum Paper beigetragen haben. Vielen Dank an Florian Adolphi, der mir unveröffentlichte Modellierungsdaten für die Diskussion meiner Daten zur Verfügung gestellt hat!

Danke an alle PUAs für die schöne Zeit! Danke vor allem auch an die aktiven und ehemaligen PhDs der Gruppe. Danke Steffen, Marleen, Inga, Jasmin, Eva, Sahra, Nils, Aaron und Yao! Vielen Dank and die Korrekturleserinnen dieser Arbeit! Danke Andrea, Marleen, Eva und Sahra!

Ein ganz großes Dankeschön an Eva und Julia, für die zahlreichen Schreib-Treffen und die Unterstützung, insbesondere der letzten Wochen. Wer hätte gedacht das diese Treffen so produktiv sein könnten?

Abschließend möchte ich mich bei meiner Familie und meinen Freunden bedanken, die mich immer unterstützt haben. Ein ganz besonderer Dank geht hier jedoch an Florian. Danke für deine immerwährende Unterstützung und Ermutigung. Danke für Dein offenes Ohr. Ich bin unendlich dankbar, Dich in meinem Leben zu haben!